

Doctoral Dissertation

博士論文

Origin of the X-ray absorbers
in Seyfert 1 galaxies

(セイファート1型銀河におけるX線吸収体の起源)

*A Dissertation Submitted for the Degree of Doctor of Philosophy
December 2022*

令和4年12月 博士（理学）申請

Department of Astronomy, Graduate School of Science,

THE UNIVERSITY OF TOKYO

東京大学大学院理学系研究科天文学専攻

Takuya MIDOOKA

御堂岡 拓哉

Abstract

Observational evidence has clearly indicated the presence of multiple kinds of X-ray absorbers in active galactic nuclei (AGNs), e.g., warm absorbers, ultra-fast outflows (UFOs), and clumpy absorbers. The physical origins of these absorbers have been vigorously studied. For example, some radiation-magnetohydrodynamic simulations have suggested that the hot and strong accretion disk wind gets unstable far from the central region and turns into fragmented gas clumps. These inner wind and outer clumps may be actually observed as the UFOs and the clumpy absorbers, respectively. However, it is challenging to observationally place constraints on the origin of the UFOs and clumpy absorbers due to complicated spectral variations.

In order to resolve such parameter degeneracy of the clumpy absorbers and other spectral components, we have developed a novel technique called “spectral-ratio model fitting”. Taking the spectral ratios of the intensity-sliced spectra enables us to make the spectral variations due to clumpy absorbers noticeable, by canceling out the less time-variable continuum and other absorption components such as warm absorbers.

We systematically applied this method to several Seyfert 1 galaxies to constrain the outflowing velocity of the clumpy absorbers and search for a plausible origin of the outflow and clumps. We found that the spectral-ratio fitting method requires certain conditions to effectively constrain the clump velocities: First, sufficient X-ray photon statistics and time variability are required. In addition, the key to disentangling the parameter degeneracy and deriving the reliable outflow velocity of the X-ray absorbers is the appearance of the dip/cliff structure in the spectral ratios. The dip structure appears only when the spectral variation is caused by a change in the clumpy absorbers and when their parameters (column density N_{H} and ionization parameter ξ) are within a specific range. When all of these conditions are satisfied, we can constrain not only N_{H} and ξ but also the clump velocities.

For all the sources where the dip structures were recognized, we found that the soft spectral variation is mostly explained by changes in the covering fraction of the mildly-ionized clumpy absorbers with constant N_{H} and ξ . We found that the partial covering fraction is smaller, and intrinsic X-ray intensity is higher as the X-ray flux increases. The determined outflow velocities of the clumpy absorber are unexpectedly fast. Furthermore, the velocity tends to be higher with increasing X-ray flux, which has been supported by a model-independent study of the most actively observed target IRAS 13224–3809. Based on the Markov Chain Monte Carlo calculation, we confirmed that the outflow velocity is determined independently, not correlated with other parameters. Assuming that the mass of outflowing gas is constant, the flux dependence of the outflow velocity supports the idea that both the UFOs and clumps are radiatively driven and share the same origin, as suggested by previous simulation studies.

The outflowing clumpy model also provides a plausible explanation of the energy spectra. Previous spectral studies of IRAS 13224–3809 and 1H 0707–495 using conventional models required a strong unexplained absorption edge around 1 keV. Our model naturally explains this residual structure due to blue shifts of the absorption edge/line energies of the outflowing clumpy absorbers.

Comparing the velocities of the UFOs and the clumps, we have found that the clump velocities can be comparable to or even faster than the UFO velocity. We have also found that the clump velocity increase trend with the X-ray flux is steeper than that of

the UFOs. Whereas the increase in UFO velocity is consistent with being driven by the UV-dominant continuum radiation, the steeper increase in the clump velocity may not be explained only by the continuum-driven scenario. This result suggests the possibility that, in addition to the continuum-driven mechanism, the line-driven mechanism contributes to the acceleration of the clumpy absorbers. In fact, while the UFO absorbers with $\log \xi \sim 4$ are highly ionized and transparent in the UV and soft X-ray energy ranges, the clumpy absorbers are mildly ionized at $\log \xi \sim 2.7$, and opaque to most UV and soft X-ray line emission.

We have found that the ionization state of the clumpy absorbers is always $\log \xi \sim 2.7 \pm 0.3$ regardless of the targets and flux levels. According to previous simulation studies, radiation hydrodynamic instability works only at a certain opacity, i.e., a certain ξ , to generate gas clumps. Therefore, the constant ξ of the clumpy absorbers is consistent with the instability scenario. Alternatively, the range of ξ corresponds to where the dip/cliff structure appears in the spectral ratio, so the invariance may be simply due to observational bias.

Contents

List of Figures	5
List of Tables	7
1 Introduction & Review	8
1.1 Active Galactic Nuclei	8
1.1.1 A brief history of the AGNs	8
1.1.2 The Eddington luminosity and Eddington ratio	10
1.1.3 Classification of the AGNs and the unified model	11
1.1.4 Co-evolution and AGN feedback	13
1.2 X-ray spectra of Seyfert 1 galaxies	15
1.2.1 Accretion disk component	16
1.2.2 Power-law component	16
1.2.3 Reflection component	18
1.2.4 Absorption component	18
1.3 Origins of the X-ray absorbers	24
1.3.1 Outflow driving mechanisms	24
1.3.2 Formation of the clumpy absorbers	26
1.3.3 Alternative models	27
1.4 Purpose of this dissertation	28
2 Instrumentation	30
2.1 Overview of the <i>XMM-Newton</i> satellite	30
2.2 X-ray telescopes	32
2.3 European Photon Imaging Camera (EPIC)	35
2.4 Optical Monitor (OM)	40
2.5 Reflection Grating Spectrometer (RGS)	42
3 Systematic Analysis of Seyfert 1 Galaxies	43
3.1 Target selection	43
3.2 Observations and Data reduction	45
3.3 Data analysis and Results	48
3.3.1 Intensity-sliced spectra and spectral ratios	48
3.3.2 Model-independent study of the spectral ratios	54
3.3.3 Introduction of the spectral-ratio model fitting	55
3.3.4 Systematic application of the spectral-ratio model fitting	61

4	Detailed Analysis of the Selected Sources	63
4.1	Simultaneous spectral-ratio model fitting	63
4.1.1	Simultaneous fitting with N_{H} and ξ tied to all the ratios	63
4.1.2	MCMC parameter estimation	70
4.2	Spectral fitting in 0.3–10 keV	77
4.3	UV–X-ray SED fitting	86
5	Discussion	91
5.1	Effectiveness of the spectral-ratio model fitting	91
5.2	The outflowing velocities of the UFO and the clumpy absorbers	93
5.2.1	Relation between the intrinsic UV/X-ray flux and the outflow velocities	97
5.2.2	Possibility of the line-force acceleration of the clumpy absorbers	99
5.2.3	Comparison of the clump velocities and the UFO velocities	102
5.3	The unexplained ~ 1 keV spectral feature	103
5.4	The constant ionization parameter of the clumps	104
6	Conclusion	105
A	Appendix A	107
A.1	Additional plots	107
A.1.1	Spectral-ratio model fitting	107
A.1.2	Simultaneous spectral-ratio model fitting with MCMC	114
	Bibliography	118
	Acknowledgements	128

List of Figures

1.1	An illustration of the standard unified model.	13
1.2	Magorrian relation.	14
1.3	Schematic view of the environments in AGNs and their X-ray spectra. . .	15
1.4	Suggested geometries for an accretion disk and X-ray emitting corona. . .	17
1.5	Power-law spectral shapes absorbed by a neutral or ionized gas.	19
1.6	Ion population of iron as a function of ξ	19
1.7	A illustration of multiphase WAs.	20
1.8	UFO absorption line in IRAS 13224–3809.	21
1.9	X-ray spectra with a seemingly broad Fe-K line in MCG–6-30-15.	22
1.10	Schematic view of a partial covering model.	23
1.11	Force multiplier as a function of t or ξ	25
1.12	Comparison of absorption profiles among various wind driving mechanisms. .	26
1.13	2D structure of the outflow with R-MHD simulation.	27
1.14	X-ray spectra fitted with both the reflection and disk wind models.	28
2.1	A schematic view of the <i>XMM-Newton</i> satellite subsystems.	31
2.2	Picture of one of the X-ray telescopes onboard the <i>XMM-Newton</i> satellite. .	32
2.3	The light path in the two <i>XMM-Newton</i> telescopes.	33
2.4	On-axis effective area of the <i>XMM-Newton</i> telescope.	34
2.5	The CCDs of a MOS camera and the pn camera.	35
2.6	The CCD layout of the MOS1 camera and the pn camera.	35
2.7	Quantum efficiency of the EPIC cameras.	37
2.8	The net effective area of all the <i>XMM-Newton</i> instruments.	38
2.9	Operating modes of the pn CCD camera.	39
2.10	A schematic view of the OM telescope module.	40
2.11	Throughput curves for the OM filters.	41
3.1	The 0.3–10 keV light curve of IRAS 13224–3809.	48
3.2	Intensity-sliced spectra and spectral ratios of IRAS 13224–3809.	50
3.3	Intensity-sliced spectra of sources with a single observation period.	51
3.4	Intensity-sliced spectra of sources with multiple observation periods. . . .	52
3.5	Intensity-sliced spectra of sources with multiple observation periods. . . .	53
3.6	Observed spectral ratios and their 1st derivatives.	54
3.7	Model spectral ratios with variations of CF, N_{H} , and ξ	57
3.8	Model spectral ratios with variations of the velocity and norm.	57
3.9	Observed spectral ratio E/A and its fitted model.	58
3.10	Ratio fitting results of IRAS 13224–3809.	59
3.11	(Cont.) Ratio fitting results of IRAS 13224–3809.	60
4.1	Simultaneous ratio fitting results of IRAS 13224–3809.	64

4.2	(Cont.) Simultaneous ratio fitting results of IRAS 13224–3809.	65
4.3	Best-fit parameters by the simultaneous fitting of IRAS 13224–3809.	65
4.4	The same as Figure 4.1, but for Mrk 335.	66
4.5	The same as Figure 4.3, but for Mrk 335.	66
4.6	The same as Figure 4.1, but for PDS 456.	67
4.7	The same as Figure 4.3, but for PDS 456.	67
4.8	The same as Figure 4.1, but for 1H 0707–495.	68
4.9	The same as Figure 4.3, but for 1H 0707–495.	69
4.10	A corner plot showing the result of the MCMC parameter estimation.	71
4.11	MCMC contours of IRAS 13224–3809.	72
4.12	The same as Figure 4.11, but for Mrk 335.	73
4.13	The same as Figure 4.11, but for PDS 456.	74
4.14	The same as Figure 4.11, but for 1H 0707–495 in the 2008 observation.	75
4.15	The same as Figure 4.11, but for 1H 0707–495 in the 2010 observation.	76
4.16	Intensity-sliced spectra of Mrk 335 with marginal UFO features.	77
4.17	Spectral fitting results of all the spectra of IRAS 13224–3809.	79
4.18	(Cont.) Spectral fitting results of all the spectra of IRAS 13224–3809.	80
4.19	The same as Figure 4.17, but for PDS 456.	81
4.20	The same as Figure 4.17, but for 1H 0707–495 in 2008.	82
4.21	The same as Figure 4.17, but for 1H 0707–495 in 2010.	83
4.22	Broadband UV–X-ray SED fitting of IRAS 13224–3809.	87
4.23	The same as Figure 4.22, but for PDS 456.	88
4.24	The same as Figure 4.22, but for 1H 0707–495 in 2008.	89
4.25	The same as Figure 4.22, but for 1H 0707–495 in 2010.	90
5.1	Velocity comparison between the UFO and clumps of IRAS 13224–3809.	94
5.2	The same as Figure 5.1, but for 1H 0707–495.	95
5.3	The same as Figure 5.1, but for PDS 456.	96
5.4	The same as Figure 5.1, but for Mrk 335.	96
5.5	Synthetic spectra of IRAS 13224–3809 calculated with XSTAR.	100
5.6	Absorbed flux estimated with XSTAR for IRAS 13224–3809.	101
5.7	A schematic view around a SMBH with super-Eddington accretion flow.	101
5.8	Other spectral models without outflowing clumps.	103
A.1	The same as Figure 3.10, but for Mrk 335.	108
A.2	The same as Figure 3.10, but for Mrk 766.	108
A.3	The same as Figure 3.10, but for NGC 985.	109
A.4	The same as Figure 3.10, but for NGC 4051.	109
A.5	The same as Figure 3.10, but for PDS 456.	110
A.6	The same as Figure 3.10, but for 1H 0707–495 in two periods.	111
A.7	The same as Figure 3.10, but for MCG–6-30-15 in two periods.	112
A.8	The same as Figure 3.10, but for NGC 3783 in two periods.	113
A.9	Best-fit parameters of IRAS 13224–3809 by simultaneous ratio fitting.	114
A.10	The same as Figure A.9, but for Mrk 335.	115
A.11	The same as Figure A.9, but for PDS 456.	116
A.12	The same as Figure A.9, but for 1H 0707–495.	117

List of Tables

2.1	Basic characteristics of <i>XMM-Newton</i> .	36
3.1	Observation targets and their characteristics.	44
3.2	<i>XMM-Newton</i> (pn) observation logs.	46
3.2	<i>XMM-Newton</i> (pn) observation logs.	47
3.3	Count rate threshold of the intensity-sliced spectra of IRAS 13224–3809.	49
3.4	Parameter ranges for the spectral-ratio model.	55
3.5	Parameter ranges for a more optimized spectral-ratio model.	59
3.6	Best-fit parameters obtained from spectral-ratio model fitting.	60
3.7	The same as Table 3.6, but for Mrk 335.	61
3.8	The same as Table 3.6, but for PDS 456.	61
3.9	The same as Table 3.6, but for Mrk 766.	61
3.10	The same as Table 3.6, but for NGC 985.	61
3.11	The same as Table 3.6, but for NGC 4051.	62
3.12	The same as Table 3.6, but for 1H 0707–495.	62
3.13	The same as Table 3.6, but for MCG–6-30-15.	62
3.14	The same as Table 3.6, but for NGC 3783.	62
4.1	Best-fit parameters obtained by spectral fitting of IRAS 13224–3809.	84
4.2	The same as Table 4.1 for PDS 456.	85
4.3	The same as Table 4.1 for 1H 0707–495 in 2008.	85
4.4	The same as Table 4.3 for 1H 0707–495 in 2010.	85
4.5	Best-fit parameters determined by the SED fitting of IRAS 13224–3809.	87
4.6	The same as Table 4.5, but for PDS 456.	88
4.7	The same as Table 4.5, but for 1H 0707–495 in 2008.	89
4.8	The same as Table 4.5, but for 1H 0707–495 in 2010.	90
5.1	UV/X-ray intrinsic flux and estimated variation of the outflow velocity	97
5.2	UV/X-ray flux of IRAS 13224–3809.	100

Chapter 1

Introduction & Review

Contents

1.1 Active Galactic Nuclei	8
1.1.1 A brief history of the AGNs	8
1.1.2 The Eddington luminosity and Eddington ratio	10
1.1.3 Classification of the AGNs and the unified model	11
1.1.4 Co-evolution and AGN feedback	13
1.2 X-ray spectra of Seyfert 1 galaxies	15
1.2.1 Accretion disk component	16
1.2.2 Power-law component	16
1.2.3 Reflection component	18
1.2.4 Absorption component	18
1.3 Origins of the X-ray absorbers	24
1.3.1 Outflow driving mechanisms	24
1.3.2 Formation of the clumpy absorbers	26
1.3.3 Alternative models	27
1.4 Purpose of this dissertation	28

1.1 Active Galactic Nuclei

Almost all the galaxies are considered to host supermassive black holes (SMBHs) with masses of 10^5 – $10^{10} M_{\odot}$, where M_{\odot} is the solar mass, at their central region. Accretion of the surrounding matter onto the SMBH releases the gravitational potential energy and radiates electromagnetic waves with a total luminosity of 10^{43} – $10^{47} \text{ erg s}^{-1}$. These bright cores of galaxies are called active galactic nuclei (AGNs).

1.1.1 A brief history of the AGNs

In the early 20th century, optical observation of nearby galaxies detected the first observational evidence for the existence of the AGNs. Fath (1909) obtained low-resolution spectra of seven spiral nebulae including M31, as part of his thesis project, with a self-constructed prism spectrometer. Most of the spectra were dominated by absorption

lines similar to those found in stars, but he noticed that the spectrum of NGC 1068, not yet known to be an extragalactic source, showed strong, broad emission lines. Later, Slipher (1917), Hubble (1926), and others similarly found emission lines in the spectra of NGC 1068, NGC 4151, and NGC 4051.

Seyfert (1943) systematically analyzed the optical spectra of six galaxies (NGC 1068, 1275, 3516, 4051, 4151, and 7469) exhibiting similar spectra with broad and highly-ionized emission lines. He attributed the broad widths of the lines to Doppler shifts and found that the bright nucleus emission dominates in these galaxies. These active galaxies observed in this study are called the “Seyfert galaxies” after his pioneering work. The number of the identified Seyfert galaxies has increased dramatically, and it has become clear that the Seyfert galaxies have unusual properties: extremely compact and bright nuclear region, many broad highly-ionized emission lines (up to $10,000 \text{ km s}^{-1}$), and variable UV-to-optical continuum (e.g., an early review is given by Weedman, 1977). These observations suggest that the Seyfert galaxies have very compact and powerful energy sources at their centers.

In addition to the optical studies, development of the radio astronomy advanced the understanding of the physics of AGNs. Starting with the radio sources Virgo A and Cen A, which were identified as the elliptical galaxies M87 and NGC 5128 respectively (Bolton, Stanley, and Slee, 1949), many radio sources were optically identified by the revised 178 MHz Third Cambridge (3C) Survey (Bennett, 1962) and others. In these surveys, most sources at high galactic latitudes were identified as galaxies, whereas some appeared almost point-like or quasi-stellar images. They are named quasi-stellar radio sources (later abbreviated as “quasars”). Schmidt (1963) found that quasar 3C 273 had a redshift of 0.158, an incredibly large value at the time. He pointed out that the extremely large redshift would signify that the galactic nucleus radiates 100 times more powerfully than any other radio galaxies previously identified. Shortly thereafter, advance of the optical spectroscopy allowed the redshifts of a number of quasars to be measured, including 3C 48 at an even more distant redshift of 0.37 (e.g., Greenstein and Matthews, 1963; Matthews and Sandage, 1963).

Quasars showed exceptionally high luminosity and peculiar spectral features, indicating that their energy sources are not ordinary stars. To explain their observational characteristics, a very compact and powerful energy source with the ability to form highly parallel jets, origin of the quasars had long been heavily debated. Salpeter (1964) argued that the accretion of gas onto a SMBH may be the energy source of quasars. Lynden-Bell (1969) proposed that a SMBH at the center of a nearby galaxy is the remnant of a “dead” quasar and that black hole (BH) accretion is the energy source of the non-stellar emission of nearby Seyfert galaxies. Finally, numerous studies using dynamical modeling of stars, emission-line gas, and molecular masers had established evidence for the existence of the SMBHs in the inner regions of the galaxies in the local universe (e.g., Sargent et al., 1978; Miyoshi et al., 1995; review in Kormendy and Richstone, 1995). Through these studies, quasars were revealed to be the distant and brighter version of the Seyfert galaxies. In the 1960s and 1970s, early X-ray astronomy observations also demonstrated that the Seyfert galaxies and quasars are powerful X-ray sources emitting from the inner regions of the BH accretion disks (e.g., Elvis et al., 1978).

Today, strong radio galaxies, quasars, and Seyfert galaxies are collectively referred to as AGNs. It is believed that all massive galaxies host BHs in their interiors, and as a result, all galaxies have the AGN activity in their lifetimes (see review by Kormendy

and Ho, 2013). The AGNs were once considered rare and exotic objects, but are now regarded as a common stage in the evolution of all the massive galaxies.

1.1.2 The Eddington luminosity and Eddington ratio

The AGNs are generally powered by gas accretion onto central SMBHs. The gas accretion requires that the inward gravitational force be greater than the outward radiation pressure. Because of this requirement, there is an upper limit to the luminosity of a spherically symmetric object, called the ‘‘Eddington luminosity’’. Principally, the gravitational force acts on the protons, while radiation pressure acts on the electrons through Thomson scattering. Let us consider an object whose radiation is isotropic and spherically symmetric, with the mass M and the luminosity L . Assuming the object consists of hydrogen atoms with the mass of m_{H} , the gravitational force F_{g} at a distance r is written as

$$F_{\text{g}} = \frac{GMm_{\text{H}}}{r^2}. \quad (1.1)$$

The radiation force on a single electron F_{r} at a distance r is

$$F_{\text{r}} = \frac{\sigma_{\text{T}}}{c} \frac{L}{4\pi r^2}, \quad (1.2)$$

with σ_{T} being the cross-section of the Thomson scattering. When the gravitational and radiative forces are balanced ($F_{\text{g}} = F_{\text{r}}$), the Eddington luminosity L_{Edd} is derived as

$$L_{\text{Edd}} = \frac{4\pi GMm_{\text{H}}c}{\sigma_{\text{T}}} \sim 1.3 \times 10^{38} \left(\frac{M}{M_{\odot}} \right) \text{ [erg s}^{-1}\text{]}. \quad (1.3)$$

Substituting observed AGN luminosities ($\sim 10^{43-47} \text{ erg s}^{-1}$) to equation (1.3), we can estimate lower limits of the central-object masses in AGNs as $10^{5-9} M_{\odot}$. The central source is believed to be the SMBH, where such a massive object is accommodated in an extremely compact radiating region.

We can also define the Eddington ratio λ_{Edd} as

$$\lambda_{\text{Edd}} = \frac{L}{L_{\text{Edd}}}. \quad (1.4)$$

In the radio-quiet AGNs, radiated luminosity is converted from the mass of the accreting gas with an efficiency of η described as $L = \eta \dot{M}c^2$, where \dot{M} is mass accretion rate in the unit of g s^{-1} . The maximum efficiency η is given by the gravitational potential released at the innermost stable circular orbit (ISCO) of the BH, which depends on the BH spin. The ISCO radius and the radiative efficiency are calculated to be $6 R_{\text{g}}$ and $\eta = 0.06$ for non-rotating Schwarzschild BHs (e.g., Longair, 2011), with $R_{\text{g}} = GM/c^2 \sim 1.5 \left(\frac{M}{M_{\odot}} \right) \text{ km}$ being the so-called gravitational radius. On the other hand, for Kerr BHs rotating at maximum, the ISCO decreases to $1 R_{\text{g}}$, and the efficiency is as high as $\eta = 0.42$ (e.g., Longair, 2011). The mass accretion rate required to radiate at the Eddington luminosity,

with the efficiency of Schwarzschild BHs, is derived

$$\dot{M}_{\text{Edd}} = \frac{L_{\text{Edd}}}{\eta c^2} \quad (1.5)$$

$$\sim 2.4 \times 10^{18} \left(\frac{M}{M_{\odot}} \right) \text{g s}^{-1} \quad (1.6)$$

$$\sim 4 \left(\frac{M}{10^8 M_{\odot}} \right) M_{\odot} \text{yr}^{-1}, \quad (1.7)$$

which is referred to as the Eddington accretion rate. The Eddington luminosity, Eddington accretion rate, and gravitational radius are convenient for comparing the properties of various black holes with different masses. We can also use a normalized accretion rate as $\dot{m} \equiv \dot{M}/\dot{M}_{\text{Edd}}$.

1.1.3 Classification of the AGNs and the unified model

AGN terminology is frequently confusing since the distinctions between various types of AGNs sometimes reflect historical differences in how the objects were discovered or initially classified rather than actual physical differences. One of the convenient classifications is to divide the AGNs into two classes, conventionally called radio-quiet and radio-loud galaxies. Radio-loud objects have emission contributions from both jets and radio lobes, which dominate the luminosity of the AGN at radio wavelengths. Radio-quiet objects exhibit simpler spectral energy distribution (SED) since the jet and any jet-related emission can be neglected at all wavelengths.

Seyfert galaxies and Quasars, representative radio-quiet galaxies, are described in the following subsections. There are various other AGN taxonomies, so refer to some textbooks (e.g., Peterson, 1997; Beckmann and Shrader, 2012) for details.

Seyfert galaxies

Radio-quiet AGNs have historically been divided into two classes depending on their B-band ($\lambda = 442 \text{ nm}$) absolute magnitude of M_{B} . Seyfert galaxies are relatively low-luminosity AGNs with $M_{\text{B}} > -21.5 + 5 \log h_0$, where h_0 is the Hubble constant in units of $100 \text{ km s}^{-1} \text{ Mpc}^{-1}$ (Schmidt and Green, 1983). Their typical luminosity and central SMBH masses are $10^{41-44} \text{ erg s}^{-1}$ and $10^{6-8} M_{\odot}$. Probably because of their modest luminosity, Seyfert galaxies have mainly been discovered in our vicinity, with redshifts of $z < 0.1$. Their host galaxies can be easily resolved, most of which are spiral galaxies.

Their optical spectra show high-excitation ionized emission lines, which allows further classification into two sub-classes, type 1 and type 2, according to the velocity widths of the emission lines (Khachikian and Weedman, 1974). Type 1 Seyfert galaxies show both broad and narrow lines: Balmer lines ($\text{H}\alpha$, $\text{H}\beta$, and $\text{H}\gamma$, etc.) are broader, which typically have line widths of thousands of km s^{-1} , whereas forbidden lines such as $[\text{O II}]$ and $[\text{O III}]$ are narrow, typically have line widths of hundreds of km s^{-1} . On the other hand, type 2 objects show similar line widths for both the Balmer lines and forbidden lines, typically hundreds of km s^{-1} . From a number of systematic optical spectroscopy, approximately 70–80% of Seyfert galaxies are classified as type 2 (e.g., Maiolino and Rieke, 1995; Dwelly and Page, 2006).

Osterbrock (1981) defined more detailed sub-classes between type 1 and type 2. For example, Type 1.9 objects only show broad components in the $H\alpha$ lines, not in higher-order Balmer lines. In Type 1.8, fragile broad lines can be detected in the $H\beta$ lines as well as $H\alpha$, even if they are very weak compared to the $H\alpha$. In Type 1.5, the strength of the $H\alpha$ and $H\beta$ lines are comparable.

Narrow line Seyfert 1 galaxies

There is a special subclass of Seyfert 1 galaxies called narrow-line Seyfert 1 (NLS1) galaxies, defined by their relatively narrow $H\beta$ emission lines ($\text{FWHM} < 2000 \text{ km s}^{-1}$) and their weak [O III] narrow-line emissions compared to $H\beta$, $[\text{O III}]/H\beta < 3$ (Osterbrock and Dahari, 1983; Goodrich, 1989). They typically show strong Fe II emission lines (e.g., Osterbrock and Pogge, 1985). NLS1s usually have steeper X-ray spectra than typical Seyfert 1 galaxies (e.g., Boller, Brandt, and Fink, 1996; Brandt, Mathur, and Elvis, 1997), and their X-ray emission is highly variable within a short timescale of $\sim 1000 \text{ s}$ (e.g., Boller, Brandt, and Fink, 1996). These characteristics are generally considered as the results of nearly or super Eddington accretions onto less massive black holes with $10^{6-7} M_{\odot}$ (e.g., NLS1 catalog in Rakshit et al., 2017; Waddell and Gallo, 2020). The high accretion rates and their small mass suggest that NLS1s are in an early stage of AGN evolution (e.g., Mathur, 2000). Roughly half of Seyfert 1 galaxies are NLS1s by statistical analysis of soft X-ray selected sample (Grupe et al., 2004).

Quasars

Quasars are the most luminous class of AGNs with $M_B < -21.5 + 5 \log h_0$ as a definition. Their typical luminosity and central SMBH masses are $10^{44-47} \text{ erg s}^{-1}$ and $10^{8-9} M_{\odot}$. One of the main characteristics of quasars compared to Seyferts is the large distances where they have been identified. With the unprecedented capability of the James Webb Space Telescope, a quasar at $z = 13.20$ with the largest known redshift was discovered by imaging and further confirmed by spectroscopy (Robertson et al., 2022). Their optical spectra are similar to those of Seyfert galaxies and exhibit broad emission lines. Their continuum spectra are also like those of Seyfert galaxies, with high time variability and substantial enhancements in the ultra-violet (UV) band. Unlike Seyfert galaxies, $\sim 98\%$ of the quasars are classified as type 1 (Zakamska et al., 2003), including radio-loud and radio-quiet sources. Although the first discovered quasar 3C 273 is radio-loud, the number of radio-loud quasars is only $\sim 5-10\%$ of the entire population, and the rests are all radio-quiet ones.

The AGN unified model

Many studies have suggested the AGN unification model as a way to explain AGN diversity with a small number of physical parameters. Figure 1.1 shows the AGN unification model. It revealed the ubiquitous presence of the so-called “torus” around the SMBH. The torus of optically thick material surrounding the central regions on a scale of 1–100 pc was proposed by R. Antonucci (1993). Both broad and narrow lines can be observed when viewed face-on (Seyfert 1 galaxies), whereas only narrow lines are observed with an edge-on view (Seyfert 2 galaxies). The unified picture is strongly supported by the discovery of the broad Balmer lines in the Seyfert 2 galaxy NGC 1068 with the optical

polarization (R. R. J. Antonucci and J. S. Miller, 1985). This means that Seyfert 2 galaxies also host the broad line region (BLR), while the broad lines are not directly visible from our line of sight and can only be observed in scattered emission.

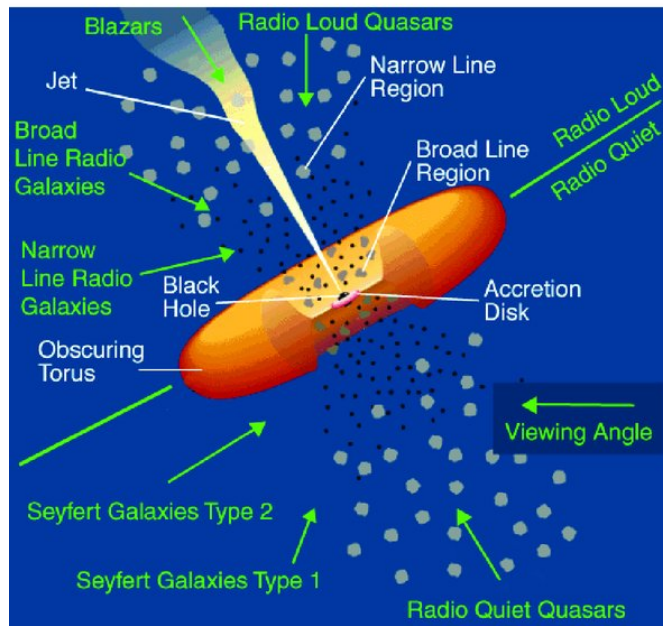


FIGURE 1.1: An illustration of the standard unified model (Urry and Padovani, 1995).

1.1.4 Co-evolution and AGN feedback

In recent years, it has been believed that almost all galaxies host SMBHs at their centers and that they become AGNs if they are accreting enough fuel. A very strong correlation between the SMBH mass and the mass of its host galaxy has been discovered (Magorrian et al., 1998). This observation strongly suggests that SMBHs and galaxies have evolved while influencing each other, i.e., SMBHs and galaxies have co-evolved (see Kormendy and Ho, 2013 and the references therein). Figure 1.2 shows the so-called “Magorrian relation”, which is a relation between SMBH mass M_{BH} and the velocity dispersion of its host galaxy σ . This relation requires a feedback process from the SMBH to its host galaxy.

Although the feedback process is a controversial issue, two major modes have been proposed. One of which is “radio mode”, also called maintenance or kinetic mode. The other is “quasar mode” also known as wind or radiative mode (e.g., Fabian, 2012; Kormendy and Ho, 2013). It has been observed that radio jets transport energy in low-accretion rate AGNs with radio mode. The AGN produces strong jets and cocoons that

heat the circumgalactic and halo gas in radio mode, thereby stopping cooling in massive haloes.

In contrast, in the AGN accreting with nearly Eddington rate, the feedback through the disk winds is expected in quasar mode. If only 0.5–5% of the AGN bolometric luminosity is available as the kinetic power of AGN winds, the outflows can eliminate gas from the host galaxies and quench the star formation and AGN activity (Hopkins and Elvis, 2010; Zubovas and King, 2012). Each feedback mechanism works in a different stage of the AGN and is crucial to the co-evolution.

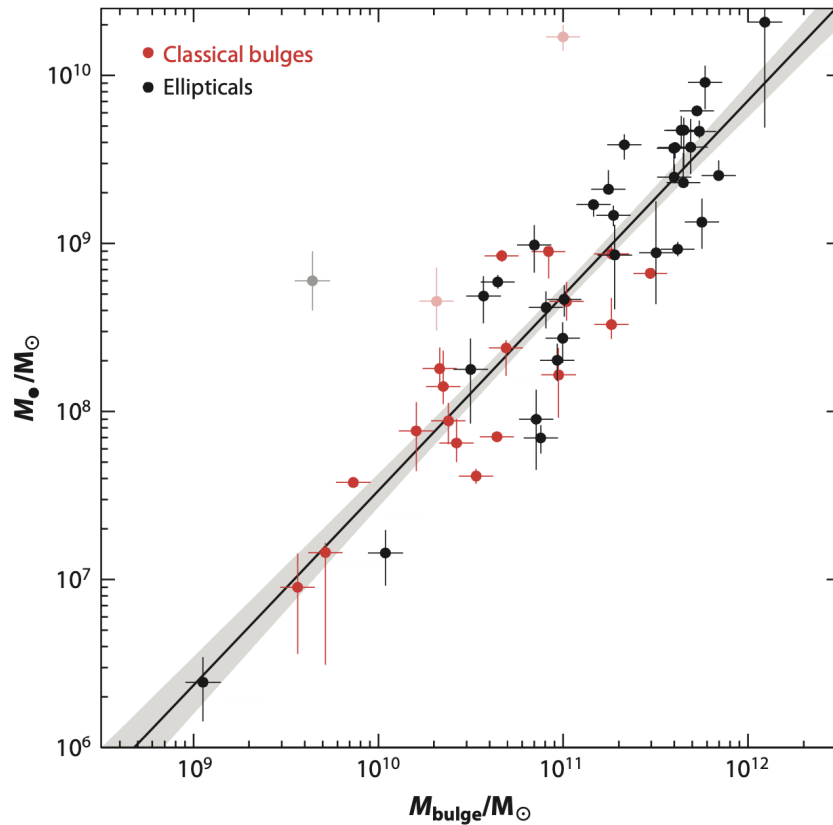


FIGURE 1.2: Magorrian relation with a best-fit linear model omitting exceptional ones, NGC 3843 and NGC 4889 pointed in light colors (Kormendy and Ho, 2013).

1.2 X-ray spectra of Seyfert 1 galaxies

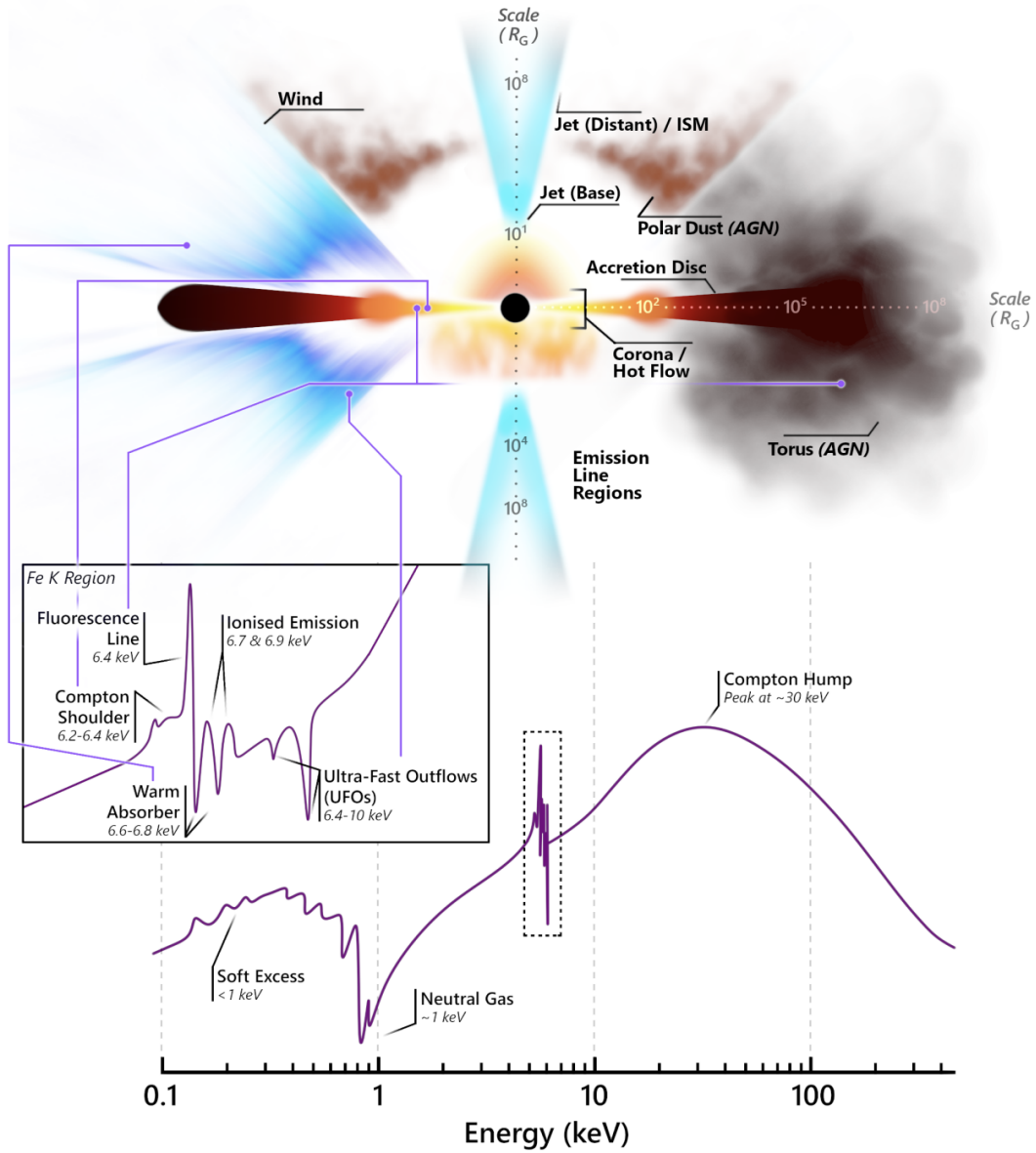


FIGURE 1.3: Schematic overview of the environments in accreting objects (AGNs and XRBs) and their typical X-ray spectra (Gandhi et al., 2022). The left and the right side depict different potential models that may be attributed to different physical conditions (e.g. some components exclusive to AGNs are labeled on the right). The “Emission Line Regions” indicate the broad and narrow line regions seen in AGNs. Approximate scales are denoted in the gravitational radius. The physical components manifest in various spectral features depicted at the bottom. The inset shows the Fe K energy band around 6–7 keV.

Figure 1.3 shows a schematic view of the environments in accreting objects, i.e., AGNs and X-ray binaries (XRBs), and their typical X-ray spectra (Gandhi et al., 2022). The subsequent sections explain the X-ray spectra of Seyfert 1 galaxies.

1.2.1 Accretion disk component

In general, the matter is accreting into the SMBHs along with its angular momentum. Considering a sort of viscosity, the angular momentum is transported outwards, and the matter can gradually fall to the center. The concept of the “standard” accretion disk was proposed by Shakura and Sunyaev (1973), which is geometrically thin and optically thick.

In the standard accretion disk, the disk temperature as a function of the radius $T(r)$ is expressed as

$$T(r) = \left[\frac{3}{8\pi\sigma} \frac{GM_{\text{BH}}\dot{M}}{r^3} \left(1 - \sqrt{\frac{R_{\text{in}}}{r}} \right) \right]^{1/4}, \quad (1.8)$$

with σ being the Stefan-Boltzmann constant, R_{in} being the innermost radius of the disk, and \dot{M} being the mass accretion rate. In the limit of $r \gg R_{\text{in}}$, this is written in more convenient way:

$$T(r) \simeq \left(\frac{3}{8\pi\sigma} \frac{GM_{\text{BH}}\dot{M}}{R_{\text{in}}^3} \right)^{1/4} \left(\frac{r}{R_{\text{in}}} \right)^{-3/4} \propto r^{-3/4}. \quad (1.9)$$

In this manner, the radiation from the disk is represented as the sum of blackbody components at multiple temperatures (multi-color disk blackbody model; Mitsuda et al., 1984). The peak energy of inner disk emission is denoted with Wien’s law, k by $h\nu_{\text{peak}} \sim 3kT(R_{\text{in}})$, where k is the Boltzmann constant. This energy corresponds to the optical/UV to soft X-ray band in AGNs.

In Newtonian mechanics, R_{in} can be as small as possible, but in general relativity, R_{in} has the lower limit to keep a stable orbit, which is called the innermost stable circular orbit (ISCO). The ISCO of Keplerian motion around a SMBH depends on the angular momentum J of the black hole. With a spin parameter denoted by $a = J/M_{\text{BH}}^2$, the ISCO for the Schwarzschild BH ($a = 0$) is $6 R_g$. The ISCO around a spinning Kerr BH monotonically decreases as the BH spins faster. When the spin parameter is the maximum ($a = 0.998$), ISCO reaches the minimum value of $1.24 R_g$.

As the mass accretion rate increases, the disk gets hotter and geometrically thicker, resulting in the so-called “slim” disk (Abramowicz et al., 1988). The peak energy of SED reaches the X-ray energy band according to the higher temperature in the disk. This is one of the possible explanations for the soft excess observed in many narrow-line Seyfert 1 galaxies (Mineshige et al., 2000). However, the origin of the soft excess is still being debated, and other interpretations have been proposed (e.g., Sobolewska and Done, 2007; Done et al., 2012; Xu et al., 2021).

1.2.2 Power-law component

A power-law component dominates X-ray energy spectra of AGNs above 2 keV, which is denoted by $E^{-\Gamma} \exp(-E/E_c)$, with Γ being a photon index and E_c being a cut-off energy (\sim hundreds keV). The shape of a power-law spectrum can be created when UV seed photons from the disk reach a heated corona and gain energy through inverse Compton scattering. Since photons cannot receive much greater energies than the coronal temperature, the cut-off energy is created.

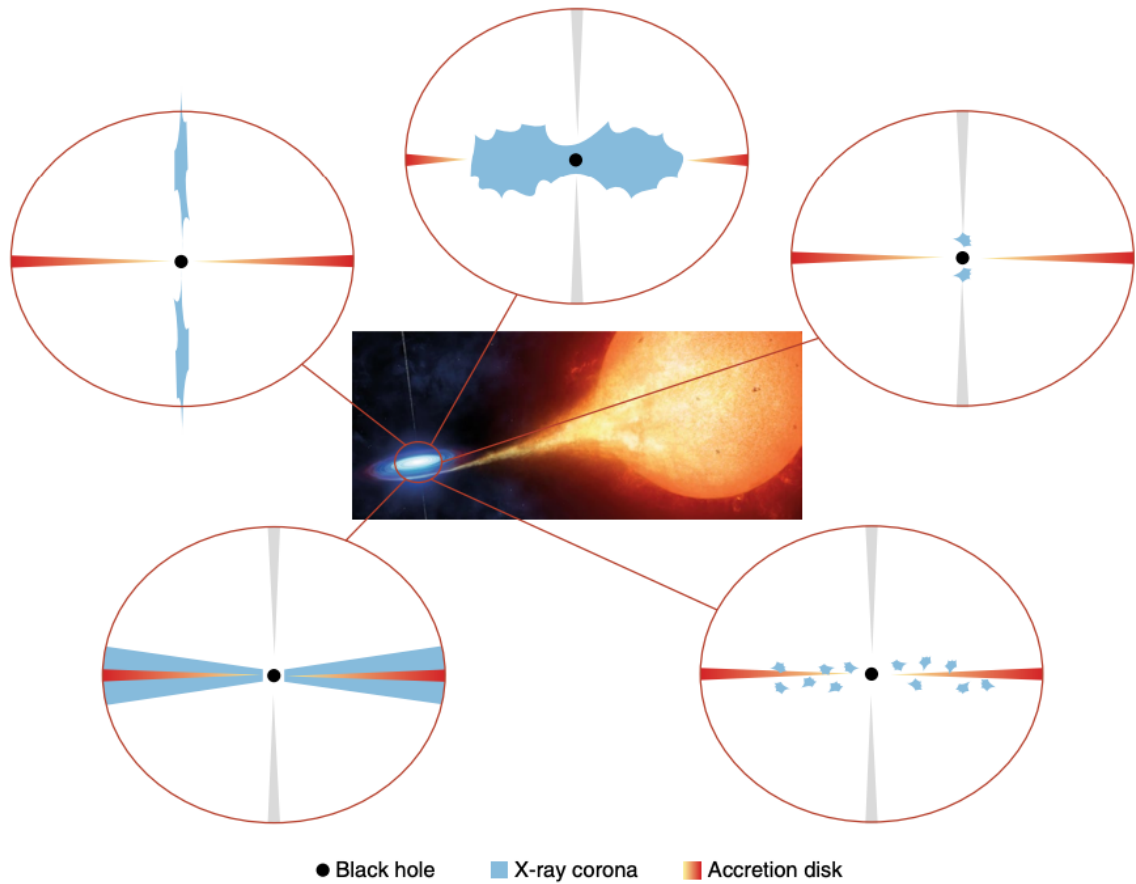


FIGURE 1.4: Suggested geometries for an accretion disk and X-ray emitting corona in XRBs and AGNs (Malzac, 2018). Clockwise from top: hot flow surrounded by a truncated disk (Done, Gierliński, and Kubota, 2007), compact lamppost geometry (Fabian et al., 2015), compact magnetically active regions distributed over the disk (Stern et al., 1995), extended slab/wedge corona (Schnittman and Krolik, 2010), and extended jet emission (Kylafis et al., 2008).

The geometries of the hot corona have not been determined uniquely by observations. Both XRBs and AGNs have coronas, which originate independently of the black hole mass. Figure 1.4 shows some suggested geometries (Malzac, 2018). A viscously-heated accretion flow, a strongly magnetized accretion disk corona (similar to the solar corona), or the base of a relativistic jet along the might all be possible configurations. These three physical models implicate quite different geometries of the inner region surrounding the black hole. The most popular geometry is a central hot geometrically thick flow surrounded by a truncated accretion disk with a variable transition radius. Another configuration considers a compact X-ray lamppost located above the black hole on the rotation axis of the disk.

Recent polarization results obtained with the *IXPE* satellite constrained the corona geometry on the low/hard state of Cygnus X-1 through a new aspect. Based on the determined polarization angle, Krawczynski et al. (2022) ruled out the aligned X-ray corona with the jet, requiring instead it to be aligned with the accretion disk.

1.2.3 Reflection component

Part of primary X-ray emission from the corona is reprocessed by ambient matters (e.g., the torus, the BLR, and the accretion disk), generating characteristic reflection features (e.g., T. J. Turner and L. Miller, 2009 for a review). The main indicators of X-ray reflection include Fe-K α fluorescent emission lines at ~ 6.4 keV, the absorption iron K-edge ($\sim 7\text{--}9$ keV), and a broad structure around 20–30 keV, which is called the ‘‘Compton hump’’. The Compton hump is created by combined effects of photo-electric absorption for lower energy photons, described later in detail, and energy loss via Compton down scattering for higher photons.

The Fe-K α fluorescent lines are produced when one of the two K-shell electrons of atoms is released due to the photoelectric absorption of photons with ≤ 7.1 keV. Following the bound-free transition, an L-shell electron enters the K-shell. The bound-bound transition energy is released from the atom in either of the following ways; released as a 6.4 keV photon and creates the Fe-K α emission line, or internally absorbed by another electron that is escaped as the so-called Auger electron. The probability of the former case called the fluorescent yield is about 0.34 for neutral iron (Bambynek et al., 1972).

1.2.4 Absorption component

In addition to the reflection, the primary X-rays from the corona are absorbed by surrounding materials in AGNs, making complex features in the X-ray spectra. The absorption is roughly divided into two varieties: neutral absorption and ionized absorption (see T. J. Turner and L. Miller, 2009 and Laha et al., 2021 for review). Recent observational and theoretical studies suggest that most AGNs have multiple ionized absorbers. In this section, we describe X-ray absorption by cold gas and three types of ionized absorbers.

Cold gas

Neutral absorption occurs by a low-temperature absorber, such as a dusty torus and interstellar medium in the host galaxy and our Galaxy. The absorption is expressed as $\exp[-N_{\text{H}}\sigma(E)]$, with N_{H} being the column density and $\sigma(E)$ being the cross-section of photoionization. The left panel of Figure 1.5 shows the power-law spectra absorbed by a neutral gas with N_{H} of 10^{21} , 10^{22} , 10^{23} , and 10^{24} cm $^{-2}$.

The amount of absorber is usually expressed in terms of the column density of hydrogen atoms, but in practice, X-ray photons are also absorbed by heavy elements such as carbon, oxygen, iron, etc. When X-rays are absorbed by neutral gases, soft X-rays below 1 keV are heavily absorbed, producing a Fe-K edge at 7.1 keV.

Warm absorbers

Mildly-ionized absorbers called the *warm absorbers* (WAs) are detected as absorption lines and edges in the soft X-ray band (e.g., Reynolds, 1997). These features are present in $\sim 65\%$ of the nearby AGNs, especially in the radio-quiet Seyfert 1 galaxies (e.g., McKernan, Yaqoob, and Reynolds, 2007, Laha et al., 2014). In general, the absorption features by the WAs are usually blue-shifted with respect to the systemic velocity of the sources, indicating that the WAs are outflowing with typical velocities of $10^2\text{--}10^3$ km s $^{-1}$.

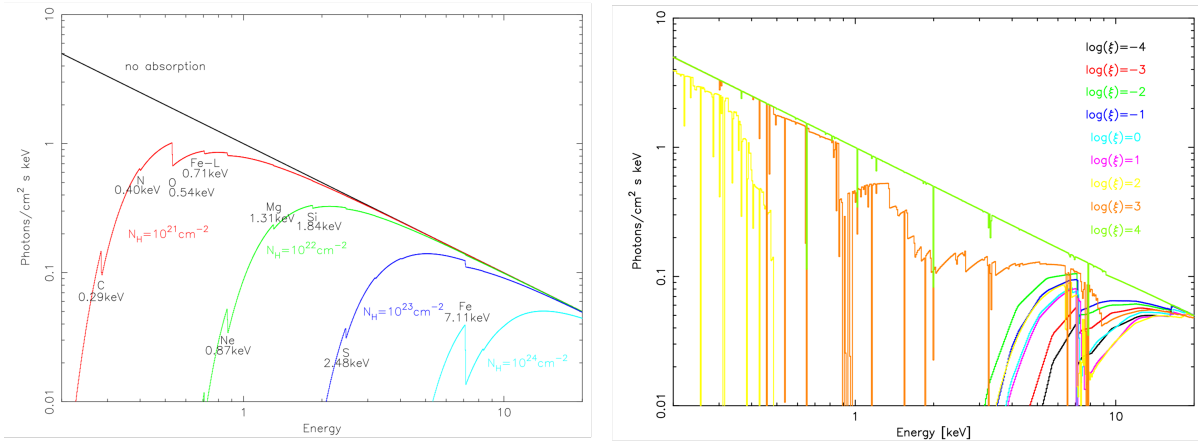


FIGURE 1.5: The left panel shows the power-law spectrum absorbed by a neutral gas with various column densities. The right shows the same but by an ionized absorber with a fixed column density of 10^{24}cm^{-2} and diverse ionization parameters. These figures are obtained from Ebisawa (2006).

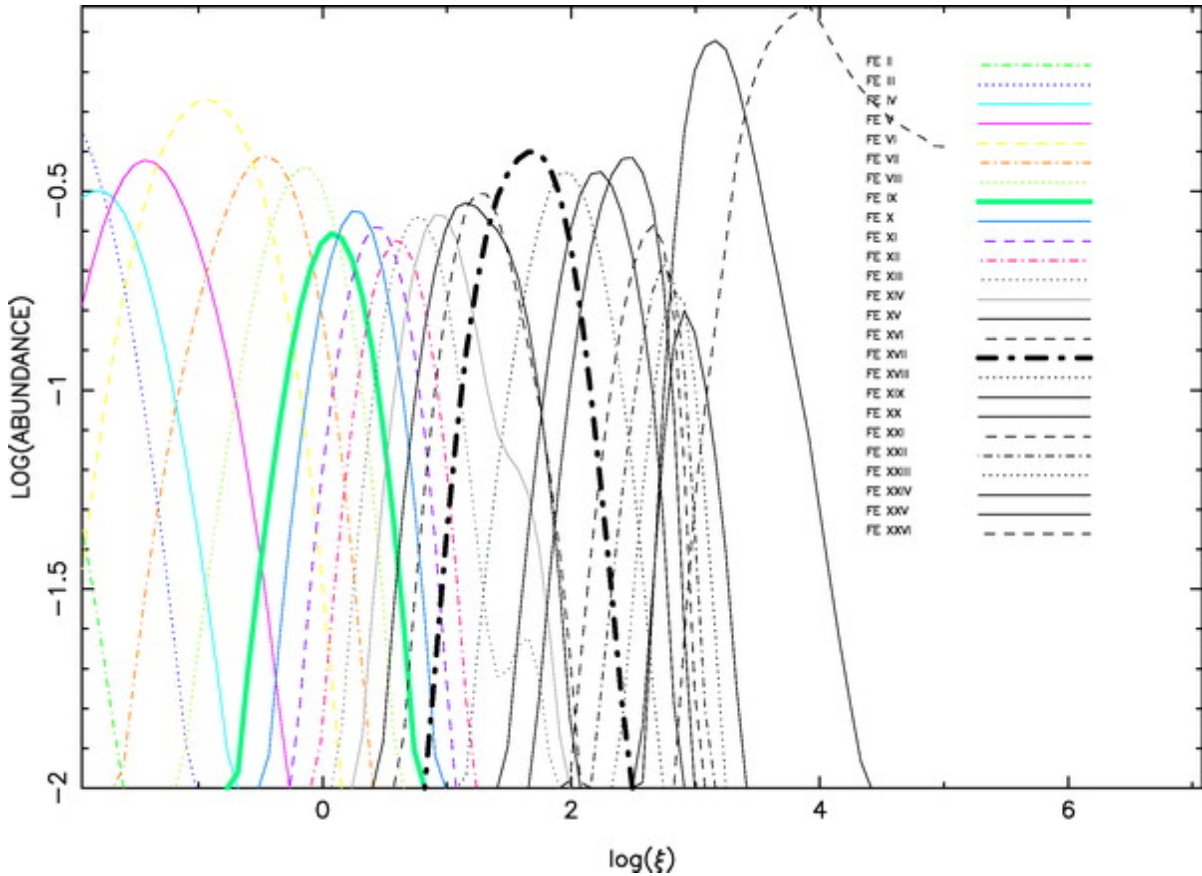


FIGURE 1.6: Ion population of iron as a function of ξ (T. R. Kallman et al., 2004). The higher-ionized ions are likely to exist for the higher ξ .

Ionized gas is parameterized, in addition to the velocity, in terms of the hydrogen column density N_{H} and the ionization parameter ξ , expressed as

$$\xi = L/nr^2 [\text{erg cm s}^{-1}], \quad (1.10)$$

where L is the ionizing luminosity integrated from 13.6 eV to 13.6 keV, n is the gas number density, and r is the distance from the X-ray source to the ionized gas. The ion population of iron as a function of ξ is shown in Figure 1.6. Their ionization parameters and column densities of WAs are roughly $\log \xi \sim 0\text{--}1.5$ erg cm s $^{-1}$ and $N_{\text{H}} \sim 10^{20}\text{--}10^{22}$ cm $^{-2}$, respectively (e.g., Laha et al., 2021). The right panel of Figure 1.5 shows the power-law spectra absorbed by ionized gas with $\log \xi$ from -4 to 4 . Iron ions are practically He-like (Fe XXV) and H-like (Fe XXVI) for $\log \xi > 3$ and almost totally ionized for $\log \xi > 4$, respectively, where the absorption is considerably decreased.

With the variability time-scale of absorption lines, we can measure the distance between the WAs and the hot corona (e.g., Crenshaw et al., 2003). Detection of such variability on short timescales is one of the main motivations for conducting UV–X-ray monitoring campaigns of AGNs (e.g., NGC 5548; see Kaastra et al., 2014). It is generally known that WAs are multiphase flows with multiple velocities and ionizations at a given source (e.g., Arav et al., 2015), as shown in Figure 1.7.

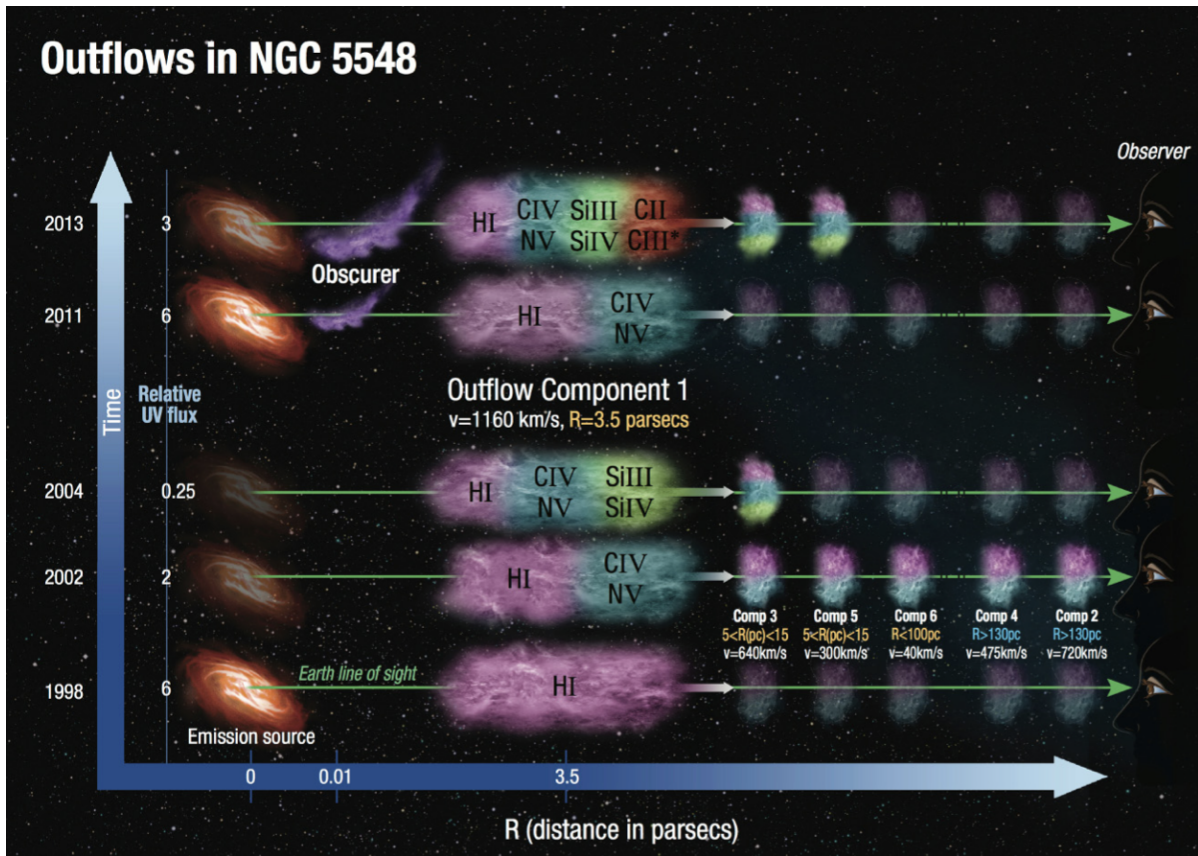


FIGURE 1.7: A illustration of multiphase WAs detected in NGC 5548 (Arav et al., 2015).

Ultra-fast outflows

Besides the absorption by the WA, extremely blue-shifted iron K-shell absorption lines around 7–9 keV have been detected in the X-ray spectra of several AGNs. These features shown in Figure 1.8 are caused by the so-called *ultrafast outflow* (UFO). Seyfert galaxies often have such highly blue-shifted and highly ionized absorption lines in their 30–40% X-ray spectra (Tombesi et al., 2010; Igo et al., 2020). The UFOs are considered to

be outflowing winds from the accretion disk at very high velocities of $0.1\text{--}0.3 c$, where c is the speed of light. Their ionization parameters and column densities are roughly $\log \xi \sim 3\text{--}6$, and $N_{\text{H}} \sim 10^{22}\text{--}10^{24} \text{ cm}^{-2}$ (Laha et al., 2021).

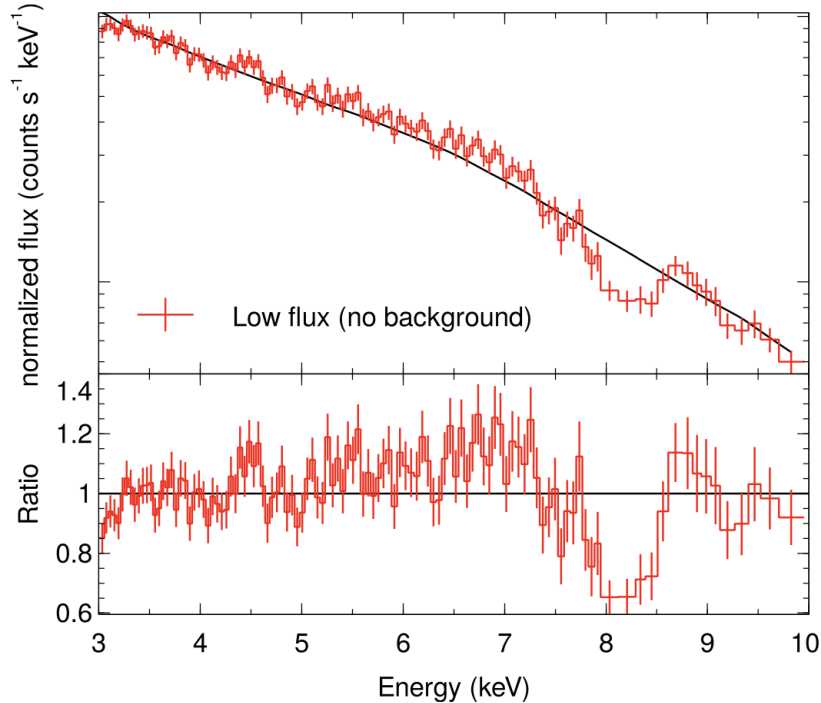


FIGURE 1.8: UFO absorption line in IRAS 13224–3809, where the spectrum is fitted with a power law (Parker et al., 2017). The outflow velocity is estimated to be $0.24 c$ or $0.21 c$ assuming either Fe XXV or Fe XXVI.

Since UFOs are likely to have larger solid angles than the relativistic jets (e.g., Nardini et al., 2015, Hagino et al., 2015), UFO contribution to the co-evolution of the SMBHs and the host galaxies may be comparable to or even exceed that of the jets (e.g., King, 2010, Tombesi et al., 2012, King and Pounds, 2015).

Partial covering absorbers

Broad Fe-K fluorescent lines with low-energy tails down to ~ 4 keV have been observed in $\sim 45\%$ of Seyfert 1 galaxies (Nandra et al., 2007), pioneered by its discovery in MCG–6-30-15 (Tanaka et al., 1995), as shown in Figure 1.9. This feature can be interpreted as broadening and distortion due to relativistic effects in the vicinity of SMBHs, as described in Section 1.3.3. However, there are complex spectral features other than the fluorescence line in the Fe-K band, such as ionized absorption lines and absorption edges, and the line profile relies on the expected continuum level. The observed broad Fe-K line profiles can thus be explained by a number of scenarios.

One of the scenarios is the existence of the *partial covering absorbers* (or also called *clumpy absorbers*). If clumpy absorbers are present in the line of sight to the X-ray radiating source, some of the primary X-rays are absorbed, while the rest are not. This “partial covering” situation can produce multiple spectral components with a common power-law emission. Based on the partial covering concept, Tanaka et al. (2004) found that the X-ray spectral variation of 1H 0707–495 can be explained by changes in the

partial covering fraction. Here, the percentage of the X-rays covered by the clumpy absorbers in the line of sight is called the partial covering fraction (CF). The X-ray spectrum of MCG–6-30-15, the best example of the apparently broad iron emission line, was also explained by the partial absorption (L. Miller, T. J. Turner, and J. N. Reeves, 2008; Miyakawa et al., 2009). So far the partial covering scenario has successfully explained the X-ray spectra of numerous Seyfert 1 galaxies (Mizumoto, Ebisawa, and Sameshima, 2014; Iso et al., 2016; Yamasaki et al., 2016; Midooka et al., 2022) A schematic view is illustrated in Figure 1.10.

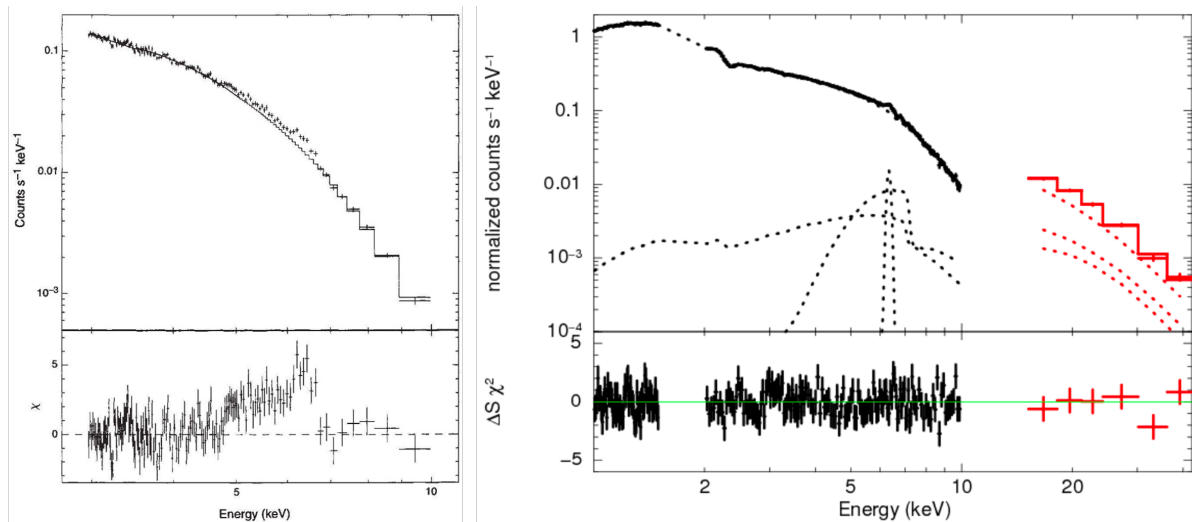


FIGURE 1.9: X-ray spectra with a seemingly broad Fe-K line in MCG–6-30-15. The left shows a residual when the continuum is assumed to be a power-law (Tanaka et al., 1995). The right explains the seemingly broad Fe-K profile with a narrow Fe line and absorbed power-law components (Miyakawa, Ebisawa, and Inoue, 2012).

The clump absorbers typically have high column densities ($\log N_{\text{H}} \sim 23$) with short timescale variability (Laha et al., 2021). So it is also called the “obscurer”, which causes simultaneous soft X-ray and UV absorption troughs (e.g., NGC 5548; Kaastra et al., 2014). The obscurer appears and disappears depending on the period, as shown in Figure 1.7. For NGC 5548, the spectrum was heavily obscured for a few years (in 2011–2013), despite the absence of any such features before (Kaastra et al., 2014). In contrast, that in NGC 3783 was a short-lived eclipsing event, which lasted only for a month (Mehdipour et al., 2017).

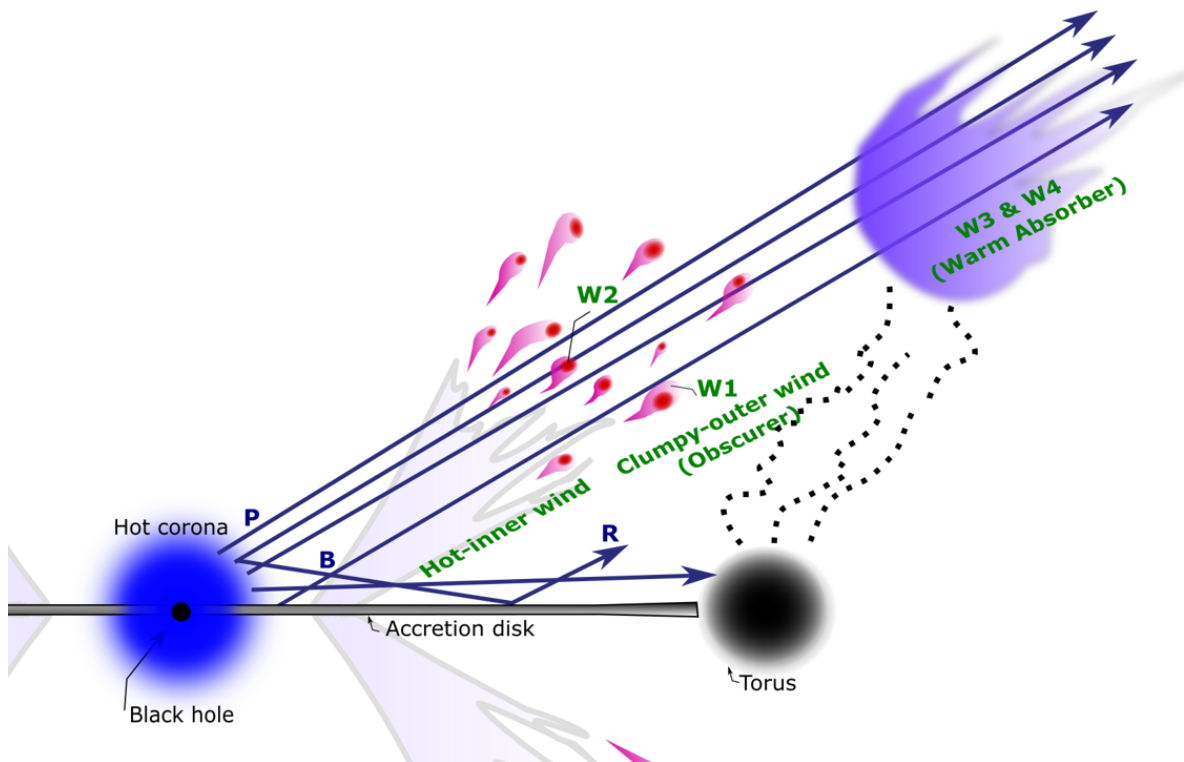


FIGURE 1.10: Schematic view of a partial covering model around the black hole and accretion disk (Midooka et al., 2022). The intrinsic X-rays of the power-law (P in the figure) and disk component (B) are emitted from the hot corona around the central black hole and the inner accretion disk, respectively. These intrinsic X-rays are partially covered by the “cold clumps”, each of which consists of two layers; a cold core (W_2) and a warm layer (W_1). These cold clumps, known as “obscurers”, cause the “double partial covering” with the same covering fraction. X-rays are fully absorbed by the outer WAs (W_3 and W_4), which are formed from the ionized material due to evaporation of the irradiated torus.

1.3 Origins of the X-ray absorbers

This section describes the scenarios proposed as the physical origins of the UFOs and partial covering clouds that are the main focus of this thesis.

1.3.1 Outflow driving mechanisms

Radiation magnetohydrodynamics (R-MHD) can be used to describe the structure, dynamics, and evolution of the wind. The equation of motion allows for the identification of potential wind-driving mechanisms:

$$\rho \frac{D\mathbf{v}}{Dt} + \rho \nabla \Phi = -\nabla P + \rho \mathbf{F}_{\text{rad}} + \frac{1}{4\pi} (\nabla \times \mathbf{B}) \times \mathbf{B} \quad (1.11)$$

where ρ , \mathbf{v} , P , and \mathbf{B} is the mass density, velocity, gas pressure, and magnetic field of the gas in the wind, respectively (Proga, 2007; Faucher-Giguère and Quataert, 2012). The terms Φ and \mathbf{F}^{rad} are the gravitational potential and the total radiation force per unit mass, respectively.

Accretion disk winds are accelerated by (1) the pressure gradient force, (2) the radiation force, or (3) the magnetic force, which corresponds to each force term in the right hand of Equation 1.11. The wind is driven when at least one of these exceeds the gravitational potential of the central SMBH. This section describes how these forces can be stronger than gravity under what physical conditions.

Thermal driven

X-rays from the corona irradiate and heat up the material on the surface of the disk. The heated layer expands due to the pressure gradient, eventually producing a thermally driven wind at radii where the sound speed is larger than the local escape velocity (e.g., Begelman, McKee, and Shields, 1983; Krolik and Kriss, 2001).

Theoretical models predict that X-ray heating can significantly influence gas dynamics. X-rays heat low-density gas through Compton scattering, thereby the temperature can reach the equilibrium, where heating of the electrons and cooling by inverse Compton scattering are balanced. The equilibrium temperature is called the Compton temperature, which typically is a high temperature of $\sim 10^7$ K.

Several studies have proposed a thermal origin for the WA, with a huge launch radius extending beyond BLR and/or torus, attributed to its low velocity and mild level of ionization (Krolik and Kriss, 1995; Mizumoto et al., 2019a). Although only this mechanism cannot accelerate faster winds like UFOs, the possibility of hybrid acceleration mechanisms also has been proposed (e.g., Dorodnitsyn, T. Kallman, and Proga, 2008).

Radiation driven

The wind launch mechanism based on radiation driven is known to depend on the Eddington ratio. As described in Section 1.1.2, the Eddington ratio is determined by the equilibrium between the gravity and Thomson scattering. In the case of the super-Eddington accretion, the radiation force with Thomson scattering exceeds the gravitational force. This type of wind is called “continuum-driven”, known to have a large solid angle (e.g., Ohsuga et al., 2005; Takeuchi, Ohsuga, and Mineshige, 2013; Nardini et al., 2015). The

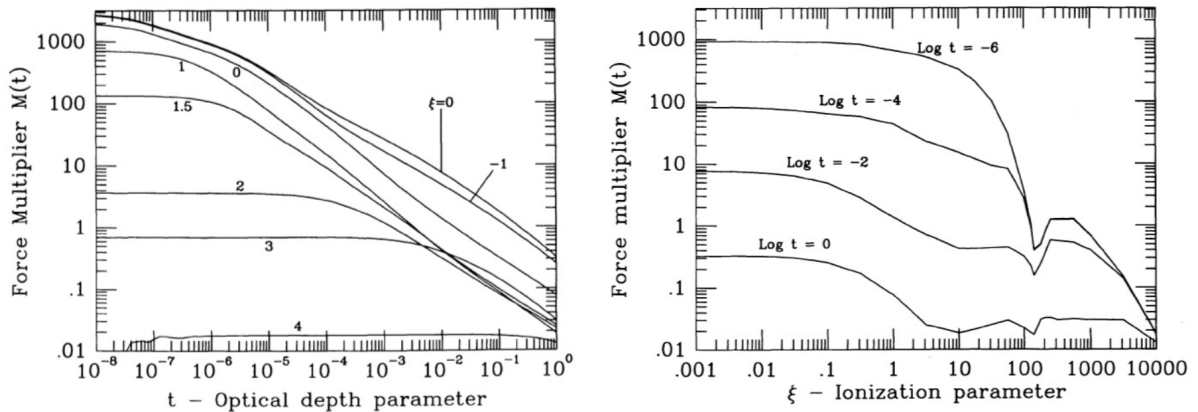


FIGURE 1.11: The force multiplier $M(t, \xi)$ with increasing X-ray ionization (Stevens and T. R. Kallman, 1990). $M(t, \xi)$ is plotted as a function of the optical depth parameter t (left) and the ionization parameter ξ (right).

wind is launched by continuum radiation pressure if the AGN emission approaches the Eddington luminosity. Even if the luminosity is below that of Eddington, the radiation pressure can contribute to launching the wind. Since the radiation pressure decreases the effective gravity by a factor of $1 - L/L_{\text{Edd}}$, a combination effect with thermal driving can launch the wind from the vicinity of a SMBH.

In the sub-Eddington case, on the other hand, the radiative force due to bound-bound transition accelerates the wind more effectively and is referred to as a “line-driven” wind (e.g., Proga, Stone, and T. R. Kallman, 2000; Proga and T. R. Kallman, 2004; Nomura et al., 2016). This wind may have a smaller solid angle than the continuum-driven wind. Even for super-Eddington objects, the line force should work at a distance from the SMBH, whereas previous outflow simulations of super-Eddington accretion flow have not taken the line force into account (e.g., Ohsuga et al., 2005; Takeuchi, Ohsuga, and Mineshige, 2013).

The radiation force, the sum of the continuum force and line force, is approximated as:

$$\begin{aligned} \mathbf{F}_{\text{rad}} &= \mathbf{F}_{\text{rad}}^{\text{C}} + \mathbf{F}_{\text{rad}}^{\text{L}} \\ &\approx \frac{\kappa_T F}{c} (1 + M(t, \xi)) \end{aligned} \quad (1.12)$$

where κ_T is the Thomson scattering opacity and F is the radiative flux. The line force often assumes the force multiplier $M(t, \xi)$, which is the function of the ionization parameter ξ and the optical depth parameter $t (= \frac{\kappa_T}{\kappa_L} \tau_L)$. Figure 1.11 shows the force multiplier as a function of t or ξ . In the left panel, $M(t, \xi)$ shows the rapid increase for $\xi \lesssim 100$. The labels on each curve are the respective values of $\log t$. In the right panel, $M(t, \xi)$ increases with the decrease of t and becomes nearly constant for small t . The labels on each curve show the values of $\log \xi$.

Magnetic driven

Since important AGN phenomena such as accretion disks (viscosity), corona presence, and jets can be explained by the MHD mechanism, it is generally suspected that some form of MHD process may be at work in most AGN outflows (Blandford and Payne,

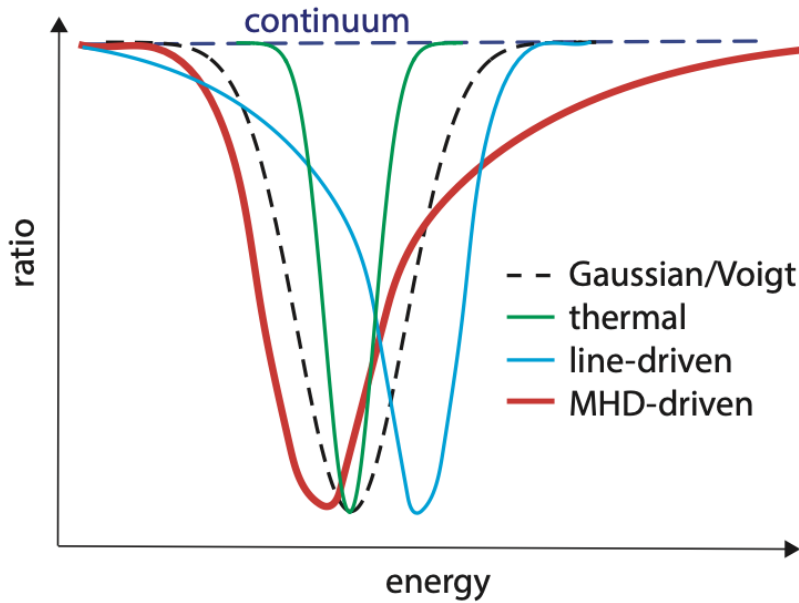


FIGURE 1.12: Schematic diagram showing a comparison of characteristic absorption profiles among various wind driving mechanisms (Fukumura et al., 2022).

1982; Fukumura et al., 2010). Although the origin of the magnetic field and its physical processes in accretion disks are not yet understood, magnetic processes are thought to play an important role in accretion processes, especially in angular momentum transport driven by magnetic rotational instability.

The line profiles can be slightly different depending on the driving mechanism (Fukumura et al., 2022). Figure 1.12 shows the comparison of the characteristic absorption profiles. The expected shape of the line profile from MHD-driven winds is generally unique compared to other models and distinctive enough to be separately identified. Its profile creates an asymmetric line shape of an extended blue wing, while line driving tends to produce a red wing profile due to an asymptotically increasing terminal wind velocity. Because of its constant and slow motion, the thermal-driven wind allows for a relatively narrow line with little asymmetry. Phenomenological Gaussian/Voigt line profiles are symmetric. Future observations by *XRISM* and *Athena* will directly constrain the driving principle based on the absorption line profile of the UFOs.

1.3.2 Formation of the clumpy absorbers

Two-dimensional R-MHD simulations of supercritical accretion flows show that the radiation pressure generates a disk wind, and the wind becomes clumpy at a few hundred Schwarzschild radii (Takeuchi, Ohsuga, and Mineshige, 2013). They argued that the clump formation is probably because the Rayleigh-Taylor instability works efficiently, where the radiation pressure is dominant over the gravitational potential. Non-magnetic radiation-hydrodynamic simulations were also performed by Takeuchi, Ohsuga, and Mineshige (2013), and they found that similar outflows were generated and also became clumpy, as shown in Figure 1.13.

To examine the instability, Takeuchi, Ohsuga, and Mineshige (2014) studied a simplified system with optically thin low-density gas in the upper layer and optically thick

high-density gas in the lower layer, with radiation streaming upward. The calculations showed that in a super-Eddington atmosphere under dynamic equilibrium between radiation, gravity, and gas pressure gradient forces, radiation hydrodynamic Rayleigh-Taylor instability occurred. After the growth of perturbations on small scales, typical length scales of clumps corresponding to one optical depth appeared. In other words, the contribution of the radiation hydrodynamic instability to the clump formation is significant as well as the Rayleigh-Taylor instability. This result is confirmed by three-dimensional radiation hydrodynamic simulations (Kobayashi et al., 2018).

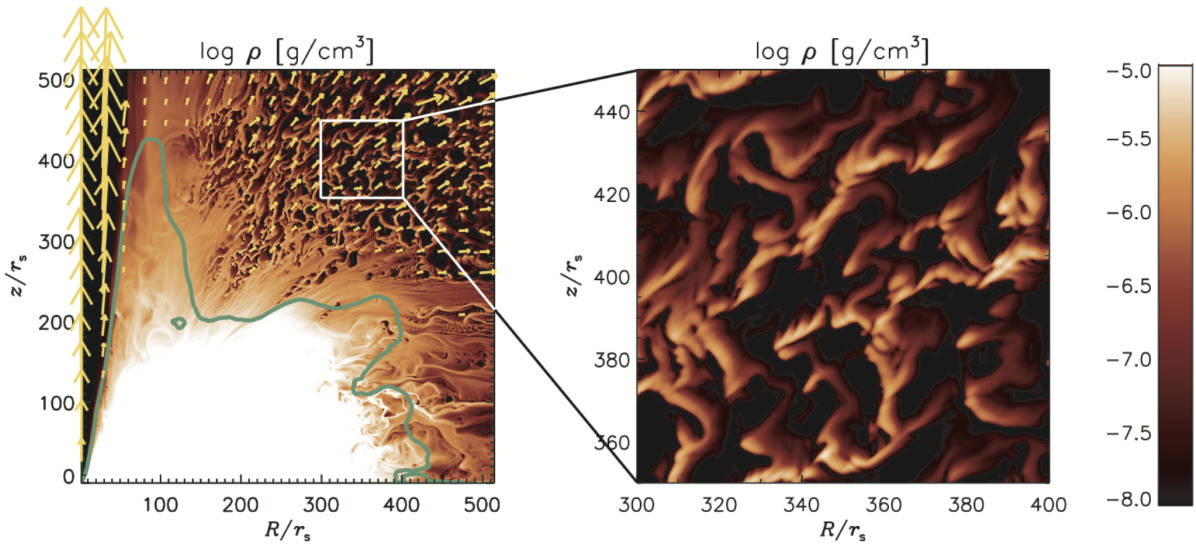


FIGURE 1.13: 2D structure of the outflow around a $10^6 M_{\odot}$ BH with R-MHD simulation of super-critical flow. A clumpy structure is shown in the distant region (Takeuchi, Ohsuga, and Mineshige, 2013).

Other mechanisms have been proposed for the disk wind to become clumpy. For example, Dannen et al. (2020) found through parsec-scale wind simulation that the dynamical thermal instability occurs in some zone, which predicts fragmentation of the outflow beyond the acceleration radius of the wind. Strong X-ray irradiation of the outflowing material may lead to thermal instability, thus resulting in clumpiness of the outflow (Krolik, McKee, and Tarter, 1981).

Mizumoto et al. (2019b) proposed the “hot inner and clumpy outer wind model”, in which the inner wind and the outer clumps are actually observed as the ultrafast outflows (UFOs) and the clumpy absorbers, respectively. However, in the standard X-ray spectral analysis, parameters of the clumpy absorbers and other components, such as WAs and soft-excess, often degenerate due to complex spectral variations in the soft X-ray band.

1.3.3 Alternative models

Another interpretation claims that the continuum is not partially absorbed and that the broad Fe-K line is relativistically broadened. Such a relativistic disk reflection model assumes extreme physical conditions (e.g., Fabian et al., 1989). This model often requires that the central black hole spin is almost maximum and most of the incident X-ray radiation from an extremely tiny corona (“lamp post”) is reflected at the innermost region of the disk, so that the reflected spectral component dominates the direct component.

Additionally, an inexplicable overabundance of iron by a factor 3–20 is required in various objects (e.g., IRAS 13224–3809; Fabian et al., 2013, Chiang et al., 2015).

In the contemporary X-ray spectral analysis of AGN, the relativistic reflection model and the partial absorption model are often indistinguishable in shape. For example, Parker et al. (2022) employed the reflection and disk wind models to interpret the randomly synthesized X-ray spectra. In the disk wind model, the Compton scattering and blue-shifted absorption by wind explain the Fe-K emission and absorption features without relativistic effects. Figure 1.14 shows four randomly selected *XMM-Newton* spectra that fit well with both models. The models are extremely similar and cover a wide range of spectral shapes.

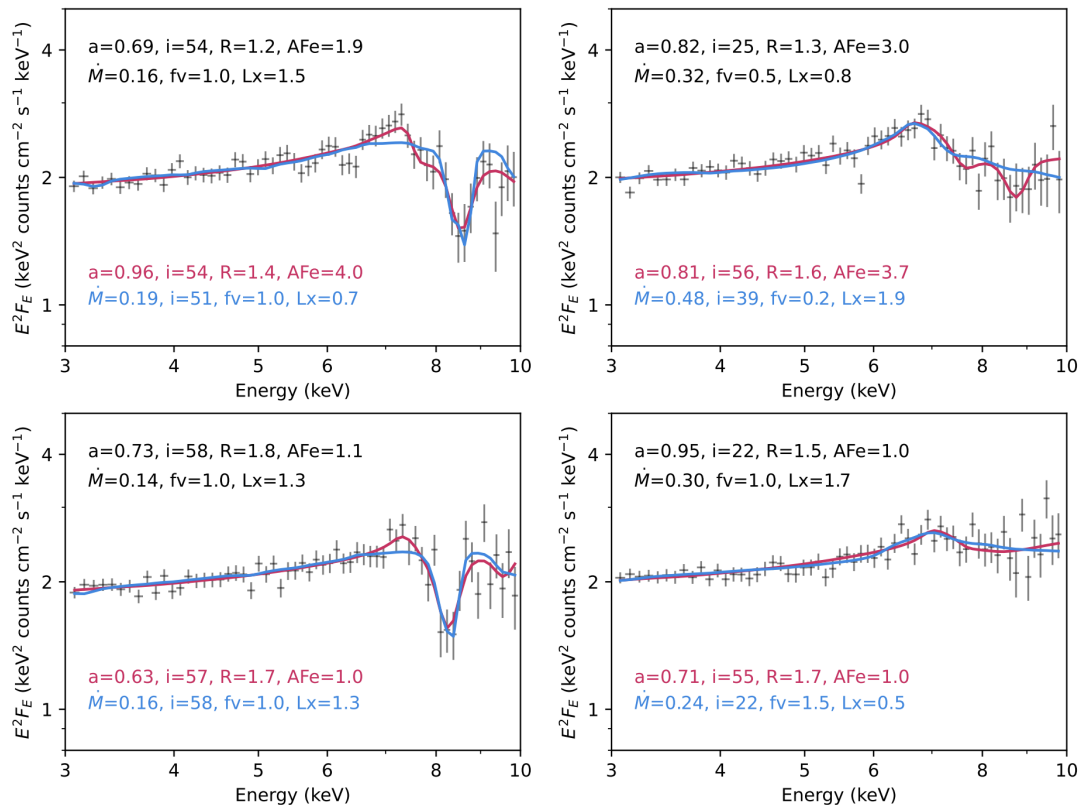


FIGURE 1.14: Four randomly selected *XMM-Newton* spectra that are well fit with both the reflection (red) and disk wind (blue) models, with both models shown. In each case, the true simulated and best-fit parameters for each model are shown at the top and bottom, respectively (Parker et al., 2022).

1.4 Purpose of this dissertation

Observational evidence has clearly indicated the presence of multiple kinds of X-ray absorbers, specifically WAs, UFOs, and clumps (e.g., Laha et al., 2021 and the references therein). The origin and formation mechanisms of these absorbers are still unclear. Some simulation studies have suggested that the UFOs become unstable far from the central region and transform into gas clumps (e.g., Takeuchi, Ohsuga, and Mineshige, 2013; Kobayashi et al., 2018). However, previous X-ray spectral analysis has been unable

to put a stringent limit on the observational parameters of the gas clumps, because of the complex entanglement of the spectral components (e.g., Midooka et al., 2022). This situation results in the degeneracy between the clumpy absorber parameters and other absorbing parameters, such as WAs and UFOs. The origin of the gas clumps is still enigmatic, especially whether the clumps are even outflowing or not. To solve this parameter degeneracy, we have developed a novel method called the “spectral-ratio model fitting”. Taking the spectral ratios of the intensity-sliced spectra enables us to make the spectral variations due to clumpy absorbers noticeable, by canceling out the less time-variable continuum and other absorption components such as WAs.

The purpose of this dissertation is to obtain a unified picture of the innermost region of the Seyfert 1 galaxies. To that end, we first try to constrain the outflowing velocity of the clumpy absorbers in Seyfert 1 galaxies using the spectral-ratio fitting method. Next, we will compare the clump velocity and the UFO velocity, and search for plausible acceleration mechanisms and origins of the UFOs and clumps.

This dissertation is organized as follows. In Chapter 2, the X-ray instruments of the *XMM-Newton* observatory used in this dissertation are described in detail. We explain the methodology and benefit of the spectral-ratio model fitting and present results of the systematic ratio analysis of the Seyfert 1 galaxies in Chapter 3. We present detailed analyses of the selected objects to constrain the clump velocity and its physical origin in Chapter 4. In Chapter 5, discussions mainly on the spectral-ratio fitting results are presented. Finally, Chapter 6 summarizes our results and conclusions.

Chapter 2

Instrumentation

Contents

2.1	Overview of the <i>XMM-Newton</i> satellite	30
2.2	X-ray telescopes	32
2.3	European Photon Imaging Camera (EPIC)	35
2.4	Optical Monitor (OM)	40
2.5	Reflection Grating Spectrometer (RGS)	42

In this study, we use the X-ray archival data obtained with the *XMM-Newton* satellite. This chapter describes telescopes and instruments onboard *XMM-Newton*.

2.1 Overview of the *XMM-Newton* satellite

The *XMM-Newton* satellite of the European Space Agency (ESA) was launched on 1999 December 10 by the Ariane-V rocket and put in a highly elliptical orbit of 47.8 hours period with a perigee of 7000 km and an apogee of 114000 km (Jansen et al., 2001). Although the orbital period is 47.8 hours (172 ksec), the exposure available for scientific data analysis is limited to about 132 ksec per orbit. This is because observations cannot be carried out during the severe radiation background period depending on the satellite's elevation concerning Earth's magnetosphere. As of 2022, the satellite is still in operation and giving us highly valuable data at the forefront of the field.

This satellite carries two types of the telescopes. One is three Wolter type-1 X-ray telescopes, represented by the satellite's name X-ray Multi-Mirror mission (XMM). The X-ray telescopes possess independent X-ray detectors in their focal planes. The other is a 30 cm optical/UV telescope with a CCD detector in its focal plane. Thus *XMM-Newton* offers simultaneous access to two windows of the electromagnetic spectrum: X-rays and optical/UV.

Figure 2.1 shows a schematic view of the *XMM-Newton* satellite with external shrouds and structure removed for clarity. There are three X-ray telescopes and a UV/optical telescope. *XMM-Newton* provides six scientific instruments in total with three different types; three X-ray CCD cameras called European Photon Imaging Camera (EPIC), two high-resolution X-ray spectroscopy instruments called the Reflection Grating Spectrometer (RGS), and an optical/UV detector for imaging and grism spectroscopy called the Optical Monitor (OM). The EPIC and RGS cameras are at the focal planes of the three X-ray telescopes, while the OM has its own telescope.

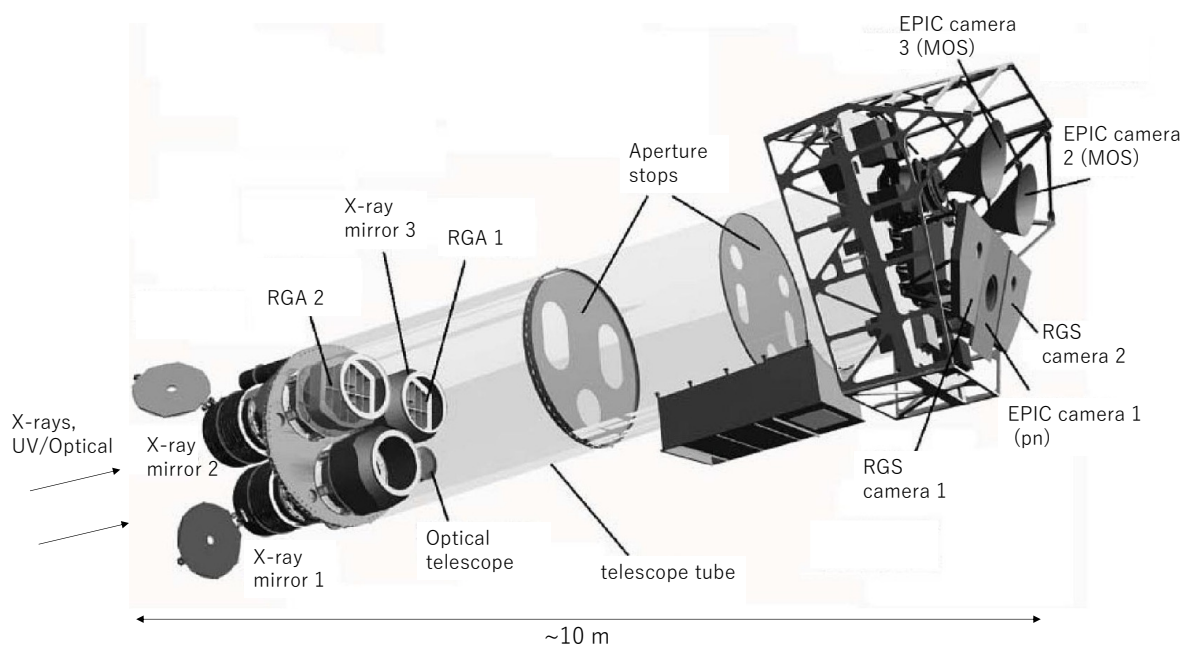


FIGURE 2.1: A schematic view of the *XMM-Newton* satellite subsystems, with external structure removed to enhance visibility, modified from the original one².

In subsequent sections, we briefly explain the characteristics of the X-ray telescope, EPIC, RGS, and OM, of which data are used in this thesis. The details are described in *XMM-Newton* User's Handbook¹.

¹https://xmm-tools.cosmos.esa.int/external/xmm_user_support/documentation/uhb/

²<https://www.cosmos.esa.int/web/xmm-newton/xmm-pay1>
<https://www.eoportal.org/satellite-missions/xmm-newton>

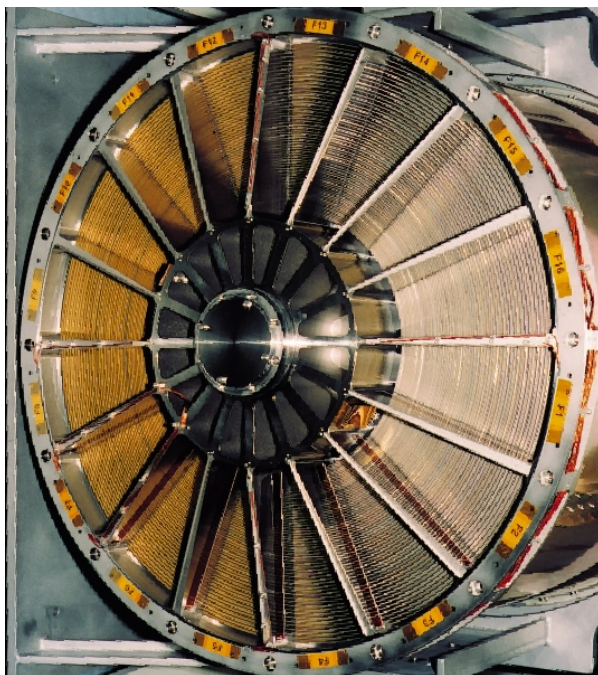


FIGURE 2.2: Picture of one of the X-ray telescopes onboard the *XMM-Newton* satellite, consisting of 58 nested mirrors³.

2.2 X-ray telescopes

The three co-aligned X-ray telescopes onboard *XMM-Newton* reflect incident X-rays with energies up to ~ 10 keV and project X-ray images on the respective focal planes. Each Mirror Module is a grazing-incidence Wolter I telescope, consisting of 58 gold-coated nested mirrors as shown in Figure 2.2. The focal length is 7.5 m, and the diameter of the largest mirrors is 70 cm.

Configuration

Two of the telescopes are designed for two pairs of EPIC-MOS, which stands for the metal oxide semiconductor, and RGS. Each has a reflection grating array (RGA) in the light path, where about 44% of the incident X-rays pass to the primary MOS focal planes while 40% is intercepted by the grating plates of the RGA towards the RGS camera. The remaining telescope is designed for the EPIC-pn camera without the RGA, which provides the maximum effective area for the focal plane detector (Figure 2.3).

Effective area of the telescope

The effective area is an indicator of the ability to collect X-ray photons. The X-ray telescope of *XMM-Newton* has the largest effective area of focusing telescopes ever. The total mirror geometric effective area at 1.5 keV is about 1,500 cm² for each telescope, i.e., in total 4,500 cm². Figure 2.4 shows the on-axis effective area of the *XMM-Newton*

³<https://www.cosmos.esa.int/web/xmm-newton/technical-details-mirrors>

⁴https://xmm-tools.cosmos.esa.int/external/xmm_user_support/documentation/uhb/xraytel.html

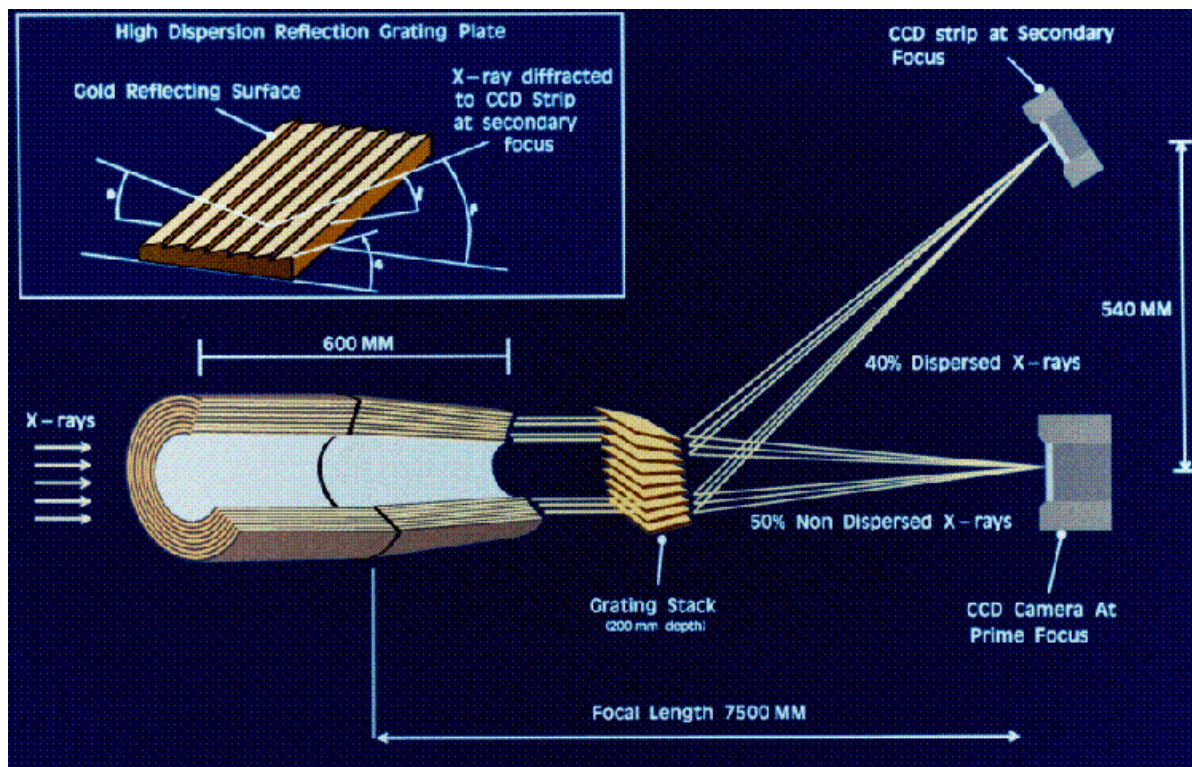


FIGURE 2.3: The light path in the two *XMM-Newton* telescopes with grating assemblies (not to scale)⁴.

telescope. The effective area with the RGA is about half that of the telescope due to the RGA intervention. The sharp decrease in these effective areas above 10 keV is caused by the fact that the total reflection by the mirror shells hit the critical angle at energies up to ~ 10 keV (depending on the shell nesting position). The feature around 2 keV is due to the Au M-edge of the mirrors.

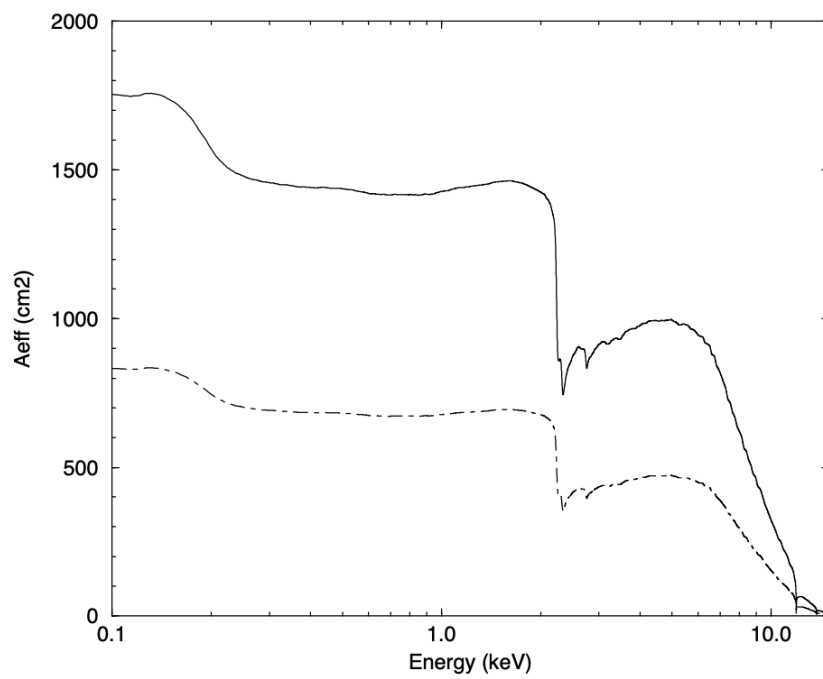


FIGURE 2.4: On-axis effective area of the *XMM-Newton* telescope without (solid line) and with (dot-dashed line) the RGA (Strüder et al., 2001).

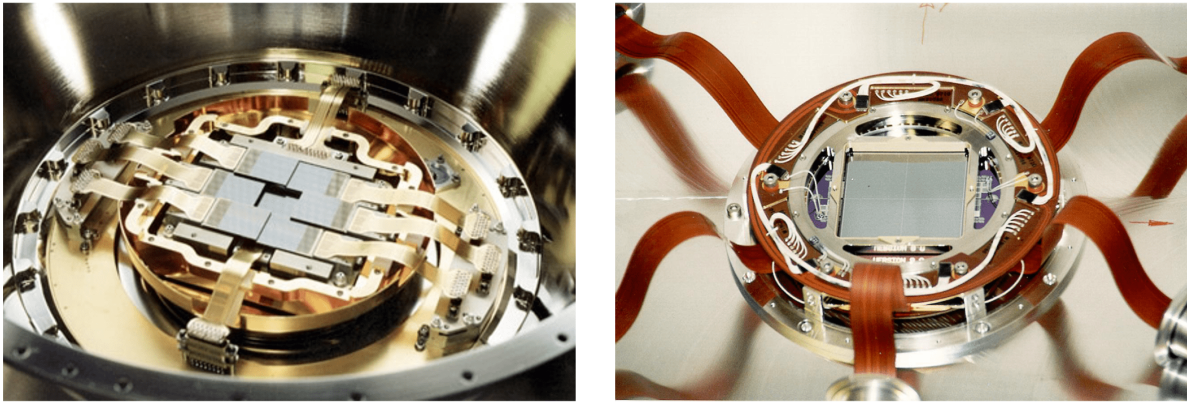


FIGURE 2.5: The CCDs of a MOS camera (left) and the pn camera (right)⁵.

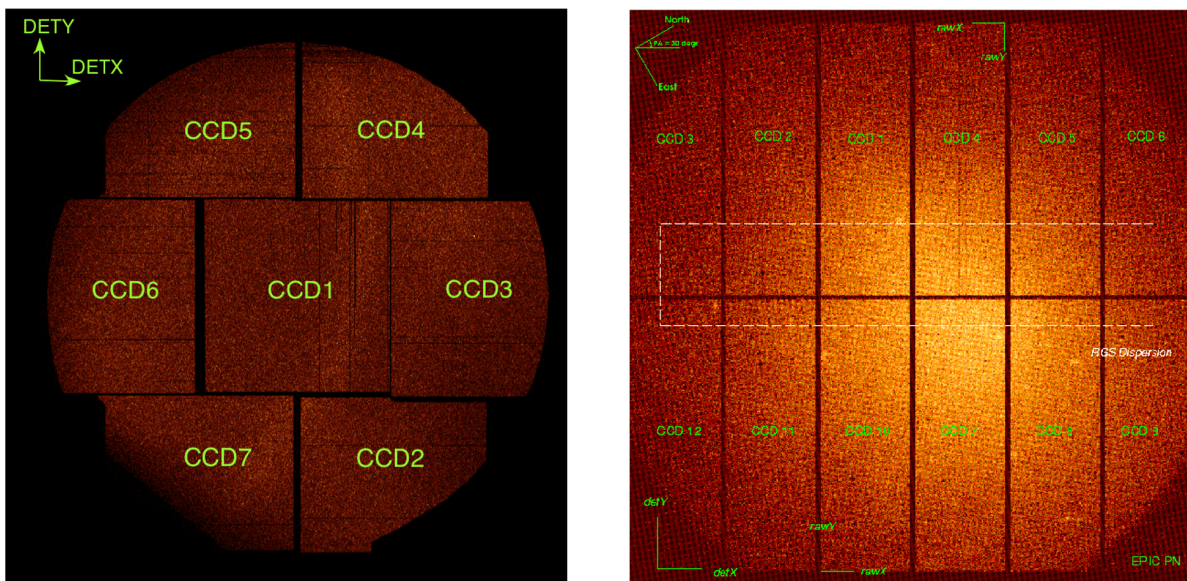


FIGURE 2.6: The CCD layout of the MOS1 camera (left) and the pn camera (right)⁶.

2.3 European Photon Imaging Camera (EPIC)

As described in Section 2.1, *XMM-Newton* has three X-ray CCD cameras namely EPIC: Two of them are MOS CCD arrays (M. J. L. Turner et al., 2001) and the other is pn CCD array (Strüder et al., 2001). The two types of EPIC differ in some major aspects, not only for the geometry of the CCD arrays and the instrument design but also for other properties such as their readout times.

Figure 2.5 and Figure 2.6 show photos and the CCD layouts of the EPIC cameras. The MOS cameras consist of seven individual CCD chips with the conventional front-illuminated method, where electrodes for the charge transfer are in front of the CCDs. On the contrary, the pn array consists of twelve back-illuminated chips, in which X-rays are radiated from the surface without electrodes.

⁵<https://www.cosmos.esa.int/web/xmm-newton/technical-details-epic>

⁶https://xmm-tools.cosmos.esa.int/external/xmm_user_support/documentation/uhb/pnchipgeom.html

TABLE 2.1: Basic characteristics of *XMM-Newton*⁷. The properties of the RGS and OM are described in the following section.

Instrument	EPIC MOS	EPIC pn	RGS	OM
Bandpass	0.15–12 keV	0.15–12 keV	0.35–2.5 keV	180–600 nm
Sensitivity	10^{-14} ^a	10^{-14} ^a	8×10^{-5} ^b	20.7 mag ^c
Field of view (FOV)	30'	30'	5'	17'
PSF (FWHM/HEW)	5"	6"	—	1.4–2.0"
Pixel size	40 μm (1.1")	150 μm (4.1")	81 μm	0.476513"
Timing resolution ^d	1.75 ms	0.03 ms	0.6 s	0.5 s
Spectral resolution	$\sim 70/150$ eV ^e	$\sim 80/150$ eV ^e	0.04/0.025 \AA ^f	180 ^g

^a In case 10 ks observation in the range 0.15–12.0 keV, in units of $\text{erg s}^{-1} \text{cm}^{-2}$.

^b O VII 0.57 keV line flux in photons $\text{cm}^{-2} \text{s}^{-1}$, for an integration time of 10 ks and a background of 10^{-4} photons $\text{cm}^{-2} \text{s}^{-1} \text{keV}^{-1}$.

^c 5- σ detection of an A0 star in 1 ks.

^d In fast data acquisition mode (i.e., timing mode for EPIC, spectroscopy mode for RGS1, and fast mode for OM).

^e At 1 keV and 6.4 keV (Fe $K\alpha$), respectively.

^f At 1 keV in the first and second order, respectively.

^g Resolving power ($\lambda/\Delta\lambda$) with UV and optical grism.

Performance of the EPIC

Characteristics of the EPIC MOS and pn cameras are summarized in Table 2.1. The EPIC cameras offer the possibility to perform sensitive imaging observations over the telescope's field of view of 30 arcmin in the energy range from 0.15 to 15 keV with moderate spectral ($E/\Delta E \sim 20\text{--}50$) and angular resolution (PSF ~ 6 arcsec FWHM). The MOS camera has a better angular resolution because of its smaller pixel size. In contrast, the pn camera has the advantage of much faster readout than the MOS camera since each pixel column of the pn chips has its own readout node, in addition to the higher quantum efficiency described below.

Quantum efficiency and net effective area

In addition to the characteristics of the telescope, one of the factors to be considered to determine the net effective area of the EPIC cameras is their quantum efficiency. Quantum efficiency is an index of how well the incident X-ray events are detected by the CCD detector as a function of the X-ray energy. Figure 2.7 shows the quantum efficiency of the MOS and pn chip.

Since the pn CCDs adopt the back-illuminated method and have thicker depletion layers, they yield a higher quantum efficiency than the MOS chips both in the lower and higher band. The decrease of the pn quantum efficiency at the lowest energies is caused by the properties of the silicon L-edge. An absorption feature at 528 eV is due to the

https://xmm-tools.cosmos.esa.int/external/xmm_user_support/documentation/uhb/moschipeom.html

⁷https://xmm-tools.cosmos.esa.int/external/xmm_user_support/documentation/uhb/basics.html

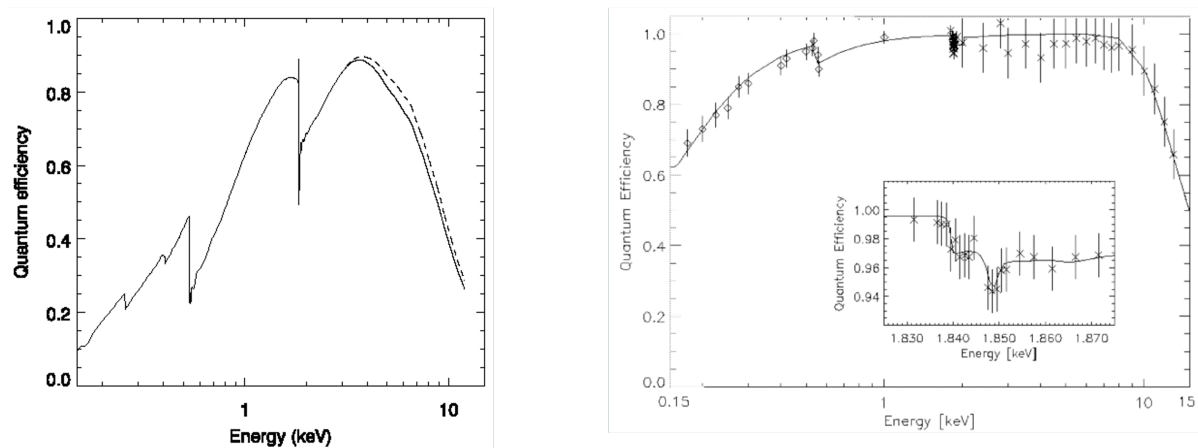


FIGURE 2.7: Quantum efficiency of the EPIC MOS1 (left solid line), MOS2 (left dashed line) CCD1 chip⁸, and the pn chip (right) as a function of photon energy (Strüder et al., 2001).

additional absorption by a SiO₂ insulator. A typical X-ray absorption fine structure is also seen at 1.838 keV by the silicon K-edge shown in the inset of the figure.

Figure 2.8 shows the net effective area of all the *XMM-Newton* instruments. The total effective area of the two EPIC-MOS cameras is lower than that of the EPIC-pn because of the lower quantum efficiency and the RGA dispersion.

Operating modes

There are several operating modes of science data acquisition for the EPIC cameras¹⁰, as shown in Figure 2.9. In the case of MOS, the six outer CCDs remain in standard imaging mode, while the central CCD can be operated separately. Thus, all CCDs are always acquiring data, independent of the operating mode selection. The pn CCDs can be operated in the common mode in all CCD chips for Full Frame, Extended Full Frame, and Large Window mode, or just with one single CCD (CCD number 4 in the right of Figure 2.6) for Small Window, Timing, and Burst mode. In the common Full Frame mode or Extended Full Frame mode (pn only), all CCD pixels are read out, and thus the full field of view is covered.

Limiting the number of pixels used improves timing resolution, enabling observation of the bright objects without pileup. In Large Window mode for pn, only half of the area in all the 12 CCDs is read out, whereas in Small Window mode, only a part of the CCD number 4 in the right of Figure 2.6 is used to collect data.

In the Timing mode, spatial information is maintained only in one dimension, along the column (RAWX) axis. It enables high-speed readout, a timing resolution of 0.03 ms for pn, in exchange for the loss of spatial information along the row direction (RAWY) axis. A unique flavor of the Timing mode of the EPIC pn camera is the Burst mode,

⁸https://xmm-tools.cosmos.esa.int/external/xmm_user_support/documentation/uhb/epicqe.html

⁹https://xmm-tools.cosmos.esa.int/external/xmm_user_support/documentation/uhb/effareaonaxis.html

¹⁰https://xmm-tools.cosmos.esa.int/external/xmm_user_support/documentation/uhb/epicmode.html

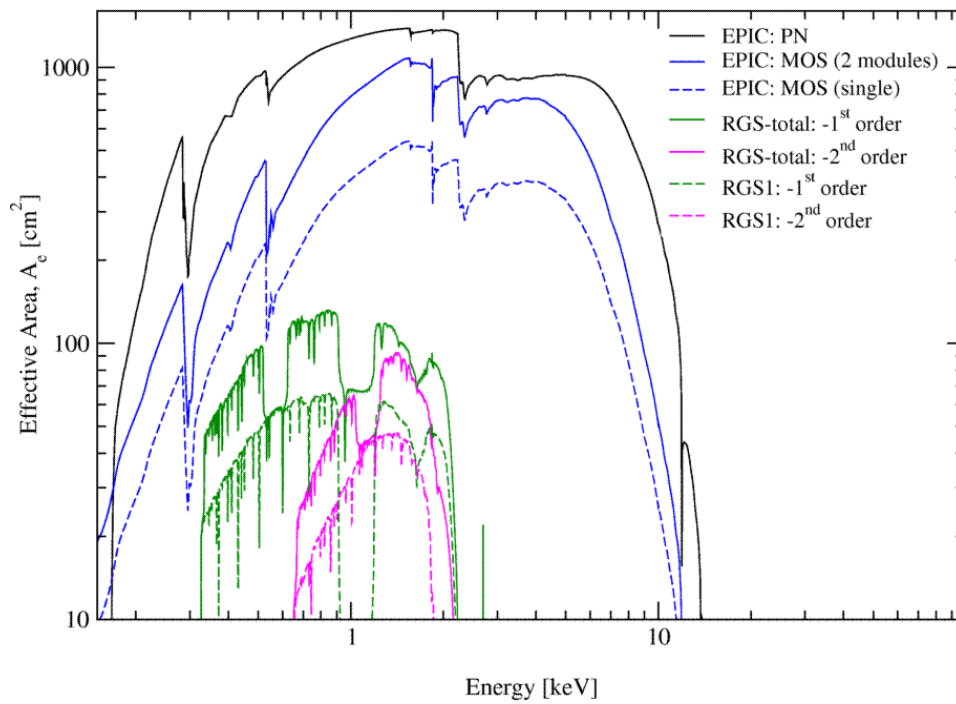


FIGURE 2.8: The net effective area of all the *XMM-Newton* X-ray instruments, EPIC and RGS (logarithmic scale)⁹.

which offers an extremely high time resolution of 7 μs , but has a very low duty cycle of 3%.

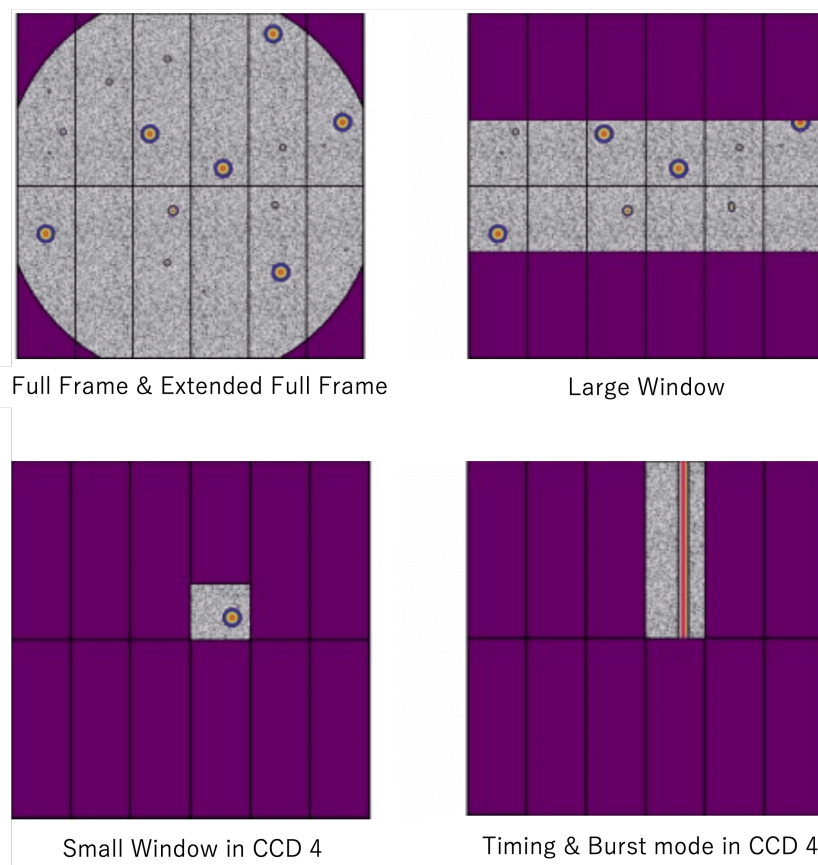


FIGURE 2.9: Operating modes of the pn CCD camera: Full frame and extended full frame mode, Large window mode, small window mode, and timing mode and burst mode (Strüder et al., 2001).

2.4 Optical Monitor (OM)

The OM instrument, mounted on the mirror platform alongside the X-ray mirror modules, extends the spectral coverage of *XMM-Newton* into the ultraviolet and optical range (Mason et al., 2001). It provides coverage between 170 nm and 650 nm of the central 17 arcmin square region of the X-ray field of view, providing the time-resolved data and images on the same target simultaneously observed with the EPIC and RGS.

Figure 2.10 shows a schematic view of the OM telescope module showing the light path to the detectors. The OM telescope tube is about 2 m long, and the telescope module contains the telescope optics and two detector chains for redundancy. The optics consist of a modified 30 cm Ritchey-Chretien telescope with a focal length of about 3.8 m. The primary mirror receives the incoming lights and reflects them to the secondary mirror, from which the lights go to the tilted mirror to be reflected onto the detector. In addition, a filter wheel is mounted immediately in front of the detectors. It contains not only the filters but also other optical elements, such as grisms and a magnifier (i.e., optics for a longer focal length and thus higher resolution on the sky).

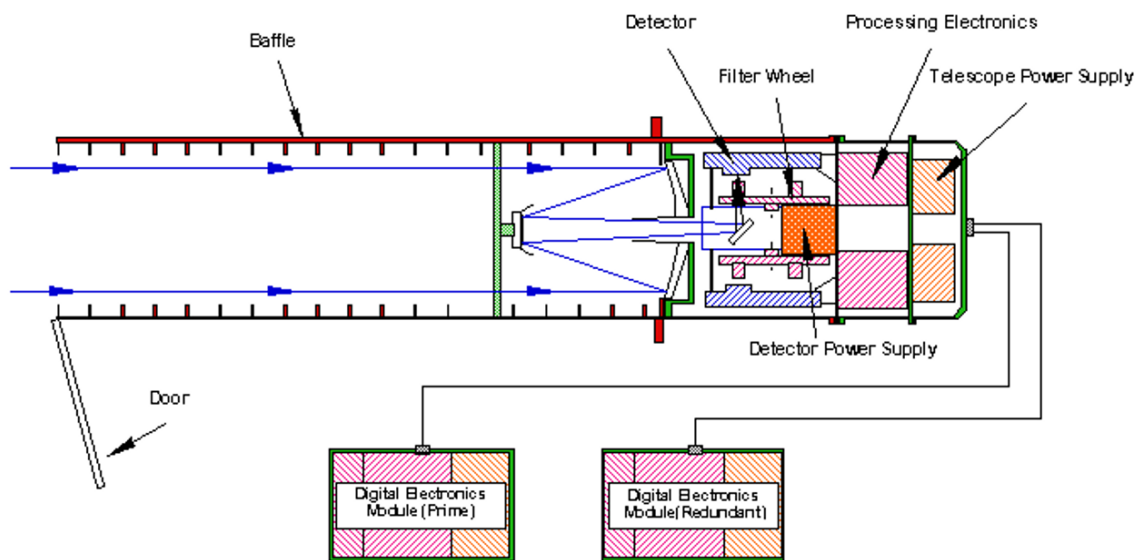


FIGURE 2.10: A schematic view of the OM telescope module showing the light path to the detectors¹¹(Mason et al., 2001).

Detectors

The detector is a micro-channel plate intensified CCD. Micro-channel plate is a detector with an electron amplification effect made from tiny glass tubes, all of which are aligned. A high electrical potential is applied across the plate operated in a vacuum. Incoming photons striking the top of the plate may cause the release of photo-electrons. The photo-electrons are focused onto a micro-channel plate stack, which amplifies the signal by a factor of a million. After that, the resulting electrons are converted back into photons by a phosphor screen and detected with a fast-scan CCD.

¹¹<https://www.cosmos.esa.int/web/xmm-newton/technical-details-om>

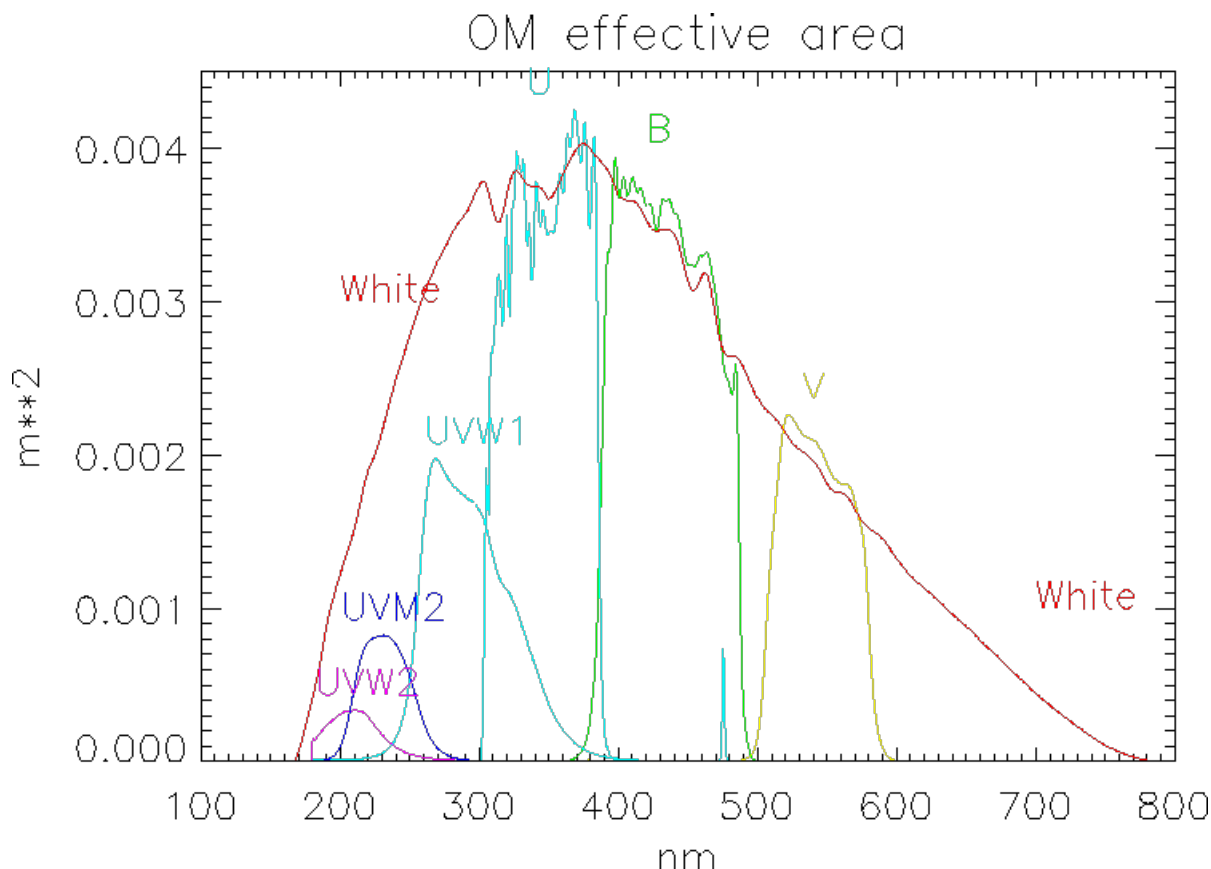


FIGURE 2.11: Throughput curves for the OM filters, folded with the detector sensitivity¹².

Filters

A filter wheel is installed in front of each detector. The filter wheel has 11 apertures, one of which is blanked off to act as a shutter, preventing light from entering the detector. Six filters comprise broad-band filters for color discrimination in the UV (UVW1, UVM2, UVW2) and optical (U, B, V) ranges between 180 nm and 580 nm (Figure 2.11). The seventh filter is a “white light” that allows light path through the whole detector range to maximize sensitivity to point sources. The remaining three positions contain two gratings, one optimized for the UV and the other for the optical, and a field expander by a factor of 4 (currently not operational) to provide high spatial resolution in the 380–650 nm band.

Operating modes

The OM instrument can operate in two modes; Imaging mode and Fast mode¹³. These allow either imaging or fast photometry or even both simultaneously. The Imaging mode emphasizes spatial coverage at the expense of timing information. Images can be taken at the full spatial sampling (0.5 arcsec) of the instrument or binned by a factor of 2 or 4 to yield an angular resolution on the sky of approximately 1.0 or 2.0 arcsec (a factor

¹²<https://www.cosmos.esa.int/web/xmm-newton/om-filter-bands>

¹³https://xmm-tools.cosmos.esa.int/external/xmm_user_support/documentation/uhb/ommodes.html

of four finer for the Magnifier). The longest integration time used in the OM imaging mode is 5 ks. Since the OM produces cumulative images in the imaging mode, there is no timing information attached to the individual incident photons. Any drift in the pointing direction of the spacecraft is corrected in the image by tracking guide stars.

In the Fast mode, the OM does not generate accumulated two-dimensional images. Timing information is prioritized over the spatial coverage, and the OM produces event lists similar to the ones in the X-ray instruments. This mode is useful for monitoring rapidly variable sources such as Blazars or accreting binaries.

2.5 Reflection Grating Spectrometer (RGS)

The reflection grating spectrometer (RGS) is a dispersive X-ray spectrometer using reflection gratings (den Herder et al., 2001) that enables precise spectroscopic observations in the soft X-ray band. The RGS consists of reflective X-ray gratings called reflection grating arrays (RGA) and an array of nine CCDs called RGS focal-plane cameras (RFC) that detect the dispersed photons. The observable energy bandwidth is 5–38 Å (0.35–2.5 keV), and the energy resolution is 2.0 eV (FWHM) for 1 keV X-rays for a point source. This energy resolution is one order of magnitude better than that of the CCDs and enables spectroscopy of the Fe L-shell transition lines. As shown in Figure 2.3, two RGAs are placed in the optical path between the telescope and MOS1 and 2. Approximately, 44% of the focused photons enter the MOS, 40% enter the RGA, and the rest are absorbed by the diffraction grating.

Chapter 3

Systematic Analysis of Seyfert 1 Galaxies

Contents

3.1	Target selection	43
3.2	Observations and Data reduction	45
3.3	Data analysis and Results	48
3.3.1	Intensity-sliced spectra and spectral ratios	48
3.3.2	Model-independent study of the spectral ratios	54
3.3.3	Introduction of the spectral-ratio model fitting	55
3.3.4	Systematic application of the spectral-ratio model fitting	61

In this chapter, we systematically apply the spectral-ratio model fitting method, which is newly developed for the present study, to 13 Seyfert 1 galaxies.

3.1 Target selection

One of the purposes of this study is to constrain the clump outflow velocities of the objects in which the UFO absorption lines have been detected and to probe their physical origin. Solving the complex parameter degeneracy with the spectral-ratio fitting method requires sufficient photon statistics within a short observation period that the less-variable spectral components are treated as constant. Therefore, we selected AGN samples from the UFO catalog by Tombesi et al. (2010) and Igo et al. (2020) where the UFOs were detected with high significance (“Likely outflows” in Igo et al., 2020) and the total exposure time was more than 200 ks. For comparison, we also included several objects for which no significant UFOs have been detected in Igo et al. (2020), but the presence of the clumpy absorbers has been confirmed. Observation targets thus selected for this study are listed in Table 3.1.

Among these targets, IRAS 13224–3809 is the most suitable source for this study, thanks to its prominent UFO absorption structures, large spectral variability due to the ionized partial absorption, and the fact that an exceptionally long 1.5 Ms observation campaign by *XMM-Newton* has been performed. Parker et al. (2017) discovered the UFO absorption lines from IRAS 13224–3809 in the 1.5 Ms deep observation in 2016. They claimed that the equivalent width of the UFO absorption lines and the X-ray luminosity

TABLE 3.1: Observation targets and their characteristics.

1. Source	2. AGN Class	3. z	4. $\log M_{\text{BH}} (M_{\odot})$	5. $v_{\text{UFO}} (/c)$
<i>UFO absorption detected in Igo et al. (2020)</i>				
IRAS 13224–3809	NLS1	0.0658	$6.0 \pm 0.3^{\text{R, a}}$	$0.238^{+0.003}_{-0.049}{}^{\text{j}}$
1H 0707–495	NLS1	0.04057	$6.5 \pm 0.2^{\text{b}}$	$0.165^{+0.002}_{-0.051}{}^{\text{j}}$
ESO 323–G77	S1, NLS1	0.014904	$\sim 7.12^{\text{D, c}}$	$0.085^{+0.006}_{-0.048}{}^{\text{j}}$
MCG–6-30-15	S1, NLS1	0.05708	$6.30^{+0.16}_{-0.24}{}^{\text{R, d}}$	$0.08^{+0.02}_{-0.05}{}^{\text{j}}$
Mrk 766	NLS1	0.01271	$6.82^{+0.05}_{-0.06}{}^{\text{R, d}}$	$0.08^{+0.02}_{-0.05}{}^{\text{j}}$
NGC 4051	NLS1	0.0023	$5.89^{+0.08}_{-0.15}{}^{\text{R, d}}$	$0.061^{+0.022}_{-0.033}{}^{\text{j}}$
NGC 7314	NLS1	0.004771	$5.9 \pm 0.3^{\text{V, e}}$	$0.04^{+0.02}_{-0.03}{}^{\text{j}}$
PDS 456	QSO	0.184	$9.3 \pm 0.4^{\text{E, f}}$	$0.255^{+0.049}_{-0.020}{}^{\text{j}}$
Ton S180	NLS1	0.06168	$7.3 \pm 0.3^{\text{E, g}}$	$0.35^{+0.05}_{-0.02}{}^{\text{j}}$
<i>UFO undetected in Igo et al. (2020), but clump features confirmed</i>				
Mrk 335	NLS1	0.025	$7.23^{+0.04}_{-0.04}{}^{\text{R, d}}$	$0.051^{+0.053}_{-0.020}{}^{\text{j}'}$
NGC 3783	S1	0.009755	$7.08^{+0.05}_{-0.06}{}^{\text{R, d}}$	No detection
NGC 985	S1	0.04271	$\sim 8.2^{\text{h}}$	No detection
PG 1126–041	S1	0.06	$\sim 8.1^{\text{V, i}}$	0.05^{k}

¹. Source name.

². AGN class based on $H\beta$ line width and redshift.

³. Cosmological redshift.

⁴. The logarithm of the estimated black hole mass, mass estimate method (R: reverberation mapping, V: stellar velocity dispersion, E: empirical relation with 5100 Å luminosity and BLR radius, D: Relation between dust size and BLR size), and references (a: Parker et al., 2017, b: Done and Jin, 2016, c: GRAVITY Collaboration et al., 2022, d: Bentz and Katz, 2015, e: McHardy, 2013, f: Emmanoulopoulos et al., 2014), g: T. J. Turner et al., 2002, h: Vasudevan et al., 2009, i: Dasyra et al., 2007)

⁵. The detected UFO velocity and references (j: Igo et al., 2020, j': Igo et al., 2020, but low significance, k: Giustini et al., 2011).

are anti-correlated, while the line-of-sight velocity of the UFO is correlated with the X-ray luminosity. They argue that the disk wind is driven by the radiation pressure so that the absorption lines were not detected when the wind was fully ionized due to intense X-ray radiations. Some previous studies including Parker et al. (2017) explained the X-ray spectra of IRAS 13224–3809 in terms of the relativistic disk reflection model which assumes extreme physical conditions as described in Section 1.3.3. Whereas, Yamasaki et al. (2016) successfully interpreted the spectral variability of IRAS 13224–3809 (*XMM-Newton* data in 2001–2011 before detection of the UFO absorption) using the partial absorption model without such extreme conditions.

3.2 Observations and Data reduction

XMM-Newton data is best suited for the present analysis thanks to its high sensitivity, simultaneous optical and UV observations, and long continuous target visibility. Table 3.2 describes the *XMM-Newton* observation logs of the targets. As we shall describe in detail in Section 3.3, spectral-ratio model fitting is effective to study relatively short time-scale (\lesssim weeks) spectral variations where the longer time-scale variation can be ignored. Thus, when there are observations within a few weeks, they are considered as a single observation group and used for the spectral-ratio analysis. Observations across years are not treated as a single observation, but as independent observation groups (e.g., Group 1, 2). For each single observation group conducted within a few weeks, the spectral-ratio analysis is performed.

We used only the observation data obtained by *XMM-Newton* EPIC-pn for all the targets. The EPIC-MOS data were not used because its effective area is much smaller than that of the pn detector in the soft X-ray band. The pn data were reduced with version 19.1.0 Science Analysis Software (SAS; Gabriel et al., 2004) which is designed to reduce and analyze *XMM-Newton* data to obtain the filtered event files. The unscheduled observations¹ were also used when available to improve the statistics. Good time intervals were calculated by removing the periods dominated by the flaring particle background when the PATTERN==0 count rate in 10–12 keV is larger than 0.4 counts s⁻¹. We used circular regions of 250 physical unit (12.5'') radius and 1600 physical unit (75'') radius from the same CCD for extracting the source events and the background events, respectively. The background region is carefully selected, avoiding chip edges and the region where the Cu background is high. Following the ‘‘SAS Data Analysis Threads’’², we extracted the light curves, spectra, and responses applying the good time intervals and the source/background regions. In addition to the pn, the OM data is reduced by the standard SAS routine `omchain`, and the spectrum is extracted using `om2pha`.

¹When there was an unexpected observation interruption due to, e.g., high radiation levels, those exposures taken immediately after the interruption are called ‘‘unscheduled’’.

²<https://www.cosmos.esa.int/web/xmm-newton/sas-thread-epic-filterbackground>
<https://www.cosmos.esa.int/web/xmm-newton/sas-thread-pn-spectrum>
<https://www.cosmos.esa.int/web/xmm-newton/sas-thread-rgs>

TABLE 3.2: *XMM-Newton* (pn) observation logs.

Source	Obs. Group	Obs. ID	Start Date	Exp. (ks) ^a	0.3–10 keV mean count rate (counts s ⁻¹)
IRAS 13224–3809	1	0780560101	2016-07-08	32.6	2.8
		0780561301	2016-07-10	127.4	
		0780561401	2016-07-12	81.8	
		0780561501	2016-07-20	130.4	
		0780561601	2016-07-22	130.4	
		0780561701	2016-07-24	129.9	
		0792180101	2016-07-26	130.6	
		0792180201	2016-07-30	130.1	
		0792180301	2016-08-01	123.7	
		0792180401	2016-08-03	130.2	
		0792180501	2016-08-07	124.0	
0792180601	2016-08-09	125.9			
1H 0707–495	1 (2008)	0511580101	2008-01-29	115.3	4.7
		0511580201	2008-01-31	96.9	
		0511580301	2008-02-02	98.6	
		0511580401	2008-02-04	96.6	
	2 (2010)	0653510301	2010-09-13	107.4	4.9
		0653510401	2010-09-15	118.7	
		0653510501	2010-09-17	111.0	
		0653510601	2010-09-19	113.4	
ESO 323–G77	1	0694170101	2013-01-17	127.4	0.4
MCG 6-30-15	1 (2001)	0029740101	2001-07-31	59.2	28.8
		0029740701	2001-08-02	89.9	
		0029740801	2001-08-04	88.5	
	2 (2013)	0693781201	2013-01-29	94.9	27.0
		0693781301	2013-01-31	94.9	
0693781401	2013-02-02	34.4			
Mrk 766	1	0304030101	2005-05-23	67.3	11.3
		0304030301	2005-05-25	69.8	
		0304030401	2005-05-27	69.5	
		0304030501	2005-05-29	67.4	
		0304030601	2005-05-31	69.6	
		0304030701	2005-06-03	24.4	
NGC 4051	1	0606320101	2009-05-03	32.1	13.9
		0606320201	2009-05-05	31.5	
		0606320301	2009-05-09	22.2	
		0606320401	2009-05-11	20.4	
		0606321301	2009-05-15	21.4	
		0606321401	2009-05-17	27.0	
		0606321501	2009-05-19	27.5	
		0606321601	2009-05-21	29.4	
		0606321701	2009-05-27	27.2	
		0606321801	2009-05-29	28.3	
		0606321901	2009-06-02	4.4	
		0606322001	2009-06-04	26.2	
		0606322101	2009-06-08	26.7	
		0606322201	2009-06-10	29.2	
		0606322301	2009-06-16	29.8	
NGC 7314	1	0725200101	2013-05-17	93.8	5.5
		0725200301	2013-11-28	92.7	
PDS 456	1	0721010201	2013-08-27	102.0	2.6
		0721010301	2013-09-06	104.2	
		0721010401	2013-09-15	111.1	

TABLE 3.2: *XMM-Newton* (pn) observation logs.

Source	Obs. Group	Obs. ID	Start Date	Exp. (ks) ^a	0.3–10 keV mean count rate (counts s ⁻¹)
		0721010501	2013-09-20	102.6	
Ton S180	1	0764170101	2015-07-03	96.1	8.7
Mrk 335	1	0842760201	2021-06-16	88.6	6.0
		0842761101	2021-06-18	88.7	
		0842761201	2021-06-20	90.4	
		0842761301	2021-06-22	88.9	
		0842761401	2021-06-14	84.4	
NGC 985	1 (2013)	0690870101	2013-07-20	17.9	2.0
		0690870501	2013-08-10	72.5	
	2 (2015)	0743830501	2015-01-13	97.5	10.5
		0743830601	2015-01-25	85.5	
NGC 3783	1 (2001)	0112210201	2001-12-17	40.1	16.7
		0112210501	2001-12-19	96.8	
	2 (2016)	0780860901	2016-12-11	78.0	12.1
		0780861001	2016-12-21	39.4	
PG 1126–041	1 (2008–9)	0556230701	2008-06-15	20.2	0.2
		0556231201	2008-12-13	10.0	
		0606150101	2009-06-21	127.0	
	2 (2014–5)	0728180201	2014-06-01	32.9	0.2
		0728180301	2014-06-12	20.0	
		0728180401	2014-06-28	25.0	
		0728180501	2015-06-14	15.0	

^a Sum of all the good time intervals. For observations with unscheduled exposure, they are combined with scheduled ones.

3.3 Data analysis and Results

We developed a new data analysis method called “spectral-ratio model fitting” to disentangle the spectral parameter degeneracy (Midooka, Mizumoto, and Ebisawa, 2022). In this section, we introduce methodology of the spectral-ratio model fitting and apply this method to the sample systematically.

3.3.1 Intensity-sliced spectra and spectral ratios

Let us focus on IRAS 13224–3809 as a representative example to explain the methodology. Since UFO properties of IRAS 13224–3809 are known to be luminosity-dependent (e.g., Parker et al., 2017, Pinto et al., 2018, and Chartas and Canas, 2018), we create the intensity-sliced spectra. First, all the 0.3–10.0 keV events from all the observation IDs were binned every 1 ks. Figure 3.1 shows the 0.3–10 keV light curve of IRAS 13224–3809 with 1 ks bins. X-ray count rate varies up to an order of magnitude or more within a few days. The variation has several peaks, and the variation timescale is from tens of ks to hundreds of ks. According to recent simulations and observations, clumps are likely to locate at $100\text{--}1,000 R_g$ (Takeuchi, Ohsuga, and Mineshige, 2013), and WAs typically locate much further, $10,000 R_g$ (10^{-3} pc) to 10 pc (e.g., Arav et al., 2015; Laha et al., 2021). In the case of IRAS 13224–3809 with the BH of $\sim 10^6 M_\odot$, the light crossing time at $100 R_g$ is 0.5 ks, and the Keplerian rotation periods at $100 R_g$ or $10,000 R_g$ from the center are about 30 or 30,000 ks. Therefore, the intensity variations of tens to hundreds of ks seen in Figure 3.1 may not be caused by the WA absorption, but more likely to be caused by the intrinsic variations and/or clump absorption.

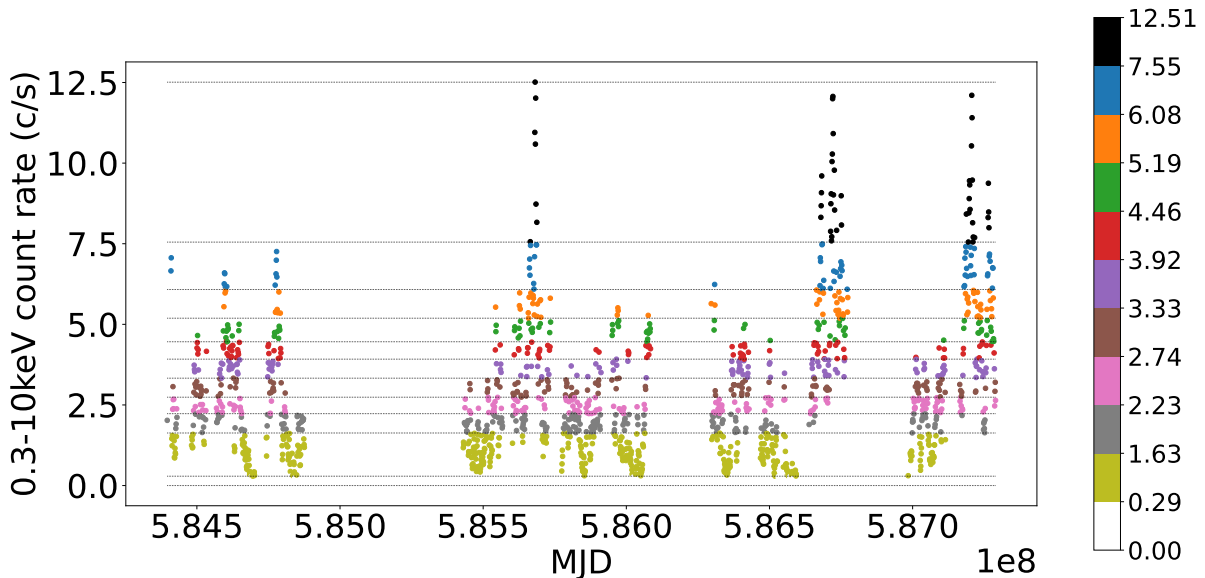


FIGURE 3.1: The 0.3–10 keV light curve of IRAS 13224–3809 with 1 ks bin. The horizontal dotted lines show the count rate thresholds. Following the right color bar, 10 divisions are arranged in different colors.

We defined 10 groups in the intensity order so that the total number of photons in each division is equal. The light curve of Figure 3.1 is colored differently according to the X-ray intensity (count rate in 0.3–10 keV). Based on the count rate threshold

(Table 3.3), we created 10 intensity-sliced spectra (A–J), where A is the brightest and J is the dimmest. The intensity-sliced spectra were grouped with 8 and 16 spectral bins in 0.3–2.0 keV and 2.0–10.0 keV, respectively. These intensity-sliced spectra are shown in the upper panel of Figure 3.2. We can see that the spectrum varies in an order of magnitude mainly due to ionized absorption, especially around 1–5 keV, and that there are conspicuous UFO absorption structures around 7–10 keV. Next, the observed spectral ratios were created by taking the ratio of each intensity-sliced spectrum (B–J) to the brightest spectrum A (lower panel of Figure 3.2). A dip- or cliff-like structure at around 1 keV is visualized by taking the spectral ratios.

TABLE 3.3: Count rate threshold of intensity-sliced spectra of IRAS 13224–3809 (0.3–10.0 keV).

Division	Minimum ^a (counts s ⁻¹)	Maximum ^a (counts s ⁻¹)
A	7.55	12.51
B	6.09	7.55
C	5.21	6.09
D	4.46	5.21
E	3.92	4.46
F	3.34	3.92
G	2.74	3.34
H	2.23	2.74
I	1.63	2.23
J	0.29	1.63

^a The count rate is calculated from a normalized light curve with the SAS task `epiclccorr`.

Intensity-sliced spectra were also created for the other 12 sources in the same manner. Since the exposure was shorter than that of IRAS 13224–3809, the spectra were sliced into 5 divisions (A–E) instead of 10. Figure 3.3–3.5 show the intensity-sliced spectra of the other objects.

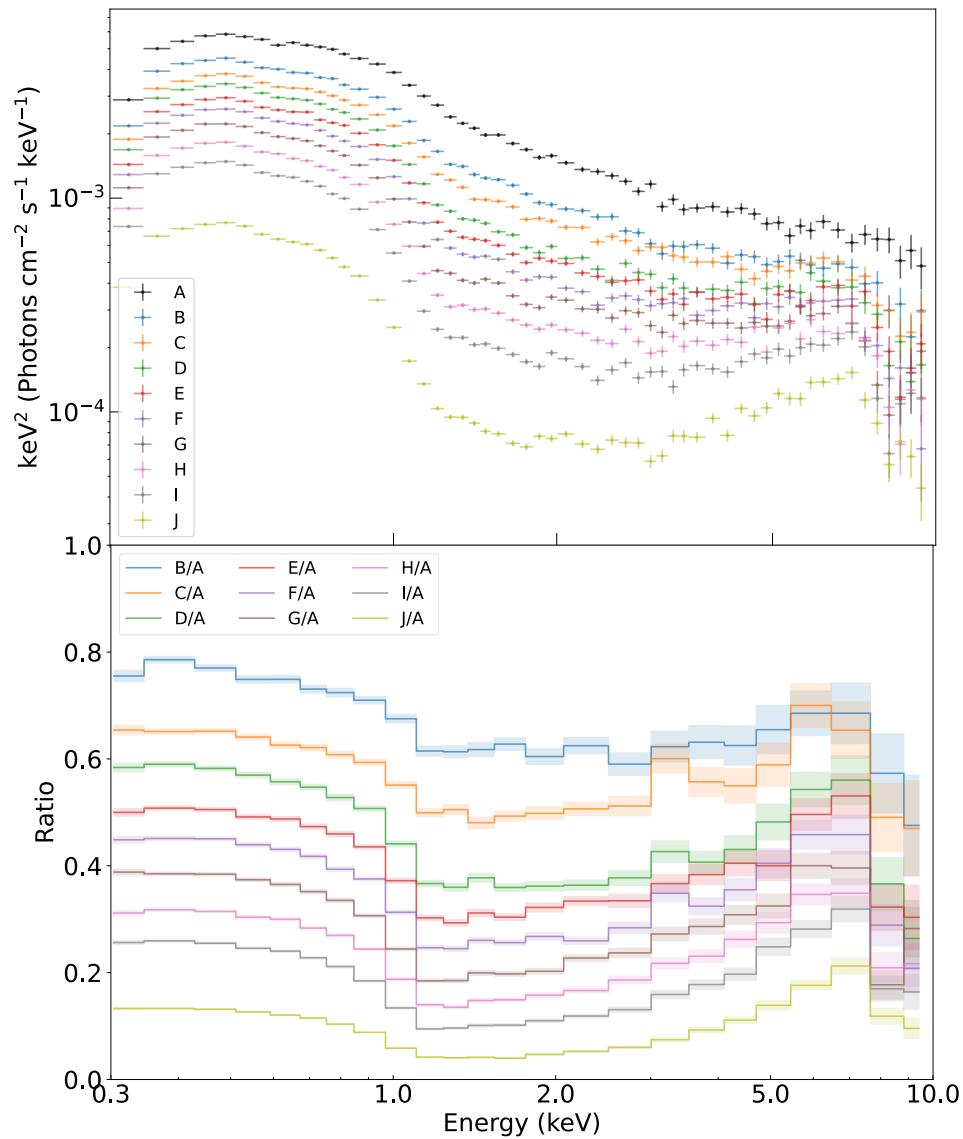


FIGURE 3.2: Top panel shows the 10 intensity-sliced spectra of IRAS 13224–3809 obtained with *XMM-Newton* pn in 0.3–10.0 keV. The νF_ν plot unfolded by the power-law with the index of 2.0 is shown. The bottom panel shows the nine spectral ratios to the brightest spectrum A (black in the top panel). Note that both panels show adequately binned spectra to enhance visibility.

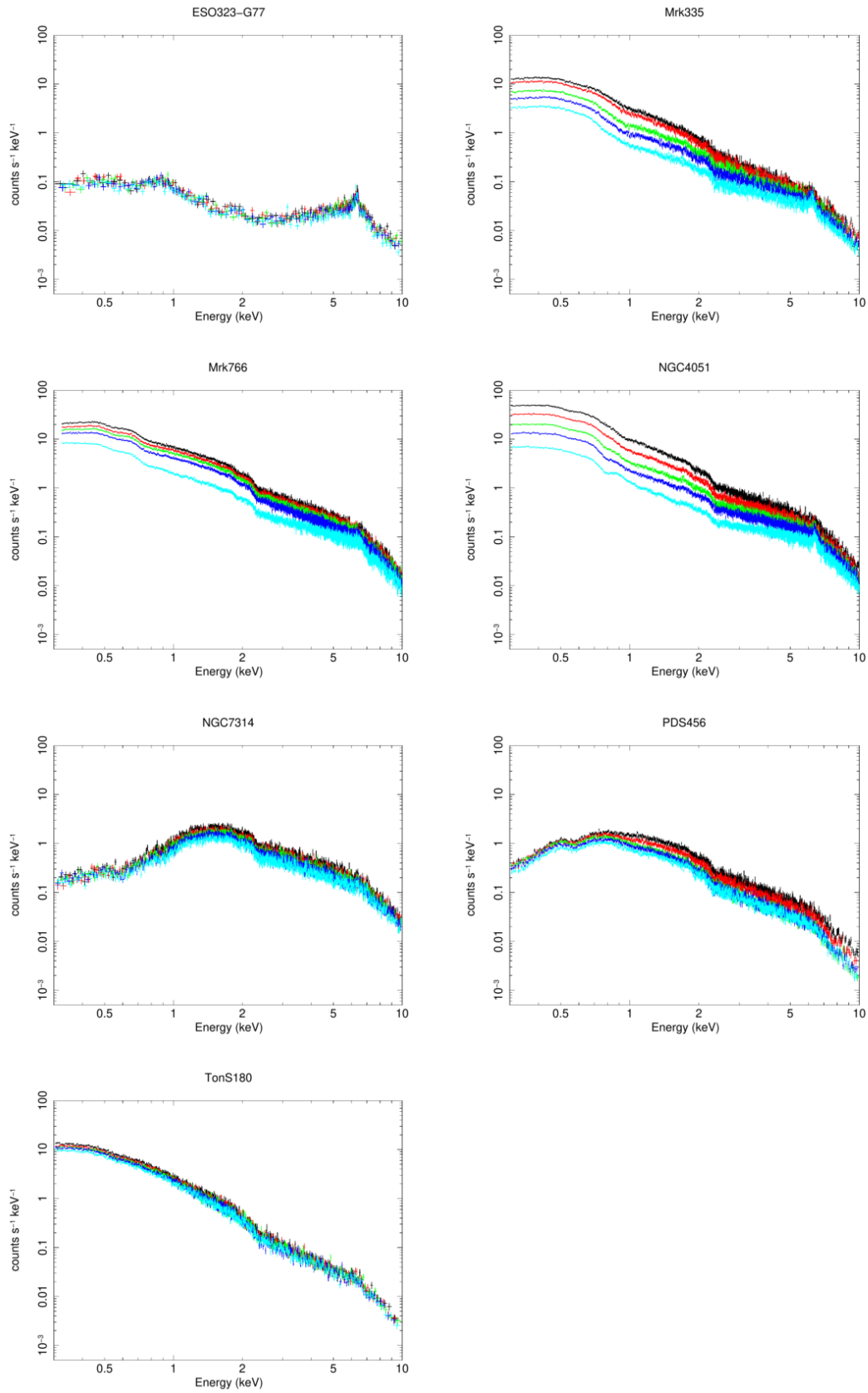


FIGURE 3.3: Intensity-sliced spectra of sources with a single observation period.

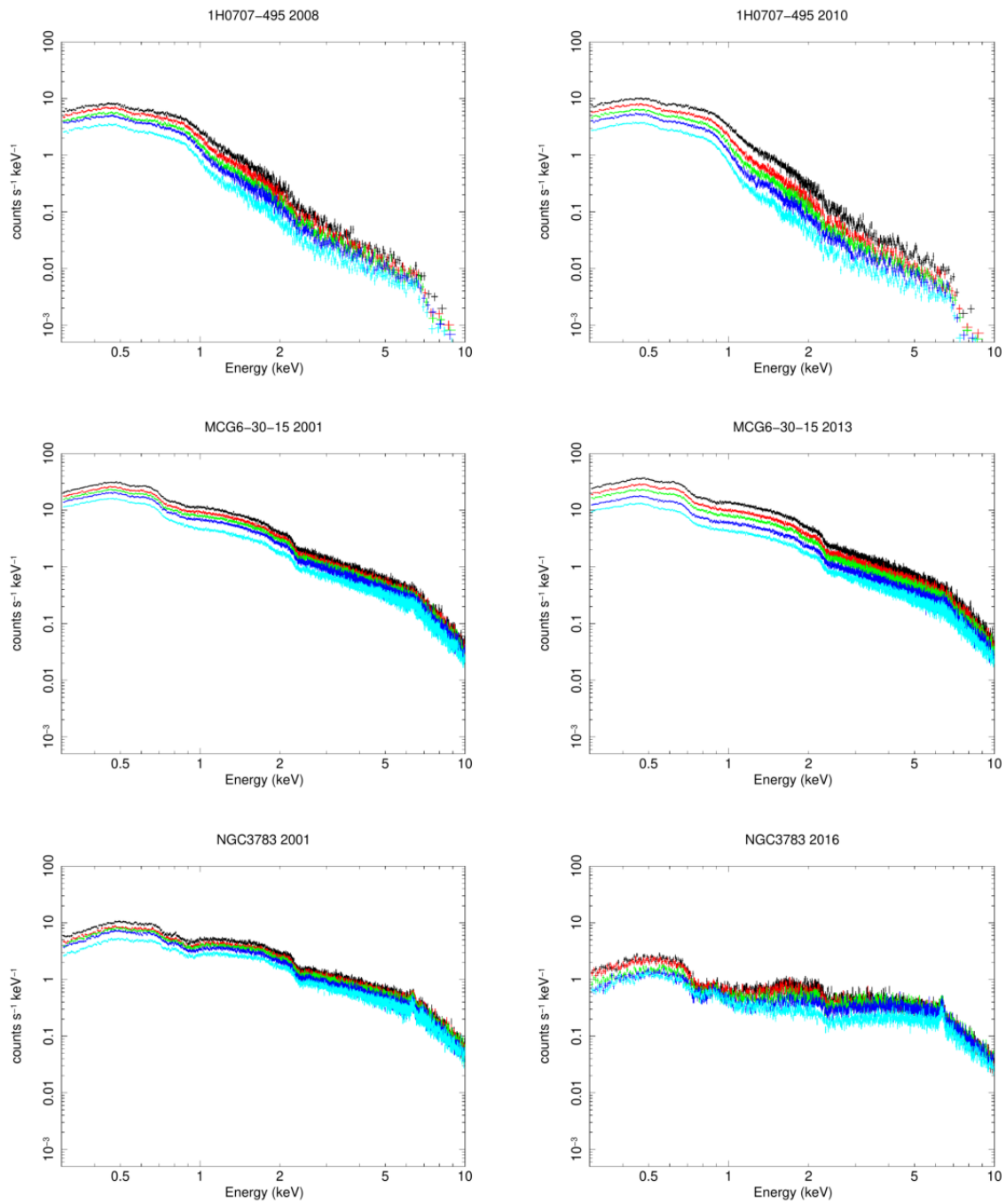


FIGURE 3.4: Intensity-sliced spectra of sources with multiple observation periods.

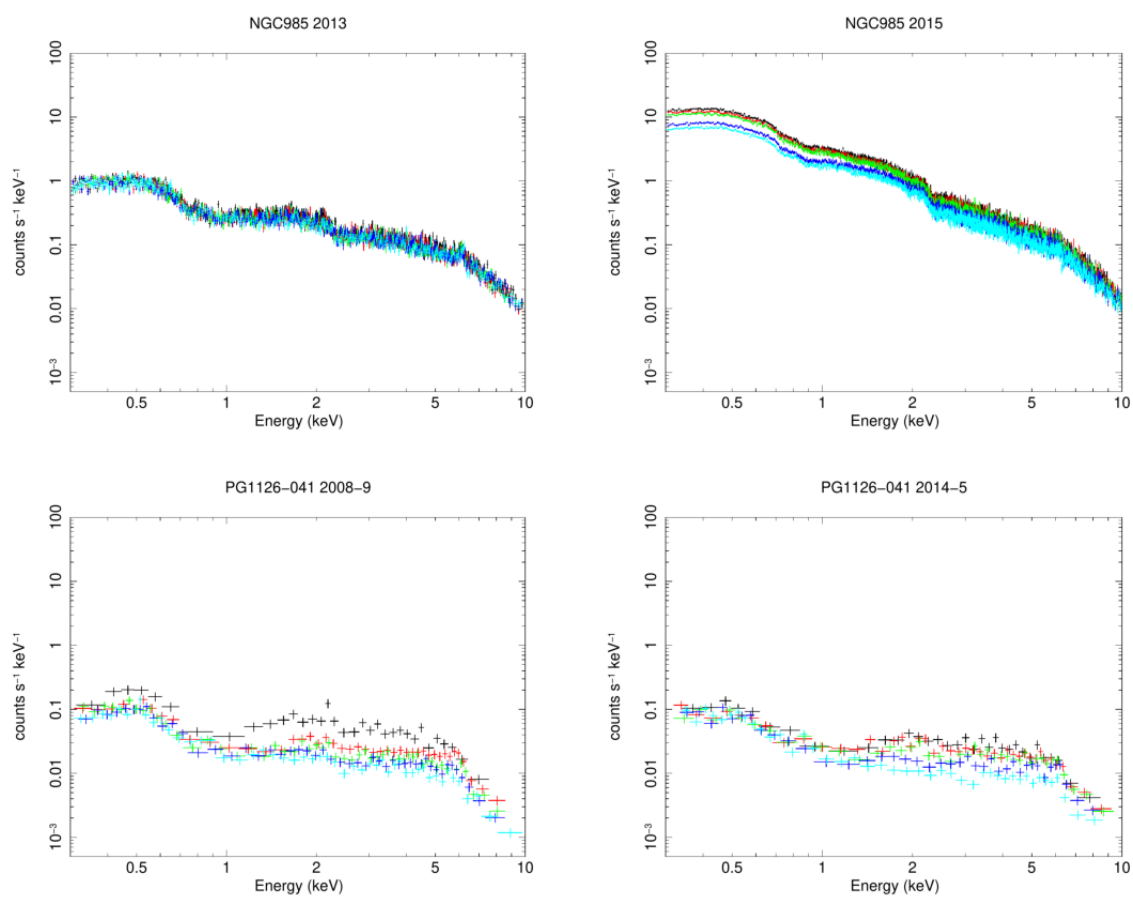


FIGURE 3.5: Intensity-sliced spectra of sources with multiple observation periods.

3.3.2 Model-independent study of the spectral ratios

In this section, we show that the flux dependency of the clump velocity of IRAS 13224–3809 can be constrained model independently from the spectral ratios. We made 9 spectral ratios from the 10 observed intensity-sliced spectra of IRAS 13224–3809. The upper panel in Figure 3.6 shows the representative spectral ratios of B/A, F/A, and J/A, each of which has a dip- or cliff-like structure at around 1 keV. We define the “dip characteristic energy” where the spectral ratio changes from convex-upward to convex-downward. To do so, first, the observed spectral ratios were fitted with 8th-order polynomial equations to remove minor fluctuation (the solid lines in the upper panel in Figure 3.6). Then, the first derivatives of the polynomial models were calculated as shown in the lower panel of Figure 3.6. The energies that give the minimums of the first derivative around 0.9–1.1 keV correspond to the dip characteristic energies defined above (dotted vertical lines in the lower panel). We find that the dip characteristic energy is *blue-shifted* when X-rays get brighter. Note that this result is obtained without assuming any spectral models.

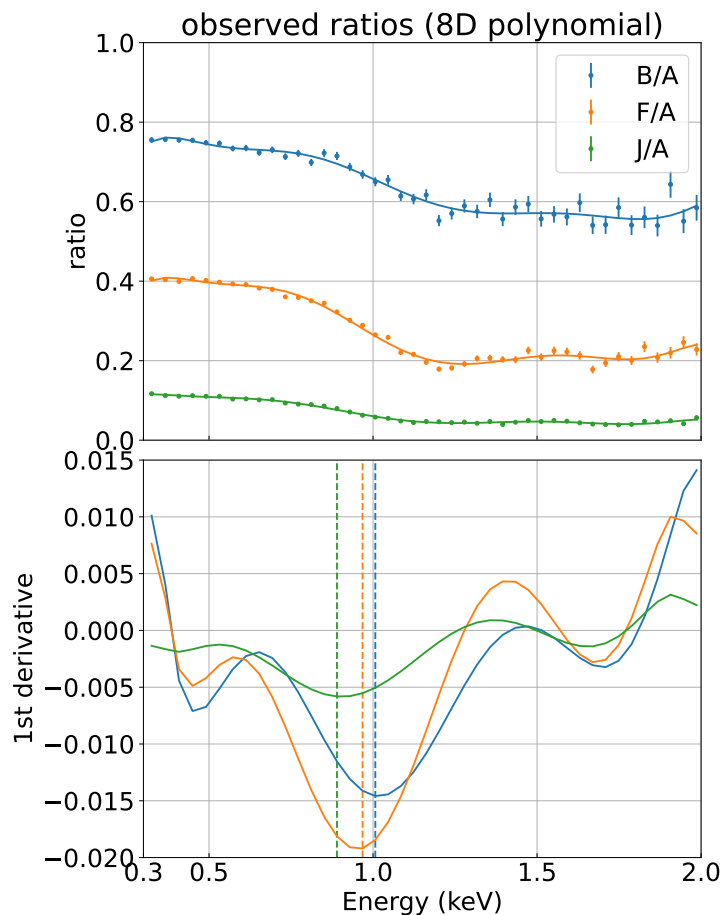


FIGURE 3.6: In the upper panel, scattered points show the observed spectral ratios B/A, F/A, and J/A. Solid lines are the best-fit 8th-order polynomial equations. The lower panel shows their 1st derivatives, in which the dotted vertical lines represent the energies where the 1st derivatives get minimum. These energies, characterizing the dip feature, increase as the X-ray flux gets higher.

3.3.3 Introduction of the spectral-ratio model fitting

Overview of the spectral-ratio analysis

The X-ray spectral continuum of typical Seyfert 1 galaxies consists of the power-law (PL) and the soft-excess component that contribute mainly above and below ~ 1 keV, respectively. The continuum is absorbed by several types of gas such as WA, UFO, and clumpy absorbers. UFOs are highly ionized and mainly absorb the hard X-rays above ~ 6 keV. The spectral shape of the continuum does not change significantly within a few weeks. WAs do not change their geometry or ionization structure significantly in a timescale of a few weeks either, while the partial covering fraction of the clumpy absorbers significantly changes on shorter timescales and significantly alters the spectral shape below ~ 5 keV (e.g., Di Gesu et al., 2015, Midooka et al., 2022).

Therefore, taking the spectral ratio below 5 keV enables us to focus on the variability of the clumpy absorbers, canceling out the less time-variable spectral components. A significant merit of this method is that it is not necessary to determine the spectral shape of the continuum precisely.

Spectral-ratio models

Model spectral ratios were created in the 0.3–5.0 keV band using XSPEC (version 12.12.0), the standard X-ray spectral analysis package (Arnaud, 1996). Our aim is to extract the spectral change due to the clumpy absorber. Therefore, we consider a simple model spectrum in which the continuum is covered by an ionized clumpy absorber (`zxipcf`; J. Reeves et al., 2008). This absorber model has three parameters; ionization parameter ξ , hydrogen column density N_{H} , and partial covering fraction (CF). We have seen that the dip characteristic energy is flux-dependent from the model-independent analysis (Section 3.3.2). Therefore, in addition to the three clump parameters (CF, N_{H} , and ξ), we introduce the outflowing velocity of the clumpy absorber, v_{out} , to blue-shift the dip energy. We also incorporate the normalization of the continuum intensity as another free parameter.

Since the instrumental responses for the different intensity-sliced spectra are almost identical within 1 %, the response of the brightest spectrum A was used to calculate the model spectra in 0.2–10.0 keV (see Table 3.3). A table model of the spectral ratio was created by taking the ratio of the absorbed model spectra to the unabsorbed one with the same continuum parameters. This operation was repeated for the number of the parameter grids, constituted of $21 \times 13 \times 13 \times 13 = 46,137$ synthetic spectra (Table 3.4).

TABLE 3.4: Parameter ranges for the spectral-ratio model.

Component	Minimum	Maximum	Step number
CF	0.0	1.0	21
velocity [c]	-0.30	0.0	13
$\log \xi$	0.0	3.0	13
$\log N_{\text{H}}$	22.0	25.0	13

Figure 3.7 shows examples of the model spectral ratios when each of CF, N_{H} , and ξ is varied at several different values while the two other parameters are fixed (the absorber velocity is null). When the absorber is mildly ionized ($\log \xi \sim 1.5-3.0$), characteristic dip

structures are seen in 0.8–1.0 keV. They are mainly created by the so-called unresolved transition array (UTA) of Fe-L and Fe-M shells; their depths, widths, and shapes are dependent on the ionization parameter and the column density. The ion population changes as the ionization increases, and the dip energy increases up to ~ 0.95 keV. It is noteworthy that the dip energy never goes beyond ~ 1 keV, no matter how much the gas is ionized. As seen from the brown line in the middle panel of Figure 3.7, at $\log \xi = 4.0$, most of the gas is fully ionized and cannot form absorption structures. If observed spectral ratios show such dips above 1 keV, that cannot be explained by the ionization, and strongly suggests that the clumpy absorber is blue-shifted. Variation of the model spectral ratios when the velocity or the norm is varied appears in Figure 3.8.

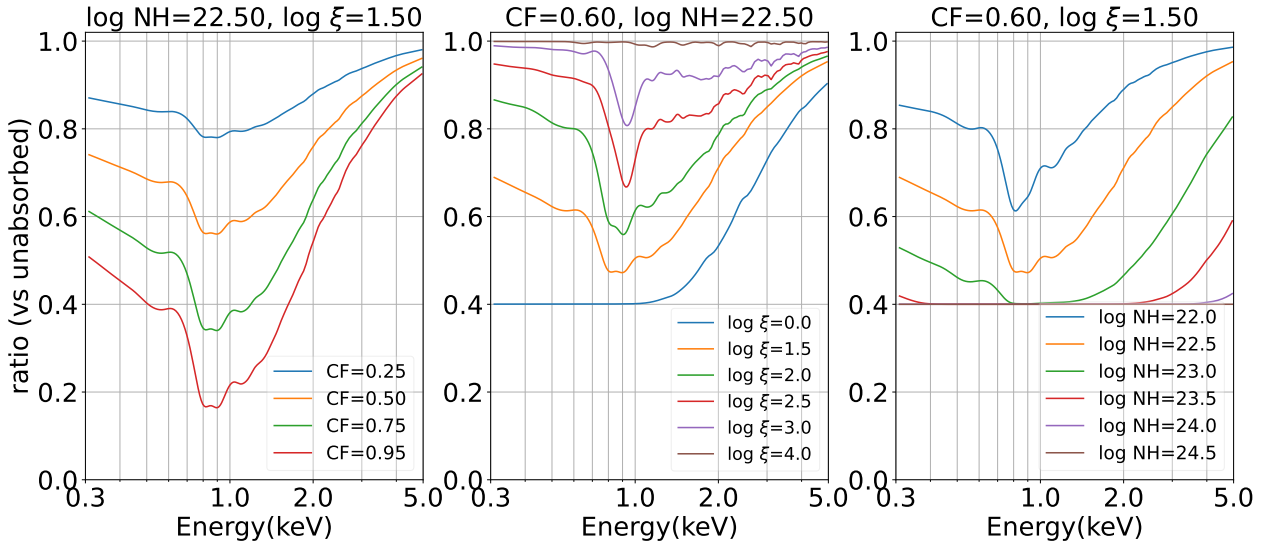


FIGURE 3.7: Model spectral ratios, where each of CF, N_H , and ξ (from left to right) is varied at several different values while the other two parameters are fixed. The absorber velocity is null.

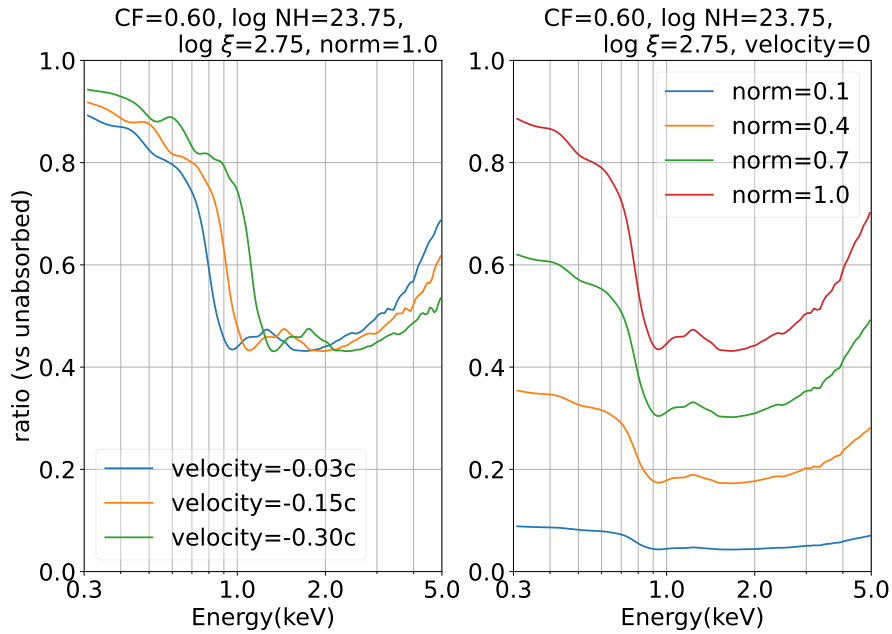


FIGURE 3.8: Model spectral ratios, where the velocity (left) or the norm (right) of the absorbed spectrum is varied at several different values, while the other parameters are fixed.

Example of Spectral-ratio model fitting

We explain the spectral-ratio model fitting with high-quality data of IRAS 13224–3809 as an example. The ratio of the fifth brightest spectrum (E) to the brightest spectrum (A) is shown in blue dots in Figure 3.9, where the dip structure is seen around 1.1–1.3 keV. We are going to compare the observed spectral ratio with models, assuming that the brightest spectrum A is unabsorbed ($CF = 0$). We consider an X-ray spectrum with $CF = 0.5$, $\log N_{\text{H}} = 23.75$, $\log \xi = 2.75$, whose ratio to the unabsorbed spectrum is the orange curve in Figure 3.9. In this spectral-ratio model, the dip structure energy does not match the observed ratio. Therefore, the clumpy absorber was given a velocity of $-0.25 c$ to blue-shift the dip energy, and also the normalization was made 0.51 times (the blue line in Figure 3.9). Now, we see that the spectrum below 2 keV is explained well by the model spectral ratio. The energy shift of the dip structure is apparent with the velocity variation so that the absorber velocity is constrained from the observed dip structure. Note that the velocity $-0.25 c$ has not yet taken into account the cosmological redshift.

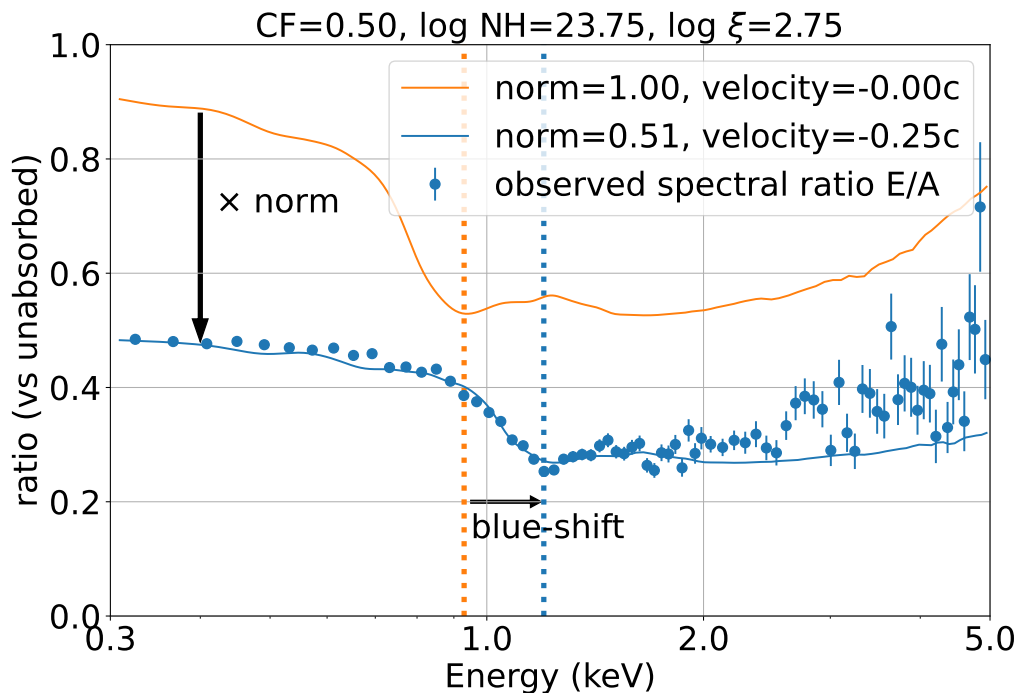


FIGURE 3.9: The blue dots show the observed spectral ratio E/A . The orange line represents a model ratio between the absorbed and unabsorbed spectra, where the absorbed spectrum has $CF = 0.5$, $\log N_{\text{H}} = 23.75$, and $\log \xi = 2.75$. We find that the dip energy of the model spectral ratio needs to be blue-shifted. After varying the norm and velocity, the orange line moves to the blue one, which fits the observed ratio.

Then, the parameter space was optimized for IRAS 13224–3809, being set more finely within a narrower range, constituted of $21 \times 16 \times 11 \times 11 = 40,656$ synthetic spectra (Table 3.5), where models were linearly interpolated between the adjacent grid points.

First, the least chi-square fitting was performed nine observed spectral ratios allowing all the five parameters free (the four parameters above and the normalization).

TABLE 3.5: Parameter ranges for a more optimized spectral-ratio model of IRAS 13224–3809.

Component	Minimum	Maximum	Step number
CF	0.0	1.0	21
velocity [c]	-0.30	-0.15	16
$\log \xi$	2.0	3.0	11
$\log N_{\text{H}}$	23.5	24.5	11

Figure 3.10 and 3.11 show the fitting results in IRAS 13224–3809. The model spectral ratios are well fitted for all the ratios, especially below 2 keV, where the dip structure appears. Fitting for the dimmer ones shows larger residuals above ~ 2 keV, suggesting changes in the PL index, which shall be confirmed later with the spectral fitting (Section 4.2). Best-fit parameters obtained from the spectral-ratio model fitting are given in Table 3.6. Hereafter the v_{out} parameters are corrected for the cosmological redshift.

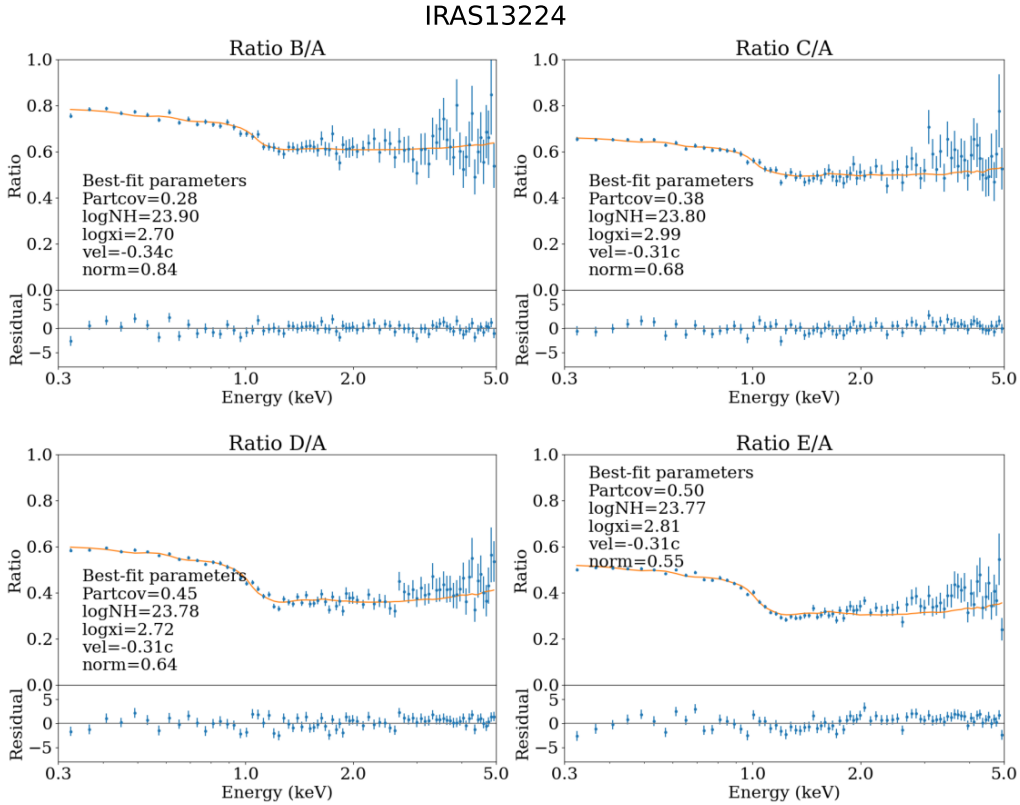
FIGURE 3.10: Ratio fitting results of IRAS 13224–3809. Four clump parameters (CF, ξ , N_{H} , and v_{out}) and the normalization are free to vary.

TABLE 3.6: Best-fit parameters obtained from spectral-ratio model fitting of IRAS 13224–3809 with the least chi-squared.

	J	I	H	G	F	E	D	C	B
CF	0.94	0.78	0.70	0.65	0.58	0.53	0.51	0.32	0.28
norm	0.15	0.29	0.35	0.43	0.49	0.55	0.64	0.68	0.84
$\log N_{\text{H}}$	23.8	23.8	23.8	23.8	23.8	23.8	23.8	23.8	23.9
$\log \xi$	2.94	2.97	3.01	2.86	2.80	2.81	2.72	2.99	2.70
v_{out} (/c)	0.25	0.26	0.27	0.28	0.29	0.31	0.31	0.31	0.34

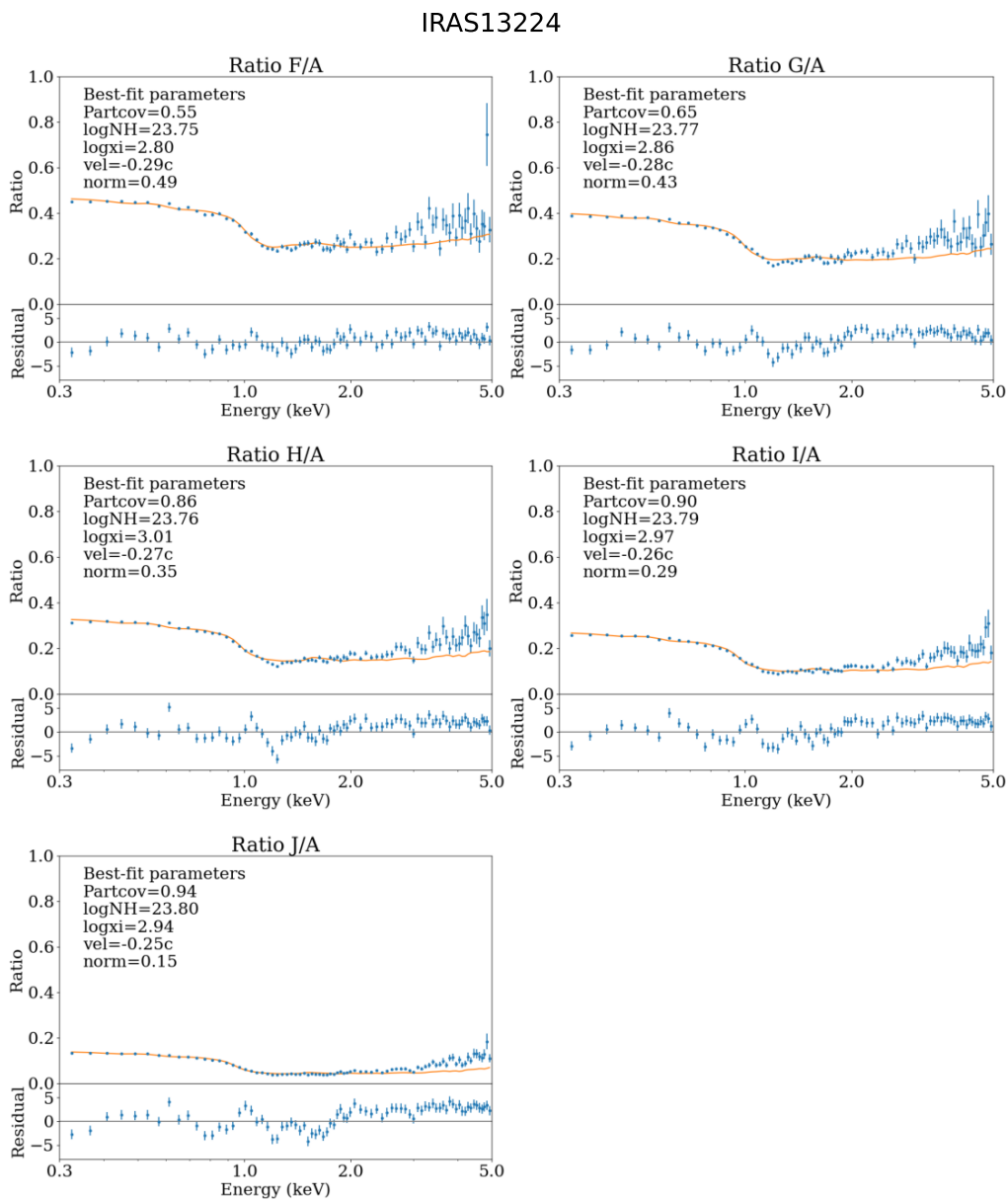


FIGURE 3.11: (Cont.) Ratio fitting results of IRAS 13224–3809. Four clump parameters (CF, ξ , N_{H} , and v_{out}) and the normalization are free to vary.

3.3.4 Systematic application of the spectral-ratio model fitting

For PG 1126–041 and ESO 323–G77, spectral-ratio fitting could not be applied due to their small flux and large statistical errors (see Figure 3.3 and 3.5). In addition, a certain amount of the time variability is essential to investigate the spectral ratio; for Ton S180 and NGC 7314 (Figure 3.3), spectral-ratio fitting was not performed either because little time variability was seen in their intensity-sliced spectra.

We apply the spectral-ratio model fitting to the other nine targets, each of which shows sufficient photon statistics and time variability (Mrk 335, Mrk 766, NGC 985, NGC 4051, PDS 456, 1H 0707–495, MCG–6-30-15, and NGC 3783). Spectral-ratio table model was created with four free parameters (CF, ξ , N_{H} , and v_{out}) to vary (see Table 3.4), where models were linearly interpolated between the adjacent grid points. The least chi-square fitting was performed with four observed spectral ratios allowing all the five parameters free (the four parameters above and the normalization).

Fitting results of the eight objects are shown in Figure A.1–A.8. For Mrk 335, PDS 456, and 1H 0707–495, the spectral ratios have dip structures around 1 keV where the model ratio is fitted well, whereas the fitting shows residuals in other energy ranges. The ratios of Mrk 766, NGC 985, NGC 4051, MCG–6-30-15, and the 2001 observation of NGC 3783 are almost flat, thereby not suitable to constrain the clump velocity with the spectra-ratio fitting. The ratio of NGC 3783 in 2016 shows a hump structure around 1 keV presumably due to the presence of the constant scattered emission from distant gas (Mao et al., 2019; Marco et al., 2020). Best-fit parameters are given in Table 3.7–3.14.

TABLE 3.7: The same as Table 3.6, but for Mrk 335.

	E	D	C	B
CF	0.62	0.46	0.45	0.16
norm	0.42	0.56	0.69	0.91
$\log N_{\text{H}}$	22.8	22.8	22.5	22.4
$\log \xi$	1.69	1.65	1.73	1.53
$v_{\text{out}} (/c)$	0.04	0.04	0.04	0.12

TABLE 3.8: The same as Table 3.6, but for PDS 456.

	E	D	C	B
CF	0.45	0.43	0.46	0.23
norm	0.80	0.88	0.97	0.99
$\log N_{\text{H}}$	23.9	23.8	23.8	23.8
$\log \xi$	2.75	2.75	2.75	2.75
$v_{\text{out}} (/c)$	0.38	0.42	0.46	0.40

TABLE 3.9: The same as Table 3.6, but for Mrk 766.

	E	D	C	B
CF	0.52	0.14	0.07	0.06
norm	0.59	0.69	0.78	0.89
$\log N_{\text{H}}$	23.1	22.8	22.0	22.0
$\log \xi$	1.82	1.25	0.25	0.25
$v_{\text{out}} (/c)$	0.16	0.01	0.01	0.01

TABLE 3.10: The same as Table 3.6, but for NGC 985.

	E	D	C	B
CF	0.24	0.20	0.07	0.01
norm	0.68	0.76	0.91	0.92
$\log N_{\text{H}}$	22.2	22.0	22.1	22.6
$\log \xi$	0.18	0.00	0.00	1.51
$v_{\text{out}} (/c)$	0.04	0.04	0.04	0.16

TABLE 3.11: The same as Table 3.6, but for NGC 4051.

	E	D	C	B
CF	0.72	0.60	0.43	0.24
norm	0.43	0.53	0.56	0.76
$\log N_{\text{H}}$	22.9	22.7	22.6	22.7
$\log \xi$	1.14	1.32	1.53	1.75
$v_{\text{out}} (/c)$	0.00	0.00	0.00	0.03

TABLE 3.12: The same as Table 3.6, but for 1H 0707–495.

2008	E	D	C	B	2010	E	D	C	B
CF	0.58	0.43	0.33	0.23		0.70	0.59	0.49	0.38
norm	0.59	0.72	0.78	0.92		0.48	0.64	0.72	0.87
$\log N_{\text{H}}$	23.8	23.8	23.8	23.8		23.8	23.8	23.8	23.8
$\log \xi$	2.46	2.55	2.55	2.56		2.58	2.60	2.68	2.66
$v_{\text{out}} (/c)$	0.24	0.23	0.22	0.26		0.25	0.25	0.24	0.28

TABLE 3.13: The same as Table 3.6, but for MCG–6-30-15.

2001	E	D	C	B	2013	E	D	C	B
CF	0.37	0.17	0.12	0.06		0.29	0.21	0.15	0.12
norm	0.62	0.72	0.80	0.87		0.45	0.56	0.69	0.81
$\log N_{\text{H}}$	22.9	22.9	22.7	22.7		23.0	23.0	23.0	23.0
$\log \xi$	2.02	2.00	1.61	1.28		1.83	1.77	2.07	2.35
$v_{\text{out}} (/c)$	0.23	0.12	0.06	0.06		0.15	0.19	0.18	0.19

TABLE 3.14: The same as Table 3.6, but for NGC 3783.

2001	E	D	C	B	2016	E	D	C	B
CF	0.18	0.04	0.07	0.08		0.41	0.46	0.34	0.00
norm	0.62	0.73	0.82	0.89		0.67	1.00	1.00	0.87
$\log N_{\text{H}}$	22.0	22.5	22.0	22.0		23.0	22.8	22.5	24.0
$\log \xi$	0.00	0.41	0.25	0.00		1.75	0.16	0.04	1.67
$v_{\text{out}} (/c)$	0.01	0.03	0.01	0.01		0.33	0.09	0.18	0.10

Chapter 4

Detailed Analysis of the Selected Sources

In Chapter 3, we systematically applied the spectral-ratio model fitting to several Seyfert 1 galaxies. In this chapter, we present more detailed analyses of the four objects (IRAS 13224–3809, Mrk 335, PDS 456, and 1H 0707–495), which show characteristic dip structures in their spectral-ratio analysis. These structures are considered to be evidence of the outflowing partial covering clouds. Thus, precise analysis of these sources is expected to constrain the clump velocities and help investigate the origin of the clumps.

4.1 Simultaneous spectral-ratio model fitting

4.1.1 Simultaneous fitting with N_{H} and ξ tied to all the ratios

We have found that the N_{H} and ξ of the clumpy absorbers were not significantly variable in the four targets as given in Table 3.6, 3.7, 3.8, and 3.12. Thus, we tied these two parameters for all the spectral ratios and performed the simultaneous fitting for each object, which physically assumes that the absorber itself remains the same and that only the covering fraction and velocity are variable. The fitting was also well on this assumption as shown in Figure 4.1–4.9. The best-fit parameters are given in the orange dots in Figure 4.3, 4.5, 4.7, and 4.9. We find that the partial covering fraction is smaller, and the norm is higher as the X-ray flux increases for all the targets. The outflow velocities of the clumpy absorber in IRAS 13224–3809, PDS 456, and 1H 0707–495 are 0.2–0.45 c , which are unexpectedly fast and even comparable to those of the UFOs reported in previous studies (Table 3.1). For Mrk 335, where the UFO velocity is small, $\sim 0.05 c$, the obtained clump velocity is also a small value, 0.02–0.07 c . Furthermore, the velocity tends to be higher as the X-ray flux increases. This result has been suggested by the model-independent analysis of IRAS 13224–3809 in Section 3.3.2 and is more robustly supported in this analysis.

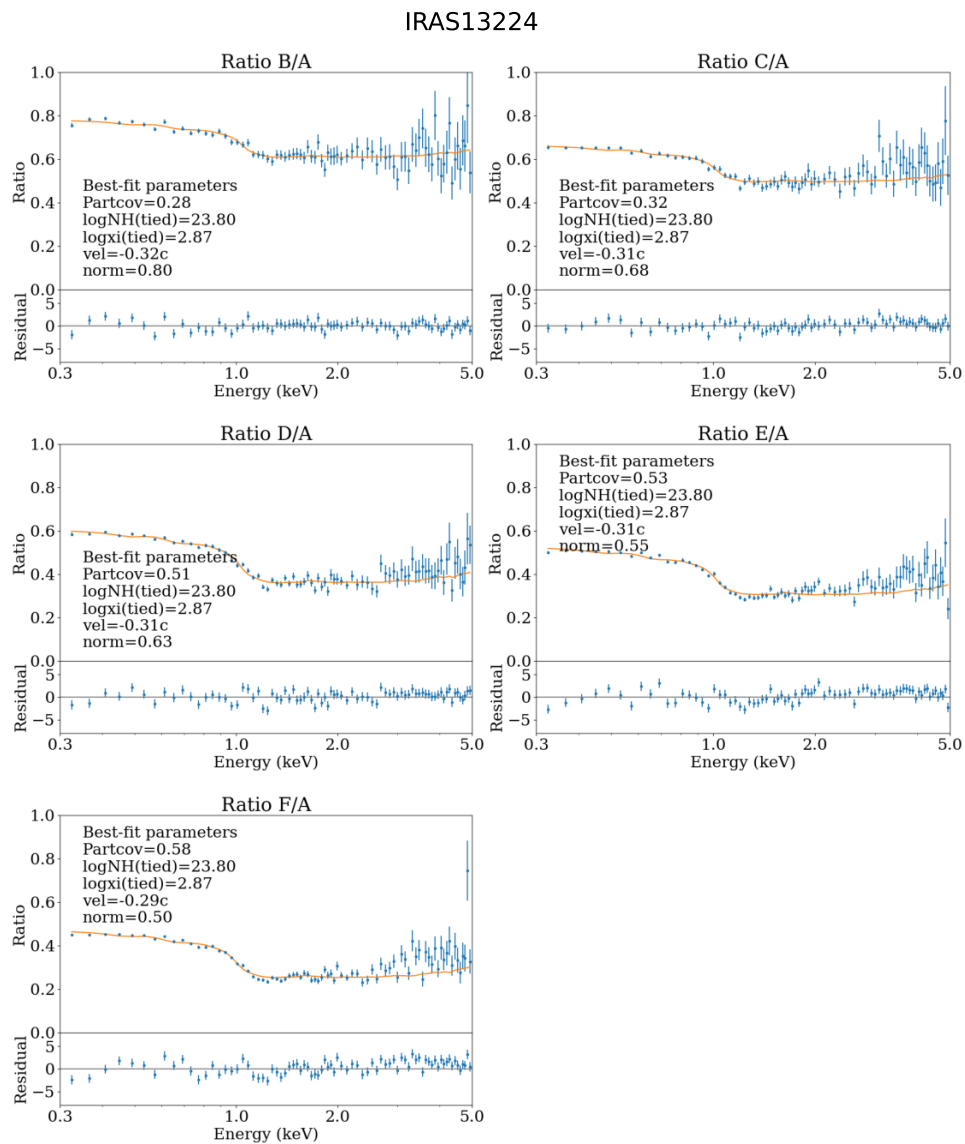


FIGURE 4.1: Simultaneous ratio fitting results of IRAS 13224–3809.

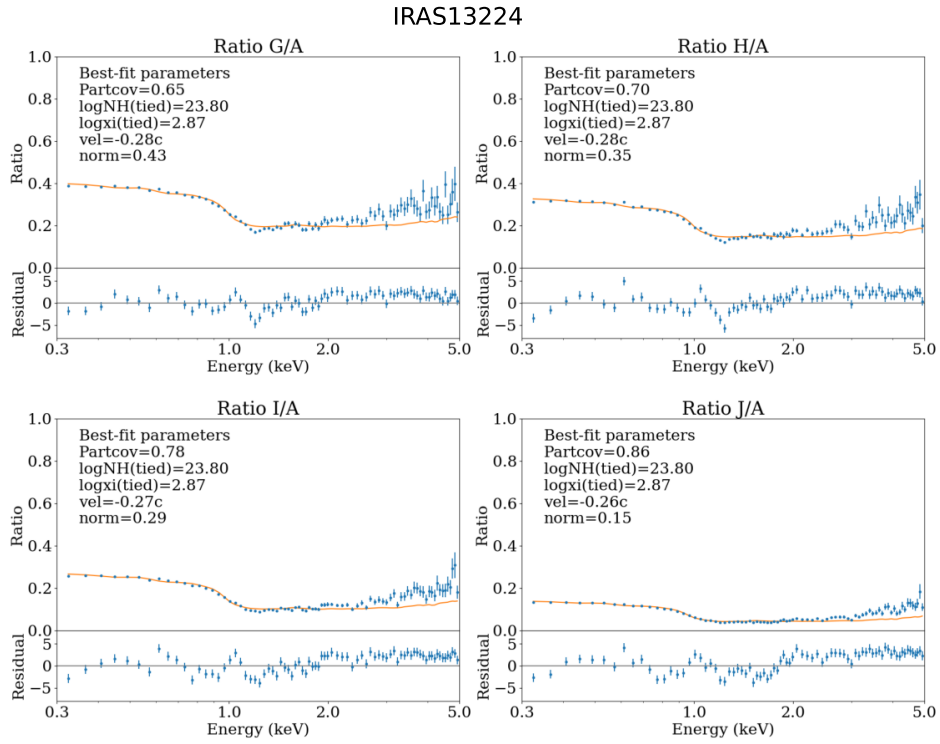
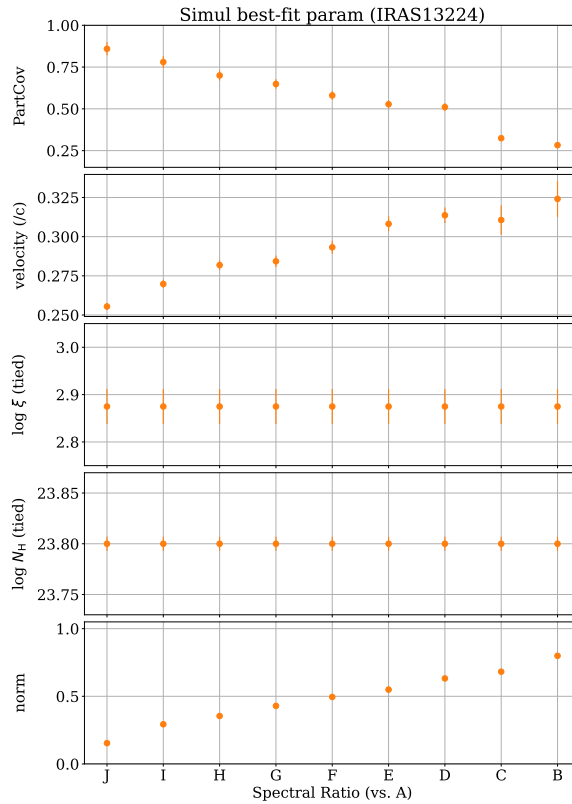


FIGURE 4.2: (Cont.) Simultaneous ratio fitting results of IRAS 13224–3809.

FIGURE 4.3: Best-fit parameters determined by the simultaneous fitting of IRAS 13224–3809, where N_H and ξ are tied for all the spectral ratios.

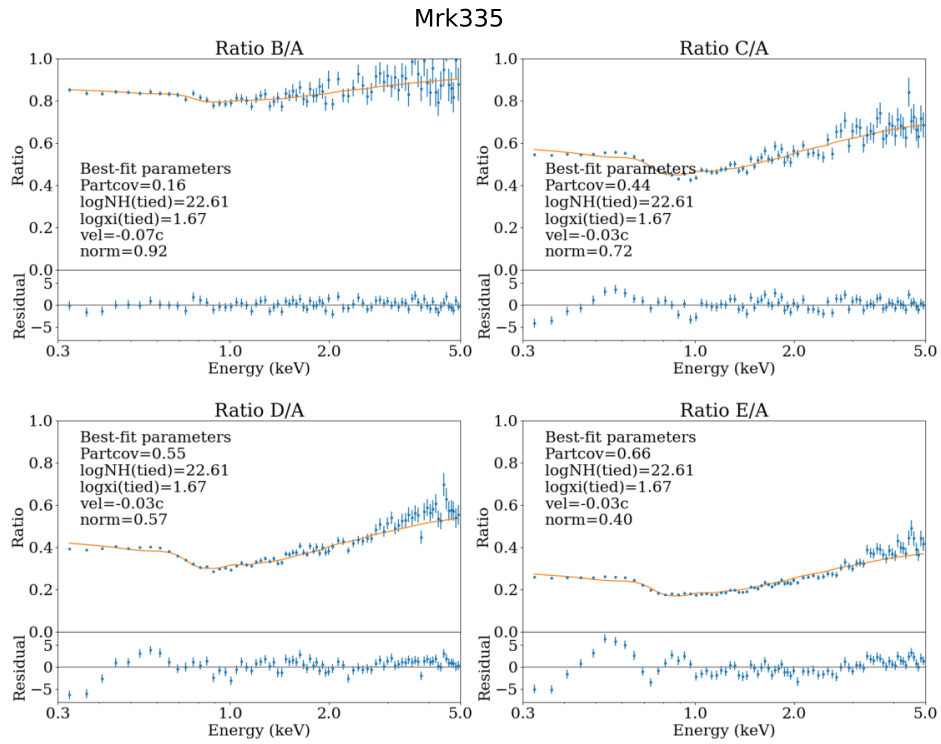


FIGURE 4.4: The same as Figure 4.1, but for Mrk 335.

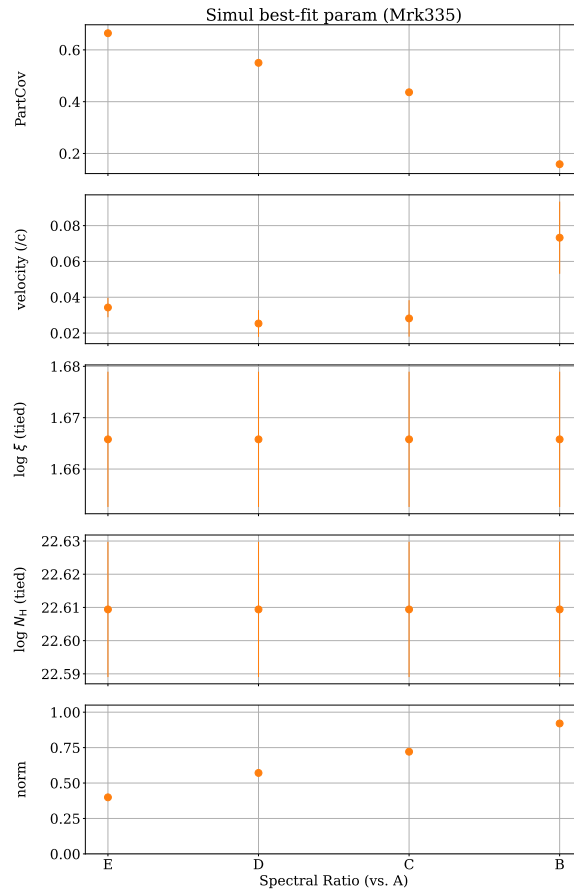


FIGURE 4.5: The same as Figure 4.3, but for Mrk 335.

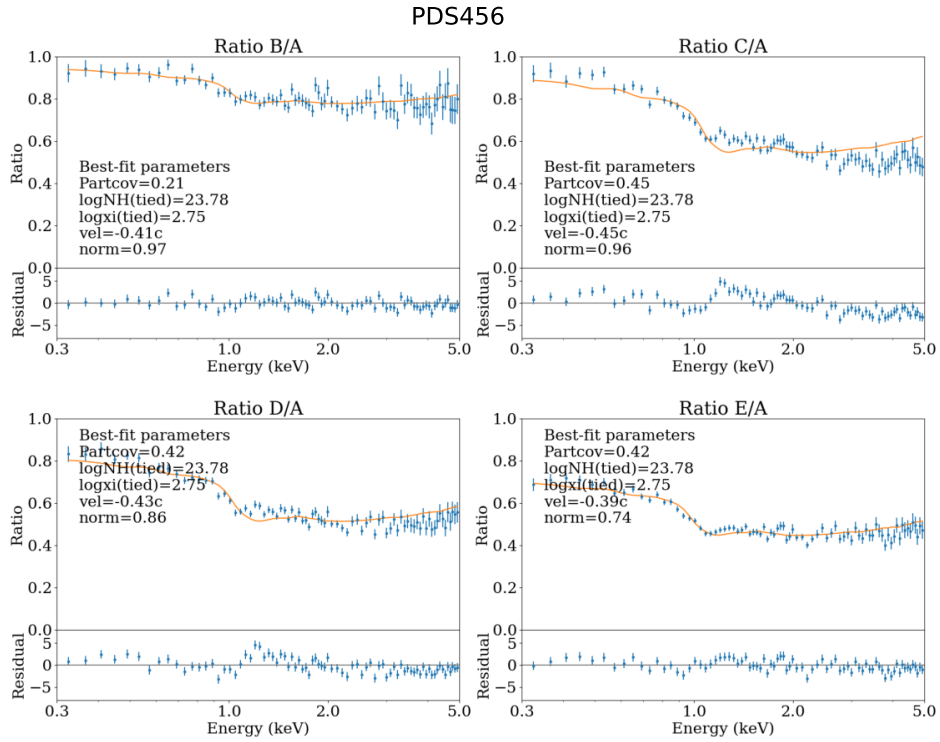


FIGURE 4.6: The same as Figure 4.1, but for PDS 456.

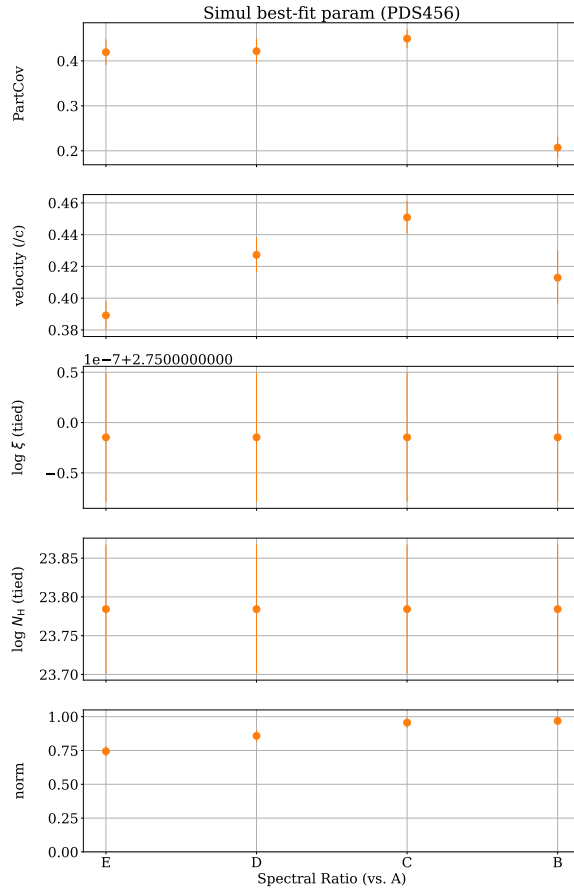


FIGURE 4.7: The same as Figure 4.3, but for PDS 456.

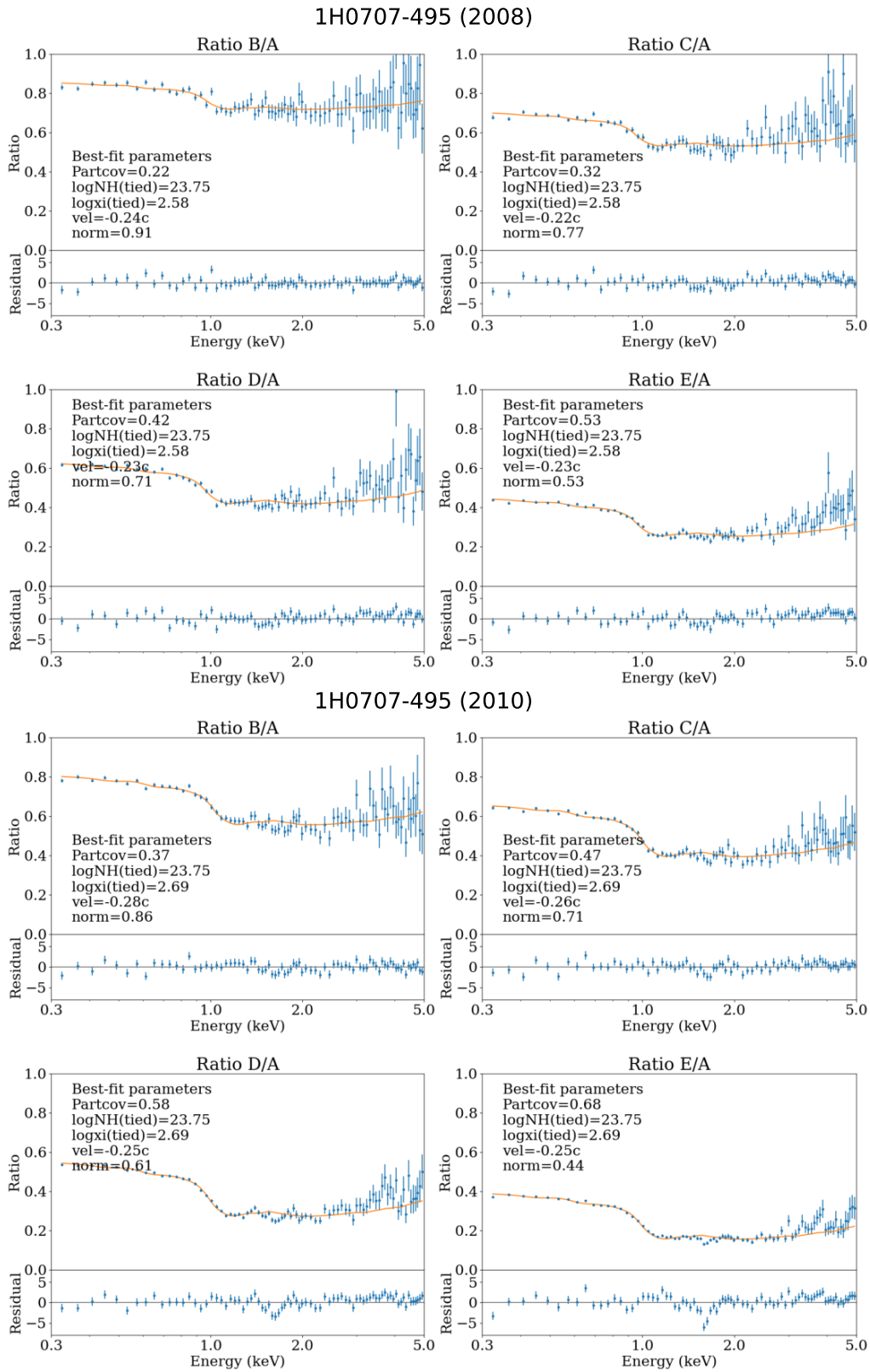


FIGURE 4.8: The same as Figure 4.1, but for 1H 0707–495 in two observation periods.

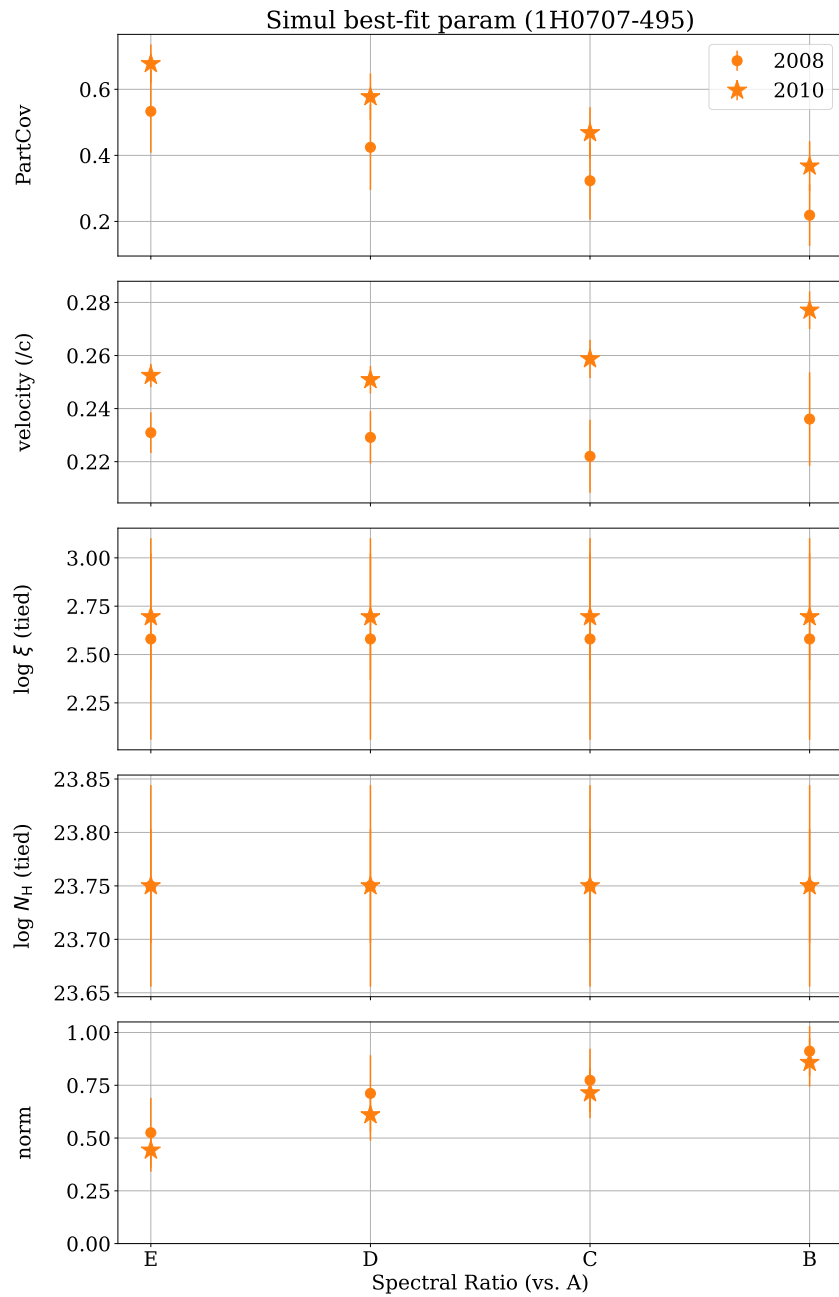


FIGURE 4.9: The same as Figure 4.3, but for 1H 0707–495. The circle and star markers indicate results in 2008 and 2010, respectively.

4.1.2 MCMC parameter estimation

The analysis so far suggests that the clumpy absorbers are fast outflowing with comparable velocities as the UFOs. However, are the estimated velocities really not degenerate with the ionization parameters ξ ? In this section, we will examine whether the velocity we have obtained degenerates with ξ or not, since both parameters similarly affect the absorption line/edge energies. To that end, we perform a Markov Chain Monte Carlo (MCMC) calculation using the “emcee” package (Foreman-Mackey et al., 2013) to determine the posterior distribution of the best-fit spectral parameters. The initial parameters in the MCMC chains are set to be close to the best-fit parameters obtained by the chi-squared fitting. We set a uniform prior distribution over the parameter ranges (Table 3.4). After the initial 5,000 steps are discarded to exclude the burn-in phase, further 10,000 steps are explored by 1,000 separate chains (“walkers”).

We performed the MCMC parameter estimation for all the spectral ratios of the four targets. The blue dots in Figure A.9, A.10, A.11, and A.12 show the mean values obtained with the MCMC calculation of IRAS 13224–3809, Mrk 335, PDS 456, and 1H 0707–495, respectively. We confirmed that the best-fit parameters and their flux-dependency are quite similar to those by the chi-squared fitting (the orange dots in the figures). Note that ξ is not tied among the different spectral-ratios, unlike the least chi-square fitting above, because the primary aim of this analysis is to examine whether there is no correlation between the outflow velocity and ξ .

Figure 4.10 shows a corner plot of the two-dimensional correlations between the posterior distributions of the estimated parameter pairs in the spectral ratio F/A of IRAS 13224–3809. The other corner plots of this object and the rest objects are shown in Figure 4.11–4.15. We confirmed that the velocity is not correlated with other parameters and is determined independently. In contrast, CF and ξ are correlated in most spectral ratios of IRAS 13224–3809. For PDS 456 and 1H 0707–495, the correlation between CF and norm, and/or anti-correlation between ξ and norm and/or CF and ξ are found. This can be regarded as some uncertainty in determining which parameters are responsible for the X-ray intensity variation.

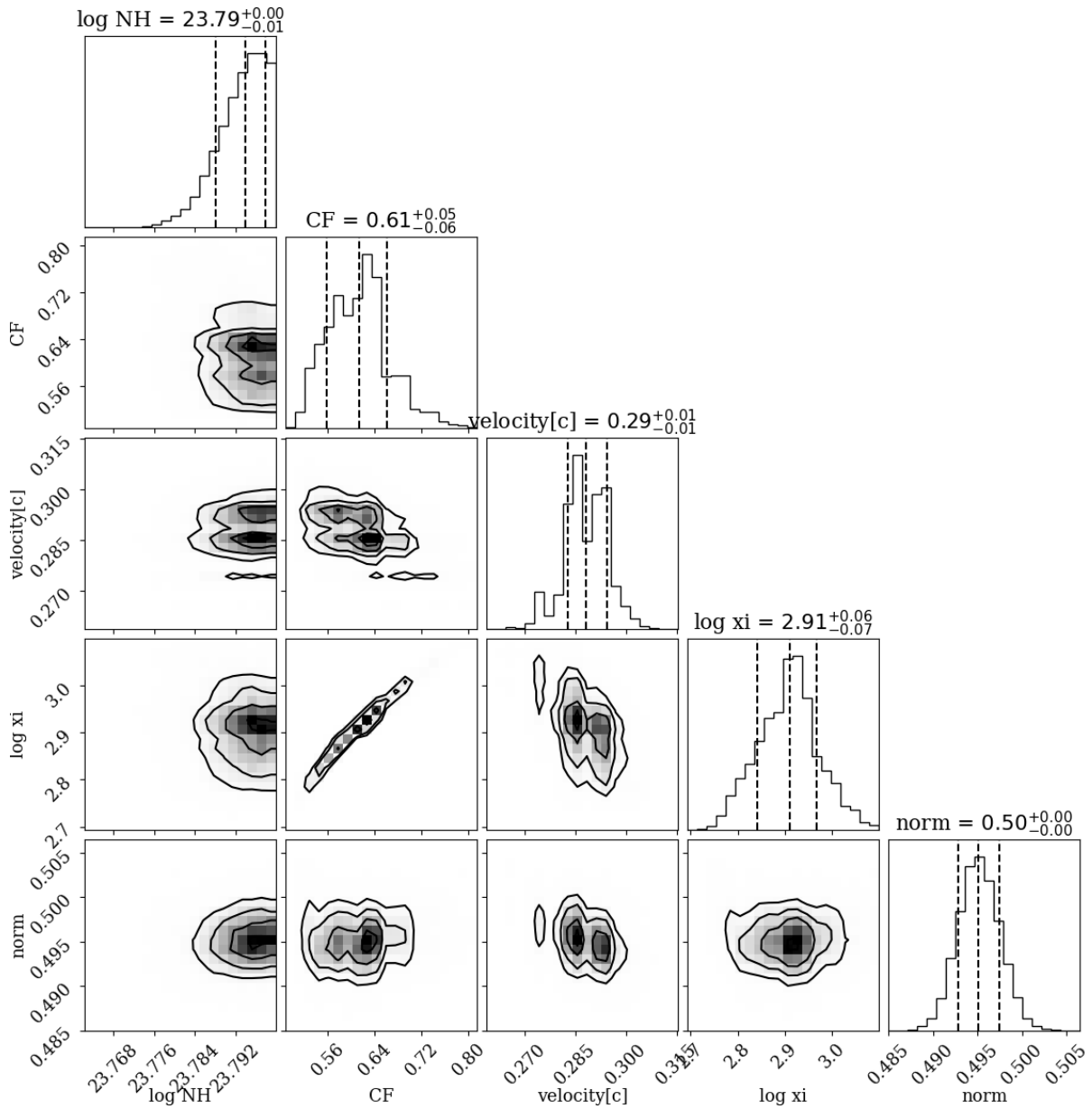


FIGURE 4.10: A corner plot showing the result of the MCMC parameter estimation for the typical spectral ratio F/A of IRAS 13224–3809.

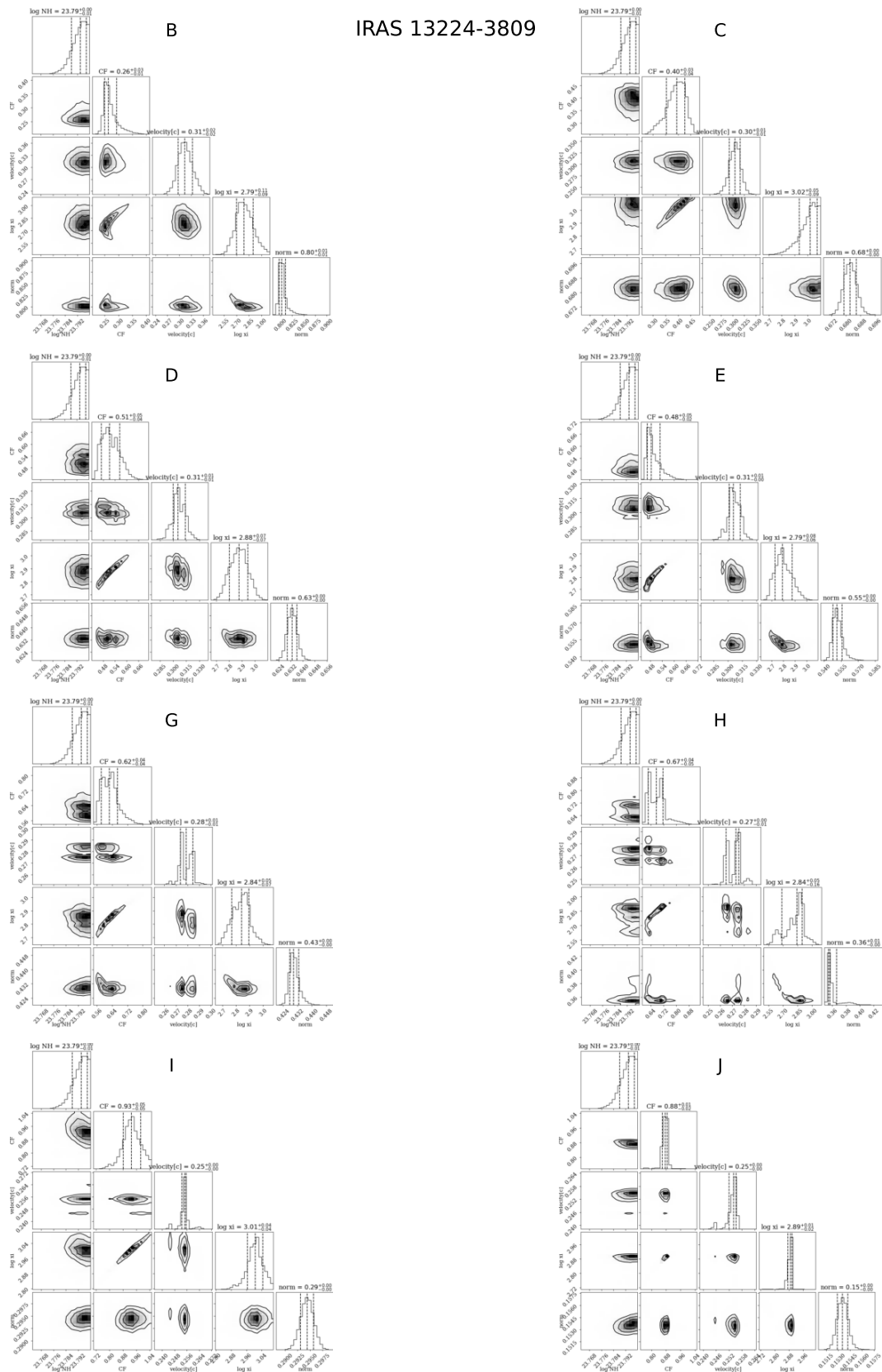


FIGURE 4.11: Corner plots of the MCMC parameter estimation for all the spectral ratios except for the enlarged plot of the spectral ratio F/A.

Mrk335

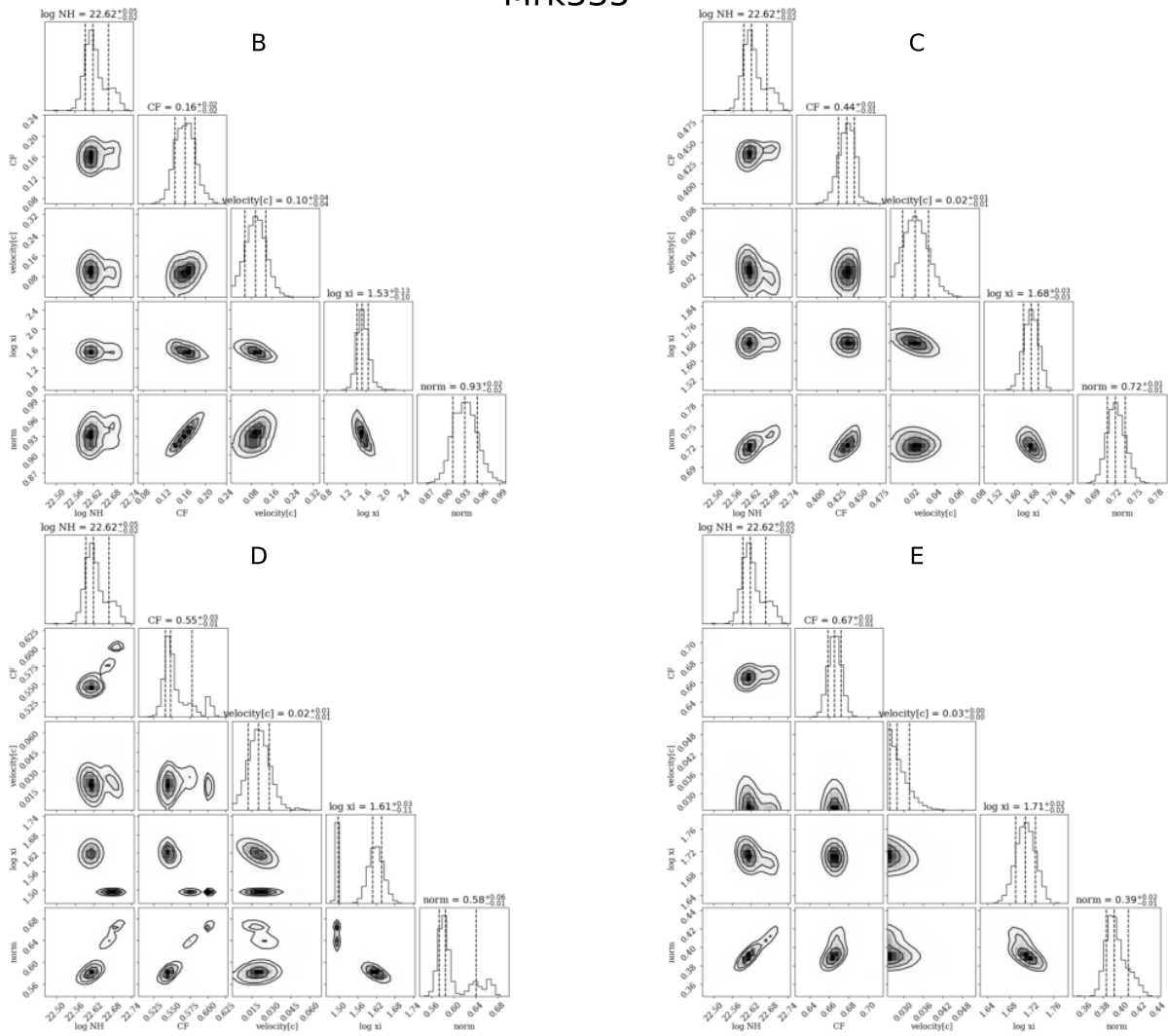


FIGURE 4.12: The same as Figure 4.11, but for Mrk 335.

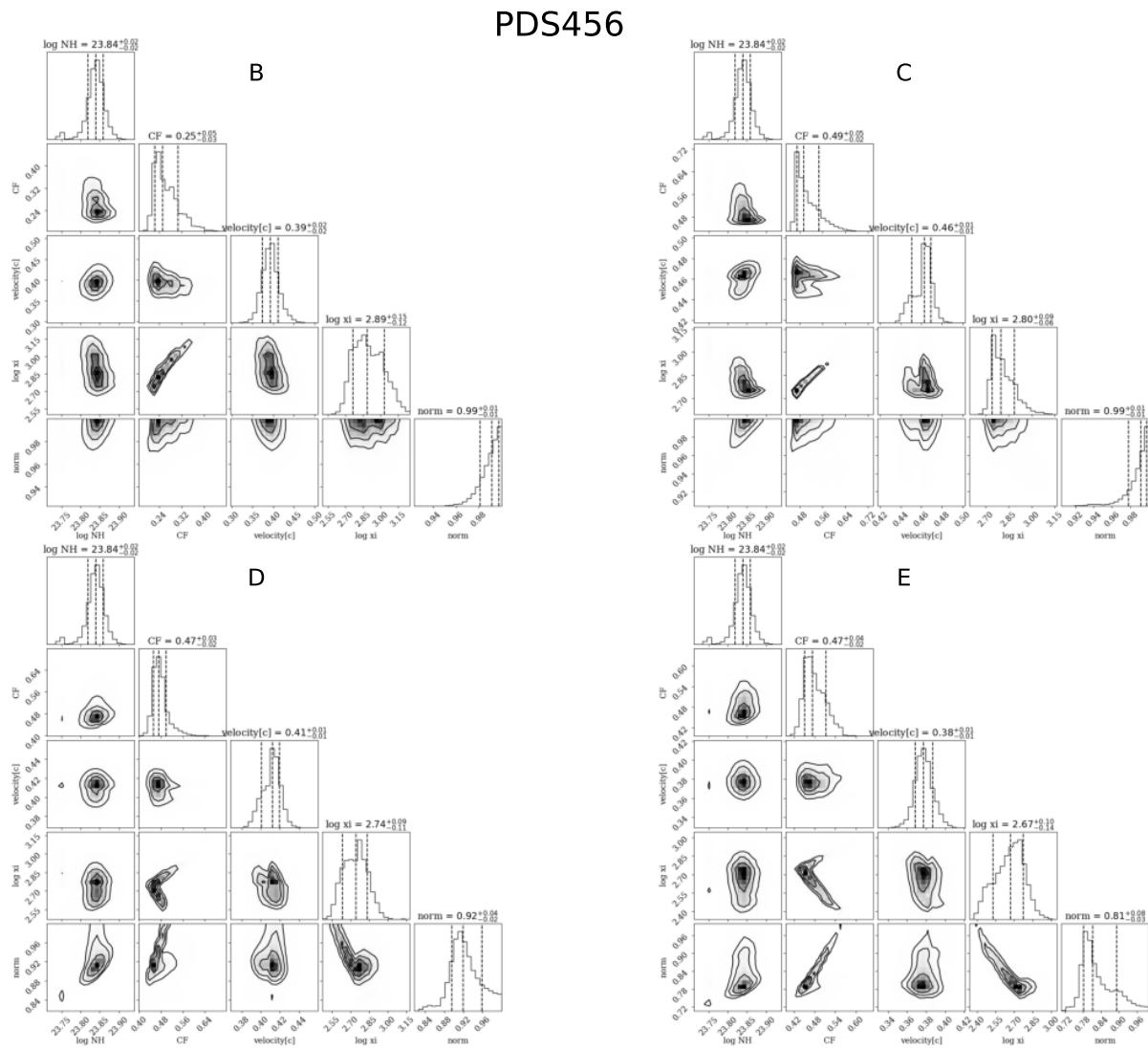


FIGURE 4.13: The same as Figure 4.11, but for PDS 456.

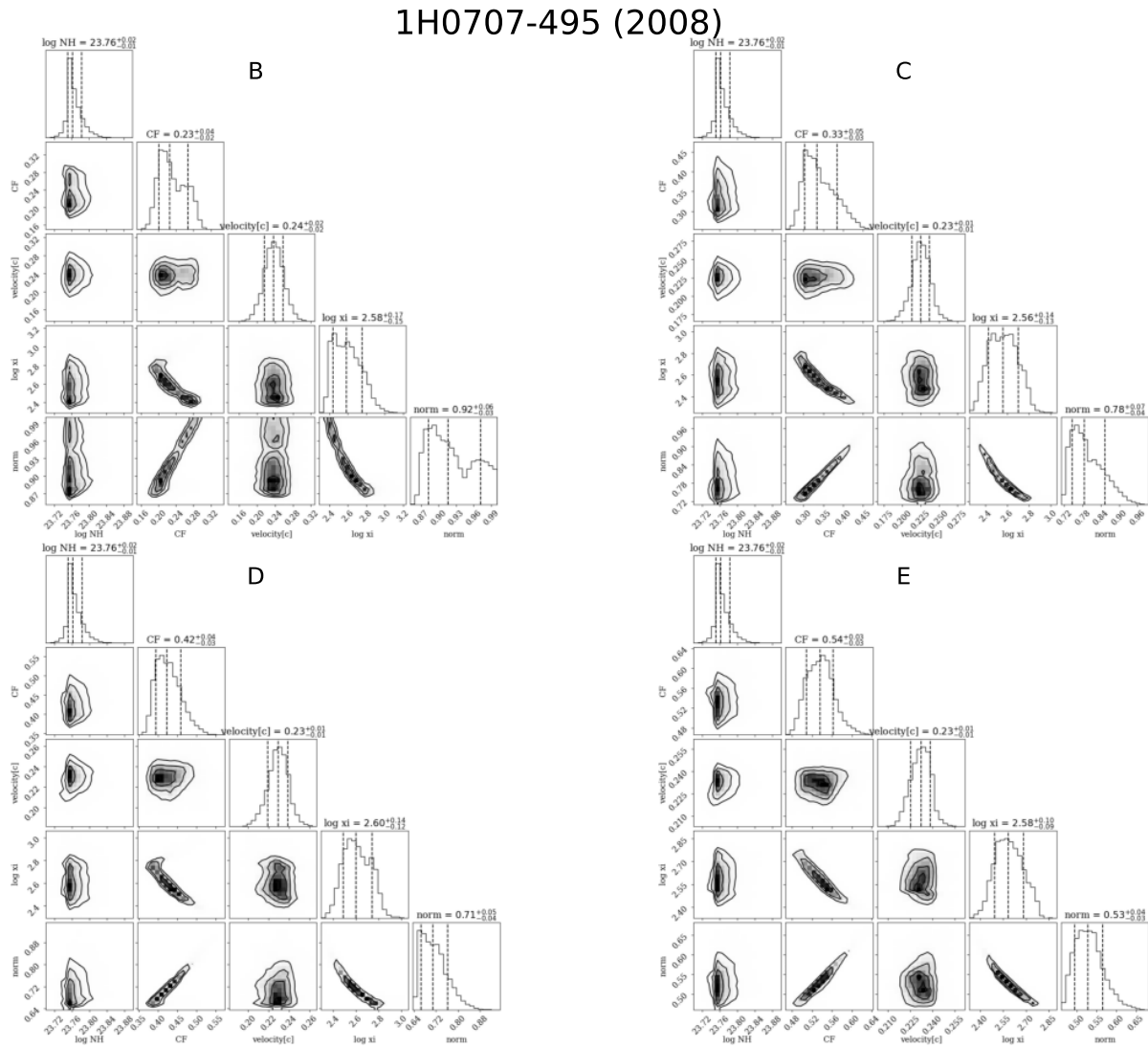


FIGURE 4.14: The same as Figure 4.11, but for 1H 0707–495 in the 2008 observation.

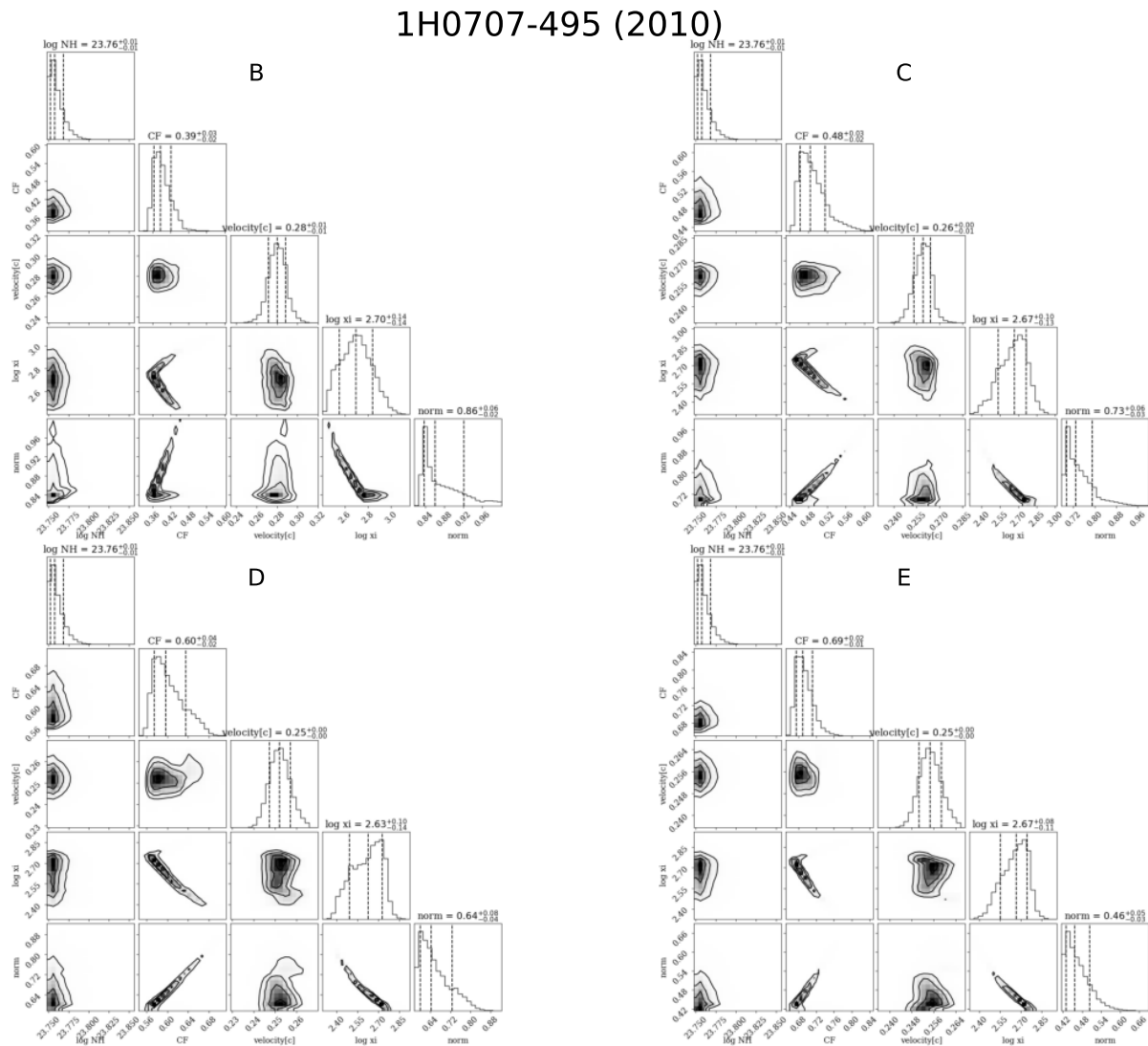


FIGURE 4.15: The same as Figure 4.11, but for 1H 0707–495 in the 2010 observation.

4.2 Spectral fitting in 0.3–10 keV

The analysis so far has yielded rather surprising results that the clump velocity v_{out} constrained from the spectral-ratio fitting below $\lesssim 5$ keV is comparable to the UFO velocity v_{UFO} constrained from the blue-shifted Fe K absorption lines at $\gtrsim 8$ keV. Next, we performed spectral fitting in 0.3–10 keV with the partial absorption model to constrain the v_{out} and v_{UFO} simultaneously. Since the equivalent width of the UFO absorption in Mrk 335 is marginal to estimate the velocity as shown in Figure 4.16, the spectral analysis was performed only for the remaining three objects, where the UFO features are significantly detected.

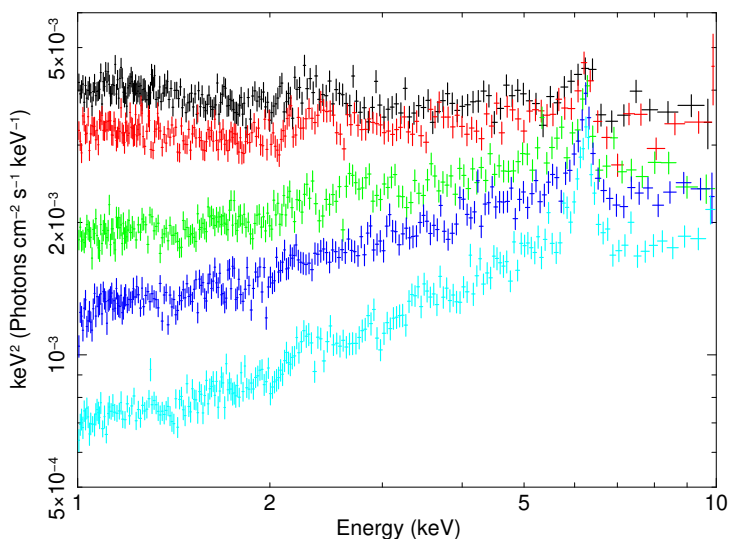


FIGURE 4.16: Intensity-sliced spectra of Mrk 335 in 1.0–10.0 keV, which hardly shows the UFO absorption features except for spectrum B (in red).

The spectral data were re-binned to have at least 30 counts per new energy bin. The XSPEC spectral model adopted is represented as

$$\text{phabs} * \text{zxcipcf} * (\text{powerlaw} + \text{diskbb}) * \text{kabs},$$

which can be described physically as

$$\text{ISM abs} * \text{clump abs} * (\text{continuum}) * \text{UFO abs}.$$

The column density of `phabs` for the interstellar medium (ISM) absorption was initially fixed at the Galactic value estimated by Bekhti et al. (2016), where we set the cosmic abundances to the `wilms` values (Wilms, Allen, and McCray, 2000). The X-ray continuum consists of a power-law component from the hot corona (`powerlaw`) plus a multi-color blackbody component from the optically thick accretion disk (`diskbb`; Mitsuda et al., 1984; Makishima et al., 1986). In this study, we selected the `diskbb` model for simplicity among several interpretations for the soft excess component as described

in Section 1.2. The `diskbb` has two parameters, temperature at the inner edge of the accretion disk kT_{in} and the normalization corresponding to the disk area.

In addition to the model for the spectral-ratio fitting, the `kabs` model (Ueda et al., 2004, updated by Tomaru et al., 2020) was incorporated to explain the Fe XXV and/or Fe XXVI UFO absorption features. The `kabs` model calculates the Voigt profile absorption lines ($K\alpha$ and $K\beta$) for Fe XXV and Fe XXVI for the given column density of the ion N_{ion} and the turbulent velocity v_{turb} . The redshift z due to the line-of-sight velocity is also a free parameter.

Initial parameters of the spectral fitting are set to the values constrained by the ratio model fitting. Both the continuum and partial absorption parameters were free to vary for the fitting. It is difficult to simultaneously place limits on the ionization parameter and the turbulent velocity v_{turb} from the absorption line profiles above 8 keV. Therefore, v_{turb} was fixed at 10,000 km/s, and the fitting was performed assuming that the UFO absorption lines are produced either by He-like Fe or H-like Fe, which are not distinguishable because the difference is only the energy shift. In the spectral fitting, we included $K\alpha$ and $K\beta$ lines as a pair, where the $K\beta$ line parameters are determined self-consistently from the $K\alpha$ line.

The assumed models well fitted all the spectra of the three objects. The result of the four targets are shown in Figure 4.17–4.21. Three $K\alpha$ lines (accompanied by three $K\beta$ lines) at maximum are necessary to fit the UFO feature depending on different spectra. This suggests that more than one velocity component of the UFO was observed.

Best-fit parameters are given in Table 4.1–4.4. For IRAS 13224–3809, the best-fit values are shown both assuming the He-like Fe or H-like Fe lines, indicating that the velocities are just uniformly shifted depending on the ionization state (see also Section 5.2). For other sources, we only show the results assuming the He-like Fe. We set N_{H} and ξ of `zxipcf` as free parameters in IRAS 13224–3809, which were found to be comparable to those obtained by the ratio fitting, so we used the fixed values for the other sources. The N_{H} of `phabs` in PDS 456 and 1H 0707–495 were free to vary because they slightly shifted from the estimated values by Bekhti et al. (2016). As suggested by the relatively large residuals of dimmer spectral ratios in the ratio fitting (e.g., see Figure 4.2), the power-law photon index Γ of IRAS 13224–3809 and 1H 0707–495 were found to be steeper as the X-ray flux increases, which is consistent with the so-called “softer-when-brighter” scenario described in Section 1.2. On one hand, spectrum A of IRAS 13224–3809 and PDS 456 did not need the ionized partial absorption, i.e., $\text{CF} = 0$. On the other hand, spectrum A of 1H 0707–495 clearly required the partial covering component ($\text{CF} > 0$) shown in Figure 4.20 (also see Figure 4.24), and fitted with the clump parameters fixed to those obtained by the ratio fitting. Since the partial covering fraction obtained by the ratio fitting is the one assuming that the denominator is not covered at all, it may underestimate the true partial covering fraction (see Figure 4.8, Table 4.3, and 4.4).

IRAS 13224-3809

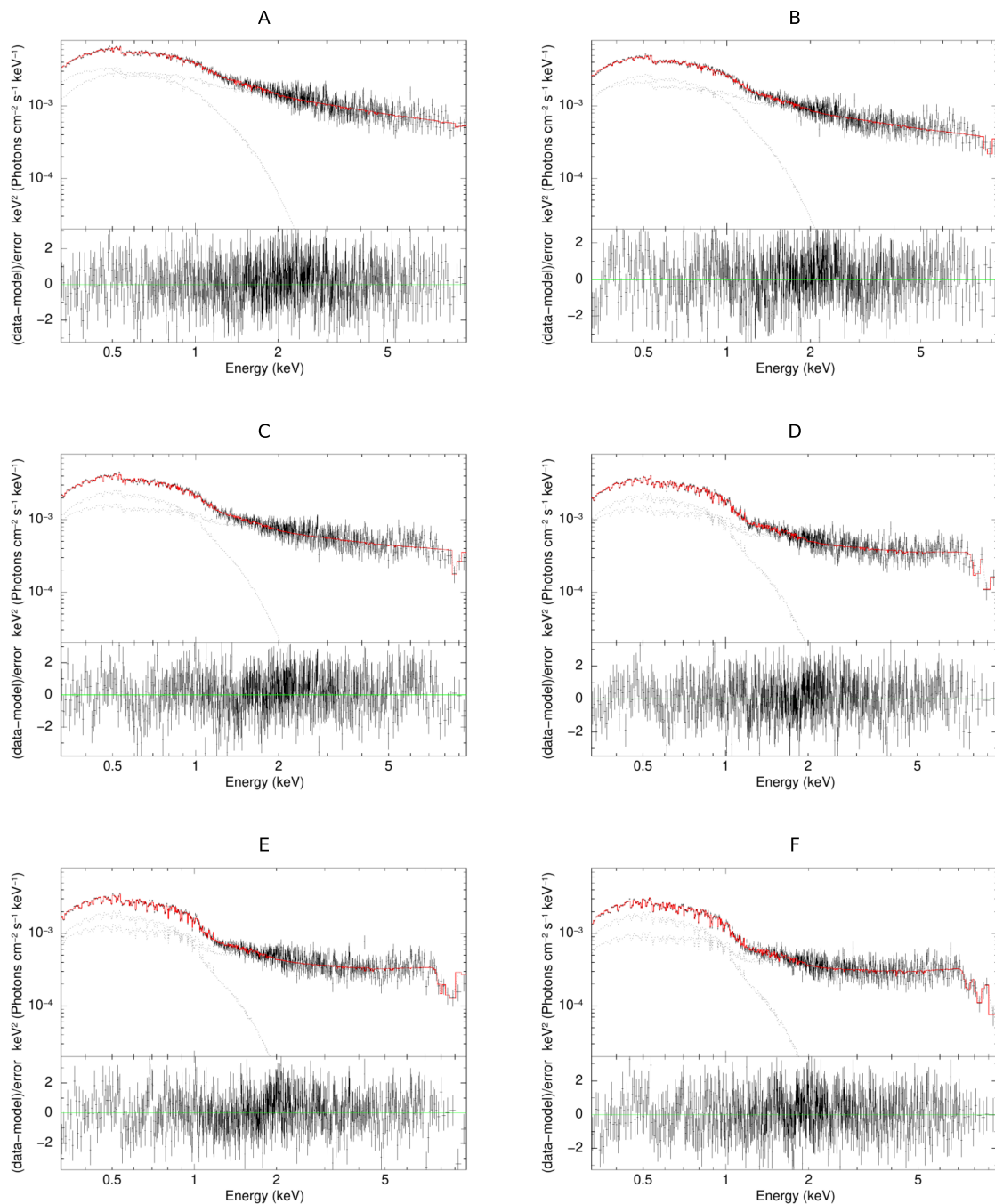


FIGURE 4.17: Spectral fitting results of all the spectra of IRAS 13224–3809 in 0.3–10 keV. The dotted lines in black show `powerlaw` and `diskbb`, respectively. The red line represents the best-fit model, including at maximum three `kabs` lines around 7–10 keV. The lower panel shows the residuals of the model fitting.

IRAS 13224-3809

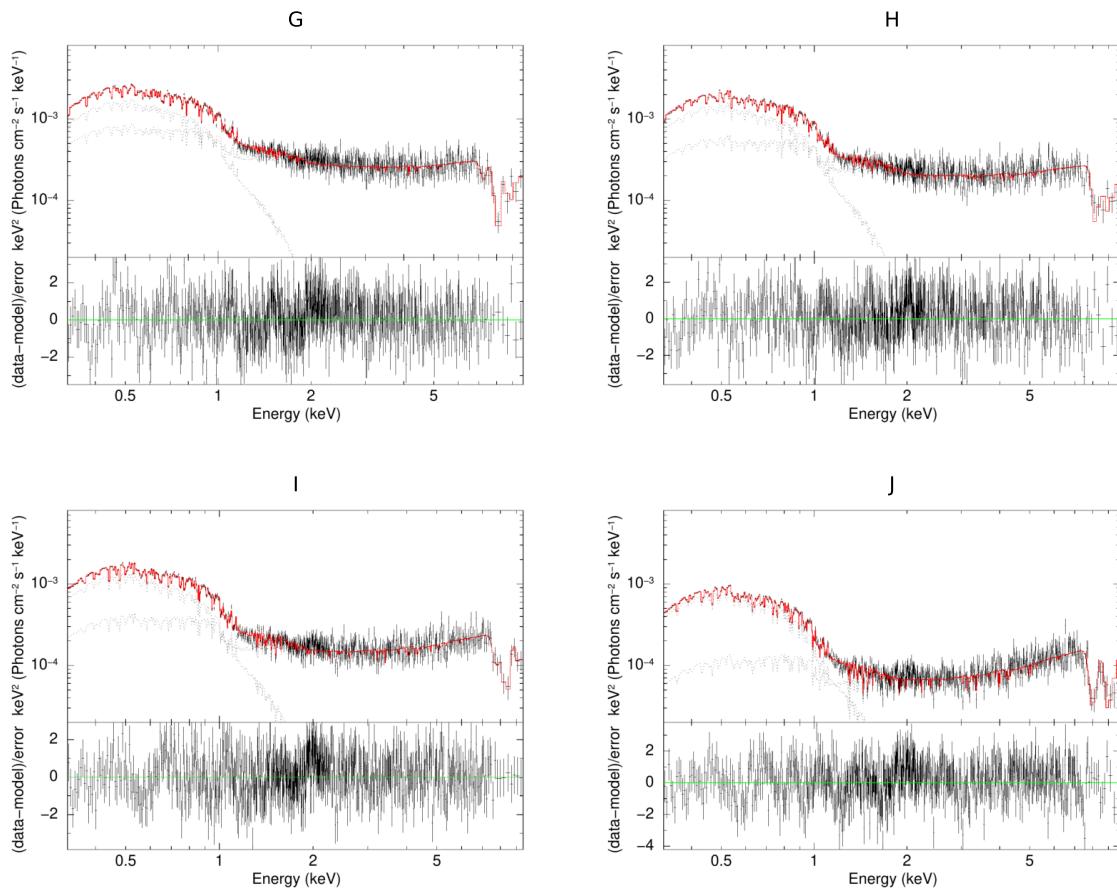


FIGURE 4.18: (Cont.) Spectral fitting results of IRAS 13224–3809 all the spectra.

PDS456

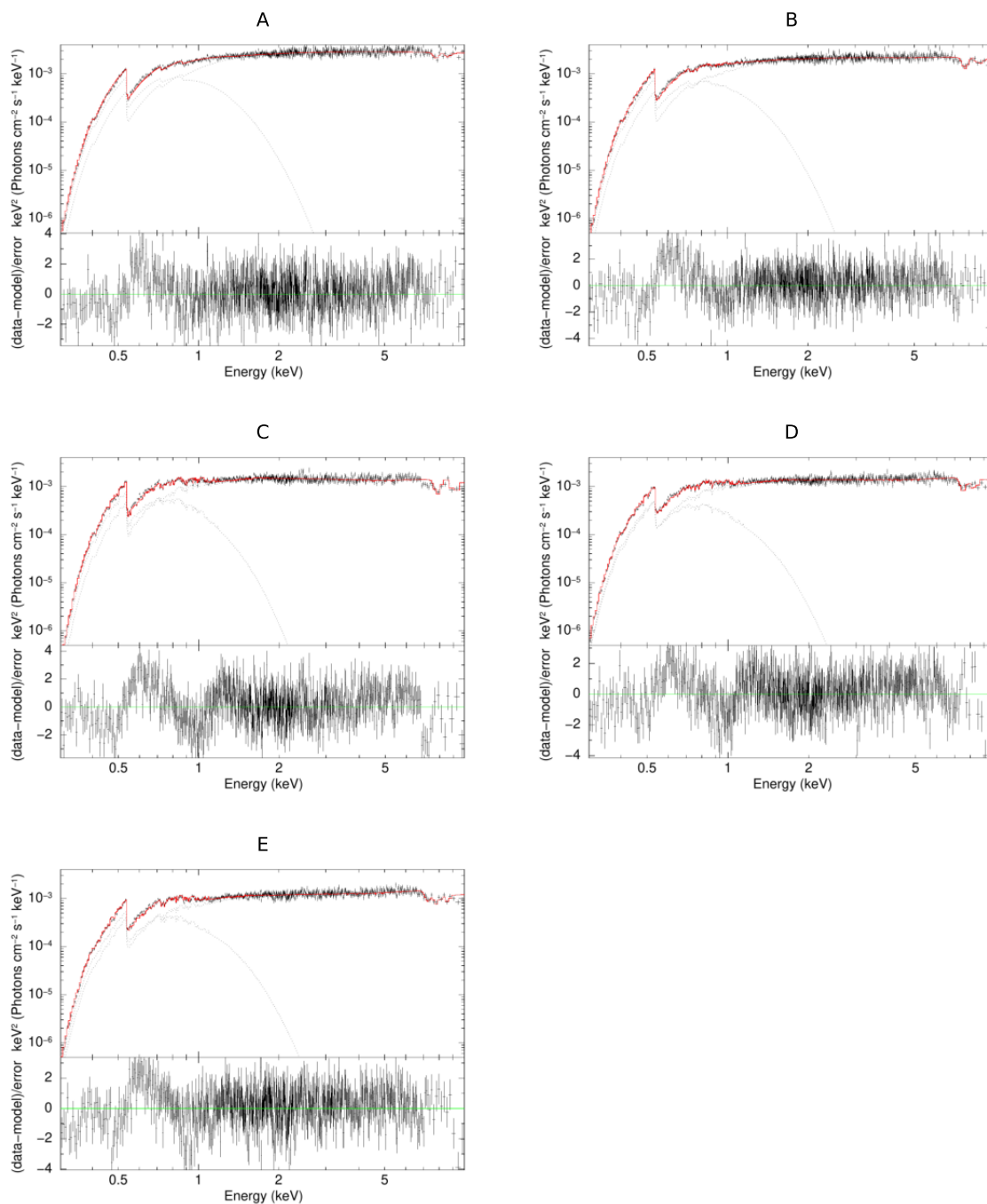


FIGURE 4.19: The same as Figure 4.17, but for PDS 456.

1H0707-495 (2008)

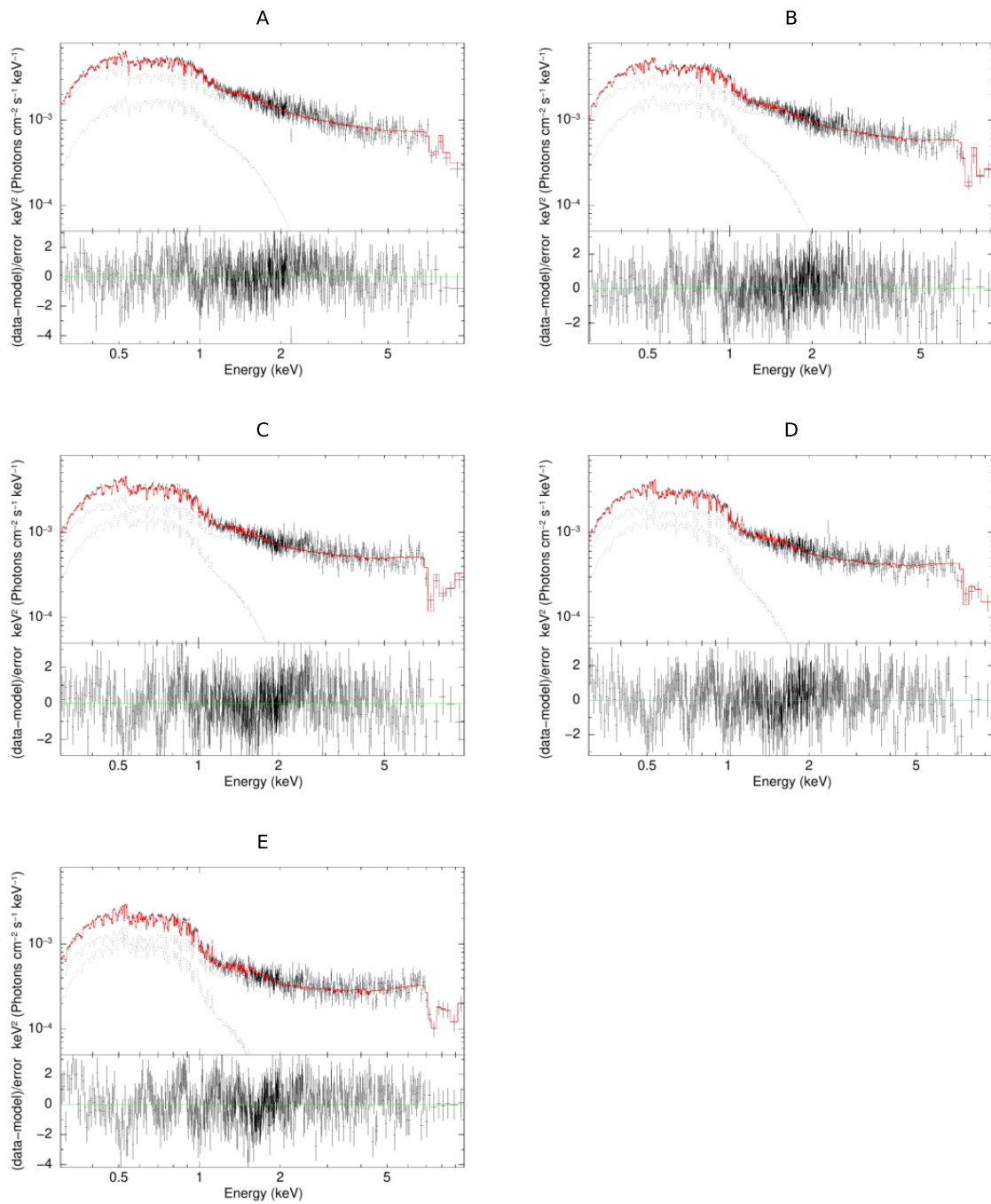


FIGURE 4.20: The same as Figure 4.17, but for 1H 0707–495 in 2008.

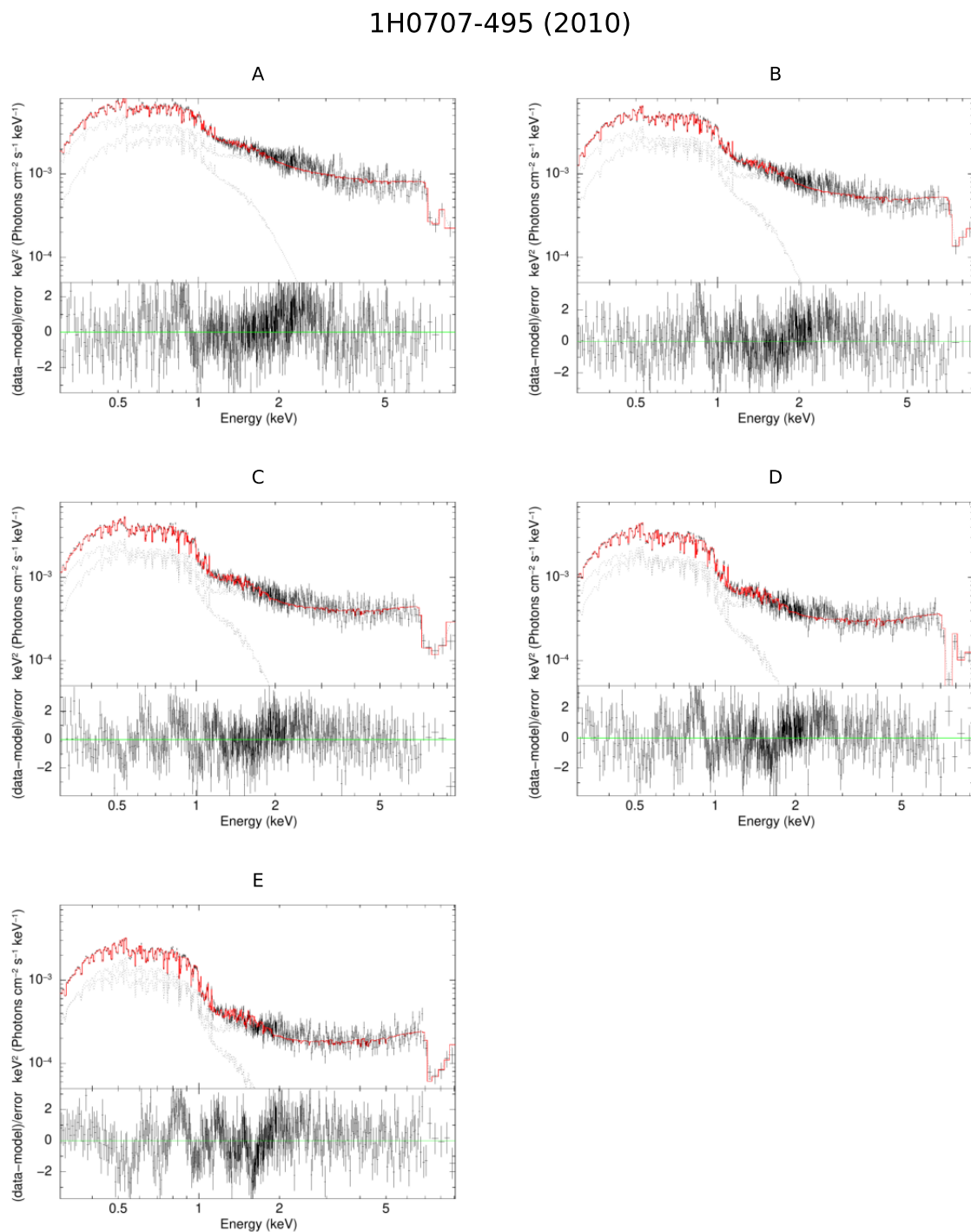


FIGURE 4.21: The same as Figure 4.17, but for 1H 0707–495 in 2010.

TABLE 4.1: Best-fit parameters determined by the spectral fitting of IRAS 13224–3809 in 0.3–10.0 keV. The CF of `zxipcf` is fixed to the values determined by the chi-squared ratio fitting. Fitting was made assuming that the UFO absorption lines are produced either by He-like Fe or H-like Fe. The parameters except `kabs` are determined assuming the He-like Fe. Hereafter the error ranges correspond to the 90% confidence level.

Components	Parameters	A	B	C	D	E
<code>zxipcf</code>	N_{H} (10^{22}cm^{-2})	—	36_{-7}^{+13}	46_{-6}^{+9}	51_{-5}^{+4}	56_{-5}^{+5}
	$\log \xi$	—	$2.72_{-0.04}^{+0.04}$	$2.73_{-0.05}^{+0.03}$	$2.73_{-0.11}^{+0.05}$	$2.72_{-0.03}^{+0.03}$
	z	—	$-0.33_{-0.02}^{+0.01}$	$-0.33_{-0.01}^{+0.01}$	$-0.32_{-0.01}^{+0.01}$	$-0.32_{-0.01}^{+0.01}$
<code>powerlaw</code>	Γ	$2.67_{-0.03}^{+0.03}$	$2.71_{-0.03}^{+0.03}$	$2.60_{-0.03}^{+0.03}$	$2.60_{-0.04}^{+0.03}$	$2.54_{-0.03}^{+0.03}$
	norm (10^{-3})	$2.2_{-0.1}^{+0.1}$	$2.3_{-0.1}^{+0.1}$	$2.2_{-0.1}^{+0.1}$	$2.3_{-0.2}^{+0.1}$	$2.4_{-0.1}^{+0.1}$
<code>diskbb</code>	kT_{in} (eV)	182_{-1}^{+1}	178_{-2}^{+2}	177_{-2}^{+2}	179_{-3}^{+2}	177_{-2}^{+2}
	norm	731_{-33}^{+34}	757_{-62}^{+45}	845_{-55}^{+46}	781_{-57}^{+89}	831_{-59}^{+72}
<i>Assuming Fe XXV</i>						
<code>kabs</code>	$N_{\text{Fe XXV}}$ (10^{18}cm^{-2})	—	2_{-1}^{+2}	4_{-1}^{+2}	4_{-1}^{+2}	5_{-2}^{+2}
	z	—	$-0.26_{-0.10}^{+0.04}$	$-0.29_{-0.02}^{+0.03}$	$-0.24_{-0.02}^{+0.01}$	$-0.25_{-0.02}^{+0.02}$
<code>kabs</code>	$N_{\text{Fe XXV}}$ (10^{18}cm^{-2})	—	—	—	8_{-3}^{+6}	6_{-2}^{+5}
	z	—	—	—	$-0.33_{-0.01}^{+0.01}$	$-0.32_{-0.02}^{+0.02}$
<code>kabs</code>	$N_{\text{Fe XXV}}$ (10^{18}cm^{-2})	—	—	—	—	—
	z	—	—	—	—	—
<i>Assuming Fe XXVI</i>						
<code>kabs</code>	$N_{\text{Fe XXVI}}$ (10^{18}cm^{-2})	—	4_{-3}^{+4}	7_{-3}^{+5}	8_{-3}^{+4}	10_{-4}^{+5}
	z	—	$-0.23_{-0.11}^{+0.04}$	$-0.26_{-0.02}^{+0.03}$	$-0.21_{-0.02}^{+0.01}$	$-0.22_{-0.02}^{+0.02}$
<code>kabs</code>	$N_{\text{Fe XXVI}}$ (10^{18}cm^{-2})	—	—	—	17_{-7}^{+12}	12_{-5}^{+9}
	z	—	—	—	$-0.30_{-0.01}^{+0.01}$	$-0.29_{-0.01}^{+0.02}$
<code>kabs</code>	$N_{\text{Fe XXVI}}$ (10^{18}cm^{-2})	—	—	—	—	—
	z	—	—	—	—	—
χ^2/dof		760.5/677	731.3/628	715.4/639	616.7/608	747.9/619
Components	Parameters	F	G	H	I	J
<code>zxipcf</code>	N_{H} (10^{22}cm^{-2})	52_{-5}^{+6}	56_{-5}^{+5}	54_{-4}^{+4}	57_{-4}^{+4}	60_{-3}^{+3}
	$\log \xi$	$2.76_{-0.16}^{+0.04}$	$2.78_{-0.03}^{+0.03}$	$2.81_{-0.03}^{+0.03}$	$2.85_{-0.02}^{+0.02}$	$2.91_{-0.02}^{+0.02}$
	z	$-0.31_{-0.01}^{+0.01}$	$-0.31_{-0.01}^{+0.01}$	$-0.30_{-0.01}^{+0.01}$	$-0.29_{-0.01}^{+0.01}$	$-0.28_{-0.01}^{+0.01}$
<code>powerlaw</code>	Γ	$2.47_{-0.04}^{+0.04}$	$2.40_{-0.04}^{+0.04}$	$2.34_{-0.04}^{+0.04}$	$2.24_{-0.05}^{+0.05}$	$1.95_{-0.05}^{+0.05}$
	norm (10^{-3})	$2.2_{-0.2}^{+0.3}$	$2.2_{-0.2}^{+0.2}$	$2.0_{-0.2}^{+0.2}$	$1.8_{-0.2}^{+0.2}$	$1.2_{-0.1}^{+0.1}$
<code>diskbb</code>	kT_{in} (eV)	173_{-2}^{+2}	170_{-2}^{+2}	168_{-1}^{+2}	165_{-1}^{+1}	165_{-1}^{+1}
	norm	986_{-99}^{+85}	1085_{-89}^{+85}	1238_{-83}^{+83}	1406_{-78}^{+77}	1589_{-62}^{+63}
<i>Assuming Fe XXV</i>						
<code>kabs</code>	$N_{\text{Fe XXV}}$ (10^{18}cm^{-2})	3_{-1}^{+1}	2_{-1}^{+1}	8_{-2}^{+3}	3_{-1}^{+1}	7_{-1}^{+2}
	z	$-0.18_{-0.02}^{+0.01}$	$-0.14_{-0.02}^{+0.02}$	$-0.24_{-0.01}^{+0.01}$	$-0.20_{-0.01}^{+0.01}$	$-0.22_{-0.01}^{+0.01}$
<code>kabs</code>	$N_{\text{Fe XXV}}$ (10^{18}cm^{-2})	5_{-1}^{+2}	10_{-2}^{+3}	6_{-2}^{+4}	7_{-2}^{+3}	7_{-2}^{+4}
	z	$-0.25_{-0.01}^{+0.01}$	$-0.23_{-0.01}^{+0.01}$	$-0.32_{-0.02}^{+0.01}$	$-0.26_{-0.01}^{+0.01}$	$-0.31_{-0.01}^{+0.01}$
<code>kabs</code>	$N_{\text{Fe XXV}}$ (10^{18}cm^{-2})	9_{-3}^{+26}	5_{-2}^{+3}	—	3_{-1}^{+2}	—
	z	$-0.34_{-0.04}^{+0.01}$	$-0.31_{-0.02}^{+0.02}$	—	$-0.33_{-0.02}^{+0.02}$	—
<i>Assuming Fe XXVI</i>						
<code>kabs</code>	$N_{\text{Fe XXVI}}$ (10^{18}cm^{-2})	6_{-2}^{+3}	5_{-2}^{+2}	16_{-4}^{+7}	7_{-3}^{+3}	16_{-3}^{+5}
	z	$-0.14_{-0.02}^{+0.02}$	$-0.10_{-0.02}^{+0.02}$	$-0.21_{-0.01}^{+0.01}$	$-0.16_{-0.01}^{+0.01}$	$-0.19_{-0.01}^{+0.01}$
<code>kabs</code>	$N_{\text{Fe XXVI}}$ (10^{18}cm^{-2})	11_{-3}^{+5}	20_{-4}^{+7}	13_{-5}^{+9}	15_{-5}^{+7}	16_{-4}^{+8}
	z	$-0.22_{-0.01}^{+0.01}$	$-0.20_{-0.01}^{+0.01}$	$-0.29_{-0.02}^{+0.01}$	$-0.22_{-0.01}^{+0.01}$	$-0.29_{-0.01}^{+0.01}$
<code>kabs</code>	$N_{\text{Fe XXVI}}$ (10^{18}cm^{-2})	18_{-6}^{+45}	10_{-4}^{+7}	—	6_{-3}^{+4}	—
	z	$-0.31_{-0.03}^{+0.01}$	$-0.28_{-0.02}^{+0.02}$	—	$-0.30_{-0.02}^{+0.02}$	—
χ^2/dof		676.4/625	712.9/624	766.9/629	665.8/612	779.4/642

TABLE 4.2: The same as Table 4.1 for PDS 456, but assuming only the He-like iron absorption line.

Components	Parameters	A	B	C	D	E
phabs	N_{H} (10^{21}cm^{-2})	$3.7^{+0.2}_{-0.2}$	$3.8^{+0.2}_{-0.2}$	$4.1^{+0.2}_{-0.2}$	$3.5^{+0.2}_{-0.2}$	$3.6^{+0.2}_{-0.2}$
zxipcf	N_{H} (10^{23}cm^{-2} ; fixed)	—	6.0	6.0	6.0	6.0
	$\log \xi$ (fixed)	—	2.75	2.75	2.75	2.75
	CF (fixed)	0.0	0.20	0.43	0.42	0.42
	v_{out} (/c) (fixed)	—	-0.42	-0.45	-0.42	-0.39
powerlaw	Γ	$2.06^{+0.02}_{-0.02}$	$2.16^{+0.02}_{-0.02}$	$2.42^{+0.02}_{-0.02}$	$2.27^{+0.02}_{-0.02}$	$2.20^{+0.02}_{-0.02}$
	norm (10^{-3})	$3.2^{+0.1}_{-0.1}$	$3.3^{+0.1}_{-0.1}$	$4.0^{+0.1}_{-0.1}$	$3.1^{+0.1}_{-0.1}$	$2.6^{+0.1}_{-0.1}$
diskbb	kT_{in} (eV)	$0.16^{+0.01}_{-0.01}$	$0.15^{+0.01}_{-0.01}$	$0.13^{+0.00}_{-0.00}$	$0.15^{+0.01}_{-0.01}$	$0.15^{+0.01}_{-0.01}$
	norm (10^2)	19^{+9}_{-6}	26^{+12}_{-9}	79^{+35}_{-25}	16^{+8}_{-6}	15^{+7}_{-5}
kabs	N_{FeXXV} (10^{18}cm^{-2})	$1.2^{+0.5}_{-0.5}$	$2.5^{+0.7}_{-0.6}$	$3.4^{+0.8}_{-0.7}$	$3.1^{+0.8}_{-0.7}$	$2.4^{+0.6}_{-0.6}$
	z	$-0.32^{+0.01}_{-0.01}$	$-0.31^{+0.01}_{-0.01}$	$-0.33^{+0.01}_{-0.01}$	$-0.29^{+0.01}_{-0.01}$	$-0.26^{+0.01}_{-0.01}$
kabs	N_{FeXXV} (10^{18}cm^{-2})	$0.9^{+0.6}_{-0.6}$	$1.7^{+0.9}_{-0.7}$	$2.2^{+1.1}_{-0.9}$	$2.6^{+0.8}_{-0.7}$	$3.1^{+0.7}_{-0.7}$
	z	$-0.40^{+0.02}_{-0.02}$	$-0.46^{+0.02}_{-0.01}$	$-0.45^{+0.02}_{-0.02}$	$-0.36^{+0.02}_{-0.02}$	$-0.32^{+0.01}_{-0.01}$
kabs	N_{FeXXV} (10^{18}cm^{-2})	—	—	—	—	$2.17^{+0.79}_{-0.70}$
	z	—	—	—	—	$-0.40^{+0.01}_{-0.01}$
χ^2/dof		1071.2/979	1094.9/939	1190.5/870	1077.6/907	1122.8/929

TABLE 4.3: The same as Table 4.1 for 1H 0707–495 in 2008, but assuming only the He-like iron absorption line. The CF parameter of spectrum A is free to vary unlike that of the other objects.

Components	Parameters	A	B	C	D	E
phabs	N_{H} (10^{20}cm^{-2})	$8.0^{+0.7}_{-0.4}$	$8.6^{+0.5}_{-0.5}$	$8.0^{+0.5}_{-0.4}$	$7.2^{+0.5}_{-0.5}$	$6.5^{+0.5}_{-0.5}$
zxipcf	N_{H} (10^{23}cm^{-2} ; fixed)	5.6	5.6	5.6	5.6	5.6
	$\log \xi$ (fixed)	2.65	2.65	2.65	2.65	2.65
	CF	$0.52^{+0.02}_{-0.02}$	$0.56^{+0.02}_{-0.02}$	$0.60^{+0.02}_{-0.02}$	$0.63^{+0.02}_{-0.02}$	$0.70^{+0.02}_{-0.02}$
	v_{out} (/c)	$-0.29^{+0.01}_{-0.01}$	$-0.28^{+0.01}_{-0.00}$	$-0.27^{+0.00}_{-0.00}$	$-0.27^{+0.00}_{-0.00}$	$-0.26^{+0.00}_{-0.00}$
powerlaw	Γ	$2.79^{+0.02}_{-0.02}$	$2.77^{+0.02}_{-0.03}$	$2.71^{+0.03}_{-0.03}$	$2.72^{+0.03}_{-0.03}$	$2.66^{+0.03}_{-0.04}$
	norm (10^{-3})	$4.4^{+0.2}_{-0.2}$	$3.4^{+0.2}_{-0.2}$	$2.8^{+0.2}_{-0.2}$	$2.4^{+0.2}_{-0.2}$	$1.7^{+0.1}_{-0.1}$
diskbb	kT_{in} (eV)	$0.23^{+0.01}_{-0.01}$	$0.21^{+0.01}_{-0.01}$	$0.20^{+0.01}_{-0.01}$	$0.19^{+0.01}_{-0.00}$	$0.18^{+0.00}_{-0.00}$
	norm (10^2)	$1.6^{+0.6}_{-0.5}$	$2.5^{+0.6}_{-0.6}$	$2.9^{+0.7}_{-0.6}$	$3.5^{+0.8}_{-0.7}$	$2.9^{+0.7}_{-0.5}$
kabs	N_{FeXXV} (10^{18}cm^{-2})	4^{+2}_{-1}	7^{+2}_{-1}	8^{+3}_{-2}	7^{+3}_{-2}	7^{+2}_{-1}
	z	$-0.14^{+0.01}_{-0.01}$	$-0.14^{+0.01}_{-0.01}$	$-0.15^{+0.01}_{-0.01}$	$-0.18^{+0.01}_{-0.01}$	$-0.13^{+0.01}_{-0.01}$
kabs	N_{FeXXV} (10^{18}cm^{-2})	15^{+5}_{-4}	11^{+6}_{-5}	10^{+9}_{-4}	9^{+9}_{-4}	3^{+1}_{-1}
	z	$-0.27^{+0.01}_{-0.01}$	$-0.25^{+0.01}_{-0.01}$	$-0.25^{+0.01}_{-0.01}$	$-0.29^{+0.01}_{-0.01}$	$-0.20^{+0.02}_{-0.02}$
kabs	N_{FeXXV} (10^{18}cm^{-2})	—	—	—	—	4^{+3}_{-2}
	z	—	—	—	—	$-0.28^{+0.02}_{-0.02}$
χ^2/dof		587.1/515	596.1/525	568.9/525	573.7/507	688.6/517

TABLE 4.4: The same as Table 4.3 for 1H 0707–495 in 2010.

Components	Parameters	A	B	C	D	E
phabs	N_{H} (10^{20}cm^{-2})	$9.0^{+0.5}_{-0.5}$	$8.6^{+0.4}_{-0.5}$	$8.0^{+0.4}_{-0.4}$	$7.7^{+0.4}_{-0.4}$	$7.2^{+0.3}_{-0.4}$
zxipcf	N_{H} (10^{23}cm^{-2} ; fixed)	5.6	5.6	5.6	5.6	5.6
	$\log \xi$ (fixed)	2.73	2.73	2.73	2.73	2.73
	CF	$0.58^{+0.02}_{-0.01}$	$0.67^{+0.01}_{-0.01}$	$0.72^{+0.01}_{-0.01}$	$0.76^{+0.01}_{-0.01}$	$0.78^{+0.01}_{-0.01}$
	v_{out} (/c)	$-0.29^{+0.01}_{-0.01}$	$-0.28^{+0.00}_{-0.00}$	$-0.27^{+0.00}_{-0.00}$	$-0.26^{+0.00}_{-0.00}$	$-0.26^{+0.00}_{-0.00}$
powerlaw	Γ	$2.78^{+0.02}_{-0.02}$	$2.80^{+0.02}_{-0.02}$	$2.77^{+0.02}_{-0.03}$	$2.76^{+0.03}_{-0.03}$	$2.69^{+0.03}_{-0.04}$
	norm (10^{-3})	$5.0^{+0.2}_{-0.2}$	$3.6^{+0.2}_{-0.1}$	$2.9^{+0.1}_{-0.1}$	$2.3^{+0.1}_{-0.1}$	$1.4^{+0.1}_{-0.1}$
diskbb	kT_{in} (eV)	$0.24^{+0.01}_{-0.01}$	$0.22^{+0.01}_{-0.01}$	$0.21^{+0.01}_{-0.01}$	$0.20^{+0.01}_{-0.00}$	$0.18^{+0.00}_{-0.00}$
	norm (10^2)	$2.3^{+0.6}_{-0.5}$	$3.1^{+0.5}_{-0.5}$	$3.0^{+0.5}_{-0.5}$	$3.4^{+0.6}_{-0.6}$	$4.0^{+0.6}_{-0.5}$
kabs	N_{FeXXV} (10^{18}cm^{-2})	10^{+3}_{-2}	7^{+6}_{-2}	8^{+3}_{-2}	15^{+8}_{-4}	11^{+4}_{-7}
	z	$-0.15^{+0.01}_{-0.01}$	$-0.15^{+0.01}_{-0.02}$	$-0.15^{+0.01}_{-0.01}$	$-0.15^{+0.01}_{-0.01}$	$-0.14^{+0.03}_{-0.01}$
kabs	N_{FeXXV} (10^{18}cm^{-2})	13^{+9}_{-4}	8^{+4}_{-3}	14^{+11}_{-6}	13^{+13}_{-6}	6^{+3}_{-2}
	z	$-0.25^{+0.01}_{-0.01}$	$-0.22^{+0.01}_{-0.02}$	$-0.23^{+0.01}_{-0.01}$	$-0.26^{+0.01}_{-0.01}$	$-0.21^{+0.05}_{-0.01}$
χ^2/dof		766.1/570	704.5/541	739.9/535	780.3/524	763.8/499

4.3 UV–X-ray SED fitting

In this section, we model the broadband SED with the pn (X-ray) and OM (UV) data to investigate the outflow driving mechanism. Since we found that the flux variation of the OM data was less than 10% during the observation period for all the three sources, we used the time-averaged OM spectrum.

Since the three targets are super-Eddington objects and their AGN components are significant, we ignored the host galaxy contamination (Castelló-Mor, Netzer, and Kaspi, 2016; Done and Jin, 2016; Parker et al., 2017). We modeled SED of the AGN component with the `agnslim` model (Kubota and Done, 2019) multiplied by the reddening (`redden`; Cardelli, Clayton, and Mathis, 1989) and the interstellar absorption (`phabs`). Here `agnslim` is a broadband spectral model for super-Eddington AGN based on the slim disk emissivity. The accretion flow is assumed to be radially stratified; the inner hot Comptonization region (R_{in} to R_{hot}) with the electron temperature kT_{hot} and photon index Γ_{hot} , the intermediate warm Comptonization region to produce the soft X-ray excess (R_{warm} to R_{hot}) with the electron temperature kT_{warm} and photon index Γ_{warm} , and the outer standard disk (R_{warm} to R_{out}).

From the spectral fitting of IRAS 13224–3809 and PDS 456 in Section 4.2, the partial covering fraction of spectrum A is found to be $\text{CF} = 0$. Since the spectrum A of 1H 0707–495 was confirmed to be obscured, its SED model was also multiplied by the `zxipcf` model, where the parameters are fixed to those obtained by the spectral fitting (Table 4.3 and 4.4).

For a highly super-Eddington slim disk, the inner radius of the disk (R_{in}) is determined not only by the black hole spin but also by the gas pressure so that R_{in} can be smaller than the inner-most stable circular orbit (Watarai et al., 2000; Kubota and Done, 2019). We assume the spin parameter $a^* = 0$, and set R_{in} to the radius calculated by Kubota and Done (2019) as follows:

$$R_{\text{in}} = \begin{cases} R_{\text{ISCO}} & (\dot{m} \leq 6) \\ R_{\text{ISCO}} \cdot \left(\frac{\dot{m}}{6}\right)^{\log\left(\frac{R_{\text{hot}}}{R_{\text{ISCO}}}\right)/\log\left(\frac{100}{6}\right)} & (6 < \dot{m} \leq 100) \\ R_{\text{hot}} & (100 < \dot{m}) \end{cases}, \quad (4.1)$$

where \dot{m} is the Eddington-normalized accretion rate introduced in Section 1.1.2. We also fixed the color excess $E(B - V)$ of the infrared/optical/UV extinction to the value derived from the relation $E(B - V) = 1.7 \times N_{\text{H}}/10^{22} \text{ cm}^{-2}$ (Bohlin, Savage, and Drake, 1978).

The averaged OM spectrum and pn spectrum A are successfully fitted with the assumed model. Figure 4.22–4.25 show the νf_{ν} plots of the broadband SED in 3 eV–10 keV for IRAS 13224–3809, PDS 456, and 1H 0707–495, respectively. The gray lines indicate the two or three representative intensity-sliced spectra. The blue line represents the best-fit SED model for spectrum A, from which the interstellar absorption and reddening model are removed to show the de-absorbed `agnslim` component (the orange dashed line). The partially absorbed best model (`agnslim * zxipcf`) is also plotted in green for 1H 0707–495 (Figure 4.24 and 4.25). Best-fit parameters are given in Table 4.5–4.8.

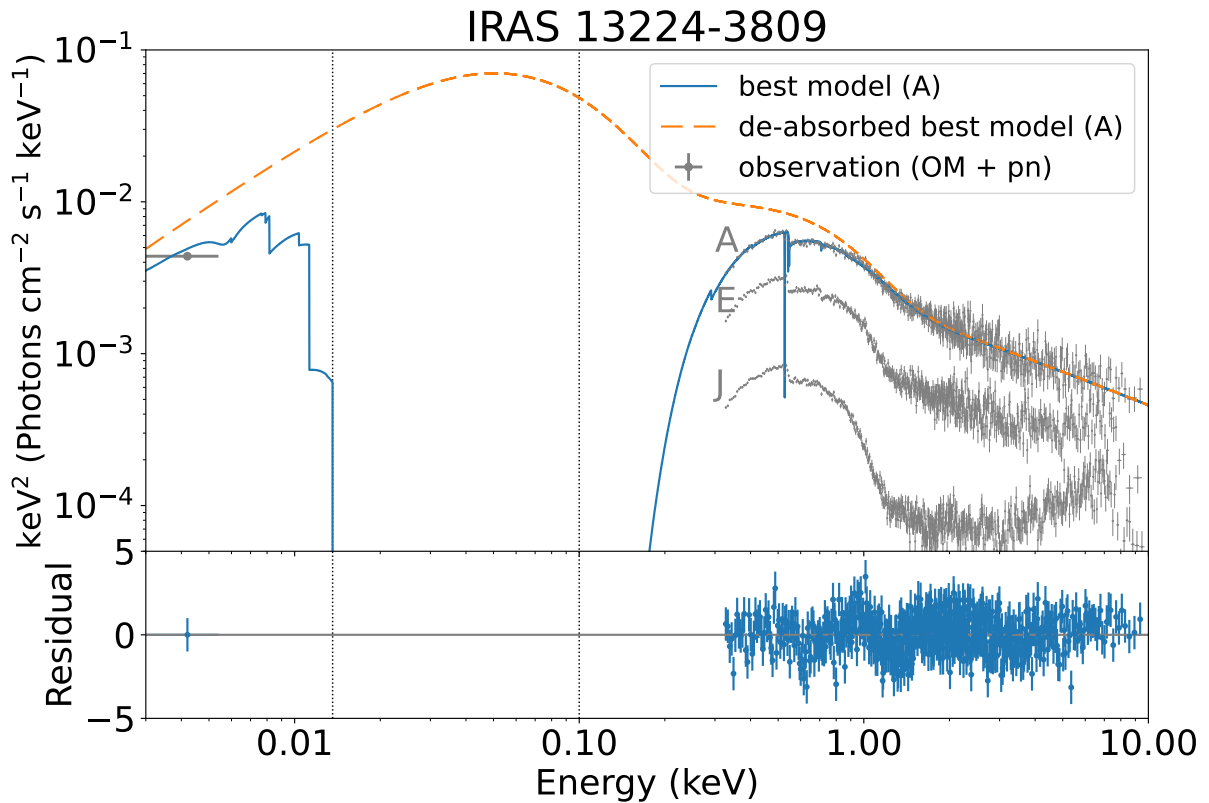


FIGURE 4.22: Broadband UV–X-ray SED fitting of IRAS 13224–3809 with pn and OM data in 3 eV–10 keV. Three gray lines show typical intensity-sliced spectra A, E, and J. The blue line shows the best-fit model for spectrum A. The orange dashed line shows the de-absorbed best-fit model. The vertical dotted lines show the boundary of the energy bands, 13.6 eV and 0.1 keV.

TABLE 4.5: Best-fit parameters determined by the SED fitting of IRAS 13224–3809 obtained with the OM and pn instruments.

Components	Parameters	Best-fit values
phabs	N_{H} (10^{20}cm^{-2})	5.0 (fixed)
redden	$E(B - V)$	0.086 (fixed)
agnslim	mass (M_{\odot})	5.4×10^6 (fixed)
	\dot{m} ($= \dot{M}/\dot{M}_{\text{Edd}}$)	6.30 ± 0.01
	a^*	0 (fixed)
	$\cos i$	0.5 (fixed)
	kT_{hot} (keV)	100 (fixed)
	kT_{warm} (keV)	0.166 ± 0.005
	Γ_{hot}	2.67 ± 0.04
	Γ_{warm}	$1.66^{+0.09}_{-0.10}$
	R_{hot} (R_{g})	8.3 ± 0.2
	R_{warm} (R_{g})	10.6 ± 0.1

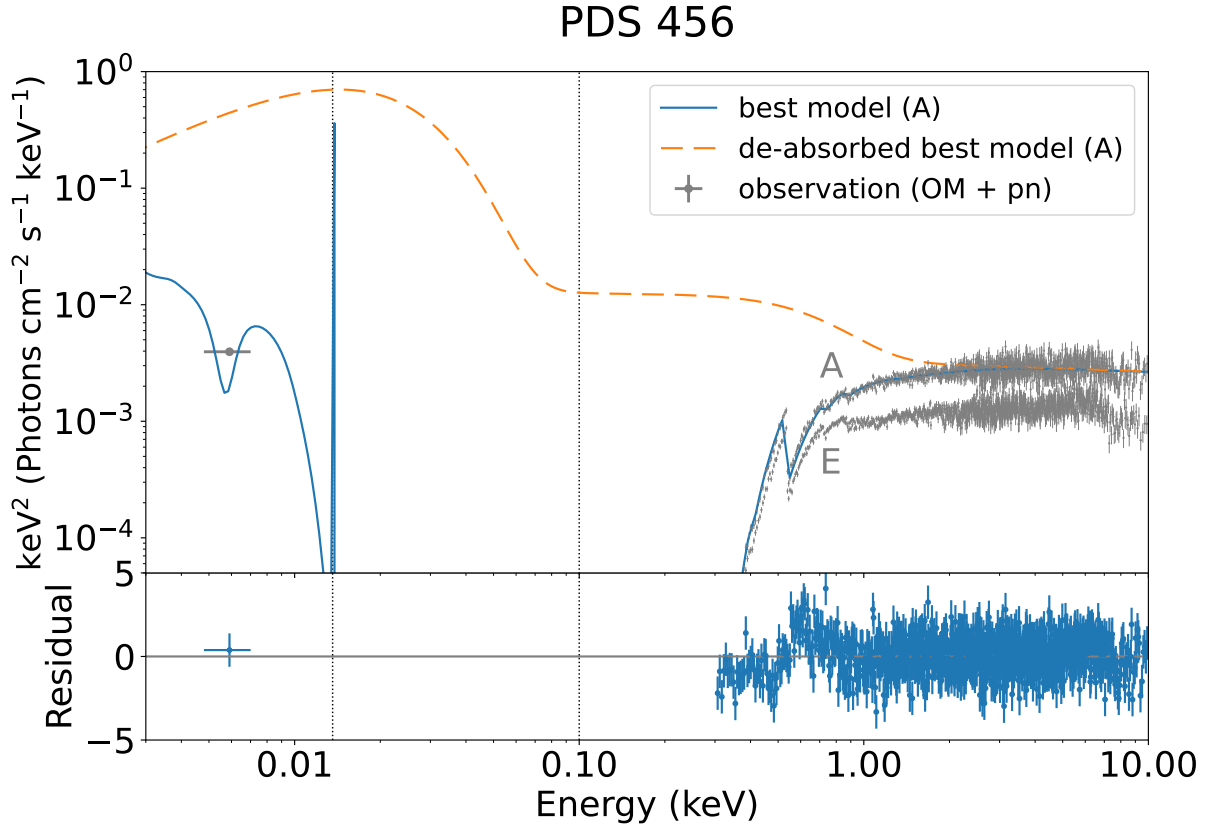


FIGURE 4.23: The same as Figure 4.22, but for PDS 456.

TABLE 4.6: The same as Table 4.5, but for PDS 456.

Components	Parameters	Best-fit values
phabs	N_{H} (10^{21}cm^{-2})	3.7 (fixed)
redden	$E(B - V)$	0.63 (fixed)
agnslim	mass (M_{\odot})	1.0×10^9 (fixed)
	\dot{m} ($= \dot{M}/\dot{M}_{\text{Edd}}$)	2.0 ± 0.7
	a^*	0 (fixed)
	$\cos i$	0.5 (fixed)
	kT_{hot} (keV)	100 (fixed)
	kT_{warm} (keV)	0.156 ± 0.005
	Γ_{hot}	2.09 ± 0.02
	Γ_{warm}	1.6 ± 0.3
	R_{hot} (R_{g})	$7.9^{+0.3}_{-0.4}$
	R_{warm} (R_{g})	$8.4^{+0.2}_{-0.5}$

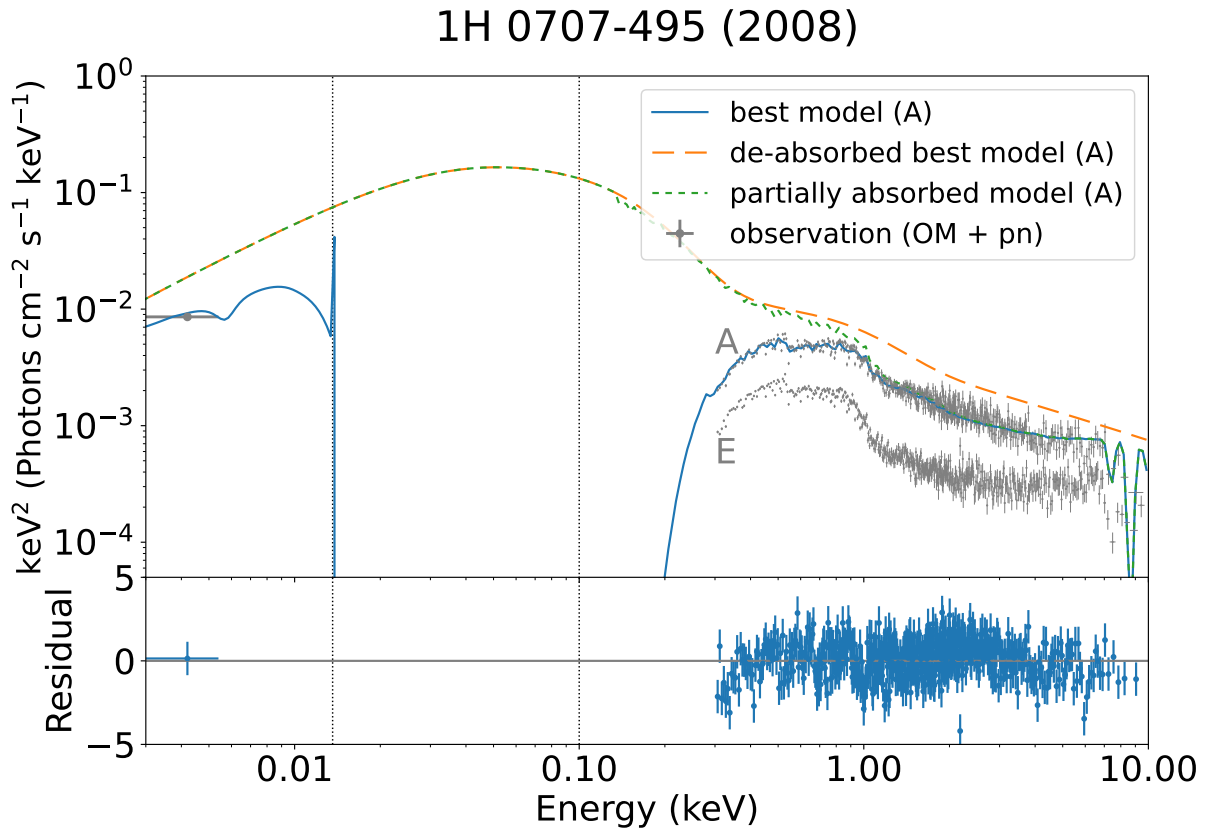


FIGURE 4.24: The same as Figure 4.22, but for 1H 0707–495 in 2008. The `zxipcf` component is added since spectrum A is also partially absorbed, but the parameters are fixed to those obtained by the ratio fitting.

TABLE 4.7: The same as Table 4.5, but for 1H 0707–495 in 2008.

Components	Parameters	Best-fit values
phabs	N_{H} (10^{20}cm^{-2})	8.0 (fixed)
redden	$E(B - V)$	0.136 (fixed)
zxipcf	N_{H} (10^{23}cm^{-2})	5.6 (fixed)
	$\log \xi$	2.65 (fixed)
	CF	0.52 (fixed)
	v_{out} ($/c$)	-0.29 (fixed)
agnslim	mass (M_{\odot})	4.0×10^6 (fixed)
	\dot{m} ($= \dot{M}/\dot{M}_{\text{Edd}}$)	9.6 ± 0.1
	a^*	0 (fixed)
	$\cos i$	0.5 (fixed)
	kT_{hot} (keV)	100 (fixed)
	kT_{warm} (keV)	0.20 ± 0.01
	Γ_{hot}	2.71 ± 0.02
	Γ_{warm}	1.60 ± 0.3
	R_{hot} (R_{g})	6.5 ± 0.1
	R_{warm} (R_{g})	7.0 ± 0.1

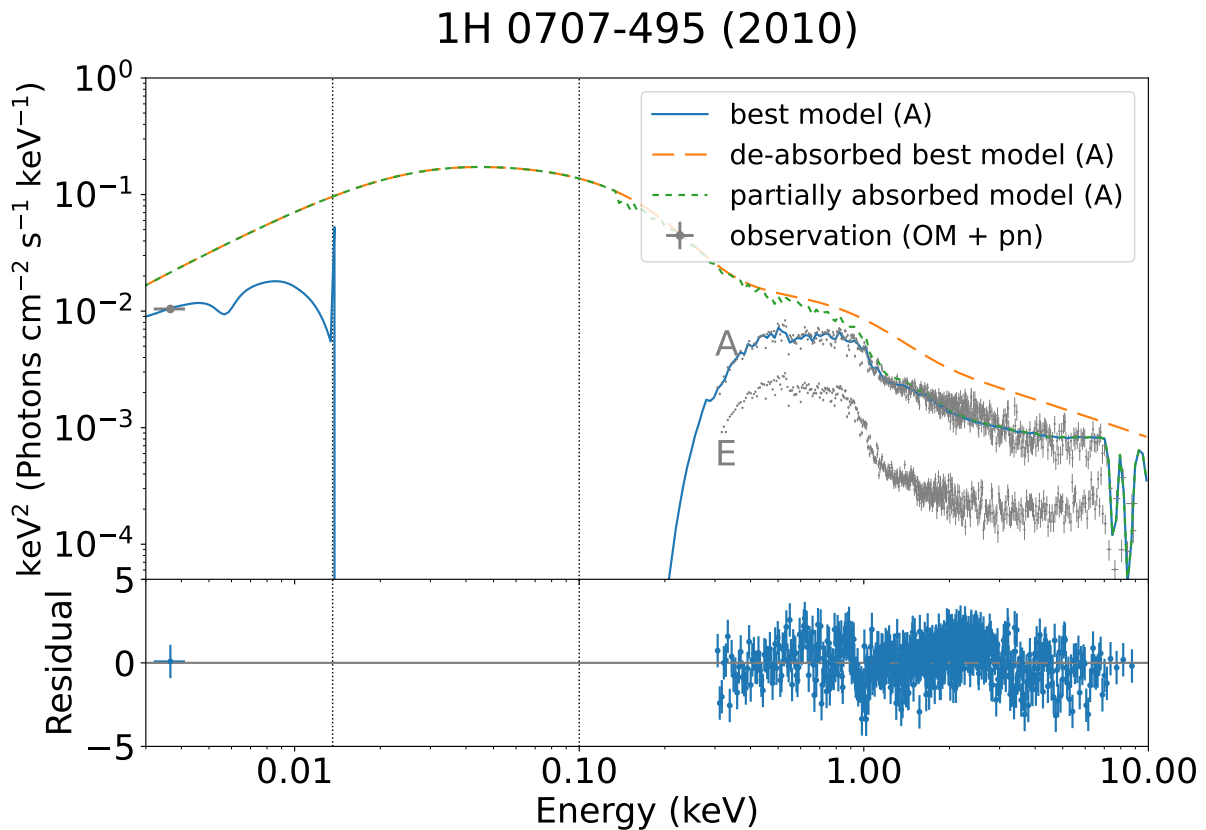


FIGURE 4.25: The same as Figure 4.22, but for 1H 0707–495 in 2010. The `zxipcf` component is added since spectrum A is also partially absorbed, but the parameters are fixed to those obtained by the ratio fitting.

TABLE 4.8: The same as Table 4.5, but for 1H 0707–495 in 2010.

Components	Parameters	Best-fit values
phabs	N_{H} (10^{20}cm^{-2})	9.0 (fixed)
redden	$E(B - V)$	0.153 (fixed)
zxipcf	N_{H} (10^{23}cm^{-2})	5.6 (fixed)
	$\log \xi$	2.73 (fixed)
	CF	0.58 (fixed)
	v_{out} ($/c$)	-0.29 (fixed)
agnslim	mass (M_{\odot})	4.0×10^6 (fixed)
	\dot{m} ($= \dot{M}/\dot{M}_{\text{Edd}}$)	15.2 ± 0.1
	a^*	0 (fixed)
	$\cos i$	0.5 (fixed)
	kT_{hot} (keV)	100 (fixed)
	kT_{warm} (keV)	0.20 ± 0.01
	Γ_{hot}	2.77 ± 0.02
	Γ_{warm}	1.60 ± 0.2
	R_{hot} (R_{g})	5.8 ± 0.1
	R_{warm} (R_{g})	6.4 ± 0.1

Chapter 5

Discussion

Contents

5.1	Effectiveness of the spectral-ratio model fitting	91
5.2	The outflowing velocities of the UFO and the clumpy absorbers	93
5.2.1	Relation between the intrinsic UV/X-ray flux and the outflow velocities	97
5.2.2	Possibility of the line-force acceleration of the clumpy absorbers	99
5.2.3	Comparison of the clump velocities and the UFO velocities	102
5.3	The unexplained ~ 1 keV spectral feature	103
5.4	The constant ionization parameter of the clumps	104

5.1 Effectiveness of the spectral-ratio model fitting

We developed a novel spectra-ratio model fitting method and systematically applied this method to several Seyfert 1 galaxies. Thereby we were able to constrain the outflow velocities of the clumpy X-ray absorbers in IRAS 13224–3809, PDS 456, 1H 0707–495, and Mrk 335 for the first time. Here, we note there are certain conditions that this method becomes effective to constrain the clump velocities. First, the spectral-ratio fitting requires several intensity-sliced spectra with enough photon statistics, even when the source is the dimmest. The X-ray fluxes of ESO 323–G77 and PG 1126–041 were too low, such that X-ray count rates in 0.3–10 keV of roughly 1 counts s^{-1} are at least required (Table 3.2). In addition, the spectral ratios need to represent characteristic spectral variations, so that sufficient time-variation is required both in the X-ray flux and the spectral shape. For NGC 985 (2013), NGC 7314, and Ton S180, the spectral variability was so small that little information can be extracted by taking the spectral ratios.

Main contributors to the X-ray spectral-ratio are variations of the intrinsic X-ray emission and the X-ray absorbers, but the former does not cause energy dependence. Thus, the key to disentangling the parameter degeneracy is the X-ray absorber variation, which is manifested in the characteristic dip/cliff structure in the spectral-ratio of IRAS 13224–3809, PDS 456, 1H 0707–495 and Mrk 335 (Figures 3.10, A.1, A.5, and A.6, respectively). In the ratio fitting of Mrk 766 and NGC 985 (Figures A.2 and A.3, respectively), however, the spectral ratios are almost flat and absorbers' parameters

are hardly constrained (Tables 3.9 and 3.10), while the fitting residuals are small. In other words, the appearance of the dip/cliff structure in the spectral-ratio is essential to estimate reliable parameters in this method.

The dip structure appears when there are some changes in the clumpy absorbers and their parameters (N_{H} and ξ) are within a specific range (see Figure 3.7 and 3.8). Therefore, we recognize that the X-ray emission is partially absorbed when the characteristic dip is found in the spectral ratios, and also we can constrain N_{H} and ξ to some extent. In addition, the dip energy shift gives us the clump velocity in the line-of-sight, which makes this method unique to constrain the radial velocity of the partial absorbing clouds. Finally, we remark that taking the ratio can cancel out the “multiplicative” contributions such as constant absorption, while cannot cancel out the “additive” contributions such as the constant emission seen in NGC 3783 (Figure A.8).

5.2 The outflowing velocities of the UFO and the clumpy absorbers

In Section 4.1, we constrained the outflow velocity v_{out} of the partial clumpy absorbers using the spectral-ratio fitting method. We also performed the conventional spectral fitting to determine the UFO velocity v_{UFO} in Section 4.2.

Comparison of the outflow velocities of the UFOs and the clumpy absorbers are shown in Figure 5.1–5.4, where these velocities are plotted against the 0.3–10.0 keV X-ray flux of the intensity-sliced spectra. Clump velocities obtained by both the ratio fitting and the spectral fitting are shown for IRAS 13224–3809 and 1H 0707–495. For PDS 456, the clump velocity in the spectral fitting was fixed to the value obtained by the spectral-ratio fitting. When the UFO feature is composed of multiple absorption lines with different velocity components, the average velocity weighted by the column density of each absorption line (N_{ion}) is plotted (see Table 4.1–4.4).

We fitted the velocities of the UFOs and clumpy absorbers as a function of the X-ray flux with linear functions. The blue, purple, and orange dotted lines and areas in Figure 5.1–5.4 show the best-fit models and their 1σ uncertainties, respectively. Since the UFO absorption of Mrk 335 in our dataset is too tiny to estimate the velocity (Figure 4.16), the UFO velocity presented in the previous study (Igo et al., 2020; see Table 3.1) is plotted with its uncertainty in pink. Note that Igo et al. (2020) did not perform UFO search for flux-resolved spectra, so the detected UFO velocity was independent of the X-ray flux. While the present analysis indicates the fast UFO and clump velocities ($>0.1c$) for IRAS 13224–3809, 1H 0707–495 and PDS 456, the clump velocity of Mrk335 is much smaller ($<0.1c$) in agreement with the small UFO velocities suggested in the previous works (Gallo et al., 2019; Igo et al., 2020). These results strengthen the reliability of the clump velocity estimation by the spectral-ratio model fitting.

The v_{out} values obtained by the ratio fitting and the spectral fitting are close to each other but do not fully agree, which presumably represents systematic limits of the present analysis. In any case, we see similar increasing trends with the X-ray flux of the clump velocities and the UFO velocities in IRAS 13224–3809 and 1H 0707–495 (Figure 5.1 and 5.2). In particular, the UFO velocities in IRAS 13224–3809 assuming the He-like Fe absorption (orange) show very similar velocity values with those of the clumpy absorbers determined by the ratio-fitting (blue; Figure 5.1). This trend was similar for 1H 0707–495 and PDS 456, where we show the UFO velocities assuming the He-like Fe.

In summary, we have found that the UFOs and clumps have similar outflowing velocities, and they also show similar increasing trends with the X-ray flux. This is consistent with the “hot inner and clumpy outer wind” scenario described in Section 1.3.2, where production of the clumpy outer absorbers is a consequence of the radiation-driven UFO winds from inside. Note that the flux dependence of the clump velocity is also obtained in the ratio fitting without fixing ξ and N_{H} (see Table 3.6, 3.7, 3.8, and 3.12).

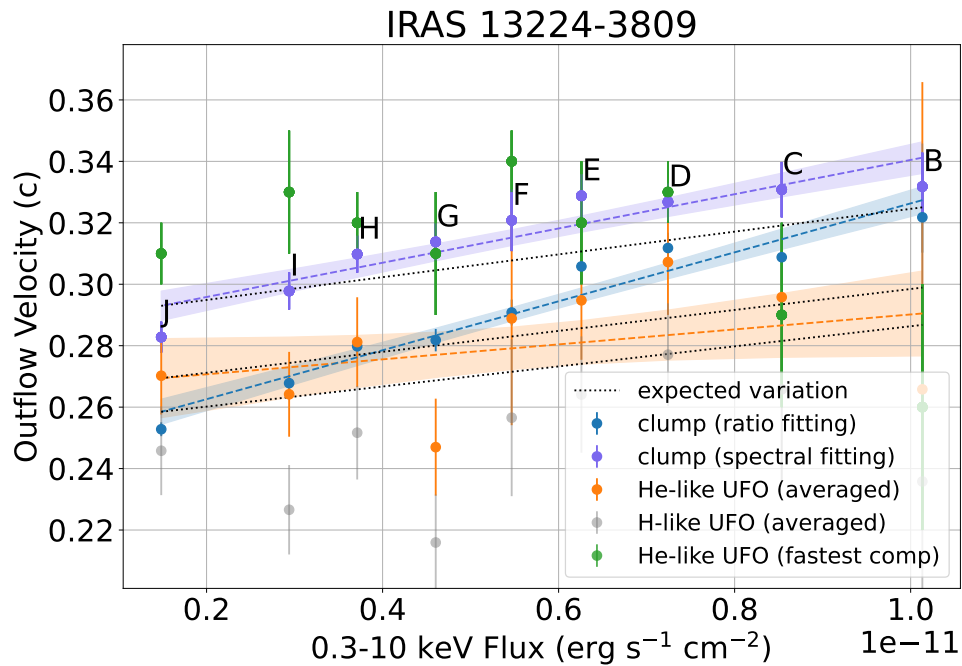


FIGURE 5.1: Comparison of the velocities between the UFOs and clumps of IRAS 13224–3809. Outflow velocities of the clumpy absorbers obtained from the spectral-ratio fitting (in blue), those from the spectral fitting (in purple), and those of the UFOs estimated from the spectral fitting (in orange and gray assuming He-like and H-like iron, respectively). The outflowing velocities are plotted against the 0.3–10 keV flux of the intensity-sliced spectra. The blue, purple, and orange dotted lines show the best-fit linear functions of each with 1σ uncertainties. The fastest UFO component obtained with spectral fitting (in green; see Table 4.1) and expected velocity variations are also plotted (in black).

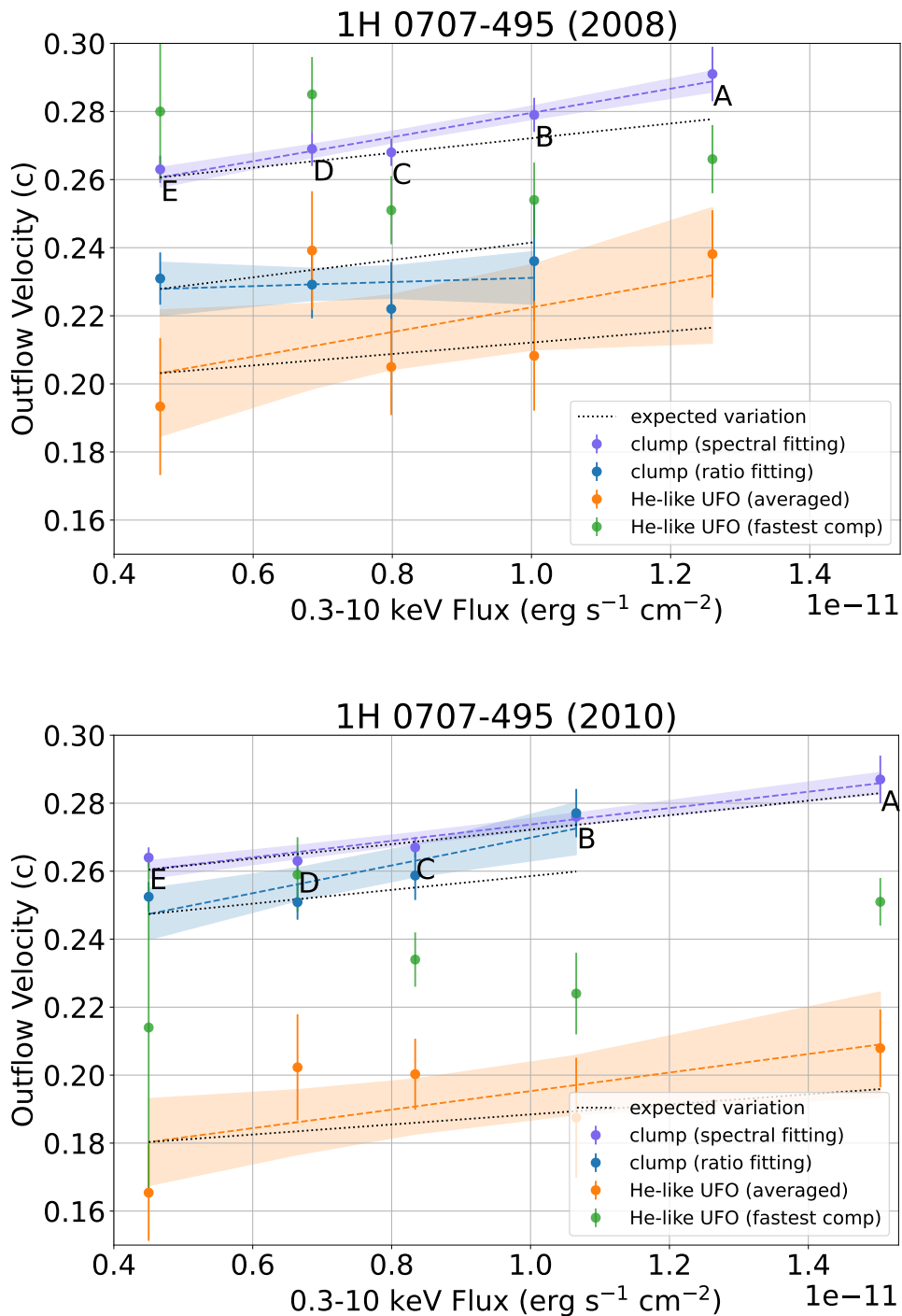


FIGURE 5.2: The same as Figure 5.1, but for 1H 0707–495 in 2008 and 2010, respectively. Since UFO absorption lines were detected even in the brightest spectrum A, its velocity is plotted. The clump velocity obtained by the ratio fitting is only obtainable from spectrum B–E.

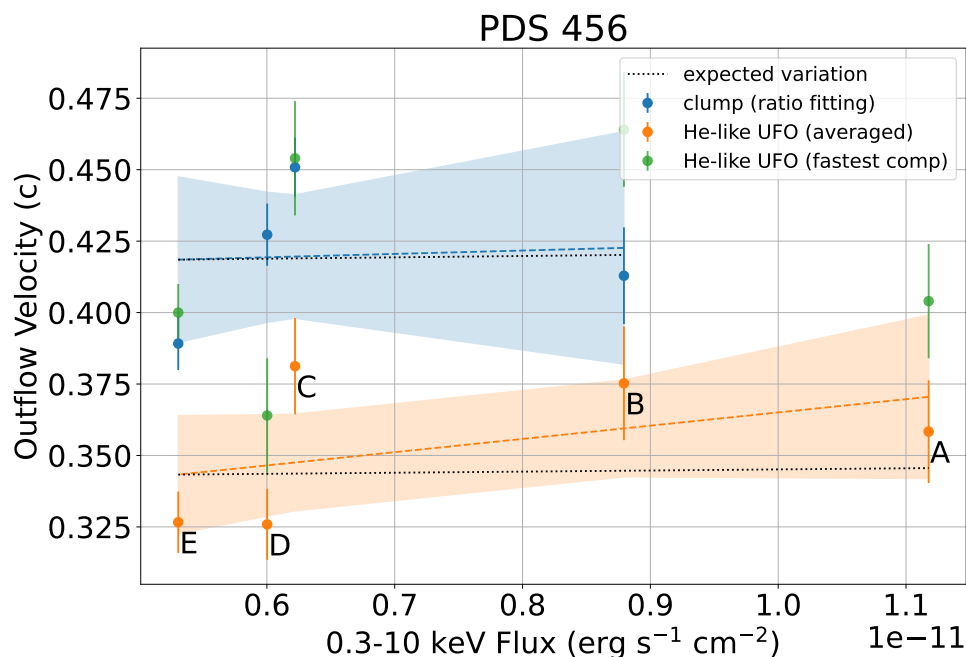


FIGURE 5.3: The same as Figure 5.1, but for PDS 456. In the spectral fitting of PDS 456, the velocity of the clumpy absorber was fixed to the value obtained by the spectral-ratio fitting, so the purple points are not plotted.

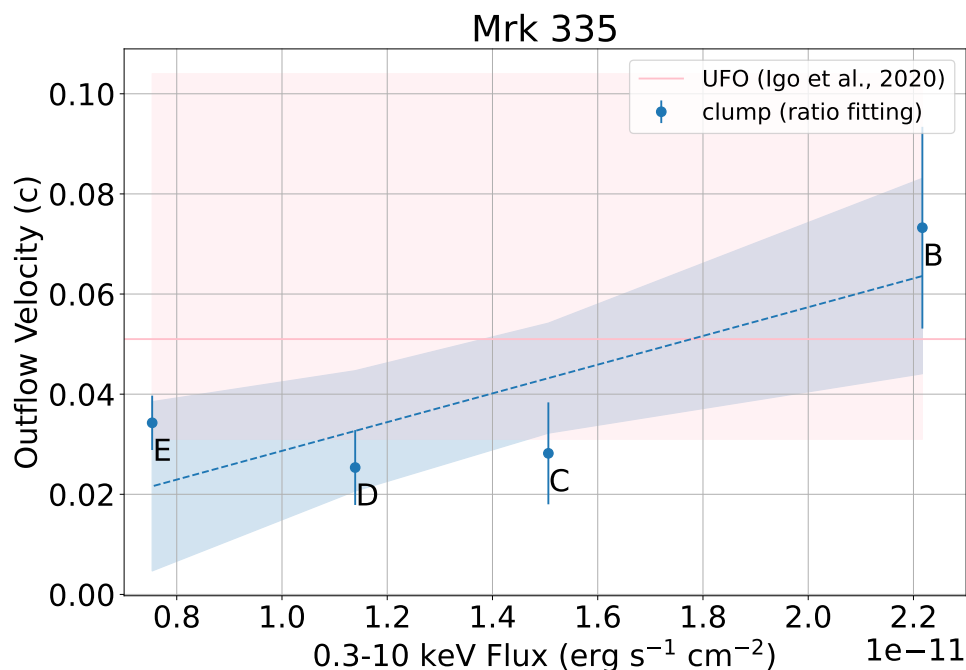


FIGURE 5.4: The same as Figure 5.1, but for Mrk 335. The UFO velocity in Igo et al. (2020) is plotted with its uncertainty in pink.

5.2.1 Relation between the intrinsic UV/X-ray flux and the outflow velocities

As shown in Figure 3.2, the observed 0.3–10 keV flux variation of IRAS 13224–3809 ranges over more than one order of magnitude. On the other hand, the ratio fitting results show that the intrinsic X-ray flux is varied by only a factor of ~ 4 , indicating that a considerable amount of the apparent flux variation is caused by changes of the partial covering fraction.

The orange dashed line in Figure 4.22–4.25 shows UV–X-ray best model for spectrum A of IRAS 13224–3809 in which the covering fraction is assumed to be null and the ISM absorption is de-absorbed. From the de-absorbed model, the intrinsic UV flux in 13.6 eV – 0.1 keV and the intrinsic X-ray flux in 0.1–10.0 keV are estimated and summarized in Table 5.1. UV flux variation is less than 10% and almost ignorable. Intrinsic X-ray flux variation is estimated from the normalization of the dimmest ratio; it is 0.15 for IRAS 13224–3809 (see Figure 4.2 and 4.3). Since the intrinsic X-ray flux varies by a factor of ~ 7 while the UV flux is invariable for IRAS 13224–3809, the total flux variation of UV and X-rays is estimated to be about a factor of ~ 1.27 , assuming that the obtained ratio (UV flux: X-ray flux = 3:1) is valid throughout the observation period.

When the disk wind is driven by the continuum radiation, the total flux variation is expected to contribute directly to the increase in the kinetic energy of the disk wind. Since the outflow velocity is proportional to the square root of the wind kinetic energy, the velocity change is estimated to be about a factor of $\sqrt{1.27} \sim 1.13$ for IRAS 13224–3809. The same calculations were performed for other sources, and the estimated velocity changes are shown in Table 5.1.

TABLE 5.1: UV (13.6–100 eV) and X-ray (0.1–10 keV) intrinsic fluxes calculated from the de-absorbed best-fit model of each object (the orange dotted line in Figure 4.22–4.25). The normalization of the dimmest ratio is determined by the ratio fitting in Figure 4.2, 4.6, and 4.8.

	UV flux [erg cm ⁻² s ⁻¹]	X-ray flux [erg cm ⁻² s ⁻¹]	Norm of the dimmest ratio	UV–X-ray flux variation	Estimated velocity variation
IRAS 13224–3809	1.8×10^{-10}	6.1×10^{-11}	0.15	1.27	1.13
PDS 456	9.4×10^{-10}	5.0×10^{-11}	0.74	1.013	1.007
1H 0707–495 (2008)	4.4×10^{-10}	1.5×10^{-10}	0.53	1.14	1.066
1H 0707–495 (2010)	4.8×10^{-10}	1.8×10^{-10}	0.44	1.18	1.09

The black dotted line in Figure 5.1–5.3 shows the thus estimated velocity increase trend for each target, taking the dimmest spectral flux as the reference. As a result, on the one hand, the increase of the observed *UFO* velocities in IRAS 13224–3809 agrees with the estimated velocity trend within the 1σ error margin. On the other hand, the observed *clump* velocities are significantly above the expected velocities.

Similar signatures are also seen in 1H 0707–495. In the 2008 data, the observed clump velocities obtained from the spectral fitting are higher than the expected velocities. In the 2010 data, both the clump velocities from the spectral fitting and the ratio fitting are higher than the estimated velocities. On the other hand, the *UFO* velocities agree with the expected velocities within the margin of error.

Furthermore, the clump velocities tend to be faster than the *UFO* velocities for all the objects. Consequently, given a simple assumption of the kinetic energy conservation, the *UFOs* are considered to be driven by the UV-dominant continuum radiation. Still,

the fast clumpy absorber velocities may not be explained only by the continuum-driven scenario.

Compared to IRAS 13224–3809 and 1H 0707–495, whose BH mass is $\sim 10^6 M_\odot$, X-ray time variability of PDS 456 is significantly smaller presumably due to its much larger BH mass of $\sim 10^9 M_\odot$. Also, the UV contribution to the SED is more significant, as shown in Figure 4.23. Therefore, the intrinsic UV–X-ray flux variation is quite small, and the velocity variation is tiny compared to IRAS 13224–3809 and 1H 0707–495 (Table 5.1).

5.2.2 Possibility of the line-force acceleration of the clumpy absorbers

The outflowing clump velocity, as well as the UFO velocity, is probably driven by the radiation pressure. Still, the results in the previous section suggest that the faster clump velocity cannot be explained by the continuum radiation pressure alone. Therefore, we propose a hypothesis that clumps are accelerated by the line force as well as the continuum force. It is believed that the line-force-driven outflow is caused by a mildly ionized gas, which efficiently absorbs the UV radiation in the SED. Since the mildly ionized gas is commonly located at the accretion disk in the *sub*-Eddington objects, it has not been considered, so far, to be a major cause of the outflow in the *super*-Eddington objects. Now, we suggest that the line force may also be effective in the super-Eddington objects, considering that the emission weakens and the ionization parameter decreases as going away from the inner part of the disk.

We used the photoionization code XSTAR (version 2.57; T. Kallman and Bautista, 2001; T. R. Kallman et al., 2004) to generate synthetic spectra affected by mildly ionized gas. The models describe transmission by the ionized absorbers as a function of the ionization parameter ξ , with the column density N_{H} fixed at $6 \times 10^{23} \text{ cm}^{-2}$ determined by the ratio fitting in IRAS 13224–3809. We fixed the gas density at $1.0 \times 10^{12} \text{ cm}^{-3}$, the gas temperature at 10^5 K , and the turbulent velocity at $1,000 \text{ km s}^{-1}$. Abundances were fixed to the solar values except for these minor elements (Li, Be, Ba, Na, Al, P, Cl, K, Sc, Ti, V, Cr, Mn, Co, Cu, and Zn) that were ignored to simplify the calculation. The incident spectrum was assumed to be the de-absorbed model determined in Section 4.3 and the ionization luminosity in 13.6 eV–13.6 keV to be $1.0 \times 10^{44} \text{ erg s}^{-1}$.

Figure 5.5 shows the transmission spectra with input SEDs of IRAS 13224–3809, where the interstellar absorption is de-absorbed. In these spectra, $\log \xi$ is varied at several different values from 2.0 to 4.0. The input SED is heavily absorbed as the ionization parameter gets lower. In addition to the characteristic dip structure around 1 keV, many UV absorption lines are found below 0.1 keV.

To estimate the line force contribution to the clump acceleration, we calculate how much the intrinsic UV and X-rays are intervened by the ionized gas, giving momentum to the gas. The momentum received by the intervening cloud is estimated by dividing the absorbed energy flux by the speed of light. The calculated UV and X-ray absorption fluxes for each ionization parameter are summarized in Table 5.2 and Figure 5.6. The total absorbed flux is the sum of the absorbed fluxes in UV and X-rays. In case of the absorption by highly ionized gas of $\log \xi \approx 4$, typical UFO values, both objects show little absorbed flux, i.e., the momentum obtained by the line force is minor. In contrast, as the ionization parameter decreases, the absorbed flux gets larger and reaches a plateau at around $\log \xi = 2$. This result suggests the occurrence of the clump acceleration due to the line force, since $\log \xi$ of the clouds obtained from the spectral fitting is ~ 2.7 (Tables 4.1 to 4.4).

Figure 5.7 presents a schematic picture of the proposed environment surrounding the central SMBH of a super-Eddington object. The highly-ionized UFO is driven by the strong continuum radiation from the inner part of the super-Eddington accretion flow, as suggested by radiation hydrodynamical simulations (e.g., Takeuchi, Ohsuga, and Mineshige, 2013, Kitaki et al., 2021). The wind turns into moderately ionized clumps

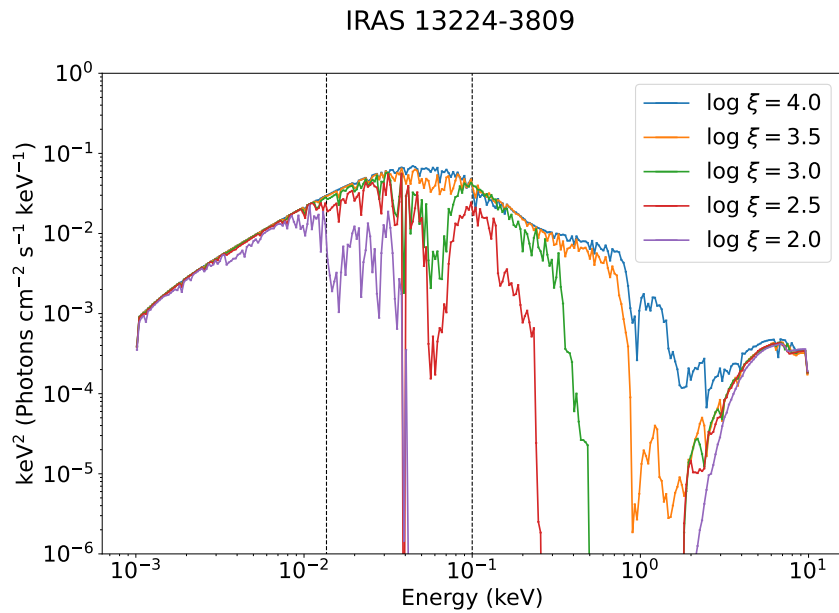


FIGURE 5.5: The transmission spectra of IRAS 13224–3809 absorbed by ionized gas are shown, calculated with XSTAR for various $\log \xi$ parameters.

TABLE 5.2: UV/X-ray flux of IRAS 13224–3809. All fluxes are in units of 10^{-12} erg cm⁻² s⁻¹.

	UV unabsorbed flux	UV absorbed flux	X-ray unabsorbed flux	X-ray absorbed flux	Total absorbed flux
de-absorbed	180.2	—	61.5	—	—
$\log \xi = 4.0$	167.1	13.1	47.6	13.9	27.0
$\log \xi = 3.5$	143.6	36.5	44.8	16.6	53.2
$\log \xi = 3.0$	93.9	86.3	32.6	28.8	115.1
$\log \xi = 2.5$	67.4	112.7	10.3	51.2	163.9
$\log \xi = 2.0$	10.0	170.1	0.5	60.9	231.1
$\log \xi = 1.5$	0.8	179.3	0.5	60.9	240.3
$\log \xi = 1.0$	0.0	180.2	0.5	61.0	241.1

away from the BH and is further accelerated by the line force. Consequently, the ionized clump velocities can be higher than the UFO velocities.

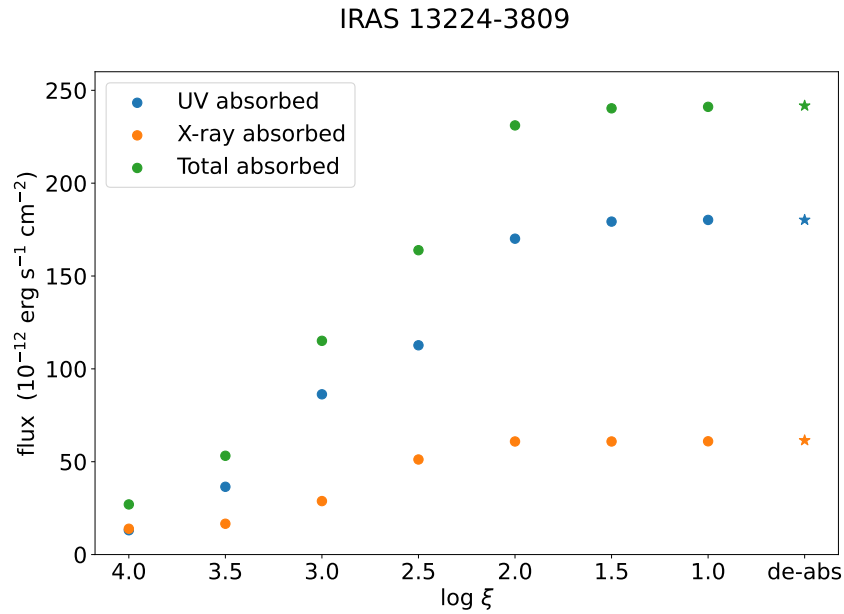


FIGURE 5.6: Absorbed flux estimated with XSTAR for IRAS 13224–3809. The blue, orange green dotted show the UV, X-ray, and total (UV + X-ray) absorbed fluxes. For comparison, the de-absorbed flux is plotted with the star marker.

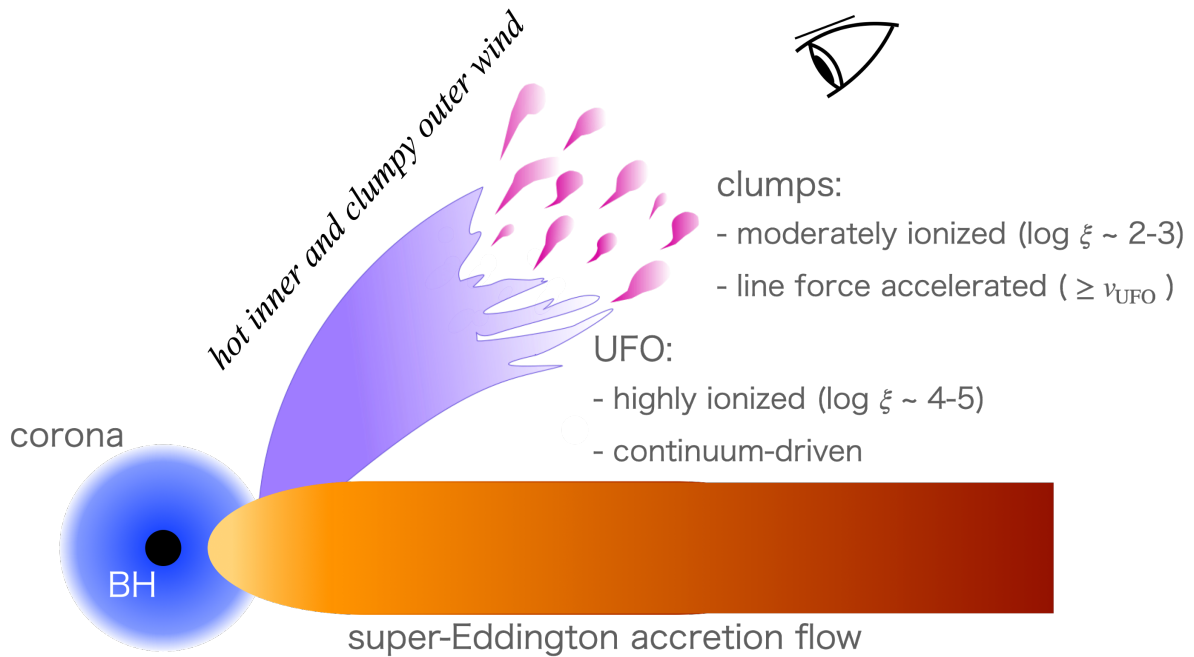


FIGURE 5.7: A schematic picture around a SMBH with super-Eddington accretion flow.

5.2.3 Comparison of the clump velocities and the UFO velocities

The spectral fitting of Section 4.2 suggests that multiple velocity components are mixed in the modeling of the UFO features. The green dots in Figure 5.1–5.3 indicate the fastest velocities of the multiple UFO components for IRAS 13224–3809, 1H 0707–495, and PDS 456. For IRAS 13224–3809, the clump velocities in purple and the fastest UFO velocities are comparable except for the spectra B and C, in which the UFO velocities are not determined precisely because the equivalent widths are too small. Meanwhile, the clump velocities are even higher than the fastest UFO velocity components for 1H 0707–495 in 2010 (Figure 5.2 bottom). These results reinforce our hypothesis that the clumps are accelerated by the line force in addition to the continuum radiation.

The gas has not yet received much acceleration at the base of the wind. On the other hand, when the gas receives sufficient acceleration, the velocity of the gas approaches the terminal velocity. In our description, the UFO becomes clumpy at a distance, so the clump velocity is expected to be close to the terminal velocity. This may suggest that the fastest velocity component of the UFO is similar to the clump velocity.

The fastest UFO components are often located around 10 keV, where the effective area of *XMM-Newton* drops rapidly, so that the result in this study is indefinite due to the current detector performance limitation. The *XRISM* satellite scheduled for launch next year will be capable of the precise spectroscopy up to ~ 12 keV and is expected to determine the fastest UFO velocity component with much higher precision. The soon-coming observations by *XRISM* of these sources will precisely determine the UFO absorption features up to ~ 12 keV and may confirm our hypothesis that the clump velocities accelerated by the line force can be higher than the UFO velocities.

5.3 The unexplained ~ 1 keV spectral feature

IRAS 13224–3809 and 1H 0707–495 have been known to exhibit unexplained characteristic spectral features at ~ 1 keV (e.g., 1H 0707–495, Fabian et al., 2009; IRAS 13224–3809, Ponti et al., 2010). When partial covering models with *static* absorbers were applied to these energy spectra, significant residuals were found at ~ 1 keV, and unexplained strong absorption edges were required (Mizumoto, Ebisawa, and Sameshima, 2014; Yamasaki et al., 2016). Alternatively, an extremely strong disk reflection component was proposed to explain this ~ 1 keV feature (e.g., Parker et al., 2017, Pinto et al., 2018, Parker et al., 2020).

In Figure 5.8, we show spectral fitting results for IRAS 13224–3809 and 1H 0707–495 in the 0.3–5.0 keV range with different models. The light-blue color shows the best-fit models and residuals with the stationary clumpy absorbers, which gives large residuals around 1 keV. The red gives the models with artificial ~ 1 keV edges to explain the residuals. The green is the best-fit model with the *outflowing* clumpy absorbers. The last model does not require such an inexplicable edge, which strongly suggests that the residual feature was caused by the energy shift of the outflowing clumpy absorbers at extremely high velocities ($\sim 0.3 c$).

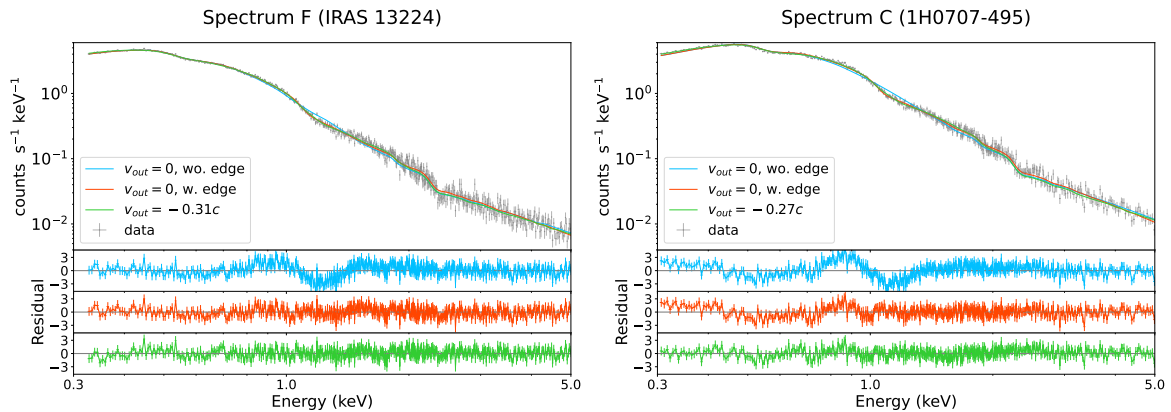


FIGURE 5.8: Spectral fitting results for the typical spectrum F of IRAS 13224–3809 (left) and spectrum C of 1H 0707–495 in 2008 (right) in 0.3–5.0 keV to compare different models. The light-blue and red lines show the best-fit models without/with artificial edges around 1.0 keV when the clump velocity is fixed at zero, while the green lines show the best-fit models when the clump velocities are blueshifted.

5.4 The constant ionization parameter of the clumps

The ionization parameter ($\xi = L/nr^2$) of the clumpy absorbers in IRAS 13224–3809 was derived by spectral model fitting individually for each flux level, and it was found invariable at $\log \xi \sim 2.7$ (Table 4.1). This value is also valid for 1H 0707–495 and PDS 456 for all the flux levels (Table 4.2–4.4). The spectral-ratio fitting without fixing ξ also shows that the ξ of these three objects ranges within $\xi = 2.7 \pm 0.3$ regardless of the X-ray flux (Table 3.6, 3.8, and 3.12). This finding, that the ionization state of the clumpy absorbers is always almost the same regardless of different targets and flux levels, is curious and may have physical implications.

The constant ξ suggests that the gas density of the clump, n , increases or that the location where the clump is formed, r , gets more distant as the X-ray luminosity increases. However, it is unlikely that the gas density or the clump location would vary so accordingly by chance across all the objects.

As described in Section 1.3.2, Takeuchi, Ohsuga, and Mineshige (2014) suggests that the clumps are formed by a sort of radiation hydrodynamic instability in addition to the Rayleigh-Taylor instability. The radiation instability should work only at a certain opacity, i.e., a specific ξ . If the wind instability is activated and the clumps are produced at this specific distance which increases with the luminosity, the result that ξ being constant may be explained. It is an intriguing future subject, both observationally and theoretically, to study if the constant ξ of the partial covering clouds is a common feature of the super-Eddington objects with continuum-driven outflows.

Alternatively, the apparent invariance of ξ may be simply due to observational bias. The range of $\xi \sim 2.4$ –3.0 corresponds to where the sharp dip/cliff structure appears in the spectral ratio (see the center plot of Figure 3.7). The spectral-ratio fitting method developed in this study focuses on this dip/cliff structure to determine the clump outflow velocity. Since the detailed analysis has not been conducted for objects with small ξ that do not produce this structure, there may be a bias toward the objects with $\xi \sim 2.4$ –3.0.

Chapter 6

Conclusion

In the present dissertation, we developed a novel technique called the “spectral-ratio model fitting method”, which enables us to investigate short-timescale spectral variation caused by clumpy absorbers of the AGNs. With this method, we systematically analyzed *XMM-Newton* data on Seyfert 1 galaxies to constrain the clump velocities and explore origins of the UFOs and the clumps.

The spectral-ratio fitting method requires sufficient X-ray photon statistics and time variability to constrain the clump velocities effectively. In addition, the appearance of the dip/cliff structures in the spectral ratios is critical to disentangle the parameter degeneracy and deriving reliable outflow velocities of the X-ray absorbers. The dip structure appears only when the spectral variation is caused by a change in the clumpy absorbers, and their parameters (N_{H} and ξ) are within a specific range. If all of these requirements are met, we can constrain not only N_{H} and ξ but also the clump velocities.

For all the sources where the dip structure was found, the spectral ratios were explained with clumpy absorbers with constant ξ and N_{H} . As the X-ray flux increases, the partial covering fraction decreases and the intrinsic X-ray intensity increases. We found that *the clumpy absorbers have unexpectedly fast outflow velocities*. Furthermore, *the clump velocity gets higher with increasing X-ray flux*, which was also confirmed by a model-independent study of IRAS 13224–3809.

Based on the MCMC parameter estimation, we confirmed that the outflow velocity is determined independently, not correlated with other parameters. Assuming that mass of the outflowing gas is constant, the flux dependence of the outflow velocity suggests that both the UFOs and clumps are radiatively driven and have the same origin, which is consistent with the “hot inner and clumpy outer wind model” proposed by previous studies.

Our proposed outflowing clumpy model shows a plausible explanation of the energy spectra. Previous spectral studies of IRAS 13224–3809 and 1H 0707–495 based on conventional models required a strong unexplained absorption edge around 1 keV. Our model explains this residual without such an inexplicable edge, that the residual feature is caused by the blueshift of the outflowing clumpy absorbers.

Based on the comparison of UFO velocities and clump velocities, *we found that the clump velocity appears faster than the UFO velocities or comparable to the fastest components of UFOs*. Given the assumption that the UV–X-ray flux variation contributes directly to the increase in the kinetic energy of the disk wind, thus the UFOs are considered to be driven by the UV-dominant continuum radiation, but the clumpy absorbers may not be explained only by the continuum-driven scenario. This study, for the first

time, proposes the possibility that *the line-driven scenario may contribute to the acceleration of the clumpy absorbers.*

According to the previous simulation, radiation hydrodynamic instability works at a certain opacity (i.e., a certain ξ) to generate gas clumps, so the constant ξ ($\log \xi \sim 2.7 \pm 0.3$) determined by the ratio fitting is consistent with the instability scenario. The invariance of ξ , however, may be due to observational bias, since the range of ξ corresponds to where the dip/cliff structure appears.

Our analysis probed the outflowing velocity of X-ray absorbers and their physical origins, but our results remain uncertain of the UFO velocities with current instruments. Future X-ray observatories such as *XRISM* and *Athena* will enable us to provide extremely high-resolution spectroscopy up to a higher energy band than that of *XMM-Newton*. Such high-quality data will precisely determine the UFO velocities and confirm whether the clump velocity is comparable to or even faster than the UFO velocity. If the clumps are accelerated by the line force as suggested in the present study, it is considered that more momentum and/or energy are transported to the interstellar medium of host galaxies than those estimated only from the UFO velocity. Therefore, the present study is expected to be a stepping stone toward a better understanding of the energy transport from the AGN innermost region to the host galaxy and the co-evolution of SMBHs and host galaxies.

Appendix A

Appendix A

A.1 Additional plots

Additional plots are given in Appendix A.

A.1.1 Spectral-ratio model fitting

Mrk335

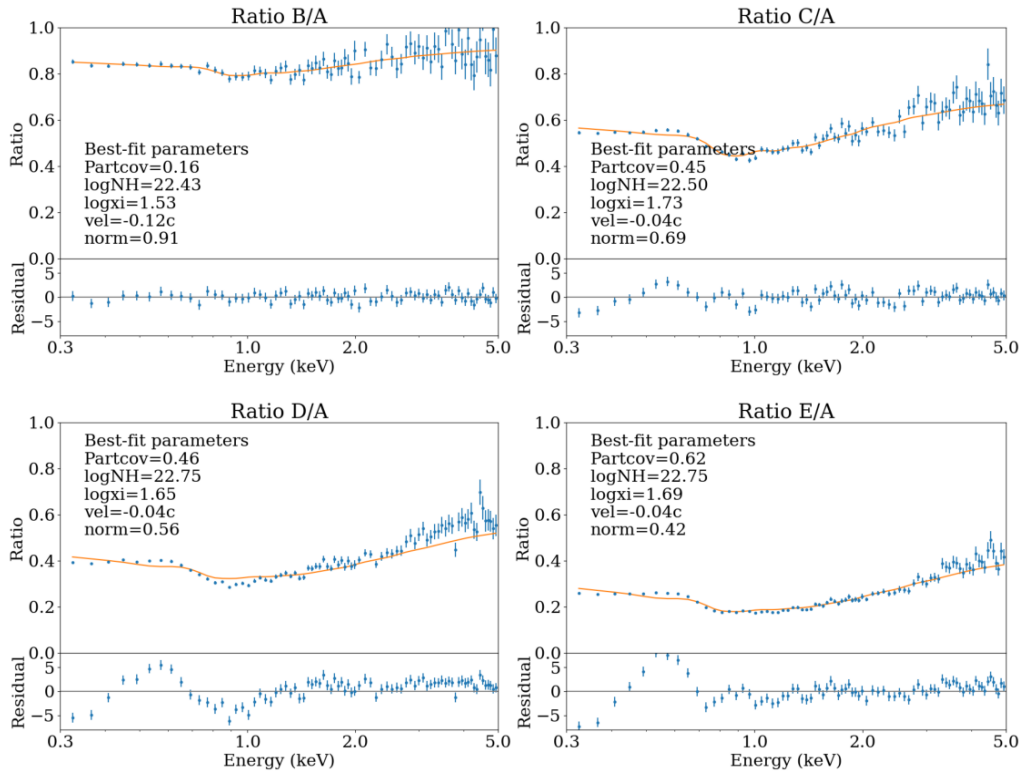


FIGURE A.1: The same as Figure 3.10, but for Mrk 335.

Mrk766

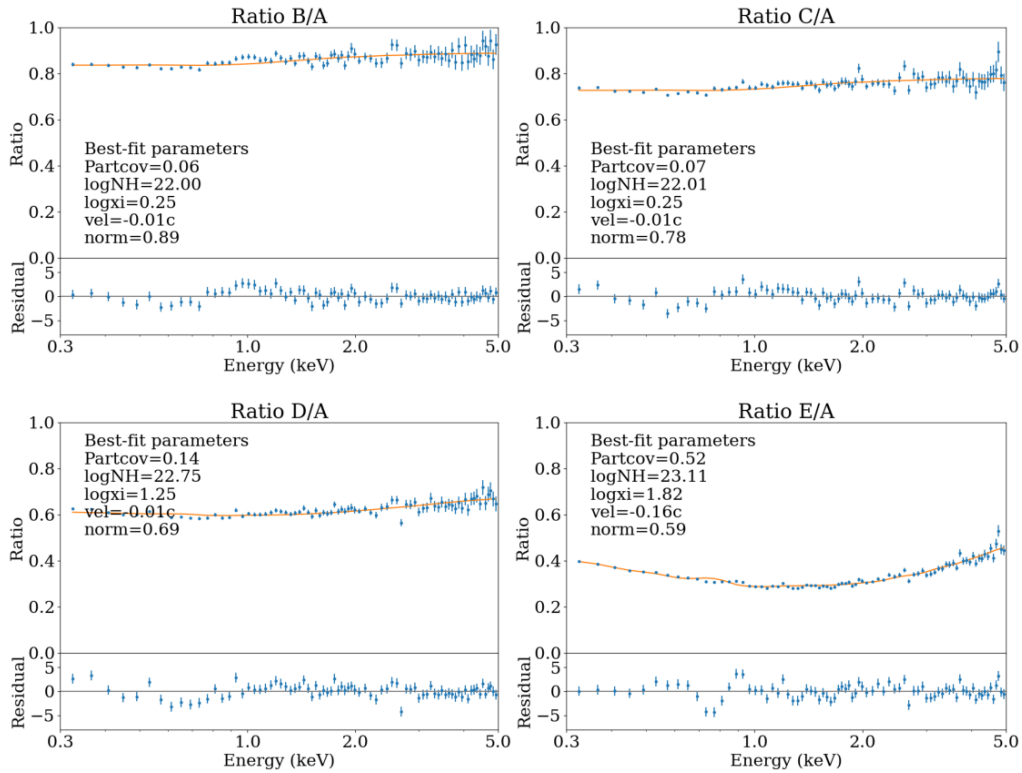


FIGURE A.2: The same as Figure 3.10, but for Mrk 766.

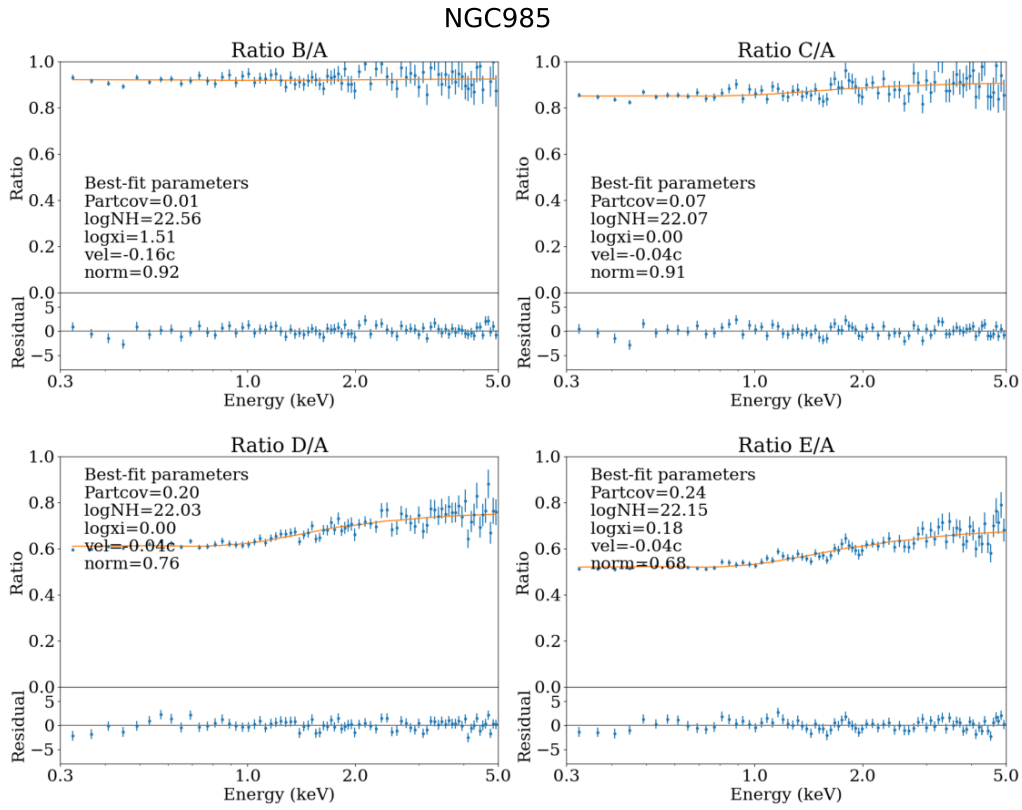


FIGURE A.3: The same as Figure 3.10, but for NGC 985.

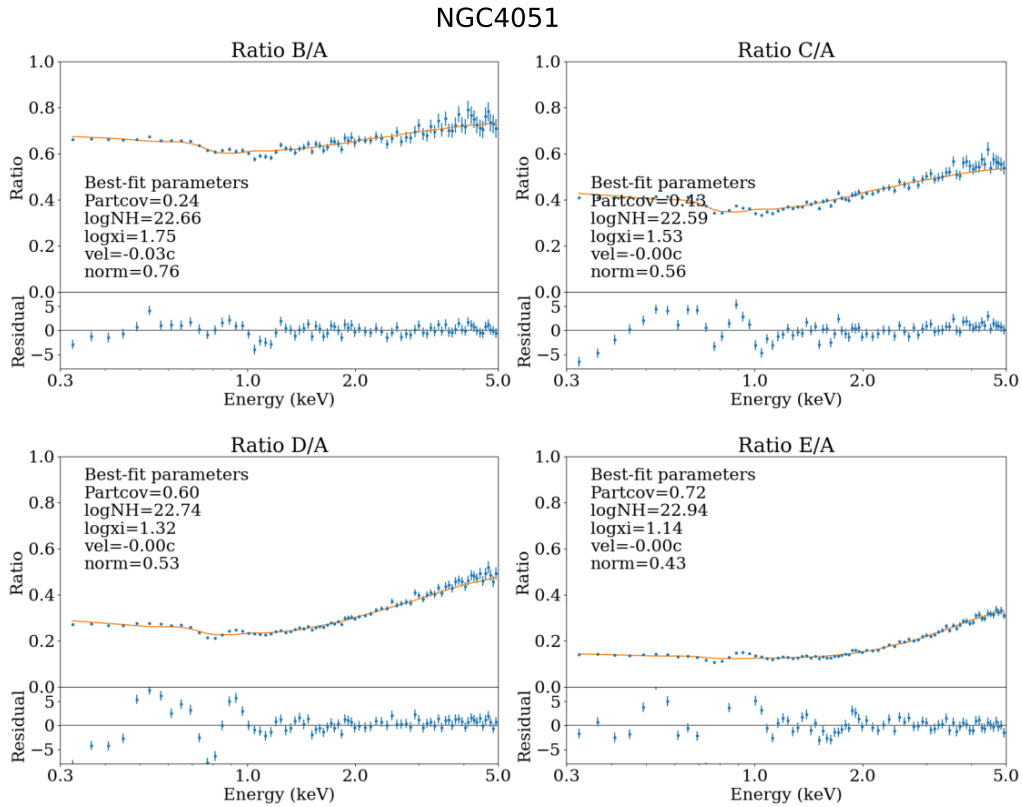


FIGURE A.4: The same as Figure 3.10, but for NGC 4051.

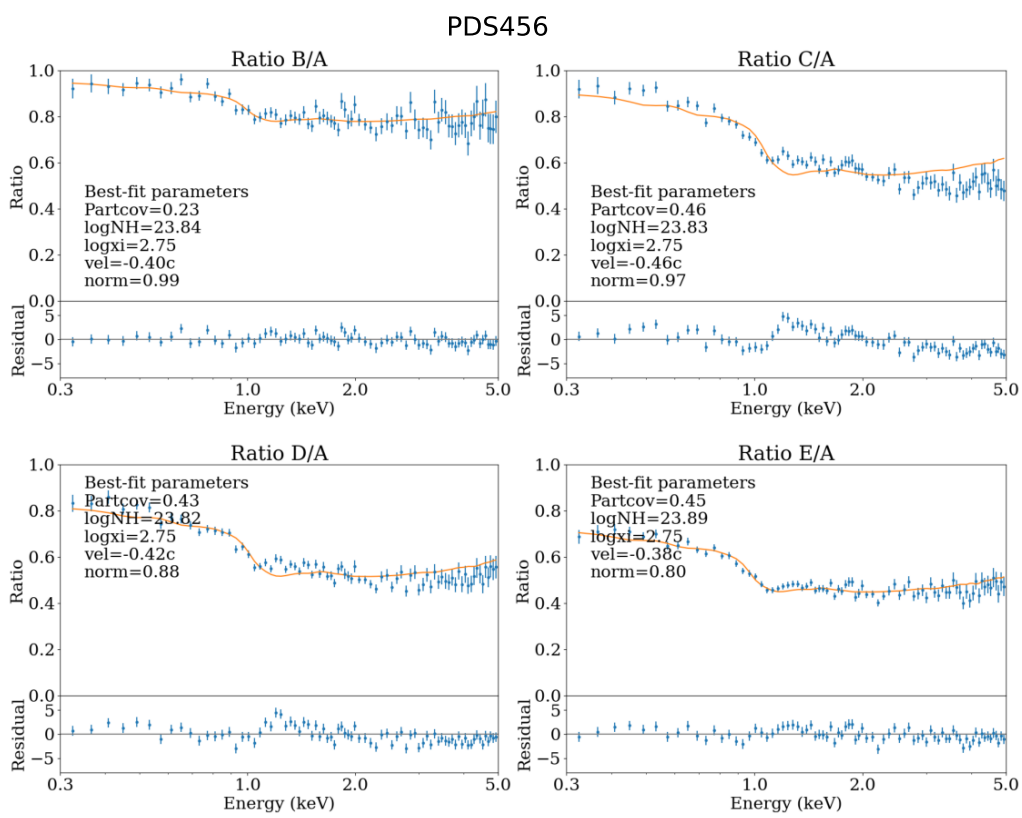


FIGURE A.5: The same as Figure 3.10, but for PDS 456.

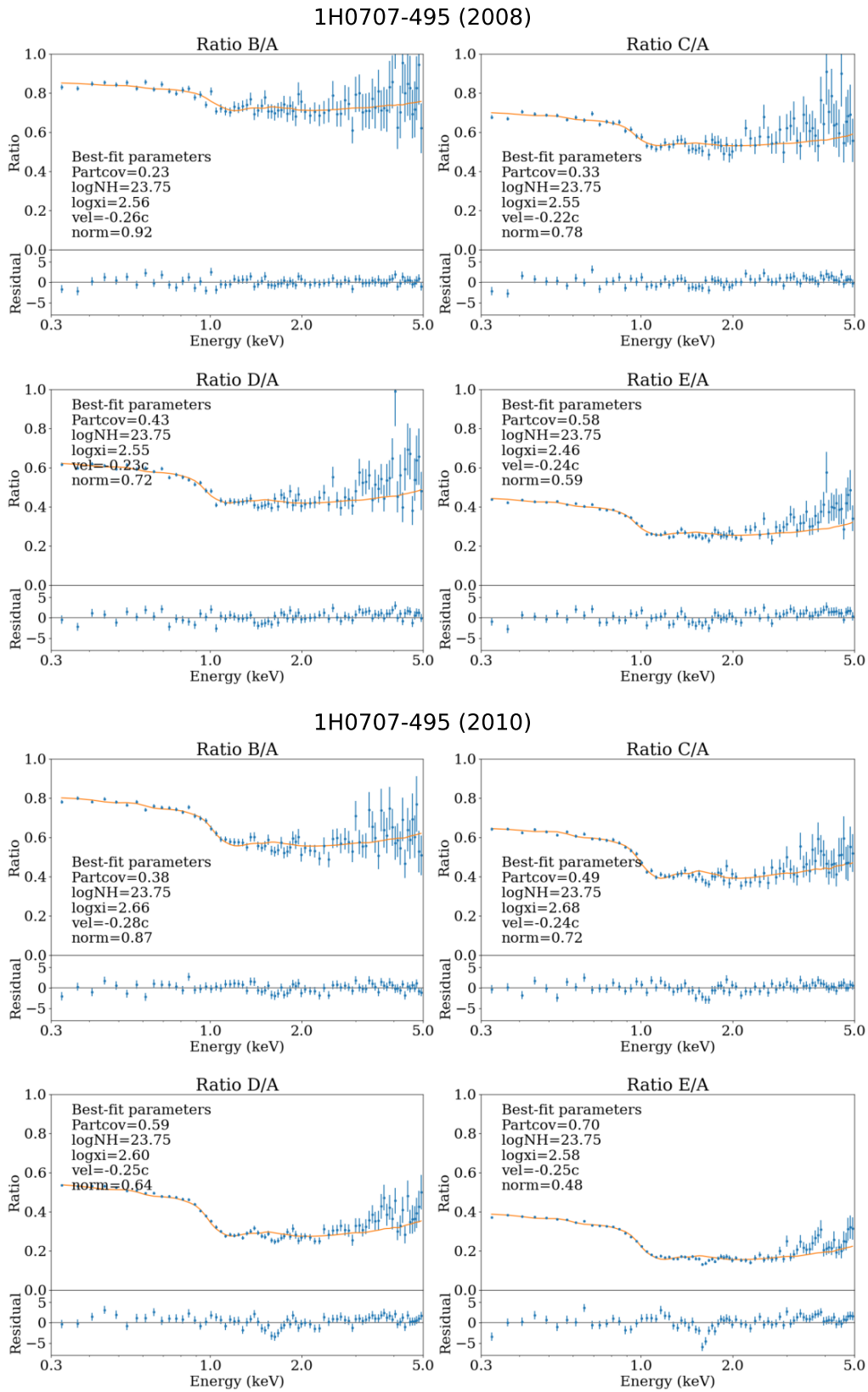


FIGURE A.6: The same as Figure 3.10, but for 1H 0707–495 in two periods.

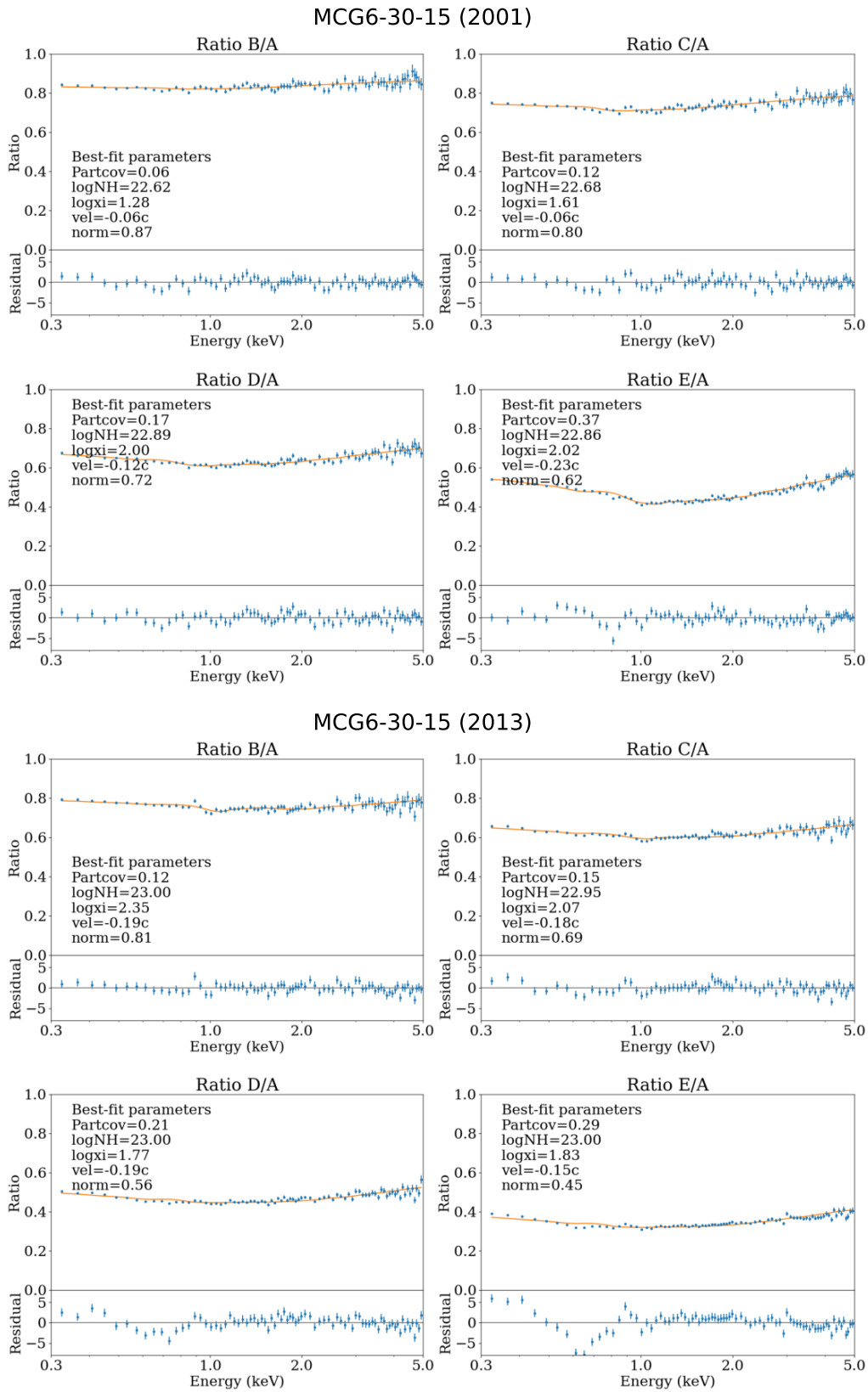


FIGURE A.7: The same as Figure 3.10, but for MCG-6-30-15 in two periods.

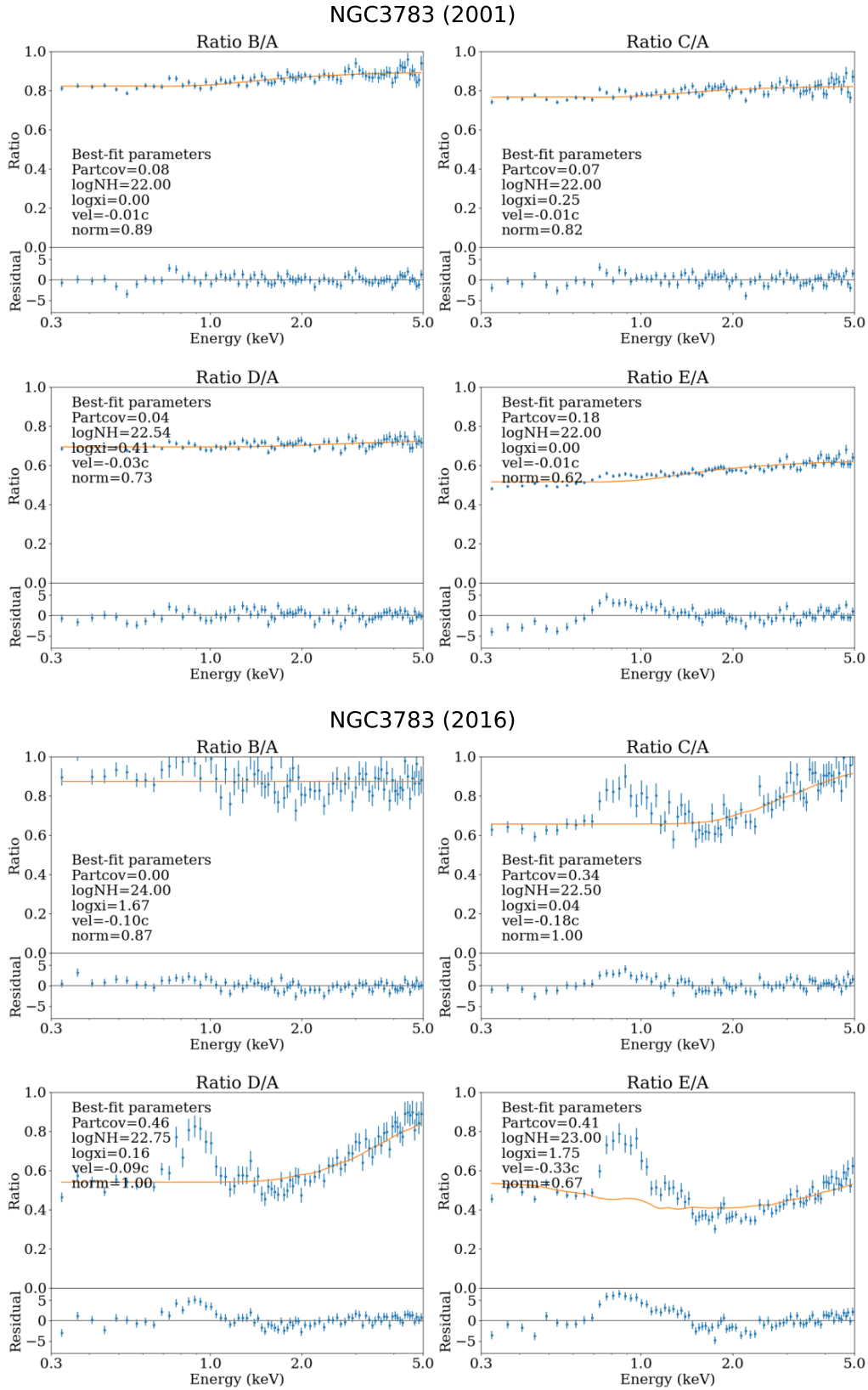


FIGURE A.8: The same as Figure 3.10, but for NGC 3783 in two periods.

A.1.2 Simultaneous spectral-ratio model fitting with MCMC

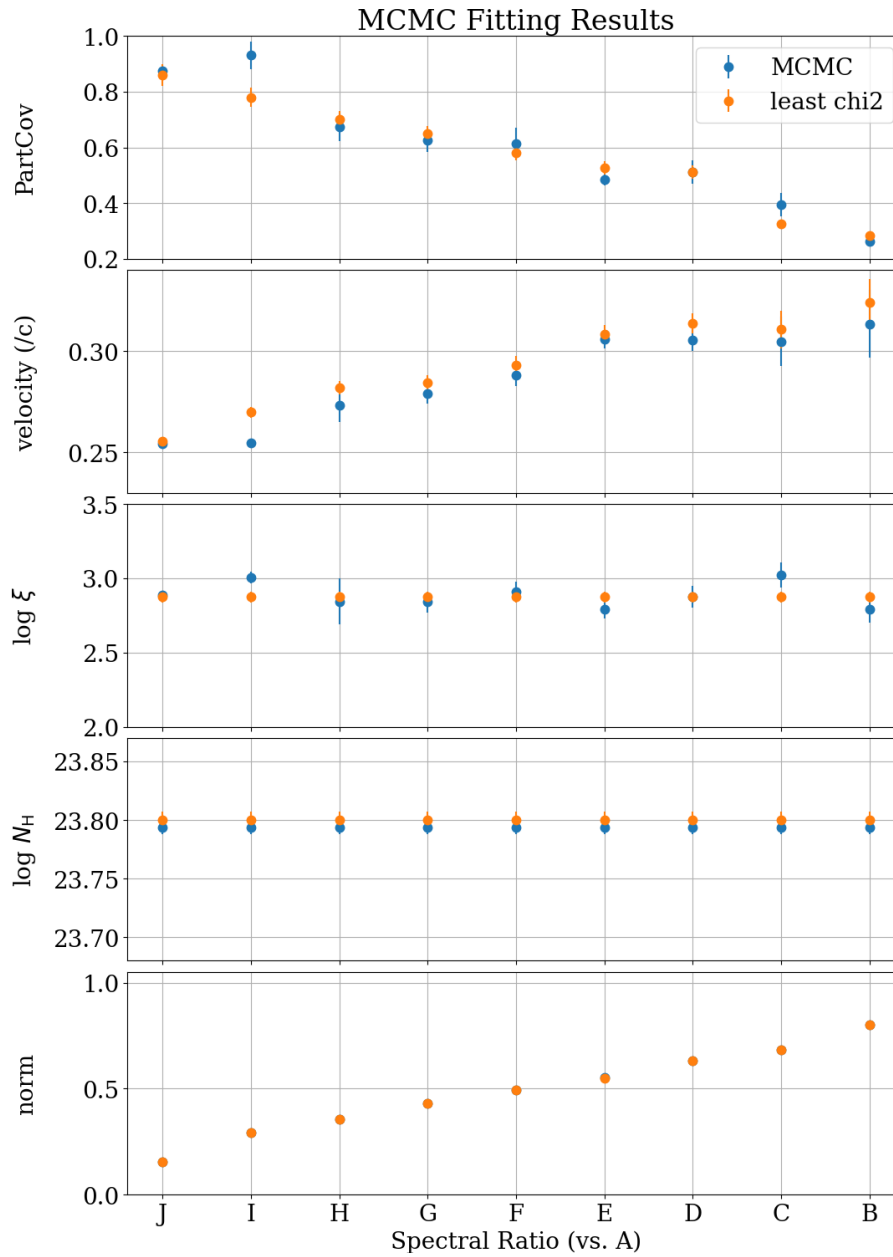


FIGURE A.9: Best-fit parameters of IRAS 13224–3809 determined by the simultaneous least chi-square fitting (in orange) and MCMC estimation (in blue) to the nine intensity-sliced spectral ratios.

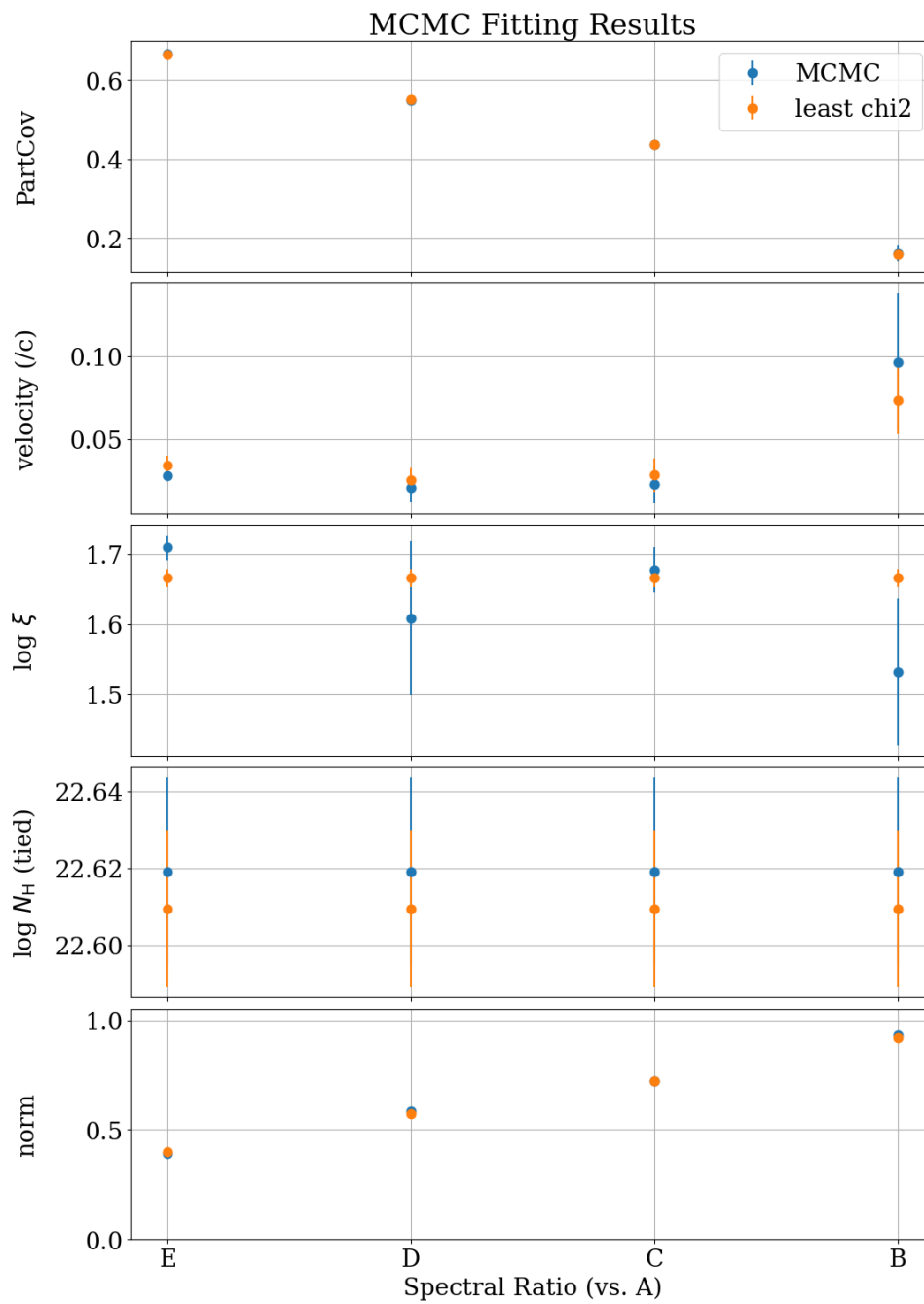


FIGURE A.10: The same as Figure A.9, but for Mrk 335.

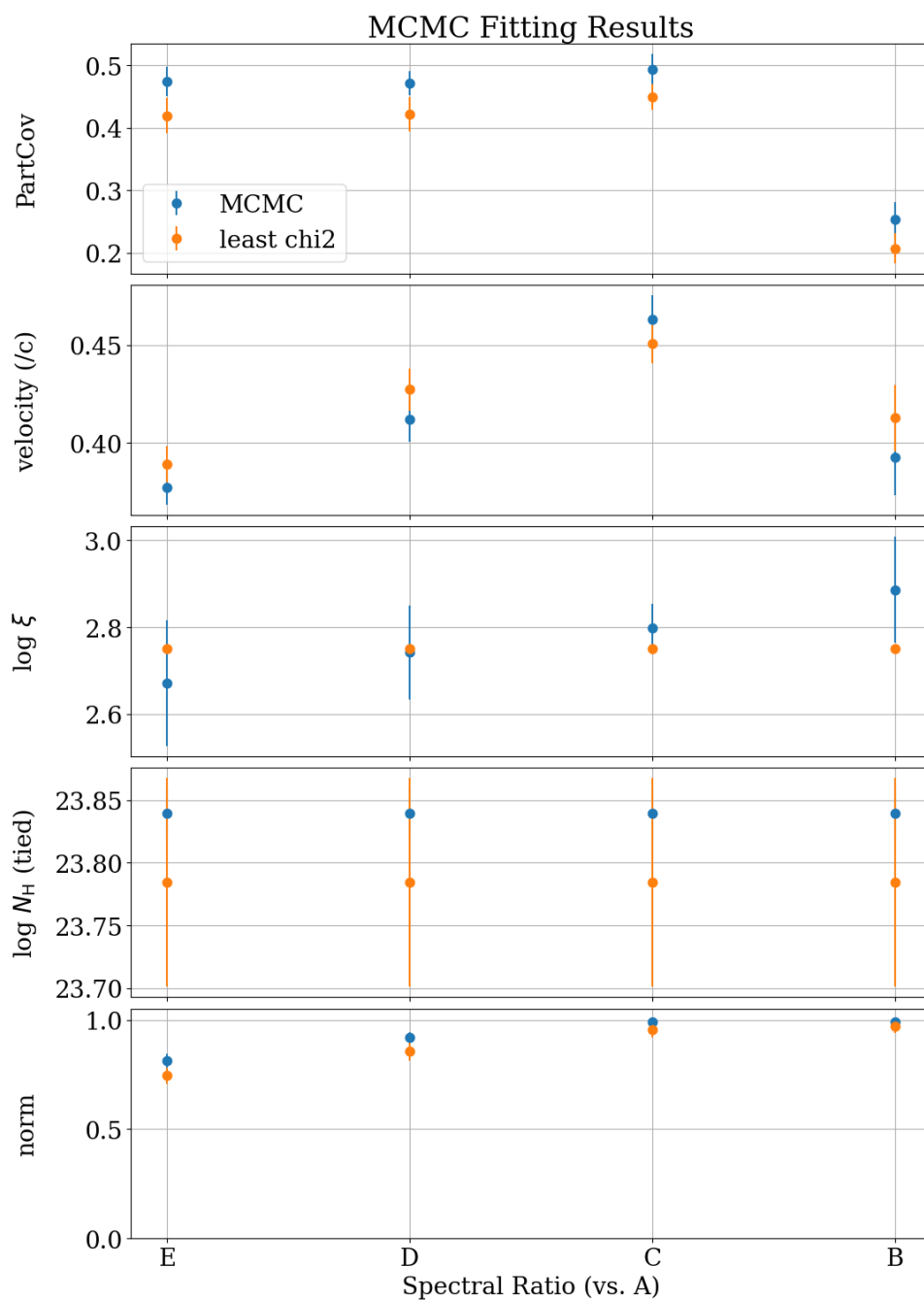


FIGURE A.11: The same as Figure A.9, but for PDS 456.

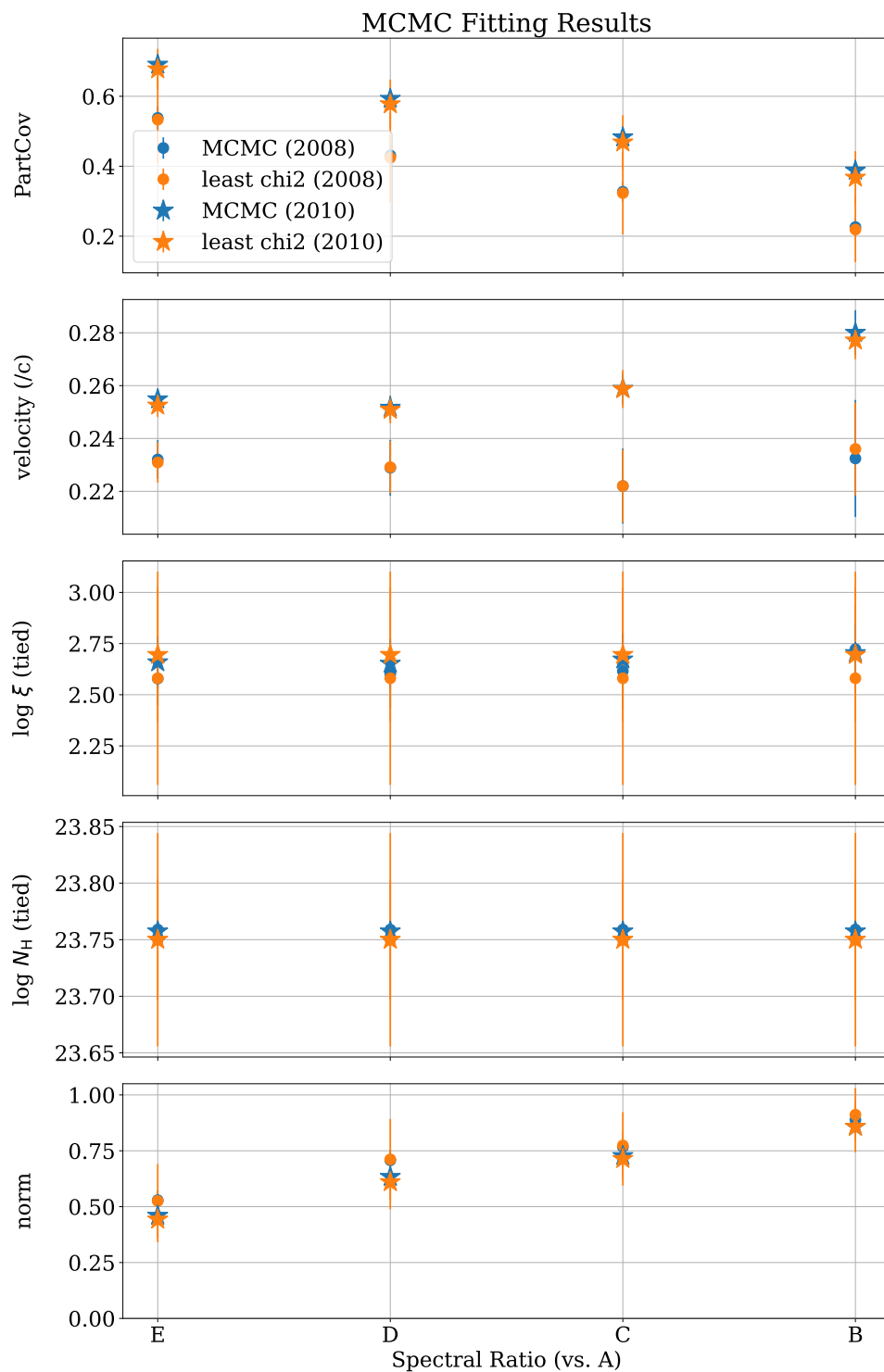


FIGURE A.12: The same as Figure A.9, but for 1H 0707–495. The circle and star markers indicate results in 2008 and 2010, respectively.

Bibliography

- Abramowicz, M. A. et al. (1988). “Slim Accretion Disks”. In: *The Astrophysical Journal* 332, p. 646. DOI: [10.1086/166683](https://doi.org/10.1086/166683).
- Antonucci, R. R. J. and J. S. Miller (1985). “Spectropolarimetry and the Nature of NGC 1068”. In: *The Astrophysical Journal* 297, pp. 621–632. DOI: [10.1086/163559](https://doi.org/10.1086/163559).
- Antonucci, R. (1993). “Unified Models for Active Galactic Nuclei and Quasars”. In: *Annual Review of Astronomy and Astrophysics* 31, pp. 473–521. DOI: [10.1146/annurev.aa.31.090193.002353](https://doi.org/10.1146/annurev.aa.31.090193.002353).
- Arav, N. et al. (2015). “Anatomy of the AGN in NGC 5548. II. The Spatial, Temporal, and Physical Nature of the Outflow from HST/COS Observations”. In: *Astronomy and Astrophysics* 577, A37. DOI: [10.1051/0004-6361/201425302](https://doi.org/10.1051/0004-6361/201425302).
- Arnaud, K. A. (1996). “XSPEC: The First Ten Years”. In: *Astronomical Data Analysis Software and Systems* 101, p. 17.
- Bambynek, W. et al. (1972). “X-Ray Fluorescence Yields, Auger, and Coster-Kronig Transition Probabilities”. In: *Reviews of Modern Physics* 44.4, pp. 716–813. DOI: [10.1103/RevModPhys.44.716](https://doi.org/10.1103/RevModPhys.44.716).
- Beckmann, V. and C. R. Shrader (2012). *Active Galactic Nuclei*.
- Begelman, M. C., C. F. McKee, and G. A. Shields (1983). “Compton Heated Winds and Coronae above Accretion Disks. I. Dynamics.” In: *The Astrophysical Journal* 271, pp. 70–88. DOI: [10.1086/161178](https://doi.org/10.1086/161178).
- Bekhti, N. B. et al. (2016). “HI4PI: A Full-Sky H I Survey Based on EBHIS and GASS”. In: *Astronomy & Astrophysics* 594, A116. DOI: [10.1051/0004-6361/201629178](https://doi.org/10.1051/0004-6361/201629178).
- Bentz, M. C. and S. Katz (2015). “The AGN Black Hole Mass Database”. In: *Publications of the Astronomical Society of the Pacific* 127, p. 67. DOI: [10.1086/679601](https://doi.org/10.1086/679601).
- Bennett, A. S. (1962). “The Revised 3C Catalogue of Radio Sources.” In: *Memoirs of the Royal Astronomical Society* 68, p. 163.
- Blandford, R. D. and D. G. Payne (1982). “Hydromagnetic Flows from Accretion Disks and the Production of Radio Jets.” In: *Monthly Notices of the Royal Astronomical Society* 199, pp. 883–903. DOI: [10.1093/mnras/199.4.883](https://doi.org/10.1093/mnras/199.4.883).
- Bohlin, R. C., B. D. Savage, and J. F. Drake (1978). “A Survey of Interstellar H I from Lambda Absorption Measurements. II.” In: *The Astrophysical Journal* 224, pp. 132–142. DOI: [10.1086/156357](https://doi.org/10.1086/156357).
- Bolton, J. G., G. J. Stanley, and O. B. Slee (1949). “Positions of Three Discrete Sources of Galactic Radio-Frequency Radiation”. In: *Nature* 164.4159, pp. 101–102. DOI: [10.1038/164101b0](https://doi.org/10.1038/164101b0).
- Boller, T., W. N. Brandt, and H. Fink (1996). “Soft X-ray Properties of Narrow-Line Seyfert 1 Galaxies.” In: *Astronomy and Astrophysics* 305, p. 53.
- Brandt, W. N., S. Mathur, and M. Elvis (1997). “A Comparison of the Hard ASCA Spectral Slopes of Broad- and Narrow-Line Seyfert 1 Galaxies”. In: *Monthly Notices of the Royal Astronomical Society* 285, pp. L25–L30. DOI: [10.1093/mnras/285.3.L25](https://doi.org/10.1093/mnras/285.3.L25).

- Cardelli, J. A., G. C. Clayton, and J. S. Mathis (1989). “The Relationship between Infrared, Optical, and Ultraviolet Extinction”. In: *The Astrophysical Journal* 345, p. 245. DOI: [10.1086/167900](https://doi.org/10.1086/167900).
- Castelló-Mor, N., H. Netzer, and S. Kaspi (2016). “Super- and Sub-Eddington Accreting Massive Black Holes: A Comparison of Slim and Thin Accretion Discs through Study of the Spectral Energy Distribution”. In: *Monthly Notices of the Royal Astronomical Society* 458.2, pp. 1839–1858. DOI: [10.1093/mnras/stw445](https://doi.org/10.1093/mnras/stw445).
- Chartas, G. and M. H. Canas (2018). “The Variable Relativistic Outflow of IRAS 13224-3809”. In: *The Astrophysical Journal* 867, p. 103. DOI: [10.3847/1538-4357/aae438](https://doi.org/10.3847/1538-4357/aae438).
- Chiang, C.-Y. et al. (2015). “Modelling the Extreme X-ray Spectrum of IRAS 13224-3809”. In: *Monthly Notices of the Royal Astronomical Society* 446, pp. 759–769. DOI: [10.1093/mnras/stu2087](https://doi.org/10.1093/mnras/stu2087).
- Crenshaw, D. M. et al. (2003). “Simultaneous Ultraviolet and X-Ray Spectroscopy of the Seyfert 1 Galaxy NGC 5548. I. Physical Conditions in the Ultraviolet Absorbers”. In: *The Astrophysical Journal* 594, pp. 116–127. DOI: [10.1086/376792](https://doi.org/10.1086/376792).
- Dannen, R. C. et al. (2020). “Clumpy AGN Outflows Due to Thermal Instability”. In: *The Astrophysical Journal* 893.2, p. L34. DOI: [10.3847/2041-8213/ab87a5](https://doi.org/10.3847/2041-8213/ab87a5).
- Dasyra, K. M. et al. (2007). “Host Dynamics and Origin of Palomar-Green QSOs”. In: *The Astrophysical Journal* 657, pp. 102–115. DOI: [10.1086/510552](https://doi.org/10.1086/510552).
- den Herder, J. W. et al. (2001). “The Reflection Grating Spectrometer on Board XMM-Newton”. In: *Astronomy & Astrophysics* 365.1, pp. L7–L17. DOI: [10.1051/0004-6361:20000058](https://doi.org/10.1051/0004-6361:20000058).
- Di Gesu, L. et al. (2015). “Anatomy of the AGN in NGC 5548. IV. The Short-Term Variability of the Outflows”. In: *Astronomy and Astrophysics* 579, A42. DOI: [10.1051/0004-6361/201525934](https://doi.org/10.1051/0004-6361/201525934).
- Done, C., M. Gierliński, and A. Kubota (2007). “Modelling the Behaviour of Accretion Flows in X-ray Binaries”. In: *The Astronomy and Astrophysics Review* 15.1, pp. 1–66. DOI: [10.1007/s00159-007-0006-1](https://doi.org/10.1007/s00159-007-0006-1).
- Done, C. et al. (2012). “Intrinsic Disc Emission and the Soft X-ray Excess in Active Galactic Nuclei”. In: *Monthly Notices of the Royal Astronomical Society* 420.3, pp. 1848–1860. DOI: [10.1111/j.1365-2966.2011.19779.x](https://doi.org/10.1111/j.1365-2966.2011.19779.x).
- Done, C. and C. Jin (2016). “The Mass and Spin of the Extreme Narrow Line Seyfert 1 Galaxy 1H 0707-495 and Its Implications for the Trigger for Relativistic Jets”. In: *Monthly Notices of the Royal Astronomical Society* 460.2, pp. 1716–1724. DOI: [10.1093/mnras/stw1070](https://doi.org/10.1093/mnras/stw1070).
- Dorodnitsyn, A., T. Kallman, and D. Proga (2008). “An Axisymmetric, Hydrodynamical Model for the Torus Wind in Active Galactic Nuclei. II. X-Ray-Excited Funnel Flow”. In: *The Astrophysical Journal* 687, pp. 97–110. DOI: [10.1086/591418](https://doi.org/10.1086/591418).
- Dwelly, T. and M. J. Page (2006). “The Distribution of Absorption in AGN Detected in the XMM-Newton Observations of the CDFS”. In: *Monthly Notices of the Royal Astronomical Society* 372.4, pp. 1755–1775. DOI: [10.1111/j.1365-2966.2006.10979.x](https://doi.org/10.1111/j.1365-2966.2006.10979.x).
- Ebisawa, K. (2006). *Lecture notes in the University of Tokyo*. URL: <https://www.isas.jaxa.jp/home/ebisawalab/ebisawa/TEACHING/note2006.pdf>.
- Elvis, M. et al. (1978). “Seyfert Galaxies as X-ray Sources.” In: *Monthly Notices of the Royal Astronomical Society* 183, pp. 129–157. DOI: [10.1093/mnras/183.2.129](https://doi.org/10.1093/mnras/183.2.129).

- Emmanoulopoulos, D. et al. (2014). “General Relativistic Modelling of the Negative Reverberation X-ray Time Delays in AGN”. In: *Monthly Notices of the Royal Astronomical Society* 439, pp. 3931–3950. DOI: [10.1093/mnras/stu249](https://doi.org/10.1093/mnras/stu249).
- Fabian, A. C. et al. (2009). “Broad Line Emission from Iron K- and L-shell Transitions in the Active Galaxy 1H 0707-495”. In: *Nature* 459.7246, pp. 540–542. DOI: [10.1038/nature08007](https://doi.org/10.1038/nature08007).
- Fabian, A. C. et al. (2013). “Long XMM Observation of the Narrow-Line Seyfert 1 Galaxy IRAS 13224-3809: Rapid Variability, High Spin and a Soft Lag”. In: *Monthly Notices of the Royal Astronomical Society* 429.4, pp. 2917–2923. DOI: [10.1093/mnras/sts504](https://doi.org/10.1093/mnras/sts504).
- Fabian, A. C. et al. (2015). “Properties of AGN Coronae in the NuSTAR Era”. In: *Monthly Notices of the Royal Astronomical Society* 451, pp. 4375–4383. DOI: [10.1093/mnras/stv1218](https://doi.org/10.1093/mnras/stv1218).
- Fabian, A. C. et al. (1989). “X-Ray Fluorescence from the Inner Disc in Cygnus X-1.” In: *Monthly Notices of the Royal Astronomical Society* 238, pp. 729–736. DOI: [10.1093/mnras/238.3.729](https://doi.org/10.1093/mnras/238.3.729).
- Fabian, A. C. (2012). “Observational Evidence of Active Galactic Nuclei Feedback”. In: *Annual Review of Astronomy and Astrophysics* 50, pp. 455–489. DOI: [10.1146/annurev-astro-081811-125521](https://doi.org/10.1146/annurev-astro-081811-125521).
- Fath, E. A. (1909). “The Spectra of Some Spiral Nebulae and Globular Star Clusters”. In: *Lick Observatory Bulletin* 149, pp. 71–77. DOI: [10.5479/ADS/bib/1909LicOB.5.71F](https://doi.org/10.5479/ADS/bib/1909LicOB.5.71F).
- Faucher-Giguère, C.-A. and E. Quataert (2012). “The Physics of Galactic Winds Driven by Active Galactic Nuclei”. In: *Monthly Notices of the Royal Astronomical Society* 425.1, pp. 605–622. DOI: [10.1111/j.1365-2966.2012.21512.x](https://doi.org/10.1111/j.1365-2966.2012.21512.x).
- Foreman-Mackey, D. et al. (2013). “Emcee: The MCMC Hammer”. In: *Publications of the Astronomical Society of the Pacific* 125, p. 306. DOI: [10.1086/670067](https://doi.org/10.1086/670067).
- Fukumura, K. et al. (2010). “MAGNETOHYDRODYNAMIC ACCRETION DISK WINDS AS X-RAY ABSORBERS IN ACTIVE GALACTIC NUCLEI”. In: *The Astrophysical Journal* 715.1, p. 636. DOI: [10.1088/0004-637X/715/1/636](https://doi.org/10.1088/0004-637X/715/1/636).
- Fukumura, K. et al. (2022). *Tell-Tale Spectral Signatures of MHD-driven Ultra-Fast Outflows in AGNs*. arXiv: [2205.08894 \[astro-ph\]](https://arxiv.org/abs/2205.08894).
- Gabriel, C. et al. (2004). “The XMM-Newton SAS - Distributed Development and Maintenance of a Large Science Analysis System: A Critical Analysis”. In: 314, p. 759.
- Gallo, L. C. et al. (2019). “Evidence for an Emerging Disc Wind and Collimated Outflow during an X-ray Flare in the Narrow-Line Seyfert 1 Galaxy Mrk 335”. In: *Monthly Notices of the Royal Astronomical Society* 484, pp. 4287–4297. DOI: [10.1093/mnras/stz274](https://doi.org/10.1093/mnras/stz274).
- Gandhi, P. et al. (2022). “Frontiers in Accretion Physics at High X-ray Spectral Resolution”. In: *Nature Astronomy* 6.12, pp. 1364–1375. DOI: [10.1038/s41550-022-01857-y](https://doi.org/10.1038/s41550-022-01857-y).
- Giustini, M. et al. (2011). “Variable X-ray Absorption in the Mini-BAL QSO PG 1126-041”. In: *Astronomy & Astrophysics* 536, A49. DOI: [10.1051/0004-6361/201117732](https://doi.org/10.1051/0004-6361/201117732).
- Goodrich, R. W. (1989). “Spectropolarimetry of “Narrow-Line” Seyfert 1 Galaxies”. In: *The Astrophysical Journal* 342, p. 224. DOI: [10.1086/167586](https://doi.org/10.1086/167586).
- GRAVITY Collaboration et al. (2022). *Towards measuring supermassive black hole masses with interferometric observations of the dust continuum*. DOI: [10.48550/ARXIV.2209.14410](https://doi.org/10.48550/ARXIV.2209.14410).

- Greenstein, J. L. and T. A. Matthews (1963). “Red-Shift of the Unusual Radio Source: 3C 48”. In: *Nature* 197.4872, pp. 1041–1042. DOI: [10.1038/1971041a0](https://doi.org/10.1038/1971041a0).
- Grupe, D. et al. (2004). “A Complete Sample of Soft X-Ray-selected AGNs. I. The Data*”. In: *The Astronomical Journal* 127.1, p. 156. DOI: [10.1086/380233](https://doi.org/10.1086/380233).
- Hagino, K. et al. (2015). “The Origin of Ultrafast Outflows in AGN: Monte Carlo Simulations of the Wind in PDS 456”. In: *Monthly Notices of the Royal Astronomical Society* 446, pp. 663–676. DOI: [10.1093/mnras/stu2095](https://doi.org/10.1093/mnras/stu2095).
- Hopkins, P. F. and M. Elvis (2010). “Quasar Feedback: More Bang for Your Buck”. In: *Monthly Notices of the Royal Astronomical Society* 401.1, pp. 7–14. DOI: [10.1111/j.1365-2966.2009.15643.x](https://doi.org/10.1111/j.1365-2966.2009.15643.x).
- Hubble, E. P. (1926). “Extragalactic Nebulae.” In: *The Astrophysical Journal* 64, pp. 321–369. DOI: [10.1086/143018](https://doi.org/10.1086/143018).
- Igo, Z. et al. (2020). “Searching for Ultra-Fast Outflows in AGN Using Variability Spectra”. In: *Monthly Notices of the Royal Astronomical Society* 493.1, pp. 1088–1108. DOI: [10.1093/mnras/staa265](https://doi.org/10.1093/mnras/staa265).
- Iso, N. et al. (2016). “Origin of the Broad Iron Line Feature and the Soft X-ray Variation in Seyfert Galaxies”. In: *Publications of the Astronomical Society of Japan* 68.SP1, S27. DOI: [10.1093/pasj/psw015](https://doi.org/10.1093/pasj/psw015).
- Jansen, F. et al. (2001). “XMM-Newton Observatory: I. The Spacecraft and Operations”. In: *Astronomy & Astrophysics* 365.1, pp. L1–L6. DOI: [10.1051/0004-6361:20000036](https://doi.org/10.1051/0004-6361:20000036).
- Kaastra, J. S. et al. (2014). “A Fast and Long-Lived Outflow from the Supermassive Black Hole in NGC 5548”. In: *Science* 345, pp. 64–68. DOI: [10.1126/science.1253787](https://doi.org/10.1126/science.1253787).
- Kallman, T. and M. Bautista (2001). “Photoionization and High-Density Gas”. In: *The Astrophysical Journal Supplement Series* 133.1, p. 221. DOI: [10.1086/319184](https://doi.org/10.1086/319184).
- Kallman, T. R. et al. (2004). “Photoionization Modeling and the K Lines of Iron”. In: *The Astrophysical Journal Supplement Series* 155, pp. 675–701. DOI: [10.1086/424039](https://doi.org/10.1086/424039).
- Khachikian, E. Y. and D. W. Weedman (1974). “An Atlas of Seyfert Galaxies.” In: *The Astrophysical Journal* 192, pp. 581–589. DOI: [10.1086/153093](https://doi.org/10.1086/153093).
- King, A. and K. Pounds (2015). “Powerful Outflows and Feedback from Active Galactic Nuclei”. In: *Annual Review of Astronomy and Astrophysics* 53, pp. 115–154. DOI: [10.1146/annurev-astro-082214-122316](https://doi.org/10.1146/annurev-astro-082214-122316).
- King, A. (2010). “Black Hole Outflows”. In: *Monthly Notices of the Royal Astronomical Society* 402.3, pp. 1516–1522. DOI: [10.1111/j.1365-2966.2009.16013.x](https://doi.org/10.1111/j.1365-2966.2009.16013.x).
- Kitaki, T. et al. (2021). “The Origins and Impact of Outflow from Super-Eddington Flow”. In: *Publications of the Astronomical Society of Japan* 73.2, pp. 450–466. DOI: [10.1093/pasj/psab011](https://doi.org/10.1093/pasj/psab011).
- Kobayashi, H. et al. (2018). “Three-Dimensional Structure of Clumpy Outflow from Supercritical Accretion Flow onto Black Holes”. In: *Publications of the Astronomical Society of Japan* 70, p. 22. DOI: [10.1093/pasj/psx157](https://doi.org/10.1093/pasj/psx157).
- Kormendy, J. and L. C. Ho (2013). “Coevolution (Or Not) of Supermassive Black Holes and Host Galaxies”. In: *Annual Review of Astronomy and Astrophysics* 51.1, pp. 511–653. DOI: [10.1146/annurev-astro-082708-101811](https://doi.org/10.1146/annurev-astro-082708-101811).
- Kormendy, J. and D. Richstone (1995). “Inward Bound—The Search For Supermassive Black Holes In Galactic Nuclei”. In: *Annual Review of Astronomy and Astrophysics* 33, p. 581. DOI: [10.1146/annurev.aa.33.090195.003053](https://doi.org/10.1146/annurev.aa.33.090195.003053).

- Krawczynski, H. et al. (2022). “Polarized X-Rays Constrain the Disk-Jet Geometry in the Black Hole x-Ray Binary Cygnus X-1”. In: *Science*. DOI: [10.1126/science.add5399](https://doi.org/10.1126/science.add5399).
- Krolik, J. H. and G. A. Kriss (2001). “Warm Absorbers in Active Galactic Nuclei: A Multitemperature Wind”. In: *The Astrophysical Journal* 561.2, p. 684. DOI: [10.1086/323442](https://doi.org/10.1086/323442).
- Krolik, J. H., C. F. McKee, and C. B. Tarter (1981). “Two-Phase Models of Quasar Emission Line Regions.” In: *The Astrophysical Journal* 249, pp. 422–442. DOI: [10.1086/159303](https://doi.org/10.1086/159303).
- Krolik, J. H. and G. A. Kriss (1995). “Observable Properties of X-Ray-heated Winds in Active Galactic Nuclei: Warm Reflectors and Warm Absorbers”. In: *The Astrophysical Journal* 447, p. 512. DOI: [10.1086/175896](https://doi.org/10.1086/175896).
- Kubota, A. and C. Done (2019). “Modelling the Spectral Energy Distribution of Super-Eddington Quasars”. In: *Monthly Notices of the Royal Astronomical Society* 489.1, pp. 524–533. DOI: [10.1093/mnras/stz2140](https://doi.org/10.1093/mnras/stz2140).
- Kylafis, N. D. et al. (2008). “A Jet Model for Galactic Black-Hole X-ray Sources: Some Constraining Correlations”. In: *Astronomy and Astrophysics* 489.2, pp. 481–487. DOI: [10.1051/0004-6361:20079159](https://doi.org/10.1051/0004-6361:20079159).
- Laha, S. et al. (2014). “Warm Absorbers in X-rays (WAX), a Comprehensive High-Resolution Grating Spectral Study of a Sample of Seyfert Galaxies - I. A Global View and Frequency of Occurrence of Warm Absorbers.” In: *Monthly Notices of the Royal Astronomical Society* 441.3, pp. 2613–2643. DOI: [10.1093/mnras/stu669](https://doi.org/10.1093/mnras/stu669).
- Laha, S. et al. (2021). “Ionized Outflows from Active Galactic Nuclei as the Essential Elements of Feedback”. In: *Nature Astronomy* 5.1, pp. 13–24. DOI: [10.1038/s41550-020-01255-2](https://doi.org/10.1038/s41550-020-01255-2).
- Longair, M. S. (2011). *High Energy Astrophysics*.
- Lynden-Bell, D. (1969). “Galactic Nuclei as Collapsed Old Quasars”. In: *Nature* 223, pp. 690–694. DOI: [10.1038/223690a0](https://doi.org/10.1038/223690a0).
- Magorrian, J. et al. (1998). “The Demography of Massive Dark Objects in Galaxy Centers”. In: *The Astronomical Journal* 115, pp. 2285–2305. DOI: [10.1086/300353](https://doi.org/10.1086/300353).
- Maiolino, R. and G. H. Rieke (1995). “Low-Luminosity and Obscured Seyfert Nuclei in Nearby Galaxies”. In: *The Astrophysical Journal* 454, p. 95. DOI: [10.1086/176468](https://doi.org/10.1086/176468).
- Makishima, K. et al. (1986). “Simultaneous X-ray and Optical Observations of GX 339-4 in an X-ray High State”. In: *The Astrophysical Journal* 308, pp. 635–643. DOI: [10.1086/164534](https://doi.org/10.1086/164534).
- Malzac, J. (2018). “A New Window on Black Hole Accretion”. In: *Nature Astronomy* 2.8, pp. 623–624. DOI: [10.1038/s41550-018-0507-z](https://doi.org/10.1038/s41550-018-0507-z).
- Mao, J. et al. (2019). “Photoionized Emission and Absorption Features in the High-Resolution X-ray Spectra of NGC 3783”. In: *Astronomy and Astrophysics* 621, A99. DOI: [10.1051/0004-6361/201833191](https://doi.org/10.1051/0004-6361/201833191).
- Marco, B. D. et al. (2020). “Incoherent Fast Variability of X-ray Obscurers - The Case of NGC 3783”. In: *Astronomy & Astrophysics* 634, A65. DOI: [10.1051/0004-6361/201936470](https://doi.org/10.1051/0004-6361/201936470).
- Mason, K. O. et al. (2001). “The XMM-Newton Optical/UV Monitor Telescope”. In: *Astronomy & Astrophysics* 365.1, pp. L36–L44. DOI: [10.1051/0004-6361:20000044](https://doi.org/10.1051/0004-6361:20000044).
- Matthews, T. A. and A. R. Sandage (1963). “Optical Identification of 3C 48, 3C 196, and 3C 286 with Stellar Objects.” In: *The Astrophysical Journal* 138, p. 30. DOI: [10.1086/147615](https://doi.org/10.1086/147615).

- Mathur, S. (2000). “Narrow-Line Seyfert 1 Galaxies and the Evolution of Galaxies and Active Galaxies”. In: *Monthly Notices of the Royal Astronomical Society* 314.4, pp. L17–L20. DOI: [10.1046/j.1365-8711.2000.03530.x](https://doi.org/10.1046/j.1365-8711.2000.03530.x).
- McHardy, I. M. (2013). “Short Time-Scale AGN X-ray Variability with EXOSAT: Black Hole Mass and Normalized Variability Amplitude”. In: *Monthly Notices of the Royal Astronomical Society: Letters* 430.1, pp. L49–L53. DOI: [10.1093/mnrasl/sls048](https://doi.org/10.1093/mnrasl/sls048).
- McKernan, B., T. Yaqoob, and C. S. Reynolds (2007). “A Soft X-ray Study of Type I Active Galactic Nuclei Observed with Chandra High-Energy Transmission Grating Spectrometer”. In: *Monthly Notices of the Royal Astronomical Society* 379.4, pp. 1359–1372. DOI: [10.1111/j.1365-2966.2007.11993.x](https://doi.org/10.1111/j.1365-2966.2007.11993.x).
- Mehdipour, M. et al. (2017). “Chasing Obscuration in Type-I AGN: Discovery of an Eclipsing Clumpy Wind at the Outer Broad-Line Region of NGC 3783”. In: *Astronomy and Astrophysics* 607, A28. DOI: [10.1051/0004-6361/201731175](https://doi.org/10.1051/0004-6361/201731175).
- Midooka, T., M. Mizumoto, and K. Ebisawa (2022). *A Novel "Spectral-Ratio Model Fitting" to Resolve Complicated AGN X-ray Spectral Variations*. arXiv: [2210.11746](https://arxiv.org/abs/2210.11746) [astro-ph.HE].
- Midooka, T. et al. (2022). “Simple Interpretation of the Seemingly Complicated X-ray Spectral Variation of NGC 5548”. In: *Monthly Notices of the Royal Astronomical Society*, stac1206. DOI: [10.1093/mnras/stac1206](https://doi.org/10.1093/mnras/stac1206).
- Miller, L., T. J. Turner, and J. N. Reeves (2008). “An Absorption Origin for the X-ray Spectral Variability of MCG–6–30–15”. In: *Astronomy & Astrophysics* 483.2, pp. 437–452. DOI: [10.1051/0004-6361:200809590](https://doi.org/10.1051/0004-6361:200809590).
- Mineshige, S. et al. (2000). “Slim-Disk Model for Soft X-Ray Excess and Variability of Narrow-Line Seyfert 1 Galaxies”. In: *Publications of the Astronomical Society of Japan* 52.3, pp. 499–508. DOI: [10.1093/pasj/52.3.499](https://doi.org/10.1093/pasj/52.3.499).
- Mitsuda, K. et al. (1984). “Energy Spectra of Low-Mass Binary X-ray Sources Observed from TENMA”. In: *Publications of the Astronomical Society of Japan* 36, pp. 741–759.
- Miyakawa, T. et al. (2009). “Spectral Variation of the Seyfert 1 Galaxy MCG –6–30–15 Observed with Suzaku”. In: *Publications of the Astronomical Society of Japan* 61.6, pp. 1355–1364. DOI: [10.1093/pasj/61.6.1355](https://doi.org/10.1093/pasj/61.6.1355).
- Miyakawa, T., K. Ebisawa, and H. Inoue (2012). “A Variable Partial Covering Model for the Seyfert 1 Galaxy MCG –6–30–15”. In: *Publications of the Astronomical Society of Japan* 64.6, p. 140. DOI: [10.1093/pasj/64.6.140](https://doi.org/10.1093/pasj/64.6.140).
- Miyoshi, M. et al. (1995). “Evidence for a Black Hole from High Rotation Velocities in a Sub-Parsec Region of NGC4258”. In: *Nature* 373, pp. 127–129. DOI: [10.1038/373127a0](https://doi.org/10.1038/373127a0).
- Mizumoto, M., K. Ebisawa, and H. Sameshima (2014). “Interpretation of the X-ray Spectral Variation of 1H 0707-495 with a Variable Double Partial Covering Model”. In: *Publications of the Astronomical Society of Japan* 66.6, p. 122. DOI: [10.1093/pasj/psu121](https://doi.org/10.1093/pasj/psu121).
- Mizumoto, M. et al. (2019a). “Thermally Driven Wind as the Origin of Warm Absorbers in AGN”. In: *Monthly Notices of the Royal Astronomical Society* 489, pp. 1152–1160. DOI: [10.1093/mnras/stz2225](https://doi.org/10.1093/mnras/stz2225).
- Mizumoto, M. et al. (2019b). “X-Ray Reverberation Lags of the Fe-K Line Due to AGN Disc Winds”. In: *Monthly Notices of the Royal Astronomical Society* 482, pp. 5316–5326. DOI: [10.1093/mnras/sty3056](https://doi.org/10.1093/mnras/sty3056).

- Nandra, K. et al. (2007). “An XMM–Newton Survey of Broad Iron Lines in Seyfert Galaxies”. In: *Monthly Notices of the Royal Astronomical Society* 382.1, pp. 194–228. DOI: [10.1111/j.1365-2966.2007.12331.x](https://doi.org/10.1111/j.1365-2966.2007.12331.x).
- Nardini, E. et al. (2015). “Black Hole Feedback in the Luminous Quasar PDS 456”. In: *Science* 347.6224, pp. 860–863. DOI: [10.1126/science.1259202](https://doi.org/10.1126/science.1259202).
- Nomura, M. et al. (2016). “Radiation Hydrodynamic Simulations of Line-Driven Disk Winds for Ultra-Fast Outflows”. In: *Publications of the Astronomical Society of Japan* 68, p. 16. DOI: [10.1093/pasj/psv124](https://doi.org/10.1093/pasj/psv124).
- Ohsuga, K. et al. (2005). “Supercritical Accretion Flows around Black Holes: Two-dimensional, Radiation Pressure-dominated Disks with Photon Trapping”. In: *The Astrophysical Journal* 628.1, p. 368. DOI: [10.1086/430728](https://doi.org/10.1086/430728).
- Osterbrock, D. E. and O. Dahari (1983). “Spectra of Seyfert Galaxies and Seyfert Galaxy Candidates.” In: *The Astrophysical Journal* 273, pp. 478–488. DOI: [10.1086/161385](https://doi.org/10.1086/161385).
- Osterbrock, D. E. and R. W. Pogge (1985). “The Spectra of Narrow-Line Seyfert 1 Galaxies.” In: *The Astrophysical Journal* 297, pp. 166–176. DOI: [10.1086/163513](https://doi.org/10.1086/163513).
- Osterbrock, D. E. (1981). “Seyfert Galaxies with Weak Broad H Alpha Emission Lines”. In: *The Astrophysical Journal* 249, pp. 462–470. DOI: [10.1086/159306](https://doi.org/10.1086/159306).
- Parker, M. L. et al. (2017). “The Response of Relativistic Outflowing Gas to the Inner Accretion Disk of a Black Hole”. In: *Nature* 543.7643, pp. 83–86. DOI: [10.1038/nature21385](https://doi.org/10.1038/nature21385).
- Parker, M. L. et al. (2020). “Modelling X-ray RMS Spectra I: Intrinsically Variable AGNs”. In: *Monthly Notices of the Royal Astronomical Society* 492.1, pp. 1363–1369. DOI: [10.1093/mnras/stz3470](https://doi.org/10.1093/mnras/stz3470).
- Parker, M. L. et al. (2022). “The X-ray Disc/Wind Degeneracy in AGN”. In: *Monthly Notices of the Royal Astronomical Society* 513, pp. 551–572. DOI: [10.1093/mnras/stac877](https://doi.org/10.1093/mnras/stac877).
- Peterson, B. M. (1997). *An Introduction to Active Galactic Nuclei*.
- Pinto, C. et al. (2018). “Ultrafast Outflows Disappear in High-Radiation Fields”. In: *Monthly Notices of the Royal Astronomical Society* 476, pp. 1021–1035. DOI: [10.1093/mnras/sty231](https://doi.org/10.1093/mnras/sty231).
- Ponti, G. et al. (2010). “Relativistic Disc Reflection in the Extreme NLS1 IRAS13224-3809”. In: *Monthly Notices of the Royal Astronomical Society* 406, pp. 2591–2604. DOI: [10.1111/j.1365-2966.2010.16852.x](https://doi.org/10.1111/j.1365-2966.2010.16852.x).
- Proga, D., J. M. Stone, and T. R. Kallman (2000). “Dynamics of Line-driven Disk Winds in Active Galactic Nuclei”. In: *The Astrophysical Journal* 543.2, p. 686. DOI: [10.1086/317154](https://doi.org/10.1086/317154).
- Proga, D. and T. R. Kallman (2004). “Dynamics of Line-driven Disk Winds in Active Galactic Nuclei. II. Effects of Disk Radiation”. In: *The Astrophysical Journal* 616, pp. 688–695. DOI: [10.1086/425117](https://doi.org/10.1086/425117).
- Proga, D. (2007). “Theory of Winds in AGNs”. In: *Proc. of ASP Conference Series* 373, p. 267.
- Rakshit, S. et al. (2017). “A Catalog of Narrow Line Seyfert 1 Galaxies from the Sloan Digital Sky Survey Data Release 12”. In: *The Astrophysical Journal Supplement Series* 229, p. 39. DOI: [10.3847/1538-4365/aa6971](https://doi.org/10.3847/1538-4365/aa6971).
- Reeves, J. et al. (2008). “On Why the Iron K-shell Absorption in AGN Is Not a Signature of the Local Warm/Hot Intergalactic Medium”. In: *Monthly Notices of the Royal*

- Astronomical Society* 385, pp. L108–L112. DOI: [10.1111/j.1745-3933.2008.00443.x](https://doi.org/10.1111/j.1745-3933.2008.00443.x).
- Reynolds, C. S. (1997). “An X-ray Spectral Study of 24 Type 1 Active Galactic Nuclei”. In: *Monthly Notices of the Royal Astronomical Society* 286.3, pp. 513–537. DOI: [10.1093/mnras/286.3.513](https://doi.org/10.1093/mnras/286.3.513).
- Robertson, B. E. et al. (2022). *Discovery and Properties of the Earliest Galaxies with Confirmed Distances*. arXiv: [2212.04480](https://arxiv.org/abs/2212.04480) [astro-ph].
- Salpeter, E. E. (1964). “Accretion of Interstellar Matter by Massive Objects.” In: *The Astrophysical Journal* 140, pp. 796–800. DOI: [10.1086/147973](https://doi.org/10.1086/147973).
- Sargent, W. L. W. et al. (1978). “Dynamical Evidence for a Central Mass Concentration in the Galaxy M87.” In: *The Astrophysical Journal* 221, pp. 731–744. DOI: [10.1086/156077](https://doi.org/10.1086/156077).
- Schnittman, J. D. and J. H. Krolik (2010). “X-Ray Polarization from Accreting Black Holes: Coronal Emission”. In: *The Astrophysical Journal* 712, pp. 908–924. DOI: [10.1088/0004-637X/712/2/908](https://doi.org/10.1088/0004-637X/712/2/908).
- Schmidt, M. and R. F. Green (1983). “Quasar Evolution Derived from the Palomar Bright Quasar Survey and Other Complete Quasar Surveys.” In: *The Astrophysical Journal* 269, pp. 352–374. DOI: [10.1086/161048](https://doi.org/10.1086/161048).
- Schmidt, M. (1963). “3C 273 : A Star-Like Object with Large Red-Shift”. In: *Nature* 197, p. 1040. DOI: [10.1038/1971040a0](https://doi.org/10.1038/1971040a0).
- Seyfert, F. C. (1943). “Nuclear Emission in Spiral Nebulae”. In: *American Astronomical Society*, p. 14.
- Shakura, N. I. and R. A. Sunyaev (1973). “Black Holes in Binary Systems. Observational Appearance.” In: *Astronomy and Astrophysics* 24, pp. 337–355.
- Slipher, V. M. (1917). “The Spectrum and Velocity of the Nebula N.G.C. 1068 (M 77)”. In: *Lowell Observatory Bulletin* 3, pp. 59–62.
- Sobolewska, M. A. and C. Done (2007). “What Is the Origin of the Soft Excess in Active Galactic Nuclei?” In: *Monthly Notices of the Royal Astronomical Society* 374.1, pp. 150–158. DOI: [10.1111/j.1365-2966.2006.11117.x](https://doi.org/10.1111/j.1365-2966.2006.11117.x).
- Stevens, I. R. and T. R. Kallman (1990). “X-Ray Illuminated Stellar Winds: Ionization Effects in the Radiative Driving of Stellar Winds in Massive X-Ray Binary Systems”. In: *The Astrophysical Journal* 365, p. 321. DOI: [10.1086/169486](https://doi.org/10.1086/169486).
- Stern, B. E. et al. (1995). “On the Geometry of the X-Ray–Emitting Region in Seyfert Galaxies”. In: *The Astrophysical Journal* 449, p. L13. DOI: [10.1086/309617](https://doi.org/10.1086/309617).
- Strüder, L. et al. (2001). “The European Photon Imaging Camera on XMM-Newton: The Pn-CCD Camera”. In: *Astronomy & Astrophysics* 365.1, pp. L18–L26. DOI: [10.1051/0004-6361:20000066](https://doi.org/10.1051/0004-6361:20000066).
- Takeuchi, S., K. Ohsuga, and S. Mineshige (2013). “Clumpy Outflows from Supercritical Accretion Flow”. In: *Publications of the Astronomical Society of Japan* 65, p. 88. DOI: [10.1093/pasj/65.4.88](https://doi.org/10.1093/pasj/65.4.88).
- Takeuchi, S., K. Ohsuga, and S. Mineshige (2014). “Radiation Hydrodynamic Instability in a Plane-Parallel, Super-Eddington Atmosphere: A Mechanism for Clump Formation”. In: *Publications of the Astronomical Society of Japan* 66.2, p. 48. DOI: [10.1093/pasj/psu011](https://doi.org/10.1093/pasj/psu011).
- Tanaka, Y. et al. (2004). “Partial Covering Interpretation of the X-Ray Spectrum of the NLS1 1H 0707-495”. In: *Publications of the Astronomical Society of Japan* 56, pp. L9–L13. DOI: [10.1093/pasj/56.3.L9](https://doi.org/10.1093/pasj/56.3.L9).

- Tanaka, Y. et al. (1995). “Gravitationally Redshifted Emission Implying an Accretion Disk and Massive Black Hole in the Active Galaxy MCG–6–30–15”. In: *Nature* 375.6533, pp. 659–661. DOI: [10.1038/375659a0](https://doi.org/10.1038/375659a0).
- Tombesi, F. et al. (2010). “Evidence for Ultra-Fast Outflows in Radio-Quiet AGNs. I. Detection and Statistical Incidence of Fe K-shell Absorption Lines”. In: *Astronomy and Astrophysics* 521, A57. DOI: [10.1051/0004-6361/200913440](https://doi.org/10.1051/0004-6361/200913440).
- Tombesi, F. et al. (2012). “Evidence for Ultrafast Outflows in Radio-Quiet AGNs — III. Location and Energetics”. In: *Monthly Notices of the Royal Astronomical Society: Letters* 422.1, pp. L1–L5. DOI: [10.1111/j.1745-3933.2012.01221.x](https://doi.org/10.1111/j.1745-3933.2012.01221.x).
- Tomaru, R. et al. (2020). “The Thermal-Radiative Wind in Low-Mass X-ray Binary H1743-322 - II. Iron Line Predictions from Monte Carlo Radiation Transfer”. In: *Monthly Notices of the Royal Astronomical Society* 494, pp. 3413–3421. DOI: [10.1093/mnras/staa961](https://doi.org/10.1093/mnras/staa961).
- Turner, M. J. L. et al. (2001). “The European Photon Imaging Camera on XMM-Newton: The MOS Cameras : The MOS Cameras”. In: 365, pp. L27–L35. DOI: [10.1051/0004-6361:20000087](https://doi.org/10.1051/0004-6361:20000087). eprint: [astro-ph/0011498](https://arxiv.org/abs/astro-ph/0011498).
- Turner, T. J. et al. (2002). “The Spectral Energy Distribution of the Seyfert Galaxy Ton S180*”. In: *The Astrophysical Journal* 568.1, p. 120. DOI: [10.1086/338925](https://doi.org/10.1086/338925).
- Turner, T. J. and L. Miller (2009). “X-Ray Absorption and Reflection in Active Galactic Nuclei”. In: *Astronomy and Astrophysics Review* 17.1, pp. 47–104. DOI: [10.1007/s00159-009-0017-1](https://doi.org/10.1007/s00159-009-0017-1).
- Ueda, Y. et al. (2004). “Chandra High-Resolution Spectroscopy of the Absorption-Line Features in the Low-Mass X-Ray Binary GX 13+1”. In: *The Astrophysical Journal* 609, pp. 325–334. DOI: [10.1086/420973](https://doi.org/10.1086/420973).
- Urry, C. M. and P. Padovani (1995). “Unified Schemes for Radio-Loud Active Galactic Nuclei”. In: *Publications of the Astronomical Society of the Pacific* 107, p. 803. DOI: [10.1086/133630](https://doi.org/10.1086/133630).
- Vasudevan, R. V. et al. (2009). “Optical-to-X-ray Emission in Low-Absorption AGN: Results from the Swift–BAT 9-Month Catalogue”. In: *Monthly Notices of the Royal Astronomical Society* 399.3, pp. 1553–1575. DOI: [10.1111/j.1365-2966.2009.15371.x](https://doi.org/10.1111/j.1365-2966.2009.15371.x).
- Waddell, S. G. H. and L. C. Gallo (2020). “A Suzaku Sample of Unabsorbed Narrow-Line and Broad-Line Seyfert 1 Galaxies – I. X-ray Spectral Properties”. In: *Monthly Notices of the Royal Astronomical Society* 498.4, pp. 5207–5226. DOI: [10.1093/mnras/staa2783](https://doi.org/10.1093/mnras/staa2783).
- Watarai, K.-y. et al. (2000). “Galactic Black-Hole Candidates Shining at the Eddington Luminosity”. In: *Publications of the Astronomical Society of Japan* 52, p. 133. DOI: [10.1093/pasj/52.1.133](https://doi.org/10.1093/pasj/52.1.133).
- Weedman, D. W. (1977). “Seyfert Galaxies.” In: *Annual Review of Astronomy and Astrophysics* 15, pp. 69–95. DOI: [10.1146/annurev.aa.15.090177.000441](https://doi.org/10.1146/annurev.aa.15.090177.000441).
- Wilms, J., A. Allen, and R. McCray (2000). “On the Absorption of X-Rays in the Interstellar Medium”. In: *The Astrophysical Journal* 542.2, p. 914. DOI: [10.1086/317016](https://doi.org/10.1086/317016).
- Xu, X. et al. (2021). “The Origin of the Soft X-ray Excess in the Narrow-Line Seyfert 1 Galaxy SBS 1353+564”. In: *arXiv:2108.05265 [astro-ph]*. arXiv: [2108.05265 \[astro-ph\]](https://arxiv.org/abs/2108.05265).
- Yamasaki, H. et al. (2016). “Origin of the Characteristic X-ray Spectral Variations of IRAS 13224-3809”. In: *Publications of the Astronomical Society of Japan* 68.5, p. 80. DOI: [10.1093/pasj/psw070](https://doi.org/10.1093/pasj/psw070).

- Zakamska, N. L. et al. (2003). “Candidate Type II Quasars from the Sloan Digital Sky Survey. I. Selection and Optical Properties of a Sample at 0.3”. In: *The Astronomical Journal* 126, pp. 2125–2144. DOI: [10.1086/378610](https://doi.org/10.1086/378610).
- Zubovas, K. and A. King (2012). “CLEARING OUT A GALAXY”. In: *The Astrophysical Journal* 745.2, p. L34. DOI: [10.1088/2041-8205/745/2/L34](https://doi.org/10.1088/2041-8205/745/2/L34).

Acknowledgements

First, I would like to express my deep gratitude to my supervisor, Prof. Ken Ebisawa, for his continuous encouragement and passionate support throughout my Ph.D. journey. I am also extremely grateful to Dr. Misaki Mizumoto for all of his expertise and generous help with my research. This work would not have been possible without the diverse discussions with them.

I am deeply grateful to Dr. Masahiro Tsujimoto for providing me with strict but powerful support and constructive feedback. I am thankful to Prof. Chris Done, Dr. Kazushi Iwasawa, and Dr. Margherita Giustini for their valuable discussions and comments during my visit to Europe. I would also like to extend special thanks to the members of the Ebisawa lab. and my colleagues at ISAS for their friendship and fruitful chats. I acknowledge the financial support provided by JSPS Grant-in-Aid for JSPS Research Fellow Grant Number JP20J20809.

Finally, I would like to express my heartfelt thanks to my parents, sisters, grandparents, and foremost my wife Suzuka for their continuous support and encouragement.